



Investigation of shape coexistence and
triaxiality in the neutron-rich $A \approx 100$
region using lifetime measurements

Inaugural-Dissertation

zur
Erlangung des Doktorgrades
der Mathematisch-Naturwissenschaftlichen Fakultät
der Universität zu Köln

vorgelegt von

Arwin Esmaylzadeh
aus Köln

Köln 2022

Berichterstatter:

Prof. Dr. Jan Jolie
Prof. Dr. Andreas Zilges

Tag der letzten mündlichen Prüfung:

14. November 2022

Abstract

This doctoral thesis presents new experimental findings on the coexistence of nuclear shapes and triaxial deformed nuclei in the neutron rich $A \approx 100$ region. In this work, the nuclei ^{97}Sr , ^{102}Mo , $^{104,106}\text{Ru}$ and ^{112}Pd are investigated by measuring lifetimes of excited states. Lifetimes of low-lying states of ^{97}Sr were measured using the fast-timing method at the Lohengrin spectrometer located at the high-flux nuclear reactor of the Institut Laue-Langevin (ILL) in Grenoble, France. Low-energy states in ^{102}Mo , $^{104,106}\text{Ru}$ and ^{112}Pd were populated by a two-neutron transfer reaction and lifetimes were measured using the recoil distance Doppler shift (RDDS) technique at the Cologne Plunger setup. The ^{18}O particle beam for the transfer reaction was provided by the 10 MV Tandem accelerator of the Institut für Kernphysik of the Universität zu Köln.

The lifetime results derived for ^{97}Sr and ^{102}Mo are discussed within the context of shape coexistence observed in the strontium, zirconium and molybdenum isotopes around neutron number $N = 60$. The results of ^{97}Sr were compared to interacting boson-fermion model calculations that are based on the microscopic energy density functional. They improve the understanding of the spherical-deformed border at $N = 59$. The lifetime measurement of a possible high seniority shell-model state gives a hint of the spherical-deformed border. The $\rho(E0)$ strength obtained from the lifetime of the 0_2^+ state in ^{102}Mo reveals signs of shape coexistence but appears to be less pronounced compared to the isotonic partners in the strontium (^{98}Sr) and zirconium (^{100}Zr) isotopes.

The transition strengths deduced from lifetimes of states in the γ band in ^{102}Mo , $^{104,106}\text{Ru}$ and ^{112}Pd were used to interpret the triaxial and γ -soft behavior which is observed in these isotopic chains. The results of ^{102}Mo and $^{104,106}\text{Ru}$ were compared to those obtained within the mapped interacting boson model framework with microscopic input from Gogny mean-field calculations. The interpretations are based on the level energy spacing in the γ band, the transition strengths and the model calculations which underline the description of the nuclei in terms of γ -softness. The experimental data of the ^{112}Pd nucleus was compared to the γ -soft model, the Davydov-Filippov model and a more simple interacting boson model (IBM-1) calculation for the description of γ -softness. The experimental observations suggest a smooth transition from a relatively rigid triaxial nuclear structure in the low spin states to a nearly γ -soft structure in the higher spin states within the γ band.

Contents

1	Introduction	3
1.1	The neutron rich $A \approx 100$ region	3
1.1.1	Shape coexistence in the $Z \sim 40$, $N \sim 60$ nuclei	3
1.1.2	Triaxiality and γ -softness in the neutron rich Mo, Ru, and Pd isotopes	7
1.2	Nuclear Models	8
1.2.1	Davydov-Filippov Model	8
1.2.2	Wilets-Jean Model	9
1.2.3	Similarities and differences of the Davydov-Filippov and Wilets-Jean Model	10
1.2.4	Interacting Boson Model (IBM)	12
1.2.5	Mean field approach	14
1.3	Lifetime measurements	15
1.3.1	Basics of the recoil distance Doppler shift method	15
1.3.2	The fast-timing method	18
1.4	Experimental details	22
1.4.1	The two neutron transfer reaction at the Cologne Plunger spectrometer	22
1.4.2	The Lohengrin mass spectrometer at the ILL facility	23
2	Lifetime measurements and shape coexistence in ^{97}Sr	27
3	Lifetime measurements to investigate γ-softness and shape coexistence in ^{102}Mo	39
4	Triaxiality in the mid-shell nucleus ^{112}Pd	51
5	Investigation of γ-softness: Lifetime measurements in $^{104,106}\text{Ru}$	65
6	Summary and Conclusion	81
7	Outlook	85
	Bibliography	89
	List of Figures	105
	List of publications	107
	Acknowledgments	113
	Contribution	115
	Curriculum vitae	117
	Erklärung zur Dissertation	119

1 | Introduction

1.1 The neutron rich $A \approx 100$ region

The nuclei discussed within the context of this work are part of the neutron rich $A \approx 100$ region. This region is interpreted to stretch from the krypton isotopes ($Z = 36$) with $N \geq 50$ up to the cadmium isotopes ($Z = 48$) with $N \geq 60$. A partial excerpt of the region of interest is shown in Fig. 1. Nuclei in this region are known for different nuclear structures that occur and coexist with the dominant phenomena indicated by the two circles in Fig. 1. The green shaded area indicates the γ -soft region, where the nuclei show indicators of a γ -soft and triaxial deformation. The orange shaded area marks the nuclei around $Z \sim 40$ and $N \sim 60$ which undergo a rapid phase transition from a nearly spherical shape to a strongly deformed one. In the scope of this thesis, the shape coexistence as well as the triaxial shape of different nuclei in these two regions will be discussed. The nuclei marked with a red circle were populated in different experiments using either fission fragments (^{97}Sr) or two-neutron transfer reaction experiments using a ^{18}O beam (^{102}Mo , $^{104,106}\text{Ru}$ and ^{112}Pd) and will be discussed in this work. The orange circle indicates ^{99}Zr where experiments have already been performed and the analysis is in progress. In the following, a description of shape coexistence and γ -softness with the most important features will be presented and a summary of previous works will be given.

1.1.1 Shape coexistence in the $Z \sim 40$, $N \sim 60$ nuclei

In general, shape coexistence describes the phenomenon that two or more structures with different origins and deformations coexist in a single nucleus, e.g. a deformed and a spherical shape coexisting at low energy. Such coexisting structures occur in different regions along the whole nuclear chart [1, 2]. In this work, we will focus on the neutron-rich $A \approx 100$ region and especially nuclei with $Z \sim 40$ and $N \sim 60$. The structure of nuclei in this particular region has been investigated by different works [3–5] and is dominated by the sudden onset of deformation going from $N = 58$ to $N = 60$ [6–8]. An example is the sudden onset of collectivity in the neutron-rich even-even strontium and zirconium isotopes that undergo a rapid change from a spherical to a deformed type of structure [1, 2, 9]. Low lying excited 0^+ states, are strongly associated with shape coexistence. Such low-lying 0^+ states have been observed in the even-even nuclei around $A \approx 100$, i.e. $^{96,98}\text{Sr}$ [10, 11], $^{98,100}\text{Zr}$ [11, 12] and $^{100,102}\text{Mo}$ [12, 13]. The transition strengths between these 0^+ states and the 0_1^+ ground state are given in $\rho(E0)$ and are important indicators for the exhibition of shape coexistence. In the case of small or nonexistent $\rho(E0)$ strength, the mixing between the states is minimal which results in sharp mean square radii variations $\Delta \langle r^2 \rangle$ [14]. On the other hand, large $\rho(E0)$ strengths correspond to strong mixing and more gradual mean square radii variations $\Delta \langle r^2 \rangle$ as shown in Fig. 5 and 6 of Ref. [14]. For $N = 60$

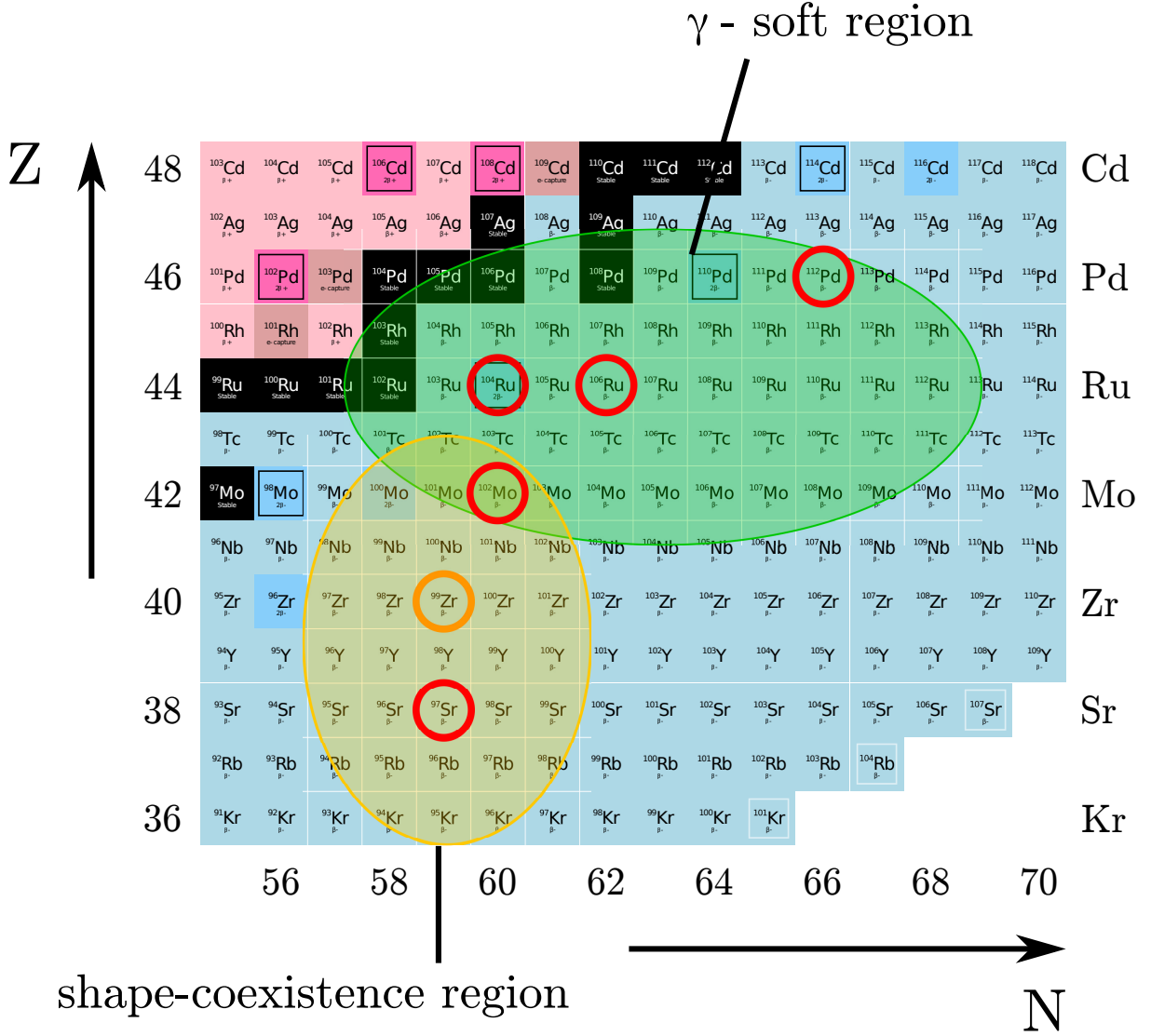


Figure 1: Partial chart of nuclei for the region of interest from $Z = 36$ and $N = 56$ up to $Z = 48$ and $N = 70$. The red circles indicate the investigated nuclei of this work, whereas the orange circle indicates ^{99}Zr where the investigation is in progress. Adapted from Ref. [15].

isotones, the $\rho(E0)$ strength are among the strongest along the nuclear chart [14, 16, 17]. These large values indicate the presence of coexisting structures, especially in the ^{98}Sr [16, 17], ^{100}Zr [16, 17] and ^{102}Mo [18] nuclei. For the higher- Z isotones, i.e. ^{104}Ru and ^{106}Pd these large $\rho(E0)$ strengths seem to diminish [2], but static and dynamic quadrupole moments in ^{104}Ru show that the shape coexistence might still persist [2, 19]. Rapid decreases in the energy of the 2_1^+ states in these nuclei can also be associated with a rapid change of structure and possibly two shapes coexisting. In Fig. 2(a) the rapid decrease in 2_1^+ state energies, going from $N = 58$ to $N = 60$, is shown for the strontium and zirconium isotopes. The isotopes undergo a shape phase transition from a spherical to a strongly deformed nucleus which is attributed to the specific ordering of the proton and neutron orbitals. In this case, the driving force is the strong isoscalar attractive

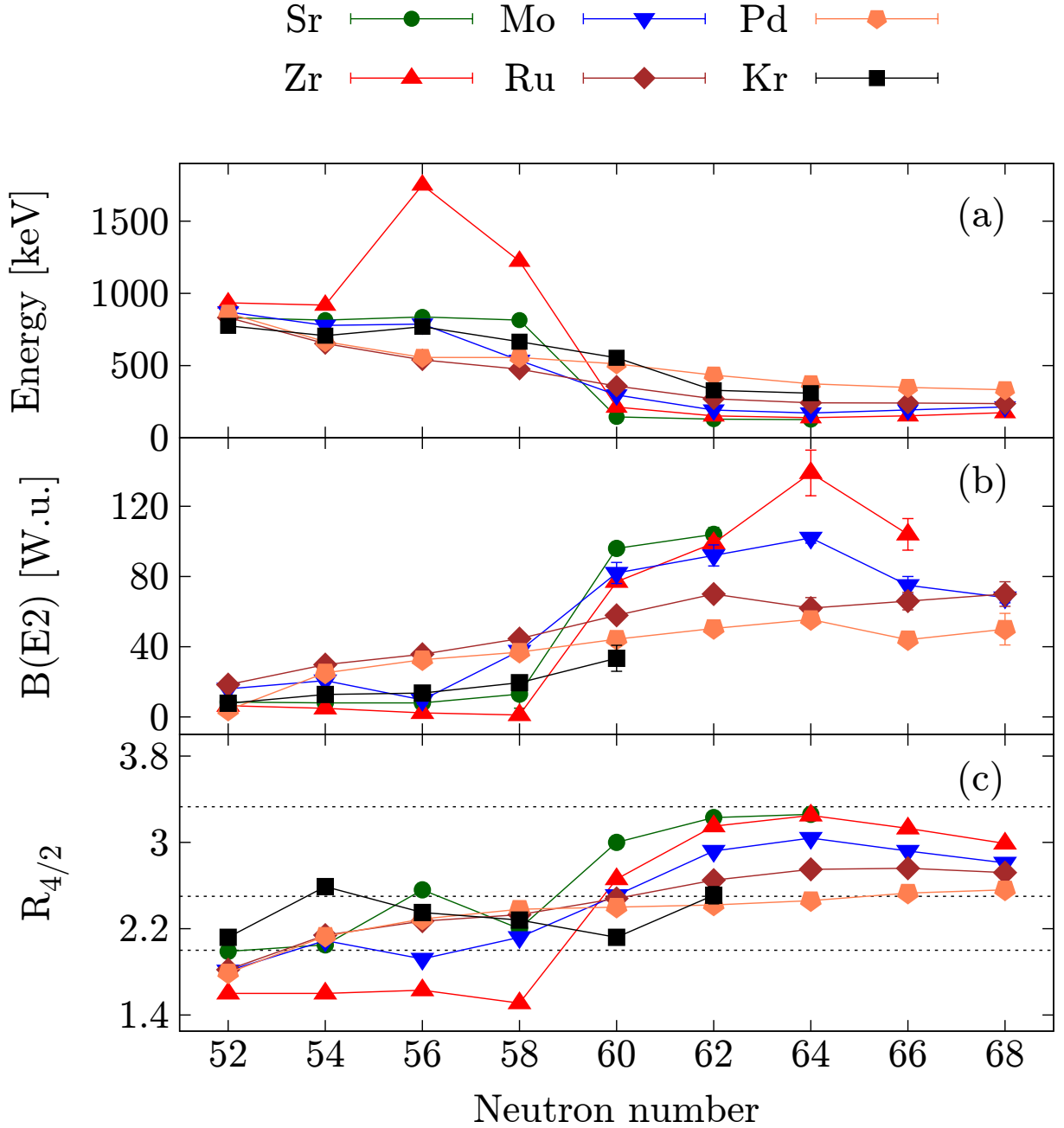


Figure 2: (a) The energies of the first excited 2_1^+ states for the Sr ($Z=38$), Zr ($Z=40$), Mo ($Z=42$), Ru ($Z=44$) and Pd ($Z=46$) isotopes for the neutron numbers $N = 52 - 68$. (b) The reduced transition probability $B(E2; 2_1^+ \rightarrow 0_1^+)$ given in Weisskopf units for the same isotopes. (c) The $R_{4/2}$ ratio for these isotopes is shown with the indication of the vibrational ($R_{4/2} = 2$), γ -soft ($R_{4/2} = 2.5$) as well as the rotational ($R_{4/2} = 3.33$) limits represented by the dashed lines. The data points of the individual isotopic chains are connected to guide the eye and are taken from [3, 5, 10–13, 20–43]

proton-neutron interaction between the spin-orbital partner $\pi(1g_{9/2})$ and $\nu(1g_{7/2})$ orbitals [7, 8, 44]. The addition of neutrons leads to a filling of the $\nu(1g_{7/2})$ orbital. The strong isoscalar interaction of proton and neutron orbitals reduces the gap between the $\pi(1g_{9/2})$ and $\pi(2p_{1/2})$

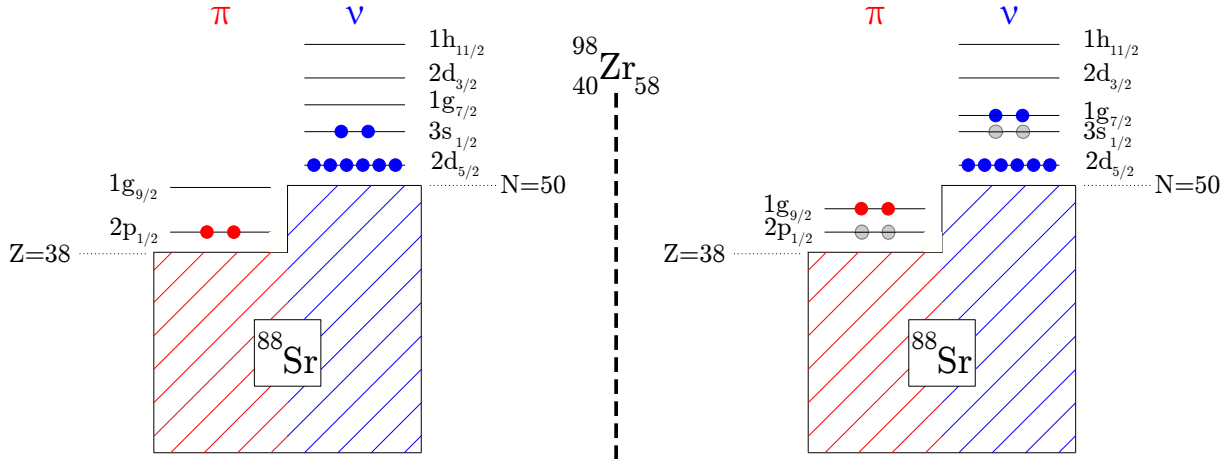


Figure 3: Schematic representation of two possible coexisting structures in ^{98}Zr . The proton (π) and neutron (ν) orbitals outside the semi-magic ^{88}Sr core are shown with the occupation of protons (red circles) and neutrons (blue circles) and proton/neutron holes (gray).

orbitals, which makes it energetically favorable to elevate protons from the $\pi(2p_{1/2})$ to the $\pi(1g_{9/2})$ orbital [7, 8, 44]. This in turn leads to a lowered $\nu(1g_{7/2})$ orbital which further promotes neutrons into it. The breaking down of the pairing π - π and ν - ν correlations and the development of spatial π - ν correlations results in a strong deformation [7, 8, 44]. The nuclei involved which undergo such a rapid change are $^{96,97,98}\text{Sr}$ and $^{98,99,100}\text{Zr}$ which have been studied in different works in recent years to investigate the underlying structure [3–5, 33–35, 45, 46]. The orbitals involved in this region are exemplary show in Fig. 3 for the case of ^{98}Zr with two possible configurations that coexist. Compared to the strontium and zirconium isotopes, the molybdenum isotopes show a less rapid shape evolution. It has been suggested that the emergence of triaxiality could play a major role [47]. The 2_1^+ state energy evolution of the molybdenum isotopes decrease at $N = 56$ and saturates after $N = 62$ (see Fig. 2(a)). On the other hand, the lower- Z krypton isotopes depict an even more gradual behavior where the energy of the 2_1^+ state decreases smoothly as a function of neutrons [32]. Although, the surrounding krypton and molybdenum isotopes show a less pronounced and more gradual evolution of 2_1^+ energies, there are still evidences of two coexisting structures as shown by different works [18, 31, 32, 48–50]. Another insightful aspect to classify the collective behavior of a nucleus, is the $R_{4/2} = E(4_1^+)/E(2_1^+)$ ratio illustrated in Fig. 2(c). A $R_{4/2}$ ratio around 2 is associated with a vibrational behavior [51] and for a $R_{4/2}$ of 2.5, a γ -soft nucleus is expected. A rigid rotor is expected at a $R_{4/2}$ ratio of 3.33, which usually occurs in well deformed or superdeformed nuclei [51]. The three important $R_{4/2}$ limits are indicated by the dashed lines in Fig. 2(c). The isotopes with $N = 52$ are located rather close to the vibrational limit which might originate from effects of the neutron shell closure at $N = 50$. By increasing the neutron number a development towards the γ -soft and even the rotational limit is observed with a sharp increase by going from 58 to 60 neutrons, especially for the zirconium isotopes. What stands out is the almost steady $R_{4/2}$ ratio evolution of the palladium isotopes which is located around the γ -soft limit with the only exceptions being the $N = 52, 54$ isotopes.

Further, Fig. 2(b) shows the reduced transition strengths for the $2_1^+ \rightarrow 0_1^+$ transition which is an important parameter in nuclear structure studies of even-even nuclei. The sudden change in 2_1^+ energy which is assumed to be a signature of shape coexistence is further underlined by the reduced transition strengths for the $2_1^+ \rightarrow 0_1^+$ transition. In the case of strontium and zirconium the $B(E2; 2_1^+ \rightarrow 0_1^+)$ value jumps from values around 10 W.u. to values larger than 100 W.u. This sudden drop in level energy as well as the significant increase in transition strength is expected to be correlated to a rapid shape change from spherical to a strongly deformed type of structure. The molybdenum isotopes show a less pronounced, but still noticeable change in the $B(E2; 2_1^+ \rightarrow 0_1^+)$ strength. Here, the increase of the transition strengths starts around $N = 56$ and saturates around $N = 62$. The higher- Z ruthenium and palladium isotopes show a smooth increase of $B(E2)$ values by approaching the neutron mid-shell at $N = 66$.

1.1.2 Triaxiality and γ -softness in the neutron rich Mo, Ru, and Pd isotopes

Some nuclei in the neutron-rich $A \approx 100$ region, especially in the molybdenum, ruthenium and palladium isotopes, show evidence of γ -softness which is related to the vibrational motion in the γ -direction and also the triaxial motion [18, 38, 41, 52–58]. Fig. 2(c) shows the evolution of the $R_{4/2}$ ratio of the even-even nuclei with $Z = 36 - 48$ for the neutron numbers $N = 52 - 68$. Some of the molybdenum, ruthenium and palladium isotopes possess a $R_{4/2}$ ratio close to the γ -soft limit ($R_{4/2} = 2.5$). In even-even nuclei the γ band with its 2^+ state band-head is strongly related to the triaxial motion of a nucleus [51] where the potential energy surface minimum is located at $\gamma = 30^\circ$ which is between $\gamma = 0^\circ$ (prolate shape) and $\gamma = 60^\circ$ (oblate shape). Another important sign is the relative position of the 2_γ^+ with respect to the 4_1^+ , which are close in energy in the triaxial case. In general, two limits of triaxial nuclei are considered, namely a rigid triaxial rotor and a so called γ -soft (or γ -unstable) rotor. The rigid triaxial rotor is assumed to have a steep and deep minimum at a particular value of γ , i.e. $\gamma = 30^\circ$ for the maximum of triaxiality. On the other hand, the γ -soft type of nucleus can freely vibrate in the γ degree of freedom (independent of the γ parameter), that is why it is often referred as γ -soft. The so-called staggering parameter can be used to distinguish between both extreme behaviors and is defined as [51, 59]

$$S(J) = \frac{E(J) - 2E(J-1) + E(J-2)}{E_{2_1^+}}. \quad (1.1)$$

In this case, $E(J)$ represents the energy of the level with spin J in the γ band. If the staggering parameter $S(J)$ is positive for odd-spin levels and negative for even spin levels, a γ -soft nucleus is assumed, whereas in the opposite case one assumes γ -rigidness for the nucleus [59]. Basically, the staggering parameter describes the position of odd-spin states relative to the even-spin states within the γ -band. In the case of a γ -soft nucleus the odd-spins are located closer to the higher spin states, e.g. the 3_γ^+ state is closer to the 4_γ^+ state than to the 2_γ^+ state. The opposite behavior is observed for the rigid triaxial case, e.g. the 3_γ^+ state is closer to the 2_γ^+ state than to the 4_γ^+ state. Two models discussing such low-lying 2_γ^+ states and triaxial shape, are the Davydov

Filippov rigid triaxial rotor model [60–62] and the Wilets-Jean γ unstable rotor model [63]. A detailed description of both models is given in chapter 1.2.

1.2 Nuclear Models

The Davydov-Filippov model [60–62] and the Wilets-Jean γ -soft model [63] are suitable tools for the complex region of interest, where shape coexistence, γ -softness and triaxiality occur. These models are used, in particular, to discuss the states in the γ band which are connected to the triaxial shape. The interacting boson model (IBM) [64] can be used for different phenomena occurring in nuclei like γ -soft behavior, vibrational behavior, rotational behavior but also shape coexistence.

1.2.1 Davydov-Filippov Model

The model of Davydov and Filippov for the description of triaxiality was developed around 1960 [60–62]. The model is based on the assumption of a steep and deep minimum of the potential $V(\gamma)$ at a particular value of γ which leads to a rigid shape with triaxial behavior [51]. Starting from the generalized nuclear model, the operator describing the rotational energy of an even nucleus has the form [60]:

$$H = \sum_{\lambda=1}^3 \frac{AJ_{\lambda}^2}{2 \sin^2(\gamma - \frac{2\pi}{3}\lambda)} \quad (1.2)$$

where A has the dimension of energy [60]. The J_{λ} operators are the projections of the nuclear angular momenta on the axes of a coordinate system connected with the nucleus [60]. The parameter γ varies between 0 and $\pi/3$ or 60° and determines the deviation of the shape of the nucleus from axial symmetry [60]. The energies and transition probabilities are only dependent on the parameter γ . For instance the energy of states with $J = 2$ (2_1^+ state and 2_2^+ state) given in any energy unit is expressed by [60]:

$$E_{2_1^+} = \frac{9 \left(1 - \sqrt{1 - \frac{8}{9} \sin^2(3\gamma)}\right)}{\sin^2(3\gamma)} \quad \text{and} \quad E_{2_2^+} = \frac{9 \left(1 + \sqrt{1 - \frac{8}{9} \sin^2(3\gamma)}\right)}{\sin^2(3\gamma)}. \quad (1.3)$$

The energy level with $J = 3$ is defined as [60]:

$$E_{3_1^+} = \frac{18}{\sin^2(3\gamma)} = E_{2_1^+} + E_{2_2^+}. \quad (1.4)$$

To calculate the energy levels with $J = 4$ the following equations needs to be solved [60]:

$$E_{4_1^+}^3 - \frac{90}{\sin^2(3\gamma)} E_{4_1^+}^2 + \frac{48}{\sin^4(3\gamma)} [27 + 26 \sin^2(3\gamma)] E_{4_1^+} - \frac{640}{\sin^4(3\gamma)} [27 + 7 \sin^2(3\gamma)] = 0. \quad (1.5)$$

The two spin $J = 5$ energy levels $E_{5_1^+}$ and $E_{5_2^+}$ are given by the formula [60]

$$E_{5_1^+/5_2^+} = \frac{45 \pm 9\sqrt{9 - 8\sin^2(3\gamma)}}{\sin^2(3\gamma)}. \quad (1.6)$$

The reduced electrical quadrupole transition probability given in units of $e^2Q_0^2/16\pi$ for $J = 2 \rightarrow J = 0$ and $J = 3 \rightarrow J = 2$ transitions are defined as [60]:

$$B(E2; 2_1^+ \rightarrow 0_1^+) = \frac{1}{2} \left[1 + \frac{3 - 2\sin^2(3\gamma)}{\sqrt{9 - 8\sin^2(3\gamma)}} \right], \quad (1.7)$$

$$B(E2; 2_2^+ \rightarrow 0_1^+) = \frac{1}{2} \left[1 - \frac{3 - 2\sin^2(3\gamma)}{\sqrt{9 - 8\sin^2(3\gamma)}} \right], \quad (1.8)$$

$$B(E2; 2_2^+ \rightarrow 2_1^+) = \frac{10}{7} \frac{\sin^2(3\gamma)}{9 - 8\sin^2(3\gamma)}, \quad (1.9)$$

$$B(E2; 3_1^+ \rightarrow 2_1^+) = \frac{25}{28} \left(1 - \frac{3 - 2\sin^2(3\gamma)}{\sqrt{9 - 8\sin^2(3\gamma)}} \right), \quad (1.10)$$

$$B(E2; 3_1^+ \rightarrow 2_2^+) = \frac{25}{28} \left(1 + \frac{3 - 2\sin^2(3\gamma)}{\sqrt{9 - 8\sin^2(3\gamma)}} \right). \quad (1.11)$$

The equations for the reduced transition probabilities involving higher spin levels $J \geq 4$ are more complex and different coefficients extracted from the wave function need to be taken into account. The formula to calculate these transition probabilities and a detailed table of the required coefficients are given in Ref. [61]. For $\gamma \rightarrow 0^\circ$ the levels of the ground state band resemble the properties of an axially-symmetric nucleus. The non-yrast energy levels tend to infinity for $\gamma \rightarrow 0^\circ$ which are called "anomalous" levels, i.e. the 2_2^+ , 3_1^+ , 4_2^+ , ... states. An illustration of this behavior can be found in Fig. 1 of Ref. [61]. By approaching $\gamma = 30^\circ$ the "anomalous" level energies decrease dramatically, where even the 2_2^+ state that is lower in energy than the 4_1^+ state, which is a sign for a rigid triaxial nucleus.

1.2.2 Wilets-Jean Model

In contrast to the rigid γ parameter in the Davydov-Filippov model, in the Wilets-Jean Model this parameter is free in the γ degree of freedom and thus allows a vibration. This feature is often described as γ -soft or γ -unstable. The γ -soft approach corresponds to a nuclear potential located at a finite β deformation, but is completely flat in the γ degree of freedom. In this case, the nucleus can oscillate with γ values ranging from 0° to 60° while having an average value of $\gamma_{\text{rms}} = 30^\circ$ [51]. The calculation of the energy levels for a given angular momentum Λ are given by the following equation [51, 63]:

$$E(\Lambda) = \nu\Lambda(\Lambda + 3), \quad \Lambda = 0, 1, 2, 3, \dots, \quad (1.12)$$

where ν is a constant given in any energy unit. The $J = 2\Lambda$ states correspond to the yrast states. Each Λ value (for $\Lambda > 1$) is degenerated with respect to the angular momentum J and different level occur for a given angular momentum. The set of levels is analogous to the γ vibrational band and to the anomalous levels of the Davydov model for large γ values [51]. The energy levels and spins for the first few Λ values are summarized in Tab. 1.1. In the Wilets-Jean model the $E2$ transitions must satisfy the selection rules $\Delta\Lambda = \pm 1$, which corresponds to a non-existing transition strengths for the $2_2^+ \rightarrow 0_1^+$ transition.

Table 1.1: The energy of the first few excited states given in any energy unit and the corresponding spins calculated with the Wilets-Jean model.

Λ	$E(\Lambda)$	J
0	0	0
1	4	2
2	10	2,4
3	18	0,3,4,6
4	28	2,4,5,6,8

1.2.3 Similarities and differences of the Davydov-Filippov and Wilets-Jean Model

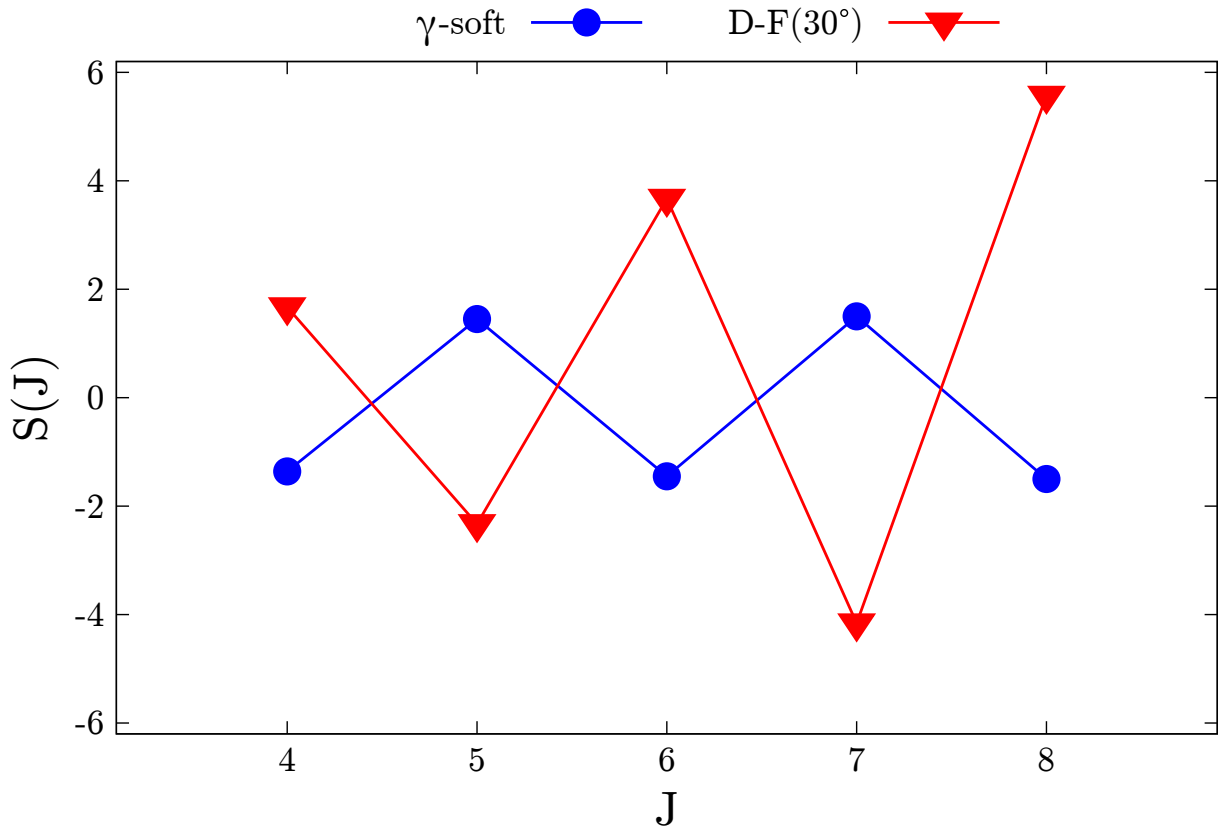


Figure 4: Comparison of the staggering parameter $S(J)$ for the Davydov-Filippov model (D-F) with $\gamma = 30^\circ$ and the Wilets-Jean model (γ -soft). For further details see text.

Table 1.2: Different ratios of the Wilets-Jean model and the Davydov-Filippov model calculated for γ values between 0° and 30° .

	γ_{rms}	$R_{4/2}$	$R_{6/2}$	$R_{8/2}$	$R_{10/2}$	$R_{22/2}$	$R_{3/2}$	$B_{4/2}$	$B_{6/2}$	$B_{22/2}$	$B'_{22/2}$
D-F model	0°	3.33	7.00	12.00	18.33	∞	∞	1.43	1.57	0.00	1.43
	5°	3.33	7.00	11.99	18.31	64.20	65.20	1.42	1.56	0.01	1.49
	10°	3.32	6.94	11.82	17.91	15.90	16.90	1.40	1.55	0.05	1.70
	15°	3.27	6.69	11.10	16.42	6.85	7.85	1.38	1.56	0.15	2.70
	20°	3.12	6.07	9.79	14.30	3.73	4.73	1.37	1.62	0.38	5.35
	25°	2.84	5.34	8.55	12.47	2.41	3.41	1.37	1.70	0.91	20.6
	30°	2.66	5.00	8.00	11.66	2.00	3.00	1.39	1.73	1.43	∞
W-J model	30°	2.5	4.50	7.00	10	2.50	4.50	1.43	1.67	1.43	∞

Both models are geometric models to describe the triaxial shape of a nucleus. The Davydov-Filippov (D-F) model is completely rigid in γ while the Wilets-Jean (W-J) model allows to move freely (or soft) in the γ degree of freedom. Similarities and differences between the D-F and W-J models are shown with different quantities. For this comparison, we define the following ratios of level energies:

$$R_{4/2} = E_{4_1^+}/E_{2_1^+}, \quad R_{6/2} = E_{6_1^+}/E_{2_1^+}, \quad R_{8/2} = E_{8_1^+}/E_{2_1^+}, \quad (1.13)$$

$$R_{10/2} = E_{10_1^+}/E_{2_1^+}, \quad R_{22/2} = E_{2_2^+}/E_{2_1^+}, \quad R_{3/2} = E_{3_1^+}/E_{2_1^+} \quad (1.14)$$

and reduced transition probability ratios which are defined as:

$$B_{4/2} = B(E2; 4_1^+ \rightarrow 2_1^+)/B(E2; 2_1^+ \rightarrow 0_1^+), \quad B_{6/2} = B(E2; 6_1^+ \rightarrow 4_1^+)/B(E2; 2_1^+ \rightarrow 0_1^+), \quad (1.15)$$

$$B_{22/2} = B(E2; 2_\gamma^+ \rightarrow 2_1^+)/B(E2; 2_1^+ \rightarrow 0_1^+), \quad B'_{22/2} = B(E2; 2_2^+ \rightarrow 2_1^+)/B(E2; 2_2^+ \rightarrow 0_1^+). \quad (1.16)$$

The ratios defined in Eqs. 1.13-1.16 are summarized and compared in Tab. 1.2. While for the Davydov-Filippov model different γ values can be used to calculate energy levels, the Wilets-Jean model has a γ_{rms} of 30° . The direct comparison between the two models for $\gamma = 30^\circ$ pronounces the differences. The $R_{4/2}$, $R_{6/2}$, $R_{8/2}$ and $R_{10/2}$ are slightly lower for the Wilets-Jean model. The two ratios including states of the γ band, i.e. $R_{22/2}$ and $R_{3/2}$, are predicted lower by the Davydov-Filippov model. The Wilets-Jean and Davydov-Filippov model calculate almost similar

values for the $B_{4/2}$ and $B_{6/2}$ ratios, while both approaches predict similar values for the $B_{2_2/2}$ and $B'_{2_2/2}$ ratios. To show differences of both models, the staggering parameter defined in Eq. 1.1 can be used. The staggering parameter for the spins $J = 4, 5, 6, 7$ of both model shows an opposite behavior as clearly illustrated in Fig. 4. The staggering parameter is a strong indicator to describe the triaxial shape and is an useful tool to classify and discuss experimental data within these two models.

1.2.4 Interacting Boson Model (IBM)

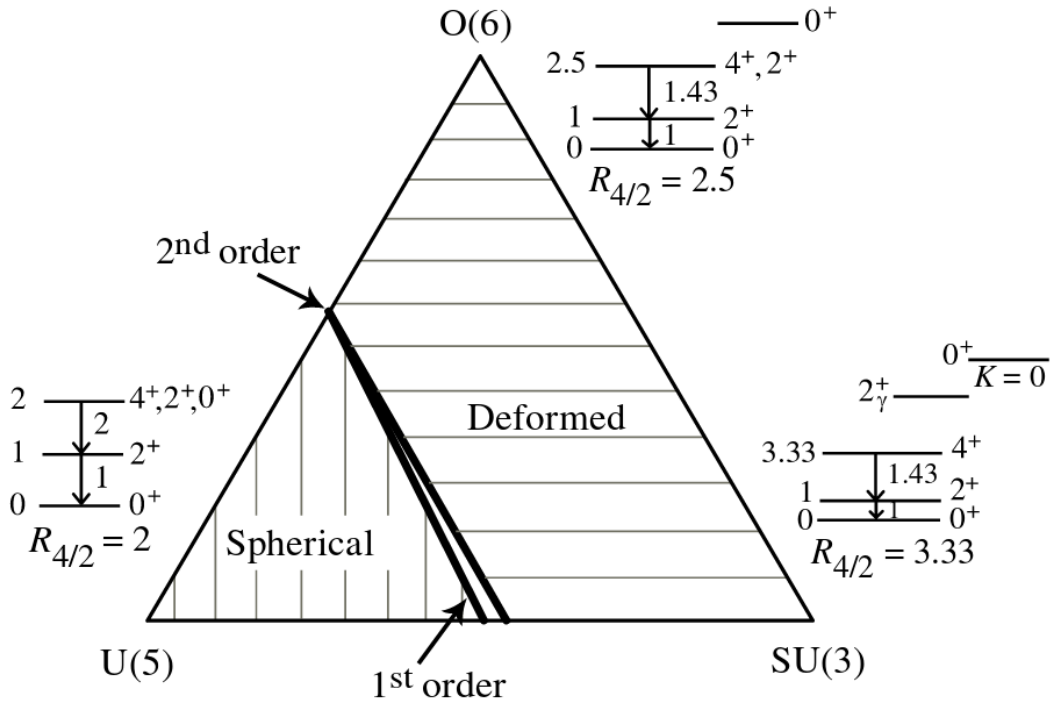


Figure 5: The Casten triangle with the three sub-algebraic chains of the $U(6)$ symmetry group. Picture adopted from [65].

The interacting boson model (IBM) was introduced in 1974 by F. Iachello and A. Arima to describe collective properties in even-even nuclei using an algebraic approach [51, 64, 66, 67]. The basic idea is to couple the free valence nucleons or holes to bosons [51, 64, 66, 67] where the general bosonic commutation relations are satisfied. In the simplest case, called the IBM-1, valence protons and neutrons are separately coupled to bosons, but are treated equally. In the simplest version of the IBM (sd-IBM), the bosons are only allowed in two states with angular momentum $L = 0$ and $L = 2$ called s-bosons and d-bosons, respectively. Different extensions of the model, which will not be discussed here, include higher and odd angular momentum bosons, like p-bosons with $L = 1$, f-bosons with $L = 3$ or g-bosons with $L = 4$. The s boson ($L = 0$) has only one magnetic orientation, whereas the d boson ($L = 2$) has five, i.e. $0, \pm 1$, and ± 2 . The elementary creation and annihilation operators are given by $\hat{s}, \hat{s}^\dagger, \hat{d}_M, \hat{d}_M^\dagger$ with M describing the magnetic quantum number. The following generators $G_{L,M}^{i,j}$ describe the coupling of these

operators [68]:

$$\begin{aligned}
G_{0,0}^{s,s} &= \left[\hat{s}^\dagger \times \hat{s} \right]_0^{(0)} \\
G_{2,M}^{s,d} &= \left[\hat{s}^\dagger \times \tilde{d} \right]_M^{(2)} \quad \text{with} \quad -2 \leq M \leq 2, \quad \Delta M = 1 \\
G_{2,M}^{d,s} &= \left[\hat{d}^\dagger \times \hat{s} \right]_M^{(2)} \quad \text{with} \quad -2 \leq M \leq 2, \quad \Delta M = 1 \\
G_{J,M}^{d,d} &= \left[\hat{d}^\dagger \times \tilde{d} \right]_M^{(J)} \quad \text{with} \quad J = 0, 1, 2, 3, 4 \quad \text{and} \quad -J \leq M \leq J, \quad \Delta M = 1
\end{aligned}$$

with $\tilde{d} = (-1)^m \hat{d}_{-m}$. The coupling results in 36 possible operators which can be described in group theory by the unitary algebra $U(6)$ in Racah's form. The $U(6)$ group is a six dimensional space and obtains three sub-group chains, which all end in the rotation group $O(3)$. All group chains and the corresponding quantum numbers are [69]:

$$\begin{aligned}
\text{I.} \quad & U(6) \supset U(5) \supset O(5) \supset O(3) & (1.17) \\
& N \quad n_d \quad \nu \quad n_{\Delta J}
\end{aligned}$$

$$\begin{aligned}
\text{II.} \quad & U(6) \supset SU(3) \supset O(3) & (1.18) \\
& N \quad (\lambda, \mu) \quad KJ
\end{aligned}$$

$$\begin{aligned}
\text{III.} \quad & U(6) \supset O(6) \supset O(5) \supset O(3) & (1.19) \\
& N \quad \sigma \quad \tau \quad v_{\Delta J}
\end{aligned}$$

The three chains, namely the $U(5)$, $SU(3)$ and $O(6)$ chains, are interpreted as spherical harmonic vibrator, an axially-symmetric rigid rotor and axially-asymmetric but γ -soft rotor. The relation between the three chains for the $U(6)$ group is shown by the so-called Casten triangle in Fig. 5 [51, 65]. Although every point within the Casten triangle can be associated with a distinct nuclear structure, not every nuclear structure can be assigned within the triangle. An example and commonly used IBM Hamiltonian is described by the following equations:

$$\begin{aligned}
\hat{H} &= \epsilon \hat{n}_d + a_1 \hat{L} \hat{L} + a_2 \hat{Q}_\chi \hat{Q}_\chi + a_3 \hat{T}_3^2 + a_4 \hat{T}_4^2 + \mathcal{O}(\hat{T}_5) & (1.20) \\
\text{with} \quad \hat{n}_d &= \hat{d}^\dagger \tilde{d} = \sqrt{5} \hat{T}_0, \\
\hat{T}_J &= \left(\hat{d}^\dagger \tilde{d} \right)^{(J)} \quad \text{with } J = 0, 1, 2, 3, 4, \\
\hat{Q}_\chi &= \left(\hat{d}^\dagger \hat{s} + \hat{s}^\dagger \tilde{d} \right) + \chi \left(\hat{d}^\dagger \tilde{d} \right)^{(2)}, \\
\hat{L} &= \sqrt{10} \hat{T}_1.
\end{aligned}$$

In most cases the Hamiltonian is reduced to:

$$\hat{H} = \epsilon \hat{n}_d + a_1 \hat{L} \hat{L} + a_2 \hat{Q}_\chi \hat{Q}_\chi, \quad (1.21)$$

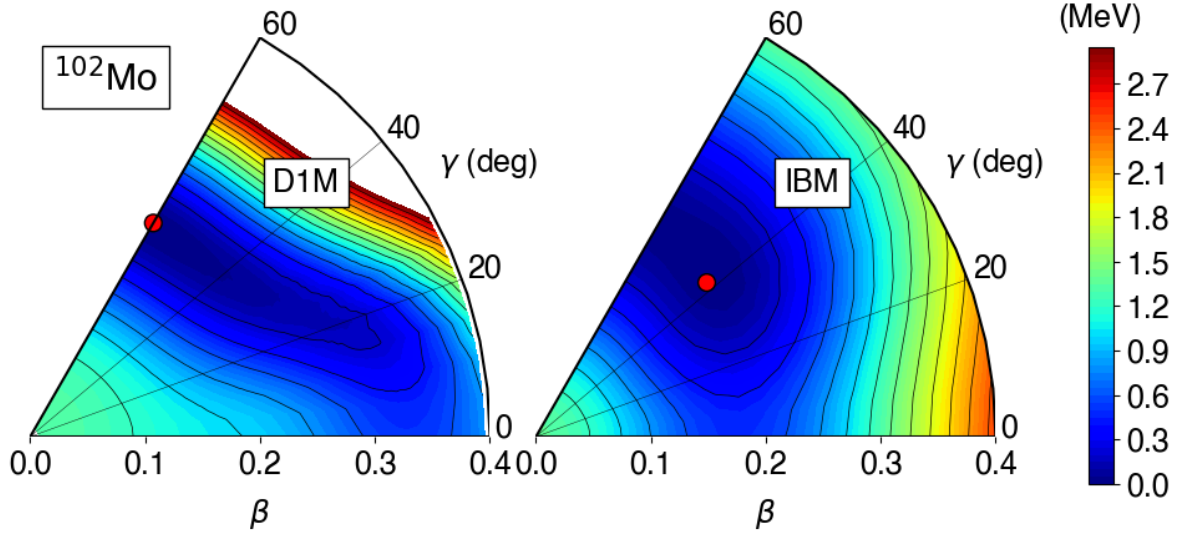


Figure 6: Contour plot of the deformation-energy surface in the (β, γ) plane for ^{102}Mo computed with the constrained HFB method by using the Gogny functional D1M (left) and with the mapped IBM (right). The red dots indicate the minimum of the energy surface plots and the difference between two neighbors contours is 100 keV. Figure taken from Ref. [18].

with \hat{L} being the angular momentum operator and \hat{Q} the quadrupole operator. Another important parameter to describe a nucleus is the E2 transition probability $T(E2)$. Within the IBM formalism, the following formula is used to calculate the transition probability:

$$\hat{T}(E2) = e_B \hat{Q}_\chi = e_B \left[\hat{s}^\dagger \hat{a} + \hat{a}^\dagger \hat{s} + \chi \left(\hat{d}^\dagger \tilde{\hat{d}} \right) \right], \quad (1.22)$$

where e_B is the effective boson charge. Note, that other Hamiltonians are possible and used in different works.

1.2.5 Mean field approach

In 2008, a new novel way of determining the parameters of the IBM Hamiltonian was proposed [70, 71], which uses mean-field interactions like Skyrme [72–76] and/or Gogny [77, 78]. The Skyrme interaction relies on an effective interaction with a three body term. It assumes a short range of the interactions and includes only nearest neighbors to interact with. While the Skyrme interaction is a successful interaction it does not account for intermediate and long range parts of the realistic effective interaction. Therefore, the Gogny interaction was introduced in 1973 to account for the longer range interactions by exchanging the two body force with a sum of two Gaussians with spin-isospin exchange mixtures [77–79]. The first step in this new approach is to perform constrained Hartree–Fock–Bogoliubov (HFB) calculations which are based on the chosen Skyrme or Gogny interaction [79]. In this work mainly the parametrization D1M of the Gogny energy density functional is used [80, 81]. The results from this calculation are visualized

in potential energy surface (PES) plots in terms of the deformation parameter β and γ . Such a contour plot of energies for ^{102}Mo in the β - γ plane is exemplary shown for the Gogny-D1M interaction on the left side in Fig. 6. With this approach, the IBM parameters are determined by drawing the IBM PES to reproduce the overall shape of the mean-field PES [70, 71]. The overall shape is characterized by the location of the minimum of the mean-field PES and the curvatures for both the β and γ direction [70, 71]. The results of the IBM PES are exemplary shown for ^{102}Mo on the right side in Fig. 6. With the determined parameters, different aspects of nuclear structure like energy levels and transition rates can be calculated accordingly. This approach has been used to determine energy levels, transition rates, quadrupole moments, octupole moments, $\log ft$ values and different other nuclear structure related signatures [82–87].

1.3 Lifetime measurements

With the knowledge of the lifetime of an excited state, electromagnetic properties of nuclei can be deduced to study the interaction of nucleons. Lifetimes and electromagnetic transition matrix elements and hence reduced transition probabilities $B(\sigma L, J_i \rightarrow J_f)$ are directly related and are common experimental observables. They can be used as a benchmark and compared to nuclear models. Lifetimes in nuclear physics cover a wide range of possible values, starting from nuclear resonances with lifetimes in the order of 10^{-22} s up to β decays with lifetimes up to 10^{10} years. Different techniques are used to obtain nuclear lifetimes depending on their magnitude. The lifetimes in this thesis are in the order of a few picoseconds up to a few hundred nanoseconds. In this work, lifetimes in the picosecond regime are determined using the recoil-distance Doppler shift (RDDS) method in combination with the Bateman equations [88] and the differential decay curve method (DDCM) [89]. For the lifetimes in the pico- and nanosecond region, the fast-timing technique in combination with the centroid difference method are used [90–94]. The basics of the RDDS and fast-timing technique will be discussed in the following chapters.

1.3.1 Basics of the recoil distance Doppler shift method

The recoil distance Doppler shift (RDDS) method relies on the Doppler shift of γ rays stemming from excited states of nuclei. The nuclear excited states of interest are produced by a beam-induced nuclear reaction in a thin target. The beam leads to an energy and momentum transfer and leaves the excited nucleus of interest with a velocity v . The nuclei are recoiling and stopped after a certain and well-defined flight time by a stopper foil. The target and stopper foil are stretched and mounted in parallel inside the Cologne Plunger device [95]. The setup is designed so that the distance between stopper and target can be changed and hence the flight time between the foils. The distance is controlled by a feedback system and held at a constant distance [95]. Usually, the de-excitation of a state happens by emitting γ rays which can be detected by commonly used high purity germanium (HPGe) detectors. If the γ -ray emits in flight, the detectors which are positioned at an angle θ with respect to the beam axis observe a Doppler-shifted energy according

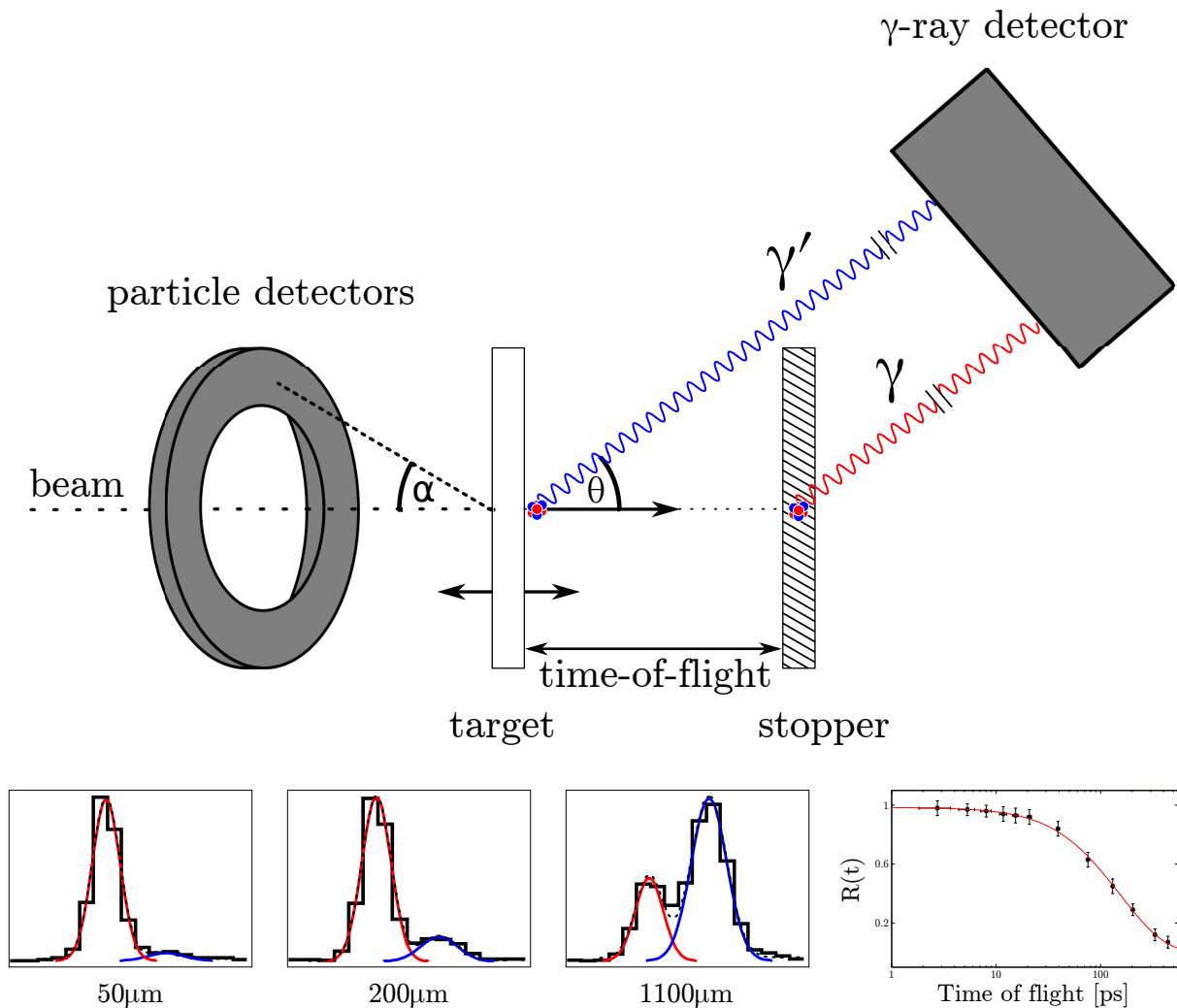


Figure 7: Schematic picture of a RDDS setup using particle detectors. The recoiling beam-like particles scatter at backward angles for the chosen beam energies and particles are detected by solar cells. The excited recoiling nuclei of interest decay via γ rays either in flight (red) or at the stopper foil (blue) which are detected by High Purity Germanium (HPGe) detectors. Further the basic principle of the RDDS method is shown in the lower part including the evolution of the Doppler shifted (blue) and non Doppler shifted (red) peak as well as the resulting decay curve.

to:

$$E = E_0 \frac{\sqrt{1 - \beta^2}}{1 - \beta \cos(\theta)}, \quad (1.23)$$

where $\beta = v/c$ and E_0 is the energy of the γ -ray depopulating the state of interest at rest. Such a setup with both foils and the emission of γ rays of the recoiling nucleus is schematically shown in Fig. 7, where the shifted component (blue) is growing by increasing the distance. By using this property, the γ -ray detectors will observe a distance (and lifetime) dependent intensity of the shifted component $I_s(t)$ (excited state decaying in flight) and of the unshifted component $I_u(t)$ (excited state decaying at the stopper foil). These two intensities can be used to define the

so-called decay curve for the state i [95]:

$$R_i(t) = \frac{I_i^u(t)}{(I_i^u(t) + I_i^s(t))} \quad (1.24)$$

and the corresponding flight curve [95]:

$$F_i(t) = \frac{I_i^s(t)}{(I_i^u(t) + I_i^s(t))} = 1 - R_i(t). \quad (1.25)$$

In the case where the state has no feeding γ rays, i.e. the state is directly populated in a nuclear reaction, the decay curve can be described by:

$$R_i(t) = n_i(0)e^{-t\lambda_i} \quad (1.26)$$

where $\lambda_i = 1/\tau_i$ with τ_i being the lifetime of the state i and $n_i(0)$ is the initial level population. Usually, more complicated feeding patterns are observed where the delayed feeding contributions need to be taken into account. An established approach is using first order differential equations which are known as Bateman equations [88]. The solution of the Bateman equations include the direct population $n_i(0)$ of the state, the time of flight t , the decay constant λ_i and branching ratios of feeding states. The Bateman equations are governed by the following differential equation:

$$\frac{d}{dt}n_i(t) = -\lambda_i n_i(t) + \sum_{k=i+1}^K \lambda_k n_k(t) b_{ki} \quad (1.27)$$

where k denotes the feeding of the excited state i , K the total number of feeding states and b_{ki} the branching ratio between the states k and i . The solution of the differential equation with respect to the decay curve is [95]:

$$R_i(t) = P_i e^{-t\lambda_i} + \sum_{k=i+1}^K M_{ki} \left[(\lambda_i/\lambda_k) e^{-t\lambda_k} - e^{-t\lambda_i} \right] \quad (1.28)$$

where M_{ki} is defined recursively as [95]:

$$M_{ki}(\lambda_i/\lambda_k - 1) = b_{ki} P_k - b_{ki} \sum_{m=k+1}^K M_{mk} + \sum_{m+1}^{k-1} M_{km} b_{mi}(\lambda_m/\lambda_k). \quad (1.29)$$

For every k , P_k denotes the direct feeding intensity of the level k [95]. As the solution above points out, it is very important to measure the absolute distance between the target and the stopper foil to obtain an accurate flight time of the recoiling nuclei. To measure the shortest achievable distance with no electrical contact the capacitance method described in Ref. [95, 96] is used. Another approach to avoid the need to measure of absolute distances and to measure lifetimes of excited states, is the Differential Decay Curve Method (DDCM) [89, 95, 97]. The DDCM has several advantages compared to the solution of the Bateman equations. The application of this

method helps to identify different types of systematic errors [89, 95]. By using the Bateman equations, an assumption on the curve shape of $R(t)$ is made which are not experimentally ensured whereas the DDCM uses no assumptions on the shape of the curve'. Further, it relies only on the relative distances between target and stopper, which has usually a known precision below $1 \mu\text{m}$ controlled by the feedback system. Following the DDCM, the lifetime of a state is determined by [89]:

$$\tau_i(x) = \frac{R_i(x) + \sum_k (b_{ki} I_k(x)/I_i(x)) R_k(x)}{v \frac{d}{dx} R_i(x)} = \frac{U_i(x)}{v \frac{d}{dx} R_i(x)}, \quad (1.30)$$

where I_i and I_k are the total intensities of the transitions depopulating and populating the state i respectively, in addition with the velocity v of the ejected nucleus. In low statistics cases the method explained in Ref. [98] can be used to obtain lifetimes. The summed spectra of all distances j can be used in combination with the following equations [98]:

$$R_{\text{sum}} = \frac{\sum_j I_j^u}{\sum_j I_j^u + \sum_j I_j^s} = \sum_j n_j R(t_j), \quad (1.31)$$

where I_j^u and I_j^s are the intensities of the unshifted and shifted component, respectively. The flight-time of each distance is described by t_j . The normalization factor n_j can be obtained experimentally by e.g. integrating the full spectra after applying a gate on both components of the strongest transition of the corresponding nucleus (in even-even nuclei usually the $2_1^+ \rightarrow 0_1^+$ transition). The normalization is applied for each distance individually.

1.3.2 The fast-timing method

The fast-timing technique is capable of measuring lifetimes from a few μs down to a few ps. The basic principle relies on the direct time difference measurement of two experimental observables related to the population and depopulation of a nuclear excited state of interest. The observables can be of different type and, in principle, any detection hit that provides a time reference corresponding to the feeding or decaying of the state of interest can be used. Often observables are provided by the detection of γ -rays, (heavy) ions, β -particles, conversion electrons, etc. To obtain lifetime information of excited states, a case dependent decision of a suitable combination of these events needs to be determined. In the scope of this work the γ - γ , particle- γ and the particle- γ - γ fast timing method were used to determine lifetimes of excited states. For example, in this work, the products stemming from a neutron induced fission reaction where a nuclear reactor provides the thermal neutrons, were recorded by a ΔE_1 - ΔE_2 ionization chamber system in combination with $\text{LaBr}_3(\text{Ce})$ scintillation detectors. The $\text{LaBr}_3(\text{Ce})$ detectors have an unique combination of good energy resolution and a fast time response which makes them suitable for lifetime measurements in the picosecond regime. A schematic drawing of an analog γ - γ fast-timing setup consisting of two $\text{LaBr}_3(\text{Ce})$ detectors is shown in Fig. 8. The first output signal, called the dynode signal, is amplified and directly connected to the data acquisition (DAQ) and is used to

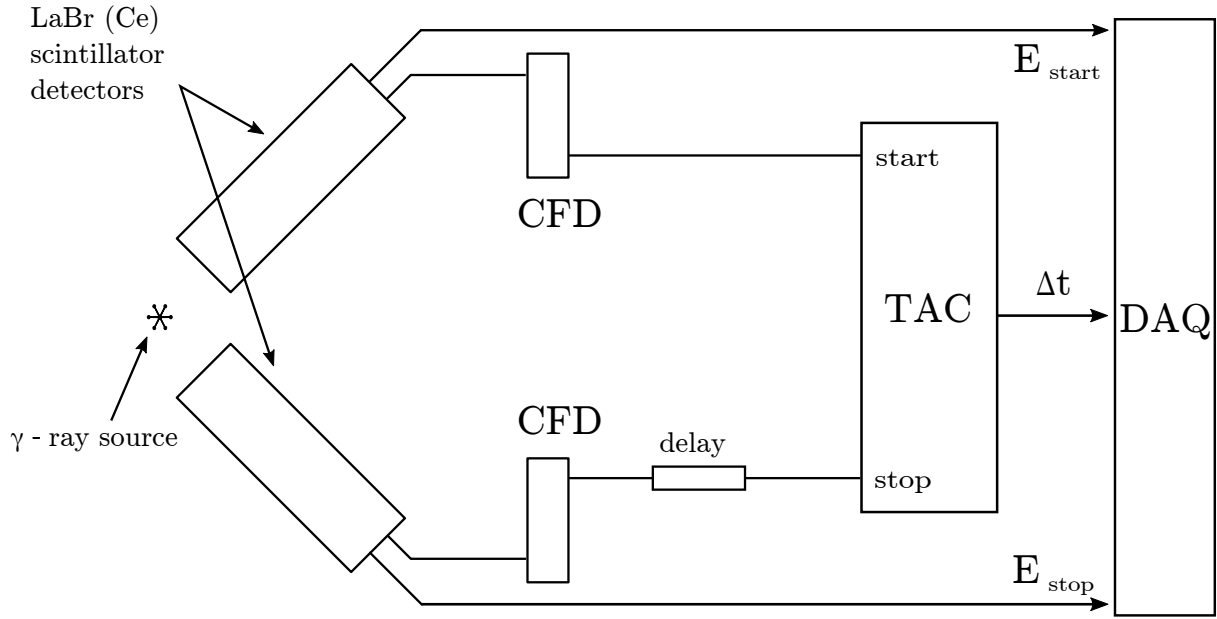


Figure 8: Schematic drawing of a fast-timing setup with two $\text{LaBr}_3(\text{Ce})$ detectors and the necessary components. Figure adapted from [90, 99]

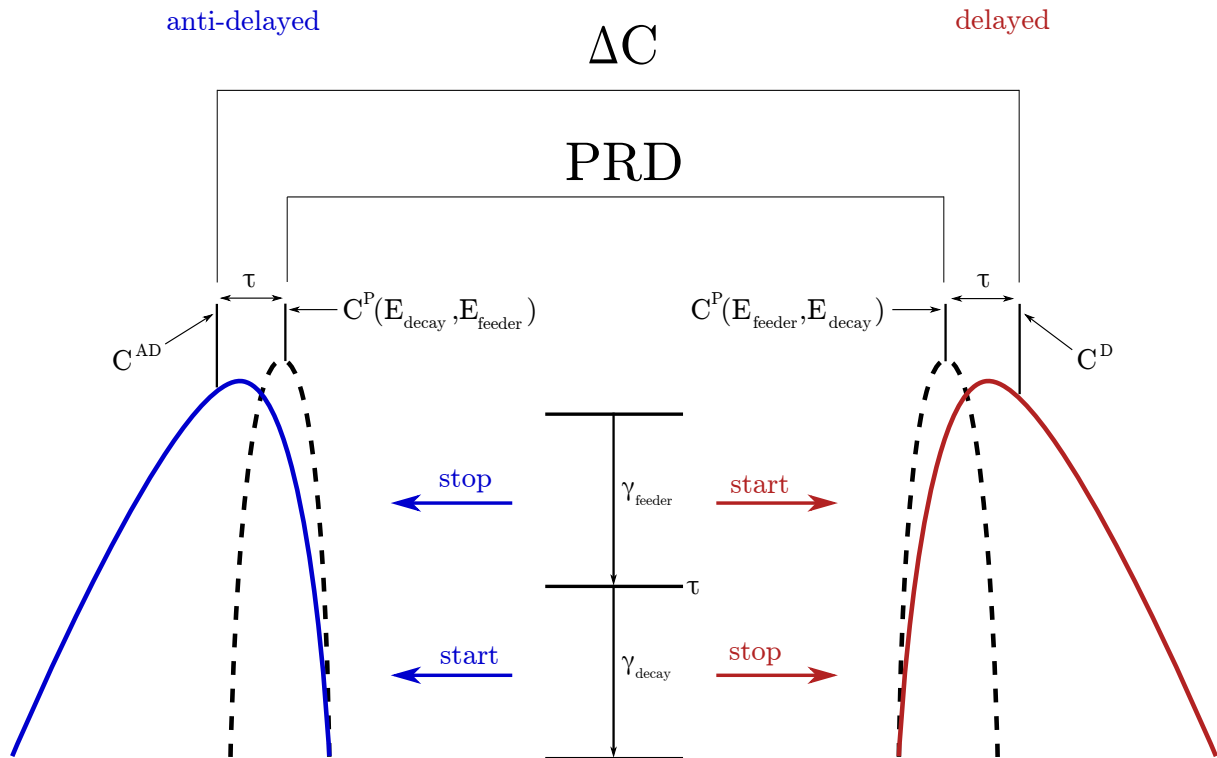


Figure 9: Schematic drawing of the delayed and anti-delayed time distributions generated by the fast-timing setup shown in Fig. 8. The prompt response functions (PRF) denoted as $C^P(E_{\text{decay}}, E_{\text{feeder}})$ and $C^P(E_{\text{feeder}}, E_{\text{decay}})$ are included. Picture adapted from [90, 99].

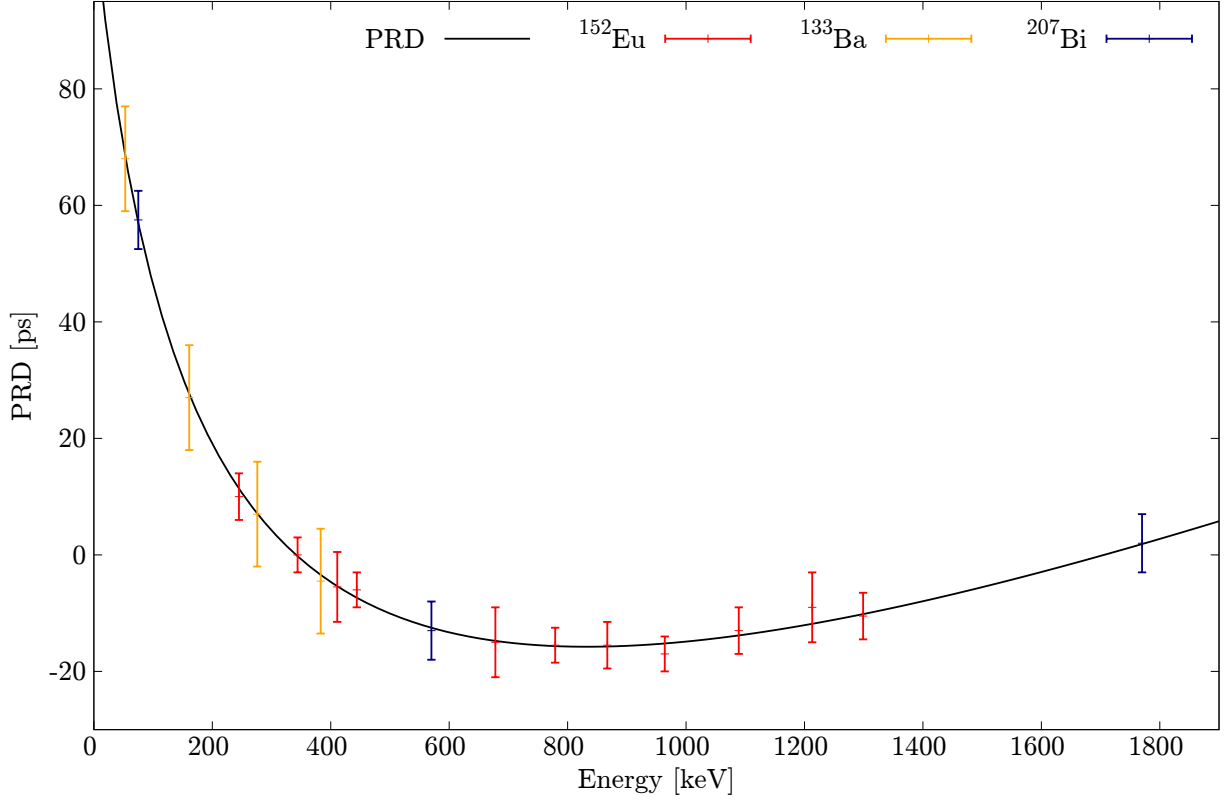


Figure 10: The prompt response difference (PRD) curve obtained using ^{152}Eu , ^{133}Ba and ^{207}Bi sources. The figure is adopted from Ref. [45].

extract the energy of the incoming radiation. The second output signal, called the anode signal, is connected to a constant fraction discriminator (CFD). Amplitude dependent timing effects can be minimized by using a CFD which triggers at a certain constant fraction of the maximum signal height. The logical output signal produced by the CFD are connected to the "start" and "stop" inputs of a time to amplitude converter (TAC). The TAC generates a logical output with an amplitude proportional to the time difference between the two input signals provided by the CFD. Recently, more and more setups and facilities introduced and installed a digital system using only one output signal to obtain the absolute time information and the energy information. The digital system requires no further modules. The data can be analyzed and correlated offline to extract the needed information. For the decay of a state with a short lifetime (for $\text{LaBr}_3(\text{Ce})$ detectors $< 1\text{ps}$) the feeding and decay γ -rays produce a so called prompt response function (PRF), which often follows a Gaussian-like distribution. The full width at half maximum (FWHM) of the PRF is defined as the time resolution of a detector system and is energy dependent. If a state has a lifetime $\tau \gg \text{FWHM}$ of the PRF and the feeding γ -ray is detected by a detector providing a start signal for the TAC and the decaying γ -ray by a detector providing a stop signal for the TAC, a delayed time distribution is produced. An interchange of these signals leads to an anti-delayed time distribution. An illustration is presented in Fig. 9 and in addition the PRF of the delayed and anti-delayed time distributions are included. The lifetime can be extracted by a fit of the

slope (exponential part) using the following equation

$$D(t) = n\lambda \int_{\infty}^t P(t' - t_0) \times e^{-\lambda(t-t')} dt', \quad (1.32)$$

where $P(t' - t_0)$ is the function describing the PRF, n is the normalization factor and $\lambda = 1/\tau$ is the decay constant. Lifetimes smaller than the time resolution of the setup can be measured with the centroid shift method [100]. The centroid of a time distribution is defined by [100]

$$C = \langle t \rangle = \frac{\int_{-\infty}^{\infty} t D(t) dt}{\int_{-\infty}^{\infty} D(t) dt}, \quad (1.33)$$

with the standard deviation defined as [100]

$$\delta C^D = \sqrt{\text{var}(D(t))} = \sqrt{\langle t^2 \rangle - \langle t \rangle^2}. \quad (1.34)$$

As in Fig. 9 indicated the lifetime can be extracted by the following relation [91]

$$\tau = C^D(E_{\text{feeder}}, E_{\text{decay}}) - C^P(E_{\text{feeder}}, E_{\text{decay}}). \quad (1.35)$$

for the delayed time distribution and [91]

$$\tau = C^P(E_{\text{decay}}, E_{\text{feeder}}) - C^{AD}(E_{\text{decay}}, E_{\text{feeder}}). \quad (1.36)$$

for the anti-delayed time distribution, where in both cases C^P describes the centroid of the PRF. An exact determination of the centroid C^P is difficult due to a time and energy correlation. To resolve this issue, recently, the generalized centroid difference (GCD) method [90], which is an extension of the centroid shift method [100], has been developed which allows an easy and straightforward way to analyze data from complex setups as shown by different works [5, 33, 46, 101–108]. Using this method the centroid difference of the delayed and anti-delayed time distribution is determined using the following equation [90]

$$\Delta C = C^D - C^{AD} = \text{PRD} + 2\tau, \quad (1.37)$$

where C^D is the centroid of the delayed distribution and C^{AD} of the anti-delayed. The prompt response difference (PRD) is the centroid difference of the PRF of the time distributions which is obtained by prompt events. The PRD is energy dependent and corresponds to the physical zero time of the γ - γ fast-timing setup. The energy dependence of the PRD is usually calibrated using standard sources like ^{152}Eu , ^{133}Ba , etc. The PRD can be calculated by selecting a feeder-decay combination of a level with known lifetime, the measuring the resulting centroid difference ΔC and by using Eq. 1.37. An example of a PRD curve calibrated with ^{152}Eu , ^{133}Ba and ^{207}Bi sources is shown in Fig. 10. The calibration of the PRD curve is of key importance for the experiment and the lifetime measurements. Over the years, the method has been optimized for different aspects

i.e. background influences [91], parameter settings of the constant fraction discriminator [92], coverage of large energy range down to X-ray energies [94] and positional effects [94].

1.4 Experimental details

1.4.1 The two neutron transfer reaction at the Cologne Plunger spectrometer

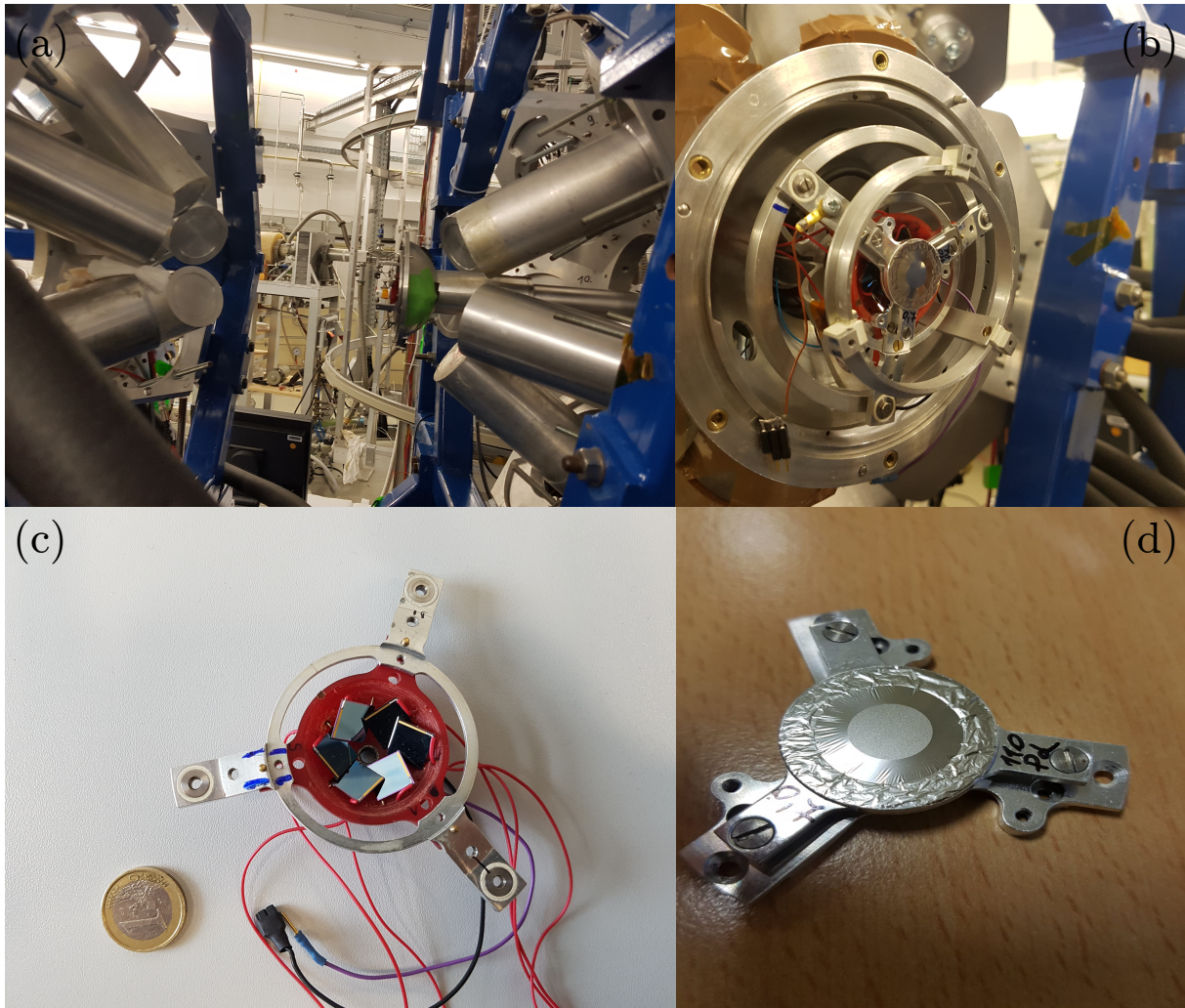


Figure 11: (a) The Cologne Plunger spectrometer equipped with 11 HPGe detectors. (b) The Cologne Plunger chamber with the installed solar cells, a mounted target and the necessary components for the feedback control system. (c) A solar cell array to detect the recoiling beam-like particles. The array consists of six solar cells to cover angles from around 120° to 160° with respect to the beam axis. (d) An enriched and stretched ^{110}Pd target with a thickness of 0.7 mg/cm^2 mounted on a Plunger cone.

The (^{18}O , ^{16}O) two neutron transfer reaction with beam energies around the Coulomb barrier of the reaction is suitable tool to populate low-spin and low-energy states in neutron rich nuclei. This property leads to a relatively simple level scheme where only a few states of the yrast band

and a few non-yrast states are populated. Usually, the two-neutron transfer reaction experiments at the Cologne facility are performed with beam energies around the Coulomb barrier of the reaction, where the two neutron transfer cross section is of the order of 10 mb. Energies around the Coulomb barrier provide a favorable balance between a high cross section for the reaction of interest and a relatively low cross section for other reactions, namely fusion evaporation channels. The impinging ^{18}O beam particle undergoes either elastic scattering or transfers two neutrons which leads to a $^{16,18}\text{O}$ particle recoiling from the target. Other reaction channels like the transfer of one neutron or an α -particle are possible as well, but less probable. Due to the reaction kinematics for the selected energy, the beam-like particles are recoiling mainly backwards with respect to the beam direction. Therefore, six solar cells (PIN diodes) used as particle detectors were placed at backward angles which is schematically illustrated in Fig. 7. This allows to gate on the recoiling beam-like particles of interest, namely $^{16,18}\text{O}$, but also other recoiling particles like ^{14}C (α -transfer) which have been observed in some experiments. Due to the energy and angular straggling of the recoiling $^{16,18}\text{O}$ particles as well as the angular coverage of the solar cells it is not possible to distinguish between ^{16}O and ^{18}O particles. To detect the γ rays produced in the reaction, eleven high-purity germanium (HPGe) detectors were used forming two rings (backward and forward) around the target chamber. The six forward detectors were positioned at an angle of 45° whereas the five backward detectors were placed at an angle of 142° with respect to the beam direction. The particle gate allows to select a reaction channel and significantly reduces the influence of other reaction channels and the resulting spectrum contains mostly γ -rays from the Coulomb excitation of the target (^{18}O scattering) and γ -rays from the two neutron transfer channel (^{16}O). The efficiency of the current plunger setup is not sufficient to perform γ - γ or particle- γ - γ coincidence analysis for such reactions and therefore the analysis in this work are performed only using particle- γ coincidences. Lifetime analysis using the two neutron transfer reaction and the plunger setup are performed using the RDDS technique in combination with the Bateman equations and the DDCM (see Sec. 1.3.1).

1.4.2 The Lohengrin mass spectrometer at the ILL facility

The Lohengrin mass spectrometer is installed in the reactor hall at the Institut Laue Langevin (ILL) in Grenoble, France [111, 112]. The spectrometer is a highly efficient fission fragment separator and a schematic drawing is shown in Fig. 12. Fission fragments are produced by thermal neutron induced fission with a thin target placed very close to the ILL nuclear research reactor core. Thermal neutron yields up to $5 \cdot 10^{14} \frac{\text{neutrons}}{\text{cm}^2 \text{s}}$ are impinging on a fissile material like ^{235}U or ^{239}Pu with a thickness of about 200-400 $\mu\text{g}/\text{cm}^2$. To collimate the emitted fission fragments, a collimator is positioned close to the target. The collimator is essentially collecting a cocktail of different fission fragments which have various kinetic energies E_{kin} , masses A and ionic charges q . The not fully ionized atomic nuclei follow a statistical distribution of ionic charges. The mean ionic charge for the fragments in this work lie between $q = 19$ and $q = 21$. The energy of the fission fragments is in the order of 1 MeV per nucleon, corresponding to an estimated

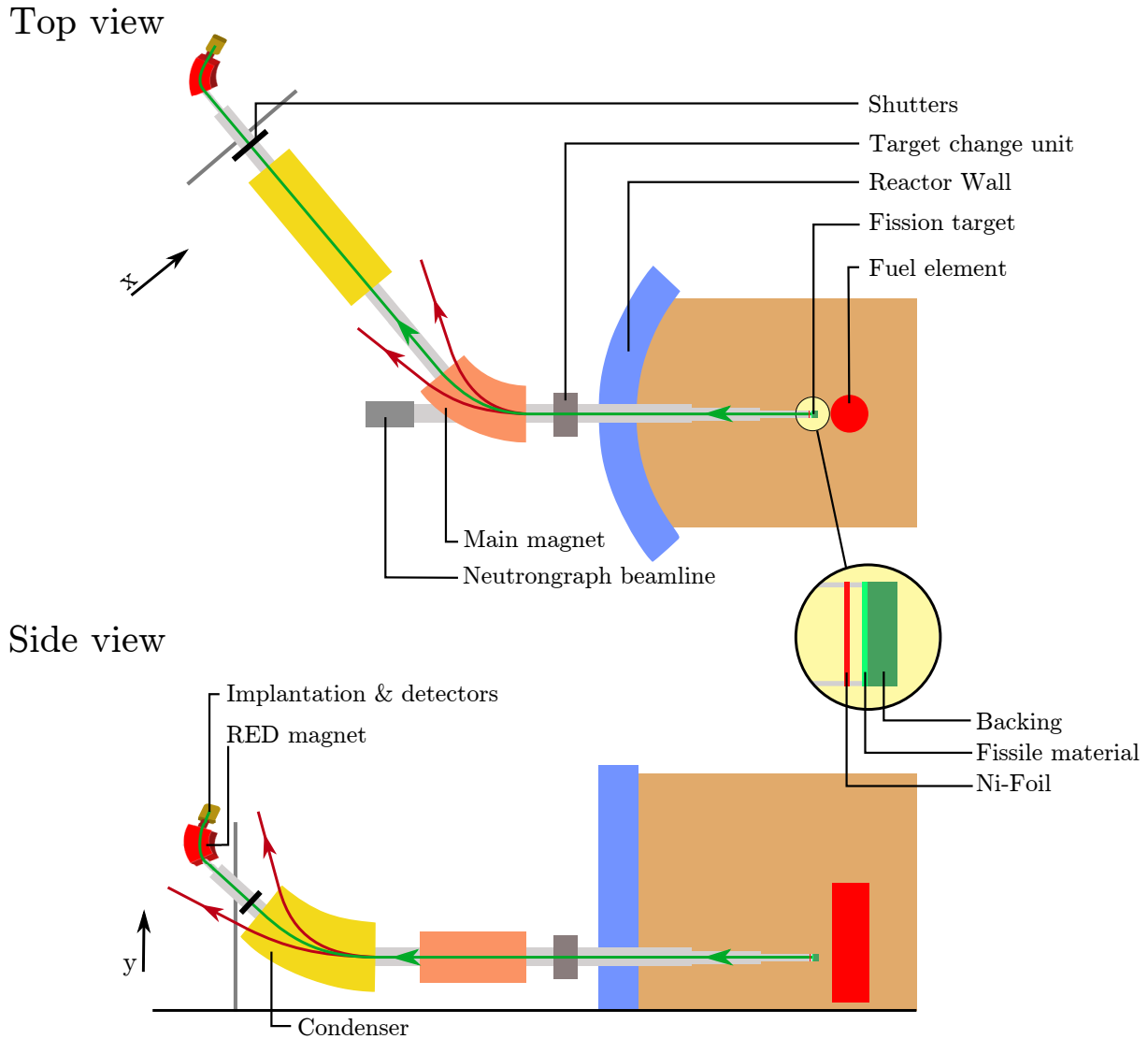


Figure 12: Schematic top view (top) and side view (bottom) of the Lohengrin mass spectrometer adopted from the Refs. [109, 110]. The top view shows the beam deflection in x-direction induced by the main magnet. The side view shows the deflection of the beam in the y-direction which is generated by the condenser. The green line corresponds to the path of focused fission fragments which are of interest. The path length from the target to the implantation zone is about 23 m and the flight time varies between $0.5 \mu\text{s}$ and $2 \mu\text{s}$ depending on the mass of the fission fragment.

energy of the incoming ^{97}Sr particle beam of the order of $E = 100 \text{ MeV}$. The separation of the different fission fragments is achieved by a combination of electric and magnetic fields to select different masses and charge states. The fission fragments pass a dipole magnet after being guided through an electric condenser (see Fig. 12) which allows to separate the same velocity into different parabolas according to their A/q value. A Reverse Energy Dispersion (RED) dipole magnet is placed further downstream to increase the particle density up to a factor of seven and strongly reduce the background at the focal position [109]. Here, the fission products are

identified by their energy loss in a $\Delta E_1 - \Delta E_2$ ionization chamber detector system. The chamber was filled with isobutane (C_4H_{10}) at a pressure of 15 mbar. An aluminum foil is used as an implantation zone for the nuclei in the target chamber. Four $1.5'' \times 1.5''$ LaBr₃(Ce) scintillator detectors were installed with a relative angle of 90° to each the neighboring detectors with a distance of 2.2 cm around the center of the implantation zone. In addition, two unshielded clover detectors each consisting of four germanium crystals were installed. Both of them were used to monitor the emitted γ rays, because the energy resolution of the LaBr₃(Ce) was insufficient to resolve transitions that were close in energy. The data from this experiment were analyzed using the fast-timing technique in combination with the GCD method.

2 | Publication I:
Lifetime measurements and shape
coexistence in ^{97}Sr

Lifetime measurements and shape coexistence in ^{97}Sr A. Esmaylzadeh^{1,*}, J.-M. Régis,¹ Y. H. Kim,² U. Köster,² J. Jolie,¹ V. Karayonchev,¹ L. Knafla,¹ K. Nomura,³ L. M. Robledo,^{4,5} and R. Rodríguez-Guzmán⁶¹Universität zu Köln, Mathematisch-Naturwissenschaftliche Fakultät, Institut für Kernphysik, D-50937 Köln, Germany²Institut Laue-Langevin, 71 Avenue des Martyrs, 38042 Grenoble, France³Department of Physics, Faculty of Science, University of Zagreb, 10000 Zagreb, Croatia⁴Departamento de Física Teórica, Universidad Autónoma de Madrid, E-28049 Madrid, Spain⁵Center for Computational Simulation, Universidad Politécnica de Madrid, Campus de Montegancedo, Boadilla del Monte, E-28660 Madrid, Spain⁶Physics Department, Kuwait University, 13060 Kuwait, Kuwait

(Received 30 July 2019; revised manuscript received 2 September 2019; published 13 December 2019)

Delayed γ rays from neutron-rich $A = 97$ fission fragments were measured using the Lohengrin spectrometer at the high-flux reactor of the Institut Laue-Langevin in Grenoble. Several lifetimes of excited states in ^{97}Sr were measured using the fast-timing technique. The nucleus ^{97}Sr exhibits shape coexistence and is located exactly at the border of the spherical ($N \leq 58$) and deformed ($N \geq 60$) ground-state deformation. It is of particular interest to study the shape-coexisting structures at the spherical-deformed border ($N = 59$). The determined lifetimes within this work are compared to an interacting boson-fermion model calculation that is based on the microscopic energy density functional to provide a better understanding of the spherical-deformed border in strontium isotopes.

DOI: [10.1103/PhysRevC.100.064309](https://doi.org/10.1103/PhysRevC.100.064309)**I. INTRODUCTION**

Shape transitions in the $A \approx 100$ region have been the subject of intense studies lately. The rapid change from the near spherical ^{96}Sr to the strongly deformed ^{98}Sr is well known [1,2]. Due to the proton subshell closures at $Z = 38$ ($\pi p_{3/2}$) and at $Z = 40$ ($\pi p_{1/2}$) and the neutron subshell closures at $N = 50$ ($\nu g_{9/2}$), $N = 56$ ($\nu d_{5/2}$), and $N = 58$ ($\nu s_{1/2}$), the $N = 50$ – 58 (88 – ^{96}Sr) strontium and (90 – ^{98}Zr) zirconium isotopes have the low-energy structure of a semimagic nucleus. By increasing the number of neutrons crossing $N = 60$ a rapid change in ground-state deformation is observed, which results in a prolate-deformed ground-state rotational band in ^{98}Sr . This rapid change in shape occurs also for Zr ($Z = 40$) and is more smooth for lower Z , i.e., the Kr nuclei and, for higher Z , i.e., the Mo-Pd nuclei. In Sr, Y, and Zr nuclei with $N = 58$ and 59 , low-lying spherical states coexist with deformed rotational bands that appear around 1 MeV [3–7]. Further there is experimental evidence in ^{98}Sr and ^{100}Zr for an additional prolate-oblate shape coexistence [8–10], which is underlined by theoretical calculations [11,12]. This variety of different structures and configurations causes the complexity of this region but also provides a lot of potential to understand the transition from single-particle to collective behavior.

To improve the understanding of such a rapid change, which can result in the phenomenon of shape coexistence, it is of particular interest to study the nuclei at the spherical-deformed border, in this case at $N = 59$. Shape coexistence has been proposed for ^{97}Sr in different works [5,6,13,14], where a spherical ground state and a rotational band structure have been assumed. The first two excited states possess a spherical shape, whereas above 550 keV few rotational bands start to evolve, i.e., on top of the $3/2^+$ state at 585.1 keV, the $(3/2)^-$ state at 644.7 keV, the $5/2^+$ state at 687.1 keV, the $(5/2)^-$ state at 713.8 keV, and the isomeric state $9/2^+$ at 830.8 keV. A possible description of the deformed states is given by the fact that once the neutron $\nu g_{7/2}$ orbit is being filled an interaction between $\nu g_{7/2}$ and $\pi g_{9/2}$ causes the proton subshell to vanish and results in a collective motion [15–17].

Another description, especially for the deformed states, is given by the Nilsson approach, which relies on the strong interaction between proton and neutron Nilsson orbitals [14]. The down-sloping $\nu 1/2^+$ [550] and $\nu 3/2^-$ [541] orbitals, which both result from the spherical $\nu h_{11/2}$ orbital, are the main forces that drive the deformation. The $\nu 9/2^+$ [404] orbital is a key factor in stabilizing the deformation at a saturation level of about $\beta \approx 0.4$, in which β represents the axially symmetric deformation [18]. The proton Nilsson orbitals $\pi g_{1/2}$ [440] and $\pi g_{3/2}$ [431] originating from the spherical $\pi g_{9/2}$ orbital are fully occupied for Sr with $Z = 38$ and Zr with $Z = 40$, respectively. The spatial overlap from the neutron orbitals with the proton orbitals creates a minimum in binding energy at a deformation level of 0.4, which at $N = 60$ is favored rather than the spherical configuration.

To study the phenomenon of shape coexistence and to assign the energy levels to the spherical or deformed

*Corresponding author: aesmaylzadeh@ikp.uni-koeln.de

configuration of the nucleus a fast-timing experiment at the Institut Laue-Langevin in Grenoble using the Lohengrin spectrometer was performed. The results should give a better understanding at the spherical-deformed border of the strontium isotopes. Especially, the $(3/2^+, 5/2^+)$ state at 522 keV is very important to understand where the rotational structure of the nucleus starts to be favored. In addition, with the newly gained knowledge a spin assumption about this state is made on the basis of the transitions and the level lifetime. The assignment of levels is underlined by calculations within the framework of the interacting boson approximation. A self-consistent mean-field calculation that is based on an energy density functional (EDF) is used to determine the parameter of the interacting boson-fermion model (IBFM) Hamiltonian.

This work is organized as follows. In Sec. II the experiment and the setup is explained in detail. Section III describes the fast-timing method that has been used to obtain the level lifetimes. In Sec. IV the analysis procedures for the measured lifetimes are presented. In Sec. V, the calculations and the discussion are explained and compared to the experimental results. In this section we especially discuss the state at 522 keV, where we give a suggestion for the spin and the parity according to the obtained results. Finally, a conclusion is given in Sec. VI.

II. EXPERIMENTAL DETAILS

Delayed γ rays from neutron-rich $A = 97$ fission fragments using the Lohengrin mass spectrometer were measured at the high-flux reactor of the Institut Laue-Langevin in Grenoble [19–21]. The nucleus of interest was produced and populated by a thermal-neutron-induced fission of a $0.7 \text{ cm} \times 7 \text{ cm}$ $^{235}\text{UO}_2$ target with a thickness of $363 \mu\text{g}/\text{cm}^2$. The fission yield for ^{97}Sr was about 1.7%. A $0.25\text{-}\mu\text{m}$ -thick Ni foil covered the target to reduce sputtering ^{235}U [22]. To investigate the mass $A = 97$ nuclei, especially ^{97}Sr , the Lohengrin spectrometer is able to select the fission products according to their mass- and energy-to-ionic-charge ratios with a vertical electric deflector and a horizontal magnetic deflector. The additional reverse energy dispersive (RED) magnet focused ions arriving in the focal plane to a beam spot that was collimated to $3 \times 1 \text{ cm}$ [19,20]. Further the fission products could be identified by their energy loss in a ΔE_1 - ΔE_2 ionization chamber (hereafter called IC). The chamber was filled with isobutane (C_4H_{10}) at a pressure of 15 mbar. The target chamber contained an aluminum foil that was used as a stopper of the fission fragments. Four cylindrical $1.5'' \times 1.5''$ LaBr_3 (Ce) scintillator detectors (hereafter called LaBr) were installed with a relative angle of (90°) to each of the neighboring detectors around the implantation zone. The compact detector ring was made such that the corners of detector heads were touching each other. They had a distance of about 2.2 cm to the center of the focal plane of the implantation zone. To minimize the distance and therefore maximize the efficiency of the setup no shielding of any kind was used. Furthermore, a typical lead shielding would introduce x-ray emissions in the energy region of interest for other experiments that were performed during the campaign, utilizing the same setup. For further details about timing effects in the low-energy region

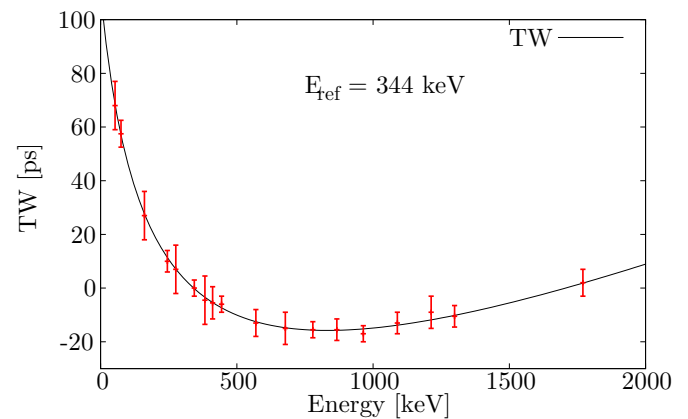


FIG. 1. The calibrated time-walk (TW) curve relative to the energy $E = 344$ keV. The standard deviation is calculated and the 2σ interval is chosen to be the error of the TW curve with 3 ps.

in particular on the effect of x-rays the reader is referred to Ref. [23]. In addition, two unshielded Clover detectors consisting of four germanium crystals each were used to monitor the γ rays, because the resolution of the LaBr was insufficient to resolve transitions that were close in energy. All Clover detectors were placed below the implantation zone. The measurement time was 1 week with a reduction in ion rates over the experiment dropping from 9000 to 3000 ions/s, due to target burnup.

III. FAST-TIMING METHOD

To perform subnanosecond lifetime measurements at the Lohengrin spectrometer, the ionization chamber gated γ - γ fast-timing technique using LaBr detectors was employed. The ionization chamber gate ensures that the isomer of interest is selected, which leads to clean LaBr coincidence spectra with few γ rays and reduced Compton background. To measure lifetimes two LaBr detectors and an analog time-to-amplitude converter (TAC) were used to determine the time difference between two γ rays feeding and de-exciting an excited state of interest (see Refs. [24,25] for details). The time-stamped data were sorted offline to generate IC-LaBr-LaBr events for the lifetime determination. The events were used to construct a so-called symmetric energy-energy-time-difference cube, where the energy axis are symmetric under the exchange of E_1 and E_2 , whereas the time-difference is antisymmetric under exchange [24,25].

A time alignment of the six detector-detector combinations was performed to improve the time resolution of the superimposed time-differences. The total γ - γ time differences were incremented twice, in two identical mirror-symmetric time-difference distributions, with mirror-symmetric mean time walk characteristics relative to a constant reference time t_0 [25], which is consistent with the generalized centroid difference method (described in Refs. [24,26]). To obtain the mean time-walk curve, which is energy dependent and shown in Fig. 1, full energy peaks (FEP) from the ^{152}Eu , ^{133}Ba , ^{207}Bi , ^{185}Os , and ^{187}W γ -ray sources have been used. The 2σ standard deviation is 3 ps and corresponds to the accuracy of the mean time walk. A detailed description of the

mean time-walk calibration procedure is given in Ref. [25]. Exact knowledge of the time walk is necessary to perform high-precision lifetime measurements using the well-known centroid shift method [27], where the centroid of a time distribution $D(t)$ is given by

$$C[D(t)] = \frac{\sum_{t_{\min}}^{t_{\max}} tD(t)}{\sum_{t_{\min}}^{t_{\max}} D(t)}. \quad (1)$$

The centroid of the antisymmetric time-difference distributions can be written as [25]

$$C_{\text{FEP}}(E_{\text{feeder}}, E_{\text{decay}}) = t_0 + \text{TW}(E_{\text{feeder}}, E_{\text{decay}}) + \tau, \quad (2)$$

where τ is the mean lifetime of the excited state. To determine the lifetime the present fast-timing data are corrected for the time walk with $\text{TW}(E_1, E_2) = \text{TW}(E_1) - \text{TW}(E_2)$ [25], where the values are derived from the curve in Fig. 1. The reference time is adjusted to $t_0 = 0$, so that the mean lifetime corresponds to the centroid $C_{\text{FEP}}(E_1 = E_{\gamma_{\text{feeder}}}, E_2 = E_{\gamma_{\text{decay}}}) - \text{TW}(E_1 = E_{\gamma_{\text{feeder}}}, E_2 = E_{\gamma_{\text{decay}}})$. As the subscript ‘‘FEP’’ indicates, this only holds for events where no time-correlated background is present. An analytical background time correction is used to interpolate the time-correlated background at the energy of interest, which has been shown to be most reliable [2,28–30]:

$$C_{\text{FEP}} = C_{\text{exp}} + \overline{t_{\text{cor}}}, \quad (3)$$

with the average of both background contributions stemming from both peaks corresponding to the transition of interest. This leads to

$$\overline{t_{\text{cor}}} = \frac{1}{2}[t_{\text{cor}}(E_{\text{decay}}) + t_{\text{cor}}(E_{\text{feeder}})], \quad (4)$$

where

$$t_{\text{cor}}(E_{\text{feeder(decay)}}) = \frac{C_{\text{exp}} - C_{\text{BG}}}{p/b_{\text{feeder(decay)}}}. \quad (5)$$

C_{exp} is the experimentally determined centroid of the FEP, p/b is the peak-to-background ratio, and C_{BG} is the centroid of the background at the considered γ -ray energy. The background time response at the position of the FEP cannot be measured directly. To determine C_{BG} an interpolation is used where the measurement of centroids from several background time spectra around the FEP is necessary. With the obtained data points from background time spectra the centroid C_{BG} at the FEP can be interpolated and the formulas (3)–(5) can be used to get the centroid of the FEP (C_{FEP}). The uncertainty is calculated via the Gaussian error propagation.

IV. ANALYSIS

In this section the measured lifetimes are presented. In Fig. 2 the level scheme of ^{97}Sr and the full spectrum of the LaBr and Clover detectors after applying a gate on the IC chamber are presented. In Fig. 2 the transitions below the isomer are observed, which are in agreement with previous experiments [31]. The disturbing lines that are next to the lines of interest are removed by gating on any transition of ^{97}Sr . Most of the contamination transitions belong to the daughter nuclei of ^{97}Sr , i.e., ^{97}Y , ^{97}Zr , and ^{97}Nb . Some of

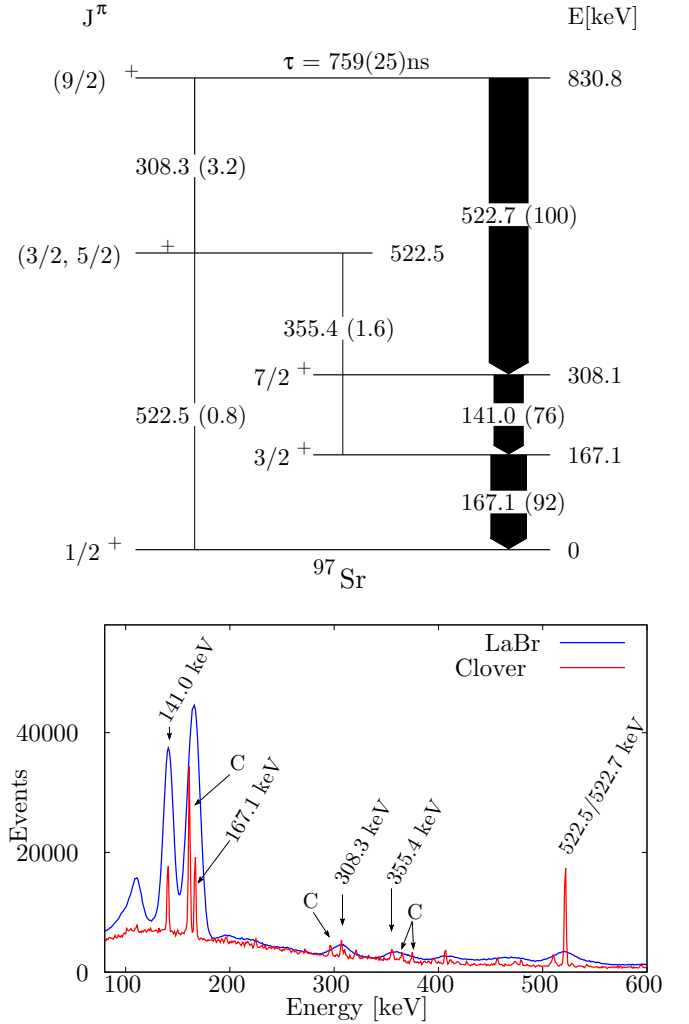


FIG. 2. Upper panel: The level scheme of ^{97}Sr below the isomeric $(9/2)^+$ state at 830.8 keV. Within the brackets the relative intensities of the transitions are given. The scheme only contains transitions observed in this work. In a similar experiment a $(3/2, 5/2)^+ \rightarrow 7/2^+$ (214.4 keV) transition has been observed [31] which is included in the calculation for the transition probabilities. Lower panel: Mass $A = 97$ gated coincidence spectra using the ionization chamber of the Lohengrin setup. The important lines of ^{97}Sr and the contaminates are indicated.

the contaminants belong to ^{88}Br , which has nearly the same mass over charge ratio as ^{97}Sr .

All lifetimes are measured using a gate on the ionization chamber and two LaBr gates that act as start and stop signals, respectively. The Clover detectors are used to monitor the measured γ rays and to assure that no contamination is lying close to the peaks, which cannot be fully resolved by the insufficient energy resolution of the LaBr detectors. In a first step the IC gate is combined with a LaBr gate to obtain doubly gated Clover spectra and check for disturbing transitions. After being sure that the transition of interest is free of any contamination, the IC-LaBr-LaBr gates are used to generate time distributions. The lifetimes are then obtained via the method explained in Sec. III. The final results are summarized in Table II.

A. Lifetime of the $3/2^+$ state

The $3/2^+$ state is located at 167.1 keV and is the first excited state of ^{97}Sr . After applying a $3\text{-}\mu\text{s}$ gate on the ionization chamber the decay transition (167.1 keV) shows a contaminant with an energy of 161.2 keV that is the $7/2_1^+ \rightarrow 3/2_1^+$ transition in ^{97}Zr , which disappears after using LaBr coincidence gates. To measure the lifetime of the $3/2^+$ one can select the strong feeder-decay cascade of 141.0–167.1 keV by applying a gate on the feeder or decay transition. The results of the applied gates are shown in Figs. 3(f) and 3(g), where Clover and LaBr spectra with an IC gate and a LaBr gate on 167.1 and 141.0 keV, respectively, were applied. As highlighted in the figure both transitions are clearly visible without any contaminants. Further the peak-to-background ratio (p/b) is around 20, which leads to a nearly background-free time spectrum as pictured in Fig. 3(h). To determine the lifetime three different methods were used, i.e., the convolution method, the slope method, and the centroid-shift method. All three results are consistent within the errors in which the determined lifetime from the centroid-shift method (explained in Sec. III) with $\tau_{3/2^+} = 448(4)$ ps is adopted. In the literature the lifetime of the state is reported to 317(57) ps [32] and 1.5 ns [33], where neither can be confirmed. The authors of Ref. [32] used planar high-purity germanium detectors, which have a time resolution worse than that of the LaBr detectors used in this work. Furthermore, the time response of the detector system is not mentioned, which could lead to the assumption that this has not been investigated. Reference [33] just mentions the 1.5-ns lifetime, but does not explain how and with which method the lifetime has been measured. Due the missing explanation of the references and the improved lifetime measurement technique in the present work, the newly determined lifetime appears more reliable.

B. Lifetime of the $(3/2, 5/2)^+$ state

To determine the lifetime of the $5/2^+$ state at 522.5 keV the $(9/2)^+ \rightarrow (5/2)^+ \rightarrow 3/2^+$ (308.3–355.4 keV) cascade and the $(9/2)^+ \rightarrow (5/2)^+ \rightarrow 1/2^+$ (308.3–522.5 keV) cascade are used. A gate on mass $A = 97$ and a LaBr gate on 355.4(308.3) keV were applied as shown in Figs. 3(a) and 3(b). As explained in Sec. III an interpolation of the background time response was performed to correct for the background time response that can disturb the time distribution of the feeder-decay cascade [see Figs. 3(c) and 3(d)]. The two resulting time distributions, which are generated with $E_{\text{ref}} = 308.3(355.4)$ keV lead to the final centroid shift of 8(6) ps. After performing the interpolation of the background time response and using Eqs. (3)–(5) the final lifetime results in 14(8) ps for the 308.3–355.4 keV cascade and 15(10) ps for the 308.3–522.5 keV cascade and thus a weighted average of $\tau_{(3/5,5/2)^+} = 14(6)$ ps is obtained.

C. Lifetime of the isomeric $7/2^+$ and $9/2^+$ states

To measure the lifetimes of the isomeric states, we used the time stamps of the detectors. A combination of all three detectors ensures that the transitions are free from contamination and other disturbing effects. For both lifetimes a gate

on the ionization chamber was applied. To generate a time distribution for the $7/2^+$ state a LaBr gate on the 522.7-keV transition and a Clover gate on the decaying 141.0-keV transition were used. The fast LaBr detector was used as a trigger while the slower germanium Clover detector was used for the lifetime measurement. The Clover gate was used as the stop signal and the time-stamp difference was generated and shows the decay of the $7/2^+$ state. The same gates were applied for the $9/2^+$ state, but with the trigger enabled for the ionization chamber, which then acted as the start signal and the LaBr detector acted as the stop signal. To improve the background noise level and to be sure that it was free of contamination the Clover gate was also applied. The lifetime of the $7/2^+$ state with $\tau_{7/2^+} = 252(10)$ ns agrees with the results of previous experiments, which are 245(14) ns [33], 238(6) ns [34], and 238(36) ns [35]. The literature for the $9/2^+$ state provides contradictory results. On the one hand the lifetime values are 382(39) ns [36] and 368(43) ns [35]. Another result is 551(16) ns [37], where it does not seem certain that the measured 522.4-keV γ ray is from ^{97}Sr [37]. The last group of results are on the order of 750 ns, like 759(19) ns [38], 750^{+231}_{-173} ns [39], and 743(14) ns [31], in which the measured lifetime of the present work, 759(25) ns, also falls.

V. CALCULATIONS AND DISCUSSION

In this section the results from this work are discussed and compared to theoretical calculations. For this purpose calculations using the Interacting Boson-Fermion model (IBFM) [40] based on the microscopic energy density functional (EDF) are used. Microscopic calculation for odd-mass nuclei is generally quite complicated because both the collective and the single-particle degrees of freedom have to be treated on the same footing. In the theoretical framework employed in the present study, the interacting boson model (IBM) Hamiltonian for the even-even core nucleus (^{96}Sr) is completely determined from a microscopic EDF calculation, and also the key ingredients of the single-fermion and fermion-boson coupling Hamiltonians, i.e., single-particle energies and occupation probabilities, are provided by the fully microscopic calculation. Even at the cost of having to fit a few strength parameters for the boson-fermion interaction terms so as to reproduce with reasonable accuracy experimental data for excitation spectra in each odd-mass nucleus, this semimicroscopic IBFM calculation provides a detailed description of spectroscopy in odd-mass systems in a computationally very efficient way. After giving a short description of the IBFM model that has been used, the energy levels from the calculation and the experiment are compared to each other. Further, transition strengths, which were calculated from the lifetime, are discussed. Also, a suggestion of the spin and the parity for the $(3/2, 5/2)^+$ state at 522 keV is given based on the lifetime measurement and the IBFM calculation.

A. Theoretical framework

Note that only a superficial description with the important formulas and features of the model is given. For a more detailed description the reader is referred to Refs. [41–44].

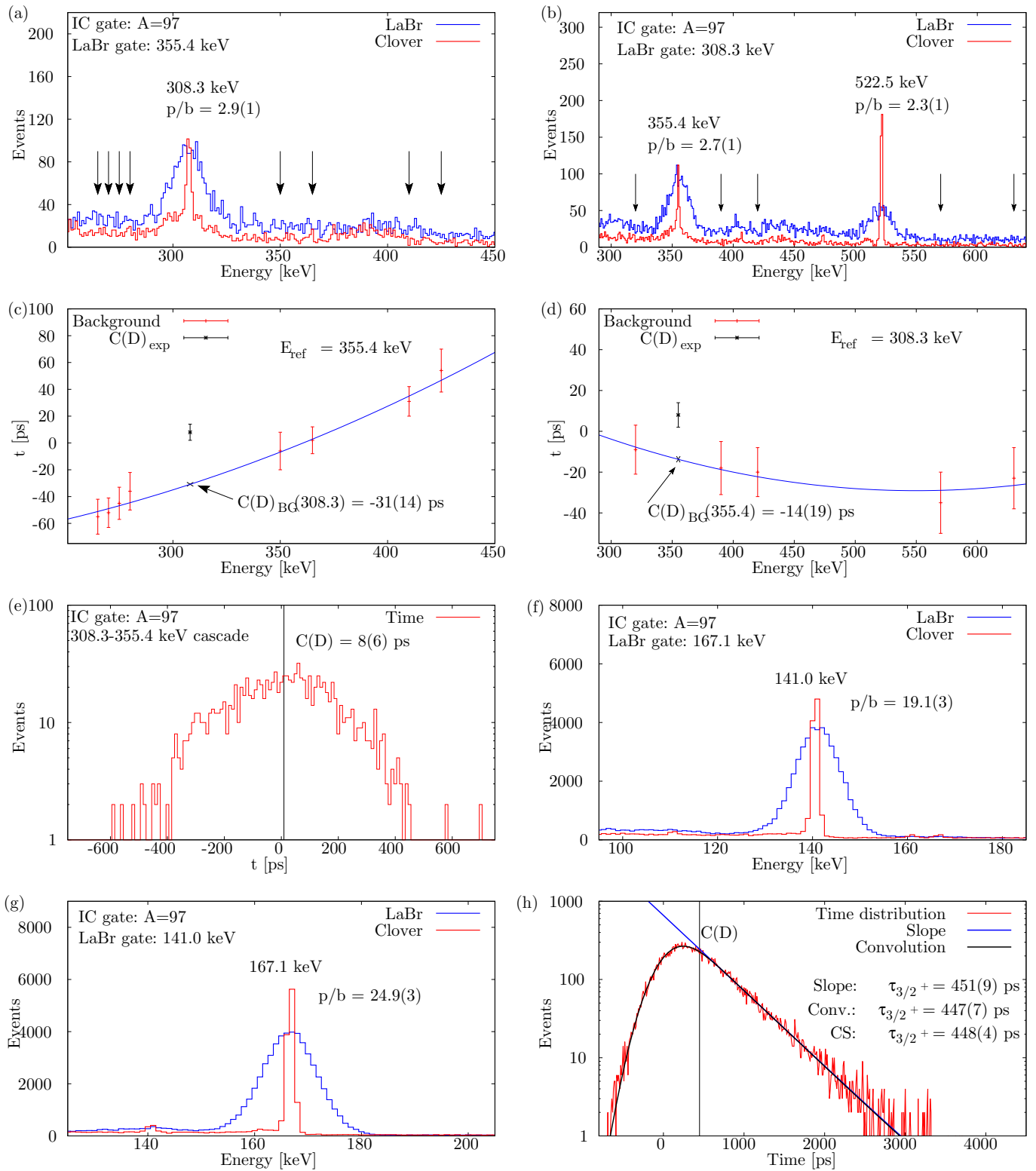


FIG. 3. (a) The 308.3-keV transition after applying a $3\text{-}\mu\text{s}$ gate on $A = 97$ on the ionization chamber and a LaBr gate on the $(3/2, 5/2)^+ \rightarrow 3/2^+$ (355.4 keV) transition. (b) The 355.4- and the 522.5-keV transition after applying a $3\text{-}\mu\text{s}$ gate on $A = 97$ on the ionization chamber and a LaBr gate on the $9/2^+ \rightarrow (3/2, 5/2)^+$ (308.3 keV) transition. (c) The interpolated background time response with the reference energy of 355.4 keV for the feeding transition of the $(3/2, 5/2)^+$ state. (d) The interpolated background time response with the reference energy of 308.3 keV for the decaying transition of the $(3/2, 5/2)^+$ state. (e) The resulting time distribution for the $(3/2, 5/2)^+$ state at 522.5 keV. (f) and (g) The 141.0 (167.1)-keV transition after applying an ionization chamber gate in $A = 97$ and a LaBr gate in the $3/2^+ \rightarrow 1/2^+$ ($7/2^+ \rightarrow 3/2^+$) transition with an energy of 167.1 (141.0) keV. (h) The resulting time distribution for the $3/2^+$ state at 167.1 keV, where three different methods were used to determine the lifetime.

To describe ^{97}Sr an IBFM Hamiltonian, \hat{H}_{IBFM} , is used which is the sum of the neutron-proton IBM (IBM-2) Hamiltonian \hat{H}_{B} , the single-particle fermion Hamiltonian \hat{H}_{F} , and the boson-fermion interaction term \hat{H}_{BF} :

$$\hat{H}_{\text{IBFM}} = \hat{H}_{\text{B}} + \hat{H}_{\text{F}} + \hat{H}_{\text{BF}}. \quad (6)$$

In the IBM-2 model, pairs of protons (neutrons) are coupled to spin $J = 0^+$ s_{π} (s_{ν}) bosons and to $J = 2^+$ d_{π} (d_{ν}) bosons, respectively [45]. For ^{97}Sr which has ten valence protons and nine valence neutrons out of the ^{78}Ni doubly magic core, five proton bosons and four neutron bosons are used for the IBM-2 Hamiltonian \hat{H}_{B} part of Eq. (6). The determination of the parameters of the IBM-2 Hamiltonian \hat{H}_{B} is described in Ref. [41]. It relies on the (β, γ) -deformation energy surfaces computed using a constrained HFB method [46] which is based on the parametrization DIM of the Gogny EDF [41,47,48]. To describe the neutron that remains after coupling the neutron/proton bosons, the fermion valence space was chosen to be the $3s_{1/2}$, $2d_{3/2}$, $2d_{5/2}$ and $1g_{7/2}$ orbitals of the whole neutron major shell $N = 50$ –82 [41]. The last part of the IBFM Hamiltonian, which is the boson-fermion interaction part \hat{H}_{BF} , is taken from Ref. [41]:

$$\hat{H}_{\text{BF}} = \Gamma_{\nu} \hat{Q}_{\pi}^{(2)} \cdot \hat{q}_{\nu}^{(2)} + \Lambda_{\nu} \hat{V}_{\pi\nu} + A_{\nu} \hat{n}_{d\nu} \hat{n}_{\nu}. \quad (7)$$

The product of the strength constant Γ_{ν} times the boson quadrupole operator for proton bosons $\hat{Q}_{\pi}^{(2)}$ times the quadrupole operator for the odd neutron $\hat{q}_{\nu}^{(2)}$ represents the quadrupole dynamical term [41]. The second term describes the exchange interaction introduced to consider that the bosons are in fact nucleon pairs. Both the quadrupole dynamical and the exchange terms act predominantly between protons and neutrons [41]. The last part is the monopole interaction, which is the product of the strength A_{ν} and the number operator for neutron d bosons, and neutron fermion \hat{n}_{ν} acts between like particles (i.e., between odd neutrons and neutron bosons) [41].

For the calculations of ^{97}Sr , the even-even core ^{96}Sr has been used, which shows a weakly oblate-deformed ground-state minimum and in which the IBFM-2 Hamiltonian is built. The used energy potential surface is shown in Fig. 2 of Ref. [44], which has a pronounced prolate ground-state minimum [44].

B. Energy levels

The results from the IBFM calculations and the experimental energy levels are visualized in Fig. 4. The first two states of the calculation, i.e., the $1/2^+$ and $3/2^+$ states, are in good agreement with the experimental energies. The experimental energy of the $7/2_1^+$ state cannot be properly described by the calculation. The calculation cannot clearly classify the spin of the $(3/2, 5/2)^+$ state at 522 keV using only energetic arguments. On the one hand the first calculated $5/2^+$ state is approximately in the energy region of the $(3/2, 5/2)^+$ state, but it is lower than the state of interest. On the other hand the calculated $3/2^+$ state could be assigned to the state of interest, but as Fig. 2 shows, two other $3/2^+$ states are located nearby this state, i.e., at 585 and 600 keV. This makes it difficult to draw a conclusion about the spin of the level at

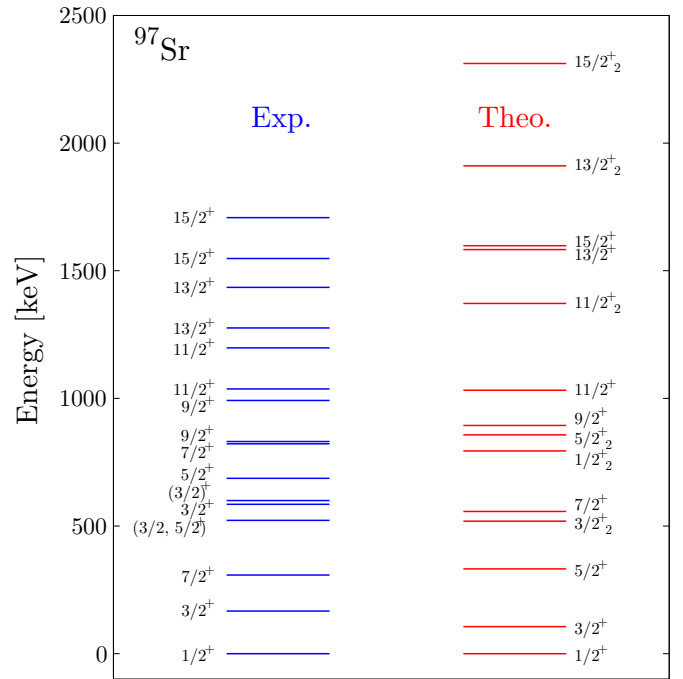


FIG. 4. The experimental (left) and theoretical (right) states with their spins and energies for ^{97}Sr up to 2.5 MeV. The experimental energies and spins are taken from Refs. [14,49–51].

522 keV from energy consideration, but further arguments about the state are given in the second part of the discussion, where the $B(E2)$ value is involved to classify the state. The experimentally observed energy of the $9/2^+$ state can be described by the model. Note that the calculated $9/2^+$ state lies in between the experimental $9/2_1^+$ and $9/2_2^+$ states, but closer to the $9/2_1^+$ state in this work. For higher states, which were not observed in this work, only the $11/2^+$ state is in good agreement with the experimental energy. The other states are mostly calculated to be higher than the experimental ones.

Furthermore, the percentage composition values of the IBFM wave function for the neutron single-particle orbitals, i.e., for the $3s_{1/2}$, $2d_{3/2}$, $2d_{5/2}$, and $1g_{7/2}$ orbitals, are given in Table I. The compositions of the $1/2_1^+$ state and the $5/2_1^+$ state have a large overlap, which may lead to the assumption that the supposed $5/2_1^+$ state could be spherical as the ground state. Additionally, the overlap of the compositions of the $3/2_1^+$ and $7/2_1^+$ states is also very large. The higher-lying $9/2^+$ state consists mainly of the $2d_{3/2}$ orbital and the $2d_{5/2}$ orbital, where a description with the highly deformed intruder $\nu 9/2$ [404] Nilsson orbital could be a better description [14,36,38]. The intruder $\nu 9/2$ [404] Nilsson orbital has also been observed in the corresponding isotone ^{99}Zr [52], but not for ^{101}Mo and ^{95}Kr , which could be due to the special proton-neutron configuration in the Sr and Zr isotopes.

C. Transition probabilities

In Table II all lifetimes and corresponding reduced transition strengths are summarized. Due to the lack of knowledge about the spin of the state at 522 keV, which could be a $3/2^+$ state or a $5/2^+$ state [6], the transitions which decay or feed

TABLE I. The composition of the IBFM wave function for the neutron single-particle orbitals ($3s_{1/2}$, $2d_{3/2}$, $2d_{5/2}$, $1g_{7/2}$) for ^{97}Sr . The values are all given in percentages and only for positive-parity states.

^{97}Sr				
J	$3s_{1/2}$	$2d_{3/2}$	$2d_{5/2}$	$1g_{7/2}$
$1/2_1^+$	12	24	56	8
$3/2_1^+$	10	20	65	5
$5/2_1^+$	12	25	54	9
$3/2_2^+$	16	41	21	22
$7/2_1^+$	10	22	61	7
$1/2_2^+$	16	36	31	17
$5/2_2^+$	14	46	17	23
$9/2_1^+$	11	32	43	14
$11/2_1^+$	17	46	9	28
$11/2_2^+$	11	22	58	9
$13/2_1^+$	10	38	33	19
$15/2_1^+$	16	51	3	30
$13/2_2^+$	13	25	48	14
$15/2_2^+$	10	35	35	20

this state have unknown multipolarities. For the other states, i.e., $1/2^+$, $3/2^+$, $7/2^+$, and $9/2^+$, the spins were known, but not all the multipolarities of the transitions connecting them were known. Therefore, the reduced transition strength for some of the states is given in an $E2$ or a $M1$ limit, where we assume that the transition is either a pure $E2$ or a pure $M1$ character.

TABLE II. The investigated and observed states of ^{97}Sr , where the energy of the initial and final levels, the lifetime, the transitions with their multipolarity, the reduced transition probability $B(E2)$, and $B(M1)$ are given. In cases where experimental multipole mixing ratios are missing or the type and the multipolarity of the transition are unclear, the transition probabilities are calculated by assuming the limits of a pure $E2$ or $M1$ transition, which are marked with *. Further details about different transitions are given in the text.

E_{Level} (keV)	$J^{\pi 2} \rightarrow J^{\pi 1}$	Intensity ^a	Multipolarity	Experimental results from this work		Theory
				$\tau(J^{\pi 2})$	$B(\sigma\lambda; J^{\pi 2} \rightarrow J^{\pi 1})$	$B(\sigma\lambda)$
167.1	$3/2^+ \rightarrow 1/2^+$	100	$M1$	448(4) ps	$260(2) \times 10^{-4} \mu_N^2$	$52 \times 10^{-3} \mu_N^2$
308.1	$7/2^+ \rightarrow 3/2^+$	100	$E2$	252(10) ns	$45(2) e^2 \text{fm}^4$	$740 e^2 \text{fm}^4$
522.5 ^b	$5/2^+ \rightarrow 1/2^+$	4(1)	$E2$	14(6) ps	$450_{-140}^{+330} e^2 \text{fm}^4$	$313 e^2 \text{fm}^4$
	$\rightarrow 3/2^+$	100(8)	$M1$		$60_{-20}^{+40} \times 10^{-3} \mu_N^2$	$120 \times 10^{-3} \mu_N^2$
	$\rightarrow 7/2^+$	46(6)	$E2^*$		$3300_{-1300}^{+2700} e^2 \text{fm}^4$	$128 e^2 \text{fm}^4$
522.5 ^c	$3/2_2^+ \rightarrow 1/2^+$	4(1)	$M1^*$	14(6) ps	$11_{-4}^{+9} \times 10^{-3} \mu_N^2$	$96 \times 10^{-3} \mu_N^2$
			$E2^*$		$450_{-140}^{+330} e^2 \text{fm}^4$	$33 e^2 \text{fm}^4$
	$\rightarrow 3/2^+$	100(8)	$M1$		$9_{-3}^{+6} \times 10^{-3} \mu_N^2$	$29 \times 10^{-3} \mu_N^2$
830.8	$\rightarrow 7/2^+$	46(6)	$E2$		$60_{-20}^{+40} \times 10^{-3} \mu_N^2$	$17 \times 10^{-3} \mu_N^2$
	$9/2^+ \rightarrow 5/2^+$ ^d	3.2(12)	$E2$	759(25) ns	$3300_{-1300}^{+2700} e^2 \text{fm}^4$	$4 e^2 \text{fm}^4$
	$\rightarrow 7/2^+$	100(28)	$E2^*$		$12_{-5}^{+7} \times 10^{-3} e^2 \text{fm}^4$	$398 e^2 \text{fm}^4$
			$M1^*$		$27(1) \times 10^{-3} e^2 \text{fm}^4$	$31 e^2 \text{fm}^4$
					$51(2) \times 10^{-8} \mu_N^2$	$102 \times 10^{-3} \mu_N^2$

^aThe intensities are taken from Refs. [31,49].

^bBy assuming it is a $5/2^+$ state.

^cBy assuming it is a $3/2^+$ state.

^dA $5/2^+$ state is preferred, because a $3/2^+$ would suggest an $M3/E4$ transition that is unlikely.

The $7/2^+ \rightarrow 3/2^+$ and $3/2^+ \rightarrow 1/2^+$ transitions were found to be pure $E2$ and pure $M1$ transitions, respectively [33]. The calculated $B(M1)$ value for the $3/2^+ \rightarrow 1/2^+$ transition is a factor of 2 higher than the experimental value. Also, the $B(E2)$ for the $7/2^+ \rightarrow 3/2^+$ transition is calculated an order of magnitude too high. The large discrepancy for both states could reflect the similarity between both states (see Table II), which could arise from the employed single-particle energies, the occupation probabilities, and the fitted strength parameters for the boson-fermion interactions.

The $9/2^+$ state decays via an $E2$ transition to the $5/2^+$ state at 522 keV and via a mixed $M1/E2$ transition to the $7/2^+$ state at 167 keV. A $5/2^+$ state is preferred, because a $3/2^+$ spin would suggest an $M3/E4$ transition which seems very unlikely. Further reasons for the preference of a $5/2^+$ spin are given in the next section. The calculated $B(M1)$ and $B(E2)$ strength values overestimate the experimental values in all cases.

D. The $(3/2, 5/2)^+$ state at 522 keV

The state at 522 keV is a bit more complicated to describe, because the spin of the state is either $3/2^+$ or $5/2^+$ [6]. For two of the three decaying transitions of the state, i.e., 522.5 keV ($3/2^+$, $5/2^+ \rightarrow 1/2^+$) and 214.4 keV ($3/2^+$, $5/2^+ \rightarrow 7/2^+$) the transitions could be of $E2$ or $M1$ character depending on whether the initial state is $3/2^+$ or $5/2^+$. Only the 355.4-keV ($3/2^+$, $5/2^+ \rightarrow 3/2^+$) transition has a known multipolarity, which is $M1$ [6]. Let us first assume the state has spin and parity $3/2^+$, so that the state is $3/2_2^+$. Then the $3/2_2^+ \rightarrow 1/2^+$ transitions could be an $M1$, an $E2$, or a

mixed $M1/E2$ transition. The multipolarity and the multipole mixing ratio are unknown and therefore the extreme limits of an $M1$ transition and an $E2$ transition are given and compared to the IBFM calculations (see Table II). The calculation underestimates the $B(E2)$ strength and overestimates the $B(M1)$ strength, by which one could conclude that the transition contains both multipolarities. The second transition, i.e., $3/2^+ \rightarrow 7/2^+$, would correspond to an $E2$ transition. The experimentally determined $B(E2)$ value is 3 orders of magnitude higher than the calculated $B(E2)$ value. Note that the experimental value has high uncertainties, which results from the high uncertainty of the lifetime but also from the imprecisely measured branching ratio with $3(1)$ [31]. For the $3/2_2^+ \rightarrow 3/2_1^+$ transition the multipolarity of $M1$ has been determined [6]. The calculated $B(M1)$ strength underestimates the experimental value by a factor of 3, which is therefore the least discrepant described transition probability by the model. Now the values are discussed within the assumption that the state has spin and parity of $5/2^+$. The $5/2^+ \rightarrow 1/2^+$ transition is a pure $E2$ transition, where the experimental $B(E2)$ value of $451_{-142}^{+329} e^2 \text{ fm}^4$ is described by the calculated value of $313 e^2 \text{ fm}^4$. The second transition, i.e., $5/2^+ \rightarrow 7/2^+$, has a mixed $M1/E2$ character in which the experimental $B(M1)$ value, which is calculated by assuming a pure $M1$ transition, is overestimated by the calculation. The opposite case occurs for the experimental $B(E2)$ value, where a pure $E2$ transition is assumed, in which the calculation underestimates the value by an order of magnitude. For the known $M1$ transition $5/2^+ \rightarrow 3/2^+$, the calculation is twice as big as the experimental $B(M1)$ value, which is quite accurate in contrast to the other transition strengths.

With the newly measured results and the theoretical calculations the spin of the state at 522 keV is discussed in the following. First, the calculated $3/2_2^+$ state is very close in energy to the state at 522 keV, but this state could also be assigned to the experimental $3/2^+$ state at 585 or 600 keV. Furthermore, by looking at the calculated $3/2_1^+$ state compared to the experimental $3/2_1^+$ state it seems likely that the calculation is underestimating the energy of the states in this region. This could lead to the conclusion that the calculated $5/2^+$ state is also underestimated. Hence, a higher energy is expected that would fit better to the state at 522 keV. Another fact is that the calculated transition strength by assuming a $5/2^+$ state describes the experimental values better. According to Ref. [31], where a partial half-life of $16.6(3) \mu\text{s}$ is obtained for the 308.3-keV transition from the $9/2^+$ state, an $E2$ transition is favored because an $M3$ multipolarity would be incompatible with the partial half-life [31]. Additionally, earlier observed experimental signatures recommend a $5/2^+$ state like the enhanced transition rate of the $(3/2, 5/2)^+$ state at 600.5 keV, which can be described as being the $1/2_{\text{g.s.}}^+ \otimes 2_{\text{phonon}}^+$ first quadrupole vibrational state [5]. The experimental data of ^{97}Sr seem to show no other remaining possibility to create a $5/2^+$ state at 522 keV

with a collective nature, and therefore it is likely to be a high-seniority, spherical shell-model state [31]. Note that the $3/2_1^+$ state has been described as a high-seniority, spherical shell-model state [6], where the state is weakly fed via the β decay of the deformed nucleus ^{97}Rb [6,31]. The β decay between those state occurs with a high $\log ft = 6.5$ value, which is a first forbidden transition type and could be a hint of shape hindrance in this transition [6,31]. Nearly the same $\log ft$ value has been reported for the state at 522 keV [6], which is an indication of a similar structure for this level [31]. According to the number of supporting experimental facts and the additional support from the IBFM calculation we suggest a spin assignment of $5/2^+$ for the state at 522 keV, although a structure corresponding to a high-seniority spherical shell-model state is also possible.

VI. CONCLUSIONS

The lifetimes of all the states that are fed by the isomeric $9/2^+$ state and the lifetime of the isomeric state itself could be measured. The lifetime of the $7/2^+$ and $9/2^+$ isomers could be confirmed within the results of some earlier works. The experimental results of the $3/2^+$ state do not agree with the literature values, where we prefer the result from this work due to the high statistics and improved technique. An important observed state was the $(3/2, 5/2)^+$ state at 522 keV, where the lifetime and the resulting transition strength lead to the suggestion that the state is a $5/2^+$ state and likely to be a high-seniority shell-model state. Based on the new experimental data of ^{97}Sr , which is exactly at the spherical-deformed border, the nuclear structure of the $5/2^+$ state gives a hint, where the deformed configuration of the nucleus is preferred. Further experiments to determine the multipolarities of the transitions would be desirable.

ACKNOWLEDGMENTS

We thank the team of the nuclear reactor for the operation at the ILL. A.E. and V.K. acknowledge the financial support by the BMBF under Grant No. 05P15PKFNA. J.-M.R. and L.K. acknowledge the financial support by the Deutsche Forschungsgemeinschaft (DFG) under Grant No. JO391/16-2. The work of the author K.N. is financed within the Tenure Track Pilot Programme of the Croatian Science Foundation and the École Polytechnique Fédérale de Lausanne and Project No. TTP-2018-07-3554, Exotic Nuclear Structure and Dynamics, with funds of the Croatian-Swiss Research Programme. The work of L.M.R. was partly supported by the Spanish MINECO under Grants No. FPA2015-65929 and No. FIS2015-63770. The open access fee was covered by FILL2030, a European Union project within the European Commission's Horizon 2020 Research and Innovation programme under Grant Agreement No. 731096.

[1] E. Clément *et al.*, *Phys. Rev. Lett.* **116**, 022701 (2016).

[2] J.-M. Régis *et al.*, *Phys. Rev. C* **95**, 054319 (2017).

[3] S. Brant, G. Lhersonneau, and K. Sistemich, *Phys. Rev. C* **69**, 034327 (2004).

- [4] K. Kawade, G. Battistuzzi, H. Lawin, H. A. Selič, K. Sistemich, F. Schussler, E. Monnard, J. A. Pinston, B. Pfeiffer, and G. Jung, *Z. Phys. A: At. Nucl.* **304**, 293 (1982).
- [5] M. Büscher, R. F. Casten, R. L. Gill, R. Schuhmann, J. A. Winger, H. Mach, M. Moszyński, and K. Sistemich, *Phys. Rev. C* **41**, 1115 (1990).
- [6] G. Lhersonneau, B. Pfeiffer, K. L. Kratz, H. Ohm, K. Sistemich, S. Brant, and V. Paar, *Z. Phys. A: At. Nucl.* **337**, 149 (1990).
- [7] P. Spagnoletti *et al.*, *Phys. Rev. C* **100**, 014311 (2019).
- [8] H. Mach, M. Moszyński, R. Gill, F. Wahn, J. Winger, J. C. Hill, G. Molnár, and K. Sistemich, *Phys. Lett. B* **230**, 21 (1989).
- [9] F. Schussler, J. Pinston, E. Monnard, A. Moussa, G. Jung, E. Koglin, B. Pfeiffer, R. Janssens, and J. van Klinken, *Nucl. Phys. A* **339**, 415 (1980).
- [10] K. Becker, G. Jung, K. H. Kobras, H. Wollnik, and B. Pfeiffer, *Z. Phys. A: At. Nucl.* **319**, 193 (1984).
- [11] J. Skalski, S. Mizutori, and W. Nazarewicz, *Nucl. Phys. A* **617**, 282 (1997).
- [12] R. Rodríguez-Guzmán, P. Sarriguren, L. Robledo, and S. Perez-Martin, *Phys. Lett. B* **691**, 202 (2010).
- [13] R. A. Meyer, *Hyperfine Interact.* **22**, 385 (1985).
- [14] W. Urban, J. A. Pinston, J. Genevey, T. Rzača-Urban, A. Złomaniec, G. Simpson, J. L. Durell, W. R. Phillips, A. G. Smith, B. J. Varley, I. Ahmad, and N. Schulz, *Eur. Phys. J. A* **22**, 241 (2004).
- [15] P. Federman and S. Pittel, *Phys. Lett. B* **69**, 385 (1977).
- [16] P. Federman and S. Pittel, *Phys. Lett. B* **77**, 29 (1978).
- [17] P. Federman and S. Pittel, *Phys. Rev. C* **20**, 820 (1979).
- [18] M. Albers *et al.*, *Phys. Rev. Lett.* **108**, 062701 (2012).
- [19] P. Armbruster, M. Asghar, J. Bocquet, R. Decker, H. Ewald, J. Greif, E. Moll, B. Pfeiffer, H. Schrader, F. Schussler, G. Siegert, and H. Wollnik, *Nucl. Instrum. Methods* **139**, 213 (1976).
- [20] G. Fioni, H. Faust, M. Gross, M. Hesse, P. Armbruster, F. Gönnewein, and G. Münzenberg, *Nucl. Instrum. Methods Phys. Res., Sect. A* **332**, 175 (1993).
- [21] J.-M. Régis, A. Esmaylzadeh, G. Häfner, J. Jolie, V. Karayonchev, Y. H. Kim, L. Knafla, U. Köster, C. Michelagnoli, M. Rudigier, and G. Simpson, Study of the abrupt shape changes in ^{97}Sr (Institut Laue-Langevin, 2018), doi: [10.5291/ILL-DATA.3-01-659](https://doi.org/10.5291/ILL-DATA.3-01-659).
- [22] U. Köster, H. Faust, T. Materna, and L. Mathieu, *Nucl. Instrum. Methods Phys. Res., Sect. A* **613**, 363 (2010).
- [23] J.-M. Régis *et al.*, *Nucl. Instrum. Methods Phys. Res., Sect. A* (to be published).
- [24] J.-M. Régis, N. Saed-Samii, M. Rudigier, S. Ansari, M. Dannhoff, A. Esmaylzadeh, C. Fransen, R.-B. Gerst, J. Jolie, V. Karayonchev, C. Müller-Gatermann, and S. Stegemann, *Nucl. Instrum. Methods Phys. Res., Sect. A* **823**, 72 (2016).
- [25] J.-M. Régis, M. Dannhoff, and J. Jolie, *Nuclear Instrum. Methods Phys. Res., Sect. A* **897**, 38 (2018).
- [26] J.-M. Régis *et al.*, *Nucl. Instrum. Methods Phys. Res., Sect. A* **726**, 191 (2013).
- [27] Z. Bay, *Phys. Rev.* **77**, 419 (1950).
- [28] S. Ansari *et al.*, *Phys. Rev. C* **96**, 054323 (2017).
- [29] A. Esmaylzadeh, L. M. Gerhard, V. Karayonchev, J.-M. Régis, J. Jolie, M. Bast, A. Blazhev, T. Braunroth, M. Dannhoff, F. Dunkel, C. Fransen, G. Häfner, L. Knafla, M. Ley, C. Müller-Gatermann, K. Schomacker, N. Warr, and K.-O. Zell, *Phys. Rev. C* **98**, 014313 (2018).
- [30] V. Karayonchev, A. Blazhev, A. Esmaylzadeh, J. Jolie, M. Dannhoff, F. Diel, F. Dunkel, C. Fransen, L. M. Gerhard, R.-B. Gerst, L. Knafla, L. Kornwebel, C. Müller-Gatermann, J.-M. Régis, N. Warr, K. O. Zell, M. Stoyanova, and P. Van Isacker, *Phys. Rev. C* **99**, 024326 (2019).
- [31] M. Rudigier, G. S. Simpson, J. M. Daugas, A. Blazhev, C. Fransen, G. Gey, M. Hackstein, J. Jolie, U. Köster, T. Malkiewicz, T. Materna, M. Pfeiffer, M. Ramdhane, J.-M. Régis, W. Rother, T. Thomas, N. Warr, D. Wilmsen, J. Le Bloas, and N. Pillet, *Phys. Rev. C* **87**, 064317 (2013).
- [32] H. Ohm, G. Lhersonneau, K. Sistemich, B. Pfeiffer, and K. L. Kratz, *Z. Phys. A* **327**, 483 (1987).
- [33] K. L. Kratz, H. Ohm, A. Schröder, H. Gabelmann, W. Ziegert, B. Pfeiffer, G. Jung, E. Monnard, J. A. Pinston, F. Schussler, G. I. Crawford, S. G. Prussin, and Z. M. de Oliveira, *Z. Phys. A* **312**, 43 (1983).
- [34] M. Czerwiński, T. Rzača-Urban, W. Urban, P. Baczyk, K. Sieja, B. M. Nyakó, J. Timár, I. Kuti, T. G. Tornyi, L. Atanasova, A. Blanc, M. Jentschel, P. Mutti, U. Köster, T. Soldner, G. de France, G. S. Simpson, and C. A. Ur, *Phys. Rev. C* **92**, 014328 (2015).
- [35] J. K. Hwang, A. V. Ramayya, J. H. Hamilton, Y. X. Luo, A. V. Daniel, G. M. Ter-Akopian, J. D. Cole, and S. J. Zhu, *Phys. Rev. C* **73**, 044316 (2006).
- [36] J. K. Hwang *et al.*, *Phys. Rev. C* **67**, 054304 (2003).
- [37] R. E. Sund, H. Weber, and V. V. Verbinski, *Phys. Rev. C* **10**, 853 (1974).
- [38] A. Złomaniec, H. Faust, J. Genevey, J. A. Pinston, T. Rzača-Urban, G. S. Simpson, I. Tsekhanovich, and W. Urban, *Phys. Rev. C* **72**, 067302 (2005).
- [39] D. Kameda *et al.*, *Phys. Rev. C* **86**, 054319 (2012).
- [40] F. Iachello and P. v. Isacker, *The Interacting Boson-Fermion Model*, Cambridge Monographs on Mathematical Physics (Cambridge University, Cambridge, England, 1991).
- [41] K. Nomura, R. Rodríguez-Guzmán, and L. M. Robledo, *Phys. Rev. C* **97**, 064313 (2018).
- [42] K. Nomura, T. Nikšić, and D. Vretenar, *Phys. Rev. C* **93**, 054305 (2016).
- [43] K. Nomura, R. Rodríguez-Guzmán, and L. M. Robledo, *Phys. Rev. C* **96**, 014314 (2017).
- [44] K. Nomura, R. Rodríguez-Guzmán, and L. M. Robledo, *Phys. Rev. C* **94**, 044314 (2016).
- [45] T. Otsuka, A. Arima, and F. Iachello, *Nucl. Phys. A* **309**, 1 (1978).
- [46] R. Rodríguez-Guzmán, P. Sarriguren, L. M. Robledo, and J. E. García-Ramos, *Phys. Rev. C* **81**, 024310 (2010).
- [47] J. Decharge, M. Girod, and D. Gogny, *Phys. Lett. B* **55**, 361 (1975).
- [48] S. Goriely, S. Hilaire, M. Girod, and S. Péru, *Phys. Rev. Lett.* **102**, 242501 (2009).
- [49] National Nuclear Data Center (NNDC), Nuclear Levels and Gamma Search, 05/2018.
- [50] W. Urban, J. Durell, A. Smith, W. Phillips, M. Jones, B. Varley, T. Rzača-Urban, I. Ahmad, L. Morss, M. Bentaleb, and N. Schulz, *Nucl. Phys. A* **689**, 605 (2001).
- [51] C. Y. Wu, H. Hua, D. Cline, A. B. Hayes, R. Teng, R. M. Clark, P. Fallon, A. Goergen, A. O. Macchiavelli, and K. Vetter, *Phys. Rev. C* **70**, 064312 (2004).
- [52] W. Urban, J. Pinston, T. Rzača-Urban, A. Złomaniec, G. Simpson, J. Durell, W. Phillips, A. Smith, B. Varley, I. Ahmad, and N. Schulz, *Eur. Phys. J. A* **16**, 11 (2003).

3 | Publication II:

Lifetime measurements to investigate
 γ -softness and shape coexistence in ^{102}Mo

Lifetime measurements to investigate γ softness and shape coexistence in ^{102}Mo A. Esmaylzadeh^{1,*}, V. Karayonchev,¹ K. Nomura,² J. Jolie,¹ M. Beckers,¹ A. Blazhev,¹ A. Dewald,¹ C. Fransen¹, R.-B. Gerst,¹ G. Häfner,^{1,3} A. Harter¹, L. Knafla¹, M. Ley,¹ L. M. Robledo,^{4,5} R. Rodríguez-Guzmán,⁶ and M. Rudigier⁷¹Universität zu Köln, Institut für Kernphysik, D-50937 Köln, Germany²Department of Physics, Faculty of Science, University of Zagreb, 10000 Zagreb, Croatia³Université Paris-Saclay, IJCLab, CNRS/IN2P3, F-91405 Orsay, France⁴Departamento de Física Teórica, Universidad Autónoma de Madrid, E-28049 Madrid, Spain⁵Center for Computational Simulation, Universidad Politécnica de Madrid, Campus de Montegancedo, Boadilla del Monte, E-28660 Madrid, Spain⁶Physics Department, Kuwait University, 13060 Kuwait, Kuwait⁷Technische Universität Darmstadt, Institut für Kernphysik, D-64289 Darmstadt, Germany

(Received 29 September 2021; accepted 7 December 2021; published 15 December 2021)

Lifetimes of low-spin excited states in ^{102}Mo populated in a $^{100}\text{Mo}(^{18}\text{O}, ^{16}\text{O})^{102}\text{Mo}$ two-neutron transfer reaction were measured using the recoil-distance Doppler-shift technique at the Cologne FN Tandem accelerator. Lifetimes of the 2_1^+ , 4_1^+ , 6_1^+ , 0_2^+ , 2_γ^+ , 3_γ^+ states and one upper limit for the lifetime of the 4_γ^+ state were obtained. The energy levels and deduced electromagnetic transition probabilities are compared with those obtained within the mapped interacting boson model framework with microscopic input from Gogny mean-field calculations. With the newly obtained signatures a more detailed insight in the γ softness and shape coexistence in ^{102}Mo is possible and discussed in the context of the $Z \approx 40$ and $N \approx 60$ region. The nucleus of ^{102}Mo follows the γ soft trend of the Mo isotopes. The properties of the 0_2^+ state indicate, in contrast with the microscopic predictions, shape coexistence which also occurs in other $N = 60$ isotones.

DOI: [10.1103/PhysRevC.104.064314](https://doi.org/10.1103/PhysRevC.104.064314)

I. INTRODUCTION

Nuclei with proton or neutron number close to the magic numbers tend to exhibit a spherical ground state. Moving away from a closed shell results in an increase of collectivity. Compared with the usual gradual process, this development is strictly different in the $A \approx 100$ region, especially for the neutron-rich Zr and Sr isotopes [1,2]. They undergo a rapid change from spherical to a deformed type of structure going from $N = 58$ to $N = 60$ (see Fig. 1). The proton subshell closures at $Z = 38, 40$ ($\pi p_{3/2}$ and $\pi p_{1/2}$) as well as the neutron subshell closures at $N = 50, 56, 58$ ($\nu g_{9/2}$, $\nu d_{5/2}$, and $\nu s_{1/2}$) lead to a low-energy structure of a semimagic nucleus for the $N = 50\text{--}58$ ($^{88\text{--}96}\text{Sr}$) strontium and ($^{90\text{--}98}\text{Zr}$) zirconium isotopes. The ruthenium isotopes ($Z = 44$) show a rather smooth transition from a more spherical shape to a deformed one. The more neutron-rich ruthenium isotopes show a triaxial behavior, where the maximum triaxiality is reached around neutron number $N = 66$ and 68 ($^{110,112}\text{Ru}$) [3–6]. The molybdenum isotopes are centered between the ruthenium, with some degree of γ softness, and the zirconium isotopes, showing a rapid change from a spherical to a deformed structure. This creates a challenge for theoretical models to accurately describe the interplay of different nuclear structure phenomena dominant in this region. The semimagic ^{92}Mo ($N = 50$) is spherical [7], where the low-energy excited

states are formed by the interaction between protons in the $\pi g_{9/2}$ orbital and the neutrons in the $\nu g_{7/2}$ orbital. The energy of the first-excited 2_1^+ state decreases with increasing neutron numbers after $N = 56$, while the $B(E2; 2_1^+ \rightarrow 0_1^+)$ strengths shows an opposite behavior (see Fig. 1). This suggests that, with increasing neutron number, the influence of collective motion becomes stronger [8]. Compared with the Sr and Zr isotopes, the molybdenum isotopes show a less rapid shape evolution where the emergence of triaxiality could play a major role [23]. Different experimental evidence for triaxiality in neutron-rich even-even molybdenum isotopes was reported [8,22,24,25]. The γ band with its 2_γ^+ state band-head is strongly related to the triaxial motion [26] where the potential-energy surface minimum is located between $\gamma = 0^\circ$ (prolate shape) and $\gamma = 60^\circ$ (oblate shape). The relative position of the 2_γ^+ states with respect to the 4_1^+ state changes at $N = 54$ and again at $N = 60$ with the 2_γ^+ states being lower in between. Two important models, that discuss this kind of low-lying 2_γ^+ states and the triaxial shape, are the Davydov-Filippov rigid triaxial rotor model [27–29] and the Wilets-Jean γ unstable rotor model [30]. In the Wilets-Jean γ unstable rotor model (hereafter γ soft model), the energies of the 4_1^+ and 2_γ^+ states are degenerate, while the Davydov-Filippov model predicts the 2_γ^+ at a lower energy than the 4_1^+ state at the maximum of triaxiality at $\gamma = 30^\circ$. The similarities of the models require the use of further parameters to distinguish between them. Therefore, the energy staggering of the γ -band can be considered, which is opposite for both models [26,31]. In the prediction of the γ -soft model, the states corresponding

*aesmalyzadeh@ikp.uni-koeln.de

to the γ band are clustered as (2_γ^+) , $(3_\gamma^+, 4_\gamma^+)$ and $(5_\gamma^+, 6_\gamma^+)$ in comparison to a $(2_\gamma^+, 3_\gamma^+)$, $(4_\gamma^+, 5_\gamma^+)$ clustering structure in the rigid triaxial rotor (Davydov-Filippov model) [32].

Further insights can be obtained by the observation of the second 0_2^+ state, which can be an indicator for β vibration or a possible coexisting shape [33,34]. The 0_2^+ state for the molybdenum isotopes starts at 1.7 MeV in ^{94}Mo , has its minimum for $^{100,102}\text{Mo}$ (with both almost at the same energy around 700 keV), and increases its energy to 1 MeV for ^{106}Mo . In ^{98}Mo the 0_2^+ state is the first-excited state and shape coexistence has been confirmed by different works [35,36].

In the present study, low-lying states of ^{102}Mo were observed and lifetimes were determined to further investigate the describe phenomena in this interesting region of the nuclear chart. The obtained lifetimes and the deduced transition probabilities of these states are powerful tools to get a detailed distinction of different models and their interpretation. The results are compared with the proton-neutron version of the interacting boson model (IBM-2) with microscopic input from the self-consistent mean-field approximation based on the Gogny-D1M energy density functional discussed in Ref. [37].

II. EXPERIMENT

The nucleus of interest was populated using a two-neutron transfer reaction, i.e., $^{100}\text{Mo}(^{18}\text{O}, ^{16}\text{O})^{102}\text{Mo}$. An average beam current of ≈ 1 pnA with an energy of 52 MeV was provided by the Cologne 10 MV FN-Tandem accelerator. The highly enriched (99.7%) ^{100}Mo target with a thickness of 1 mg/cm^2 and a 1.9 mg/cm^2 thick natural magnesium backing was stretched inside the Cologne Plunger device [38]. In addition, a natural magnesium stopper foil was stretched in parallel to the target and acted as a stopper for the ejectiles. To detect the γ rays produced in the reaction, eleven high-purity germanium (HPGe) detectors were used forming two rings (backward and forward) around the target chamber. The six forward detectors were positioned at an angle of 45° , whereas the five backward detectors were placed at an angle of 142° with respect to the beam direction. Similar to previous experiments using the same configuration [39–41], six solar cells were installed at backward angles to detect the backscattered light recoiling fragments. To apply the recoil distance Doppler-shift (RDDS) technique, twelve target-to-stopper distances (15, 29, 44, 64, 84, 114, 214, 414, 714, 1114, 1814, and 2414 μm) were measured in approximately 12 days of beam time. The absolute values of these distances were obtained by using the capacitive method which is described in Refs. [38,42] and verified by different lifetimes of the Coulomb excitation of ^{100}Mo . The origin of the uncertainty arises from the fit of the data points using the capacitive method but also from the different used lifetimes of ^{100}Mo , where each lifetime obtains a different so-called zero point. Therefore, the uncertainty of the zero-point determination was calculated to be $5 \mu\text{m}$. The velocity of the recoiling ^{102}Mo was determined using the shifted and unshifted components of the most intensive transitions and results in $v/c = 1.83(10)\%$. A particle spectrum and a particle-gated γ spectrum of the shortest distance is shown in Fig. 2. In addition, a partial level scheme is shown that was built using the information given in

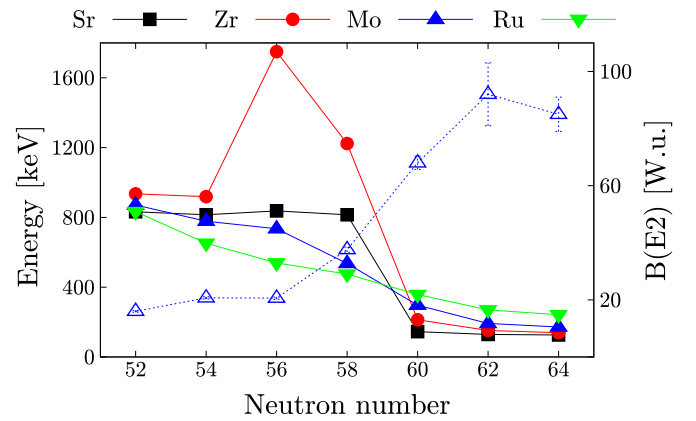


FIG. 1. The energies of the first-excited 2_1^+ states (filled symbols) for Sr ($Z = 38$), Zr ($Z = 40$), Mo ($Z = 42$), and Ru ($Z = 44$) isotopes with $N = 52$ –64. Data are taken from the Nuclear Data Sheets [9–18]. Also the $B(E2; 2_1^+ \rightarrow 0_1^+)$ for the Mo isotopes are shown (open symbols) where the values are taken from Refs. [13–15,19–22].

the spectrum with spins and parities of the states taken from the literature [15]. The dashed lines in Fig. 2(a) indicate γ -ray transitions that were not observed due to their low intensity. The observation limit is about 2% relative to the $2_1^+ \rightarrow 0_1^+$ transition and the intensities are summarized in Table I. The strongest γ rays belong to ^{100}Mo and ^{102}Mo . An exclusion of the Coulomb excitation channel (^{100}Mo) with the particle gate was not possible due to the energy and angular struggling of the recoiling ^{18}O and ^{16}O particles as well as the angular coverage of the solar cells.

III. ANALYSIS

The lifetimes of the 2_1^+ , 4_1^+ , 6_1^+ , 0_2^+ , 2_γ^+ , 3_γ^+ states and an upper limit for the lifetime of the 4_γ^+ state have been determined using the Bateman equations [44] to analyze the recoil distance Doppler-shift data. In addition, the well-established differential decay curve method (DDCM) [45] has been used, which has some advantages like the detection of certain systematic errors. It uses only experimental accessible values and no assumption on the $R(t)$ curve shape are used. Another advantages in contrast to the Bateman equations is the use of relative distances, which eliminates the uncertainty of the absolute distance determination. Only particle-gated single γ -ray spectra were used to analyze the data, where γ - γ coincidences could not be employed due to lack of statistics. A detailed description of both methods is given in Ref. [38]. Due to the low statistics, for the 4_γ^+ state the method explained in Refs. [40,46] was used to obtain the lifetime. The summed spectra of all distances j was used in combination with the following solution of the Bateman equations [40,46]:

$$R_{\text{sum}} = \frac{\sum_j I_j^u}{\sum_j I_j^u + \sum_j I_j^s} = \sum_j n_j R(t_j), \quad (1)$$

where I_j^u and I_j^s are the intensities of the unshifted and shifted component, respectively. The normalization factor n_j needs to be obtained for each distance, and t_j corresponds to the

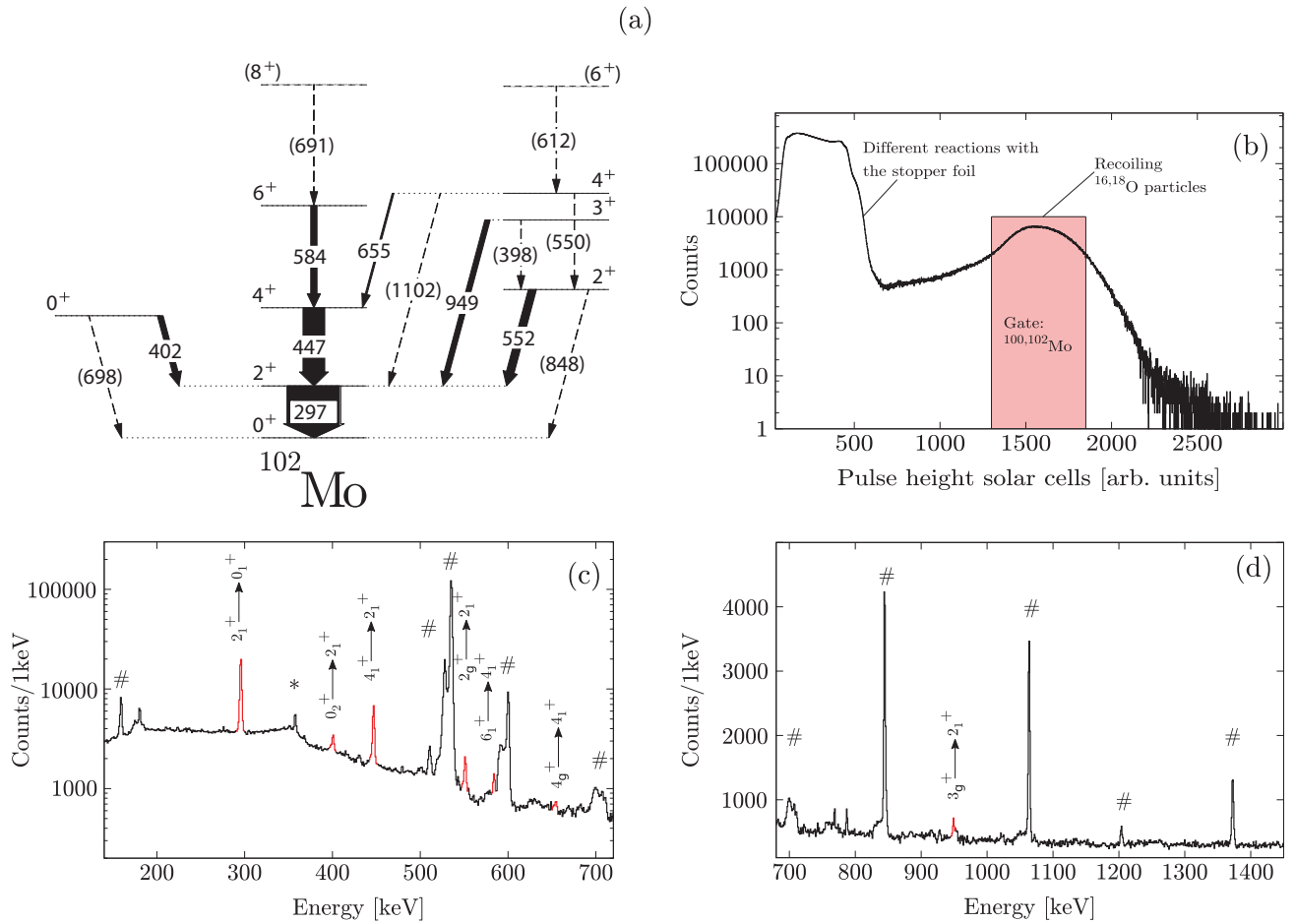


FIG. 2. (a) Partial level scheme of the observed states in ^{102}Mo using the $^{100}\text{Mo}(^{18}\text{O}, ^{16}\text{O})^{102}\text{Mo}$ two-neutron transfer reaction. The width of the transition arrows corresponds to the intensities (see Table I) and the dashed lines indicate known transitions not observed in this experiment. (b) The solar cell spectrum of the 15 μm distance. The rectangle shows the gate that has been used for the analysis of ^{102}Mo . (c) Particle gated singles γ -ray spectrum of the backward HPGe detector ring for the shortest distance of 15 μm . The spectrum is shown for the energy range from 120 keV up to 720 keV in which the observed transitions of ^{102}Mo are indicated and colored in red. The transitions marked with # belong to the Coulomb excitation of ^{100}Mo and transitions marked with * stem from ^{104}Ru , populated by the α -transfer reaction channel. Note that the y scale is logarithmic. (d) Same for the energy range 680 up to 1450 keV with a linear y scale.

flight-time of each distance. As discussed in Refs. [39,40] a top-to-bottom approach was used to determine the lifetimes to adjust the feeding pattern for lower-lying states. The uncertainties for the single measurements were determined using

TABLE I. Relative transition intensities observed in the two neutron transfer $^{100}\text{Mo}(^{18}\text{O}, ^{16}\text{O})^{102}\text{Mo}$ reaction. The intensities were normalized to the $2_1^+ \rightarrow 0_1^+$ transition and the energies are taken from Ref. [15].

Transition	Transition energy [keV]	Intensity
$2_1^+ \rightarrow 0_1^+$	296.6	100.0(7)
$0_2^+ \rightarrow 2_1^+$	401.9	10.4(14)
$4_1^+ \rightarrow 2_1^+$	447.1	40.3(8)
$2_2^+ \rightarrow 2_1^+$	551.6	12.2(15)
$6_1^+ \rightarrow 4_1^+$	584.2	11.5(11)
$4_2^+ \rightarrow 4_1^+$	654.6	2.5(20)
$3_1^+ \rightarrow 2_1^+$	948.9	5.0(24)

a Monte Carlo simulation were all parameters were varied within their uncertainties. The adopted values are calculated using the weighted average of the results. A systematic error of 5% is added which can be caused by different sources, like the opening angle of the detectors, slowing down effects within the target and deorientation effects, especially for $\tau > 100$ ps.

A. The analysis of the 4_1^+ state

The highest observed state in this experiment is the 4_1^+ state. Due to the low population of the state only Eq. (1) could be employed to obtain its lifetime. After the determination of the normalization factors n_j and R_{sum} , a Monte Carlo simulation (with 10^6 iterations) was used to obtain the final lifetime. All the input parameters (n_j , R_{sum} , v/c and the distance) used in the fit are independently varied within their corresponding experimental uncertainty. The resulting lifetime of $\tau_{4_1^+} = 3(1)$ ps has been obtained for which no feeding is assumed. The small intensity is almost at the observation limit and possible unobserved feeders can influence the resulting

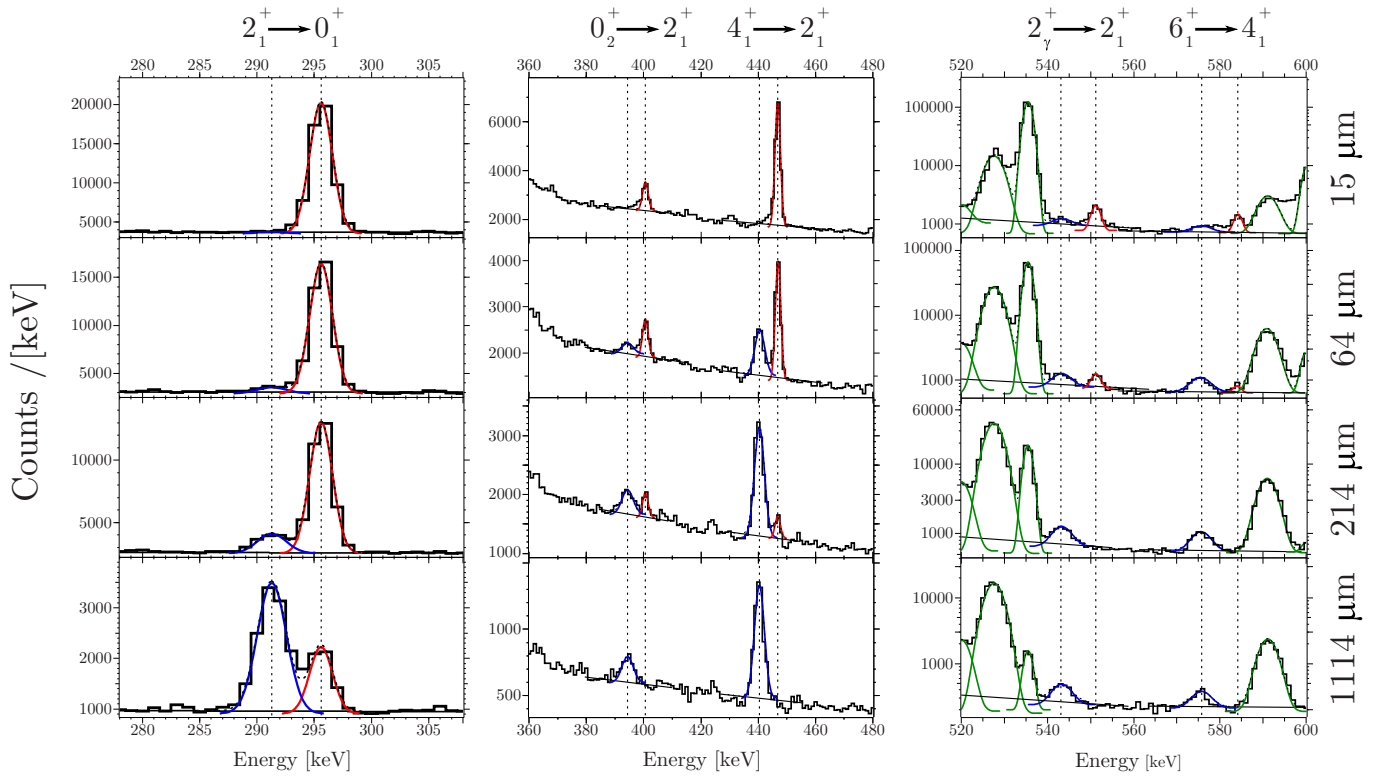


FIG. 3. The evolution of the shifted (blue) and unshifted (red) components in the backward ring for the $2_1^+ \rightarrow 0_1^+$ (left panel), $0_2^+ \rightarrow 2_1^+$ (middle panel), $4_1^+ \rightarrow 2_1^+$ (middle panel), $2_\gamma^+ \rightarrow 2_1^+$ (right panel) and $6_1^+ \rightarrow 4_1^+$ (right panel) transitions for four distances, namely 15, 64, 214, and 1114 μm . The solid line indicates the background level and different disturbing peaks were also fit (green). The disturbing transitions, i.e., at 536 and 600 keV with their shifted components belong to ^{100}Mo .

lifetime. To account for these factors a simulation to account for the feeding contribution was performed. A possible feeder is the 6_γ^+ state which is indicated in Fig. 2(a). An assumption for the maximum feeding from this state and possible other but unobserved states can be extrapolated from the feeding of the lower-lying states and by the fact that the population of states in transfer reactions is decreasing with increasing spin and excitation energy [39–41]. A realistic amount of feeding contribution would in this case be 20%. In other words, 80% is directly populated through the reaction. For the sake of simplicity, the feeding is modeled by a single hypothetical state with an effective lifetime of 100 ps which is sufficiently long to be considered as a pure long-lived feeding [40,41]. After including the feeding intensity and lifetime in the simulation, a lifetime of $\tau_{4_\gamma^+} = 1(1)$ ps was calculated. The lower limit of the simulation is used as the lower limit of the lifetime [40,41]. This leads to a range of 0–4 ps for the lifetime of this state or an upper limit of $\tau_{4_\gamma^+} < 4$ ps. Although this is only an upper limit, it is important for the lower-lying states (2_1^+ , 2_γ^+ , and 3_γ^+) to know the feeding contribution of this state.

B. The analysis of the 6_1^+ and 3_γ^+ states

The lifetimes of the 6_1^+ and 3_γ^+ states were analyzed using the Bateman equations and the differential decay curve method (DDCM) without taking into account unobserved feeding. The mean average of the lifetimes result in

$\tau_{6_1^+} = 6.7(7)$ ps and $\tau_{3_\gamma^+} = 5.7(10)$ ps, respectively. The decay curves and the evolution of the shifted and unshifted component for the 6_1^+ state are shown in Figs. 3–5. For the determination of the lifetimes, the $6_1^+ \rightarrow 4_1^+$ transition with 584 keV and the $3_\gamma^+ \rightarrow 2_1^+$ transition with 949 keV were used. To investigate possible feeding contributions from higher-lying

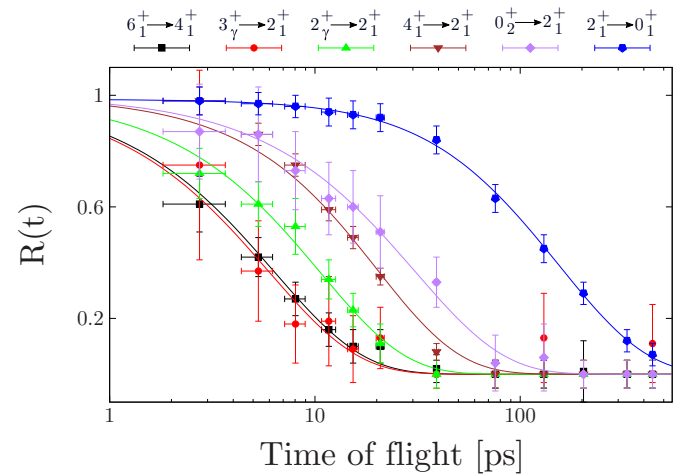


FIG. 4. The decay curves for the lifetimes of the 6_1^+ , 3_γ^+ , 2_γ^+ , 4_1^+ , 0_2^+ , and 2_1^+ states using the Bateman equations to fit the data of the backward ring at 142° . Note that the x scale is logarithmic. The lifetimes are summarized in Table II.

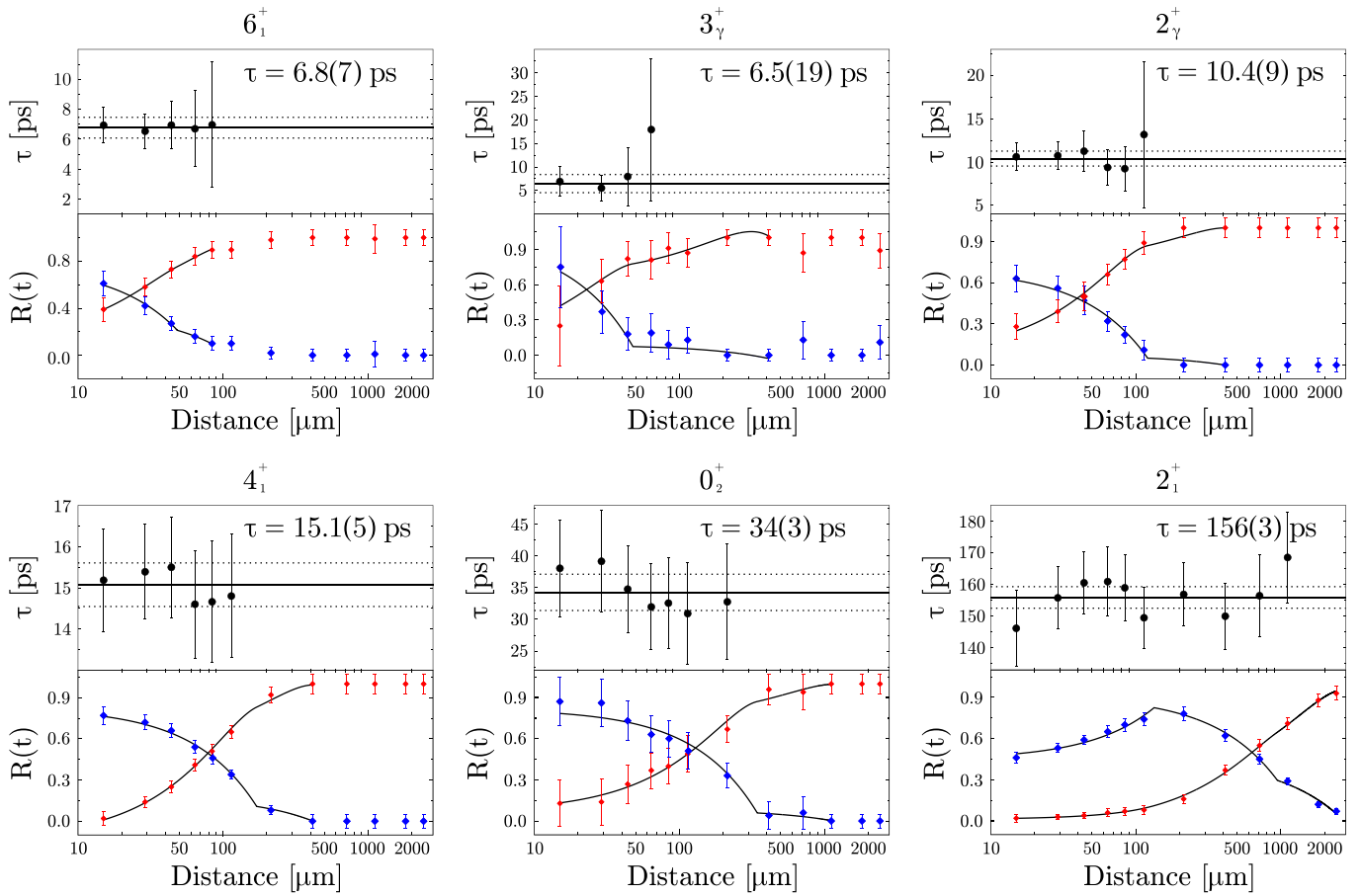


FIG. 5. The DDC method for the 6_1^+ , 3_γ^+ , 2_γ^+ , 4_1^+ , 0_2^+ , and 2_1^+ states using the program NAPATAU [43] for the backward angle. The upper panel shows the individually obtained lifetimes. The lower panel the evolution of the shifted and unshifted component in addition with a fit which is used to obtain the derivative $\frac{d}{dx}R_i(x)$.

unobserved states (e.g., 8_1^+ state as a feeder of the 6_1^+ state) and other unobserved feeding γ rays, a simulation similar as explained in Sec. III A was performed to account for this. The final results for these states with the inclusion of the feeding contribution are given by $\tau_{6_1^+} = 6.7^{+0.7}_{-3.1}$ ps and $\tau_{3_\gamma^+} = 5.5^{+1.0}_{-3.5}$ ps.

C. The analysis of the 2_1^+ , 4_1^+ , 0_2^+ , and 2_γ^+ states

After the determination of the lifetimes of the higher-lying states, the lifetimes of the lower lying states can be obtained. The shifted and unshifted components of these states are shown in Fig. 3 for four representative distances. All lifetimes have been obtained using the Bateman equations and the DDCM. The decay curves of these states are shown in Fig. 4.

For the 2_γ^+ state, the 551.6 keV transition ($2_\gamma^+ \rightarrow 2_1^+$) was used to determine the lifetime. The second decay transition (848 keV) of this state could not be used due to the $3^- \rightarrow 2_2^+$ (845 keV) transition populated in Coulomb excitation of ^{100}Mo . The evolution of the shifted and unshifted components can be seen in the right panel of Fig. 3. The lifetime was determined for the backward angle detectors but not for the forward angle detectors due to the $2_1^+ \rightarrow 0_1^+$ transition with an energy of 536 keV populated in Coulomb excitation of ^{100}Mo . A possible contamination could be the 550 keV ($4_1^+ \rightarrow 2_\gamma^+$)

transition. However, according to the intensities (see Table I), the population of the 4_1^+ is very low. Furthermore, the lifetime is short ($\tau < 4$ ps) and therefore the effect of this state can be neglected in the analysis procedure. After applying the Bateman equations and the DDCM, the final lifetime is $\tau_{2_\gamma^+} = 10.3(12)$ ps, which is the weighted average of both methods (see Table II).

The $0_2^+ \rightarrow 2_1^+$ transition with 402 keV was used to obtain the lifetime of the 0_2^+ state. The increase of the shifted component with increasing distance is shown in the middle panel of Fig. 3. The weighted average of $\tau_{0_2^+} = 33(4)$ ps is consistent with a former RDDS lifetime measurement with a result of 40(16) ps [47] within the uncertainties.

The evolution of the intensities of the 447 keV ($4_1^+ \rightarrow 2_1^+$) transition is also shown in the middle panel of Fig. 3. A weighted average of $\tau_{4_1^+} = 15.9(12)$ ps is consistent with a former RDDS lifetime measurement [47] that has a result of 18(4) ps. Another lifetime measurement [48] with the result of $\tau_{4_1^+} = 27.8^{+10.5}_{-8.1}$ ps was obtained by the Doppler-shift-attenuation method using a fragment separator in combination with the PreSPEC-AGATA experimental setup [48]. Although the uncertainty of this result is relatively large, it is not consistent with the lifetime value of this work. A reason could be the low statistics of the lifetime determination described in Ref. [48] which makes it difficult to observe possible feeding

TABLE II. Lifetimes measured in the experiment using the Bateman equation (BE), the DDCM method together with the adopted values. The literature values from Refs. [21,47,48] are summarized in the last column.

State	Backward ring		Lifetime [ps]			Lit.
	BE	DDCM	BE	DDCM	Adopted	
2_1^+	149(6)	156(3)	146(6)	147(3)	150(10)	164(19) ^a 180(6) ^b 186.9 ^{+18.3} _{-18.7} ^c
4_1^+	18.3(14)	15.1(5)	18.3(20)	16.6(9)	15.9(12)	18(4) ^a 27.8 ^{+10.5} _{-8.3} ^c 3.2(7) ^c
6_1^+	6.2(9)	6.8(7)	6.0(9)	7.1(7)	6.7 ^{+0.7} _{-3.1}	3.2(7) ^c
0_2^+	30(6)	34(3)	33(8)	34(3)	33(4)	40(16) ^a
2_2^+	9.9(13)	10.4(9)			10.3(12)	
3_2^+	5.9(18)	6.5(18)	5.2(12)	5.1(11)	5.5 ^{+1.0} _{-3.5}	
4_2^+	<4				<4	

^aFrom Ref. [47].

^bFrom Ref. [21].

^cFrom Ref. [48].

states of the 4_1^+ other than the 6_1^+ state. Therefore, the possible lifetimes of feeder states could have a significant effect on the lifetime and would possibly lower the value if taken into account during the analysis. The lifetime determination in this experiment benefits from the low level density populated from transfer reactions and the higher statistics (see Fig. 3).

After obtaining the lifetimes of all states above the 2_1^+ state, the lifetime of this state is now accessible and the feeding pattern can be included in its determination. The evolution of the components is shown in the left panel of Fig. 3, and the decay curve in Fig. 4. The lifetimes and intensities of the feeding 0_2^+ , 4_1^+ , 2_2^+ , 3_2^+ , and 4_2^+ states are included in the calculation. The final lifetime $\tau_{2_1^+} = 150(10)$ ps is obtained, which is in agreement with a former lifetime measurement with a result of 164(19) ps [47]. Two other lifetimes with 180(6) ps [21] and 186.9^{+18.3}_{-18.7} ps [48] are not consistent within the 1σ range.

IV. CALCULATIONS

Calculations using the proton-neutron interacting boson model (IBM-2), where a distinction between proton bosons and neutron bosons is made [49], based on the microscopic energy density functional (EDF), were performed. The parameters of the IBM-2 Hamiltonian are determined by mapping the deformation-energy surface, which is provided by the constrained Gogny-D1M SCMF calculations, onto the expectation value of the IBM Hamiltonian computed with the boson condensate (intrinsic) wave function [37,50]. From the resulting IBM Hamiltonian, energy levels and transition probabilities can be calculated.

The potential-energy surface shown in left part of Fig. 6 exhibits a single minimum. Therefore, only a single configuration of the Hamiltonian in Eq. (2) of Ref. [37] is used. Here only a short description is given and for a more detailed description, the reader is referred to Ref. [37].

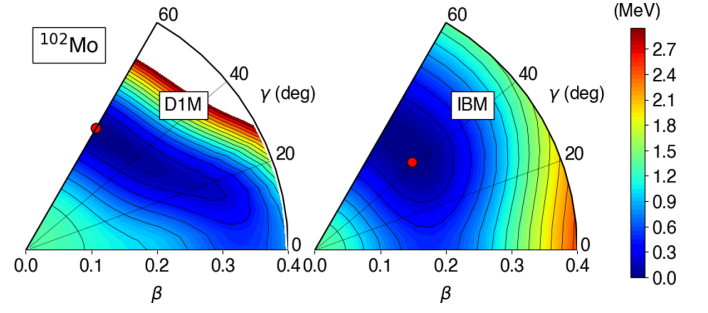


FIG. 6. Contour plot of the deformation-energy surface in the (β, γ) plane for ^{102}Mo computed with the constrained HFB method by using the Gogny functional D1M (left) and with the mapped IBM (right). The red dot indicates the minimum of the energy surface plots and the difference between two neighboring contours is 100 keV.

To describe ^{102}Mo , the Hamiltonian \hat{H}_B is defined as

$$\hat{H}_B = \epsilon \hat{n}_d + \kappa \hat{Q}_\pi \cdot \hat{Q}_v + \kappa' \sum_{\rho' \neq \rho} \hat{T}_{\rho\rho\rho'}, \quad (2)$$

where $\hat{n}_d = \hat{n}_{d\nu} + \hat{n}_{d\pi}$ and $\hat{n}_{d\rho} = d_\rho^\dagger \cdot \tilde{d}_\rho$ ($\rho = \nu, \pi$) describe the d -boson number operator. The quadrupole operator is defined as $\hat{Q}_\rho = s_\rho^\dagger \tilde{d}_\rho + d_\rho^\dagger \tilde{s}_\rho + \chi_\rho [d_\rho^\dagger \times \tilde{d}_\rho]^{(2)}$ ($\rho = \nu, \pi$) and the third term is a specific three-boson interaction term with $\hat{T}_{\rho\rho\rho'} = \sum_L [d_\rho^\dagger \times d_\rho^\dagger \times d_{\rho'}^\dagger]^{(L)} \cdot [\tilde{d}_{\rho'} \times \tilde{d}_\rho \times \tilde{d}_\rho]^{(L)}$ with L being the total angular momentum in the boson system. The electromagnetic $E2$ transition rates are calculated via:

$$\hat{T}^{(E2)} = e_B \hat{Q}, \quad (3)$$

where e_b and \hat{Q} are the effective charge and the quadrupole operator, respectively.

The shell closures at $Z = N = 50$ were used to get the boson numbers which are half of the valence protons and neutrons. The ^{102}Mo nucleus is eight protons and ten neutrons away from the closed shell and hence the proton and neutron valence numbers are $N_\pi = 4$ and $N_\nu = 5$, respectively. The adopted Hamiltonian parameters are $\epsilon = 0.66$ MeV, $\kappa = -0.171$ MeV, $\chi_\pi = 0.15$, $\chi_\nu = 0.35$, and $\kappa' = 0.1$ MeV. The effective $E2$ charge is $e_B = 0.141$ eb and the effective g factors are $g_\nu = 0$ for neutrons and $g_\pi = 1$ for protons in units of μ_n .

The mean field and (mapped) IBM potential-energy surfaces (PESs) are shown in Fig. 6. As can be seen, the Gogny-D1M PES displays an oblate minimum around $\beta \approx 0.15$ which was used to obtain the IBM parameters. Note that the Gogny-D1M PES shows two minima in the case of $^{104}, ^{106}\text{Mo}$ (see Fig. 1 in Ref. [37]). On the right-hand side, the IBM PES shows a minimum around $\beta \approx 0.15$ and a γ deformation of $\gamma \approx 40^\circ$. This can be interpreted as signatures for γ softness in ^{102}Mo , where the maximum γ softness has a very broad minimum at $\gamma = 30^\circ$ spreading to $\gamma = 0^\circ$ (prolate) and $\gamma = 60^\circ$ (oblate).

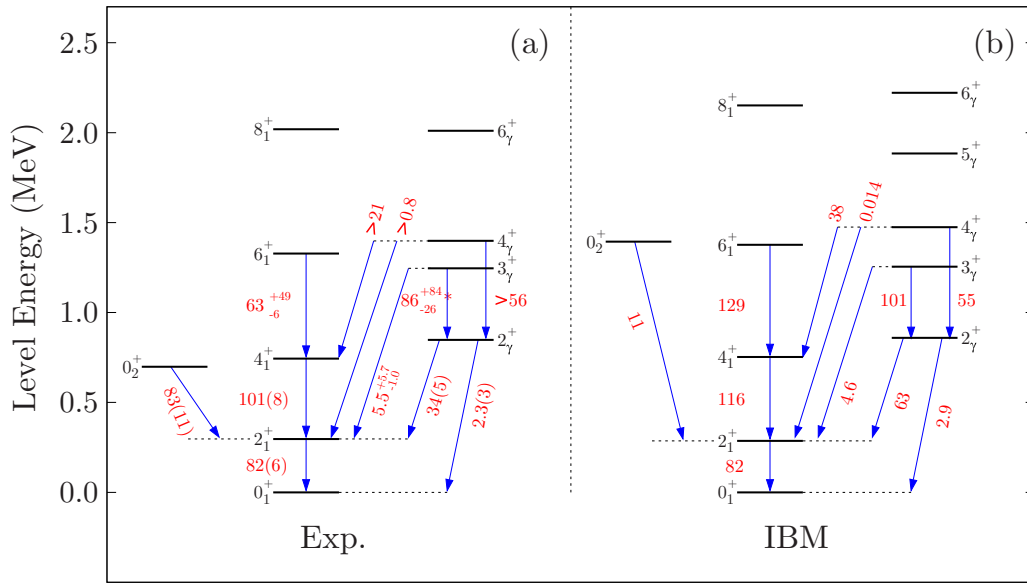


FIG. 7. The level energies of the ground-state band up to the 8_1^+ , the γ band up to the 6_2^+ and the 0_2^+ state which were observed in different experiments (a) and the same level energies for the IBM calculations. The numbers (in red) close to the arrows indicate the $B(E2)$ values in Weisskopf units. The $B(E2; 3_2^+ \rightarrow 2_2^+)$ value indicated with an * is calculated using the limits of a pure $E2$ transition due to a lack of multipole mixing ratios.

V. RESULTS AND DISCUSSION

A. Energy levels

In Fig. 7, the experimental and calculated level energies and transition strengths are shown. The 2_1^+ and 4_1^+ states of the ground-state band are well described by the calculation with an accuracy of 10 keV or better. Although the energy levels of 6_1^+ and 8_1^+ states differ by ≈ 50 and ≈ 150 keV, respectively, the IBM is still able to give a reasonable description of these states. The 2_2^+ bandhead and the 3_2^+ are described with a difference of less than 10 keV with respect to the experimental observations. The energy level of higher lying states of this band, namely, the 4_2^+ and 6_2^+ states, are overestimated by the calculations. The calculations locate the 5_2^+ state in between the 4_2^+ and 6_2^+ state. Three states with level energies of 1617, 1748, and 1870 keV, respectively, could be possible candidates for this proposed 5_2^+ . These states have no adopted spin and lie between the 4_2^+ and 6_2^+ . They were observed by the β decay of the (4^+) ground state of ^{102}Nb [15] which makes it an allowed β decay to a 5^+ state according to the β -decay selection rules. However, all three states decay to at least one 2^+ state, i.e., 1617 keV \rightarrow 296 (1250) keV, 1748 keV \rightarrow 296 keV and 1870 keV \rightarrow 848 keV. These transitions would imply an $M3/E4$ transition which makes this assignment unlikely. In this case no clear assignment of calculated states to experimental states can be made and further experiments are needed to give a final conclusion. The low-lying 0_2^+ state differs from the calculations by a wide margin, which makes it difficult to interpret this state based on the IBM calculations. A possible explanation for the difference might be that the PES in Fig. 6 shows a pronounced deformation (minimum). This leads to a rotational-like energy spectra with the result of a high 0_2^+ energy level.

B. Reduced transition probabilities

In Fig. 7, the transitions and their respective reduced transition probabilities $B(E2)$ given in Weisskopf units are shown. The corresponding $B(E2)$ and $B(M1)$ values can be found in Table III. Using the microscopic interacting boson approach explained in Sec. IV, the theoretically calculated reduced transition strengths are compared with the experimentally deduced ones. The $B(E2; 2_1^+ \rightarrow 0_1^+)$ fits exactly to the experimental observed reduced transition probability. Going up the yrast band the calculation overestimates the values slightly for the $4_1^+ \rightarrow 2_1^+$ transition and by a factor of two for the $6_1^+ \rightarrow 4_1^+$. Although the experimental uncertainty of the $B(E2; 6_1^+ \rightarrow 4_1^+)$ is high, the calculations are not able to reproduce this value within the error.

The 2_2^+ state has two decay branches to the 2_1^+ and 0_1^+ state. The $2_2^+ \rightarrow 0_1^+$ transition with an experimental reduced transition probability of 2.3(3) W.u. is overestimated with 2.9 W.u. by the model. The second decay transition $2_2^+ \rightarrow 2_1^+$ with a multipole mixing ratio of $\delta = 7.0_{-0.6}^{+1.8}$ [51] has an overestimated $B(E2)$ value and a $B(M1)$ value that is in good agreement with the calculations. The multipole mixing ratio suggests a predominantly $E2$ type of transition with a more collective nature, which is also supported by the calculation although the value is two times larger with $B(E2) = 63$ W.u.

For the $3_2^+ \rightarrow 2_1^+$ transition, a multipole mixing ratio of $\delta = -9_{-3}^{+2}$ [51] was used. The corresponding $B(E2)$ value is slightly overestimated whereas the $B(M1)$ value is reproduced by the model. For the decay of the 3_2^+ to the 2_2^+ state, the multipole mixing ratio is unknown and, therefore, the transition rates are calculated in limits of a pure $E2$ or $M1$ transition. The $B(E2; 3_2^+ \rightarrow 2_2^+)$ is reproduced by the model, while the calculation underestimates the $B(M1; 3_2^+ \rightarrow 2_2^+)$ strength. A multipole mixing ratio of $\delta \approx |19|$ would fit to the calculations

TABLE III. The reduced transition probabilities obtained from the measured lifetimes. The branching ratios are taken from the Nuclear Data Sheets [15]. Due to a lack of $M1/E2$ mixing ratios of some transitions the transition probabilities are calculated by assuming the limits of a pure $E2$ and $M1$ transition, which are marked with *. The $B(E2)$ values are given in W.u. and the $B(M1)$ values are given in $10^{-4}\mu_N^2$.

$J^{\pi 2} \rightarrow J^{\pi 1}$	Multipolarity	$B(\sigma\lambda; J^{\pi 2} \rightarrow J^{\pi 1})$	IBM
$2_1^+ \rightarrow 0_1^+$	$E2$	82(6)	82
$4_1^+ \rightarrow 2_1^+$	$E2$	101(8)	116
$6_1^+ \rightarrow 4_1^+$	$E2$	63_{-6}^{+49}	129
$0_2^+ \rightarrow 2_1^+$	$E2$	83(11)	11
$2_2^+ \rightarrow 2_1^+$	$E2^a$	34(5)	63
	$M1^a$	$4.2_{-1.6}^{+3.4}$	3.6
$2_2^+ \rightarrow 0_1^+$	$E2$	2.3(3)	2.9
$3_2^+ \rightarrow 2_1^+$	$E2^b$	$5.5_{-1.0}^{+5.7}$	4.6
	$M1^b$	$1.4_{-0.6}^{+1.8}$	2.0
$3_2^+ \rightarrow 2_2^+$	$E2^*$	86_{-26}^{+84}	101
	$M1^*$	270_{-80}^{+260}	0.8
$4_2^+ \rightarrow 2_1^+$	$E2$	>0.8	0.014
$4_2^+ \rightarrow 2_2^+$	$E2$	>56	55
$4_2^+ \rightarrow 4_1^+$	$E2^c$	>21	38
	$M1^c$	>29	27
$0_2^+ \rightarrow 0_1^+$	$E0^d$	145(30) ^d	

^aAn $M1/E2$ mixing ratio of $\delta = 7.0_{-0.6}^{+1.8}$ was used [51].

^bAn $M1/E2$ mixing ratio of $\delta = -9_{-3}^{+2}$ was used [51].

^cAn $M1/E2$ mixing ratio of $\delta = 2_{-1}^{+3}$ was used [51].

^dThe electric monopole transitions strength between 0^+ state is given in $10^3 \times \rho^2(E0)$ and were calculated using the method explained in Ref. [52].

for both transitions rates, which would be a dominant $E2$ transition.

Lastly, the $B(E2; 0_2^+ \rightarrow 2_1^+) = 83(11)$ W.u. is underestimated by almost one order of magnitude. The overprediction of the energy level and the weak $0_2^+ \rightarrow 2_1^+$ transition strength indicate that the 0_2^+ might be of other origin.

C. Shape coexistence

The $E0$ transition probability obtained by the lifetime of the 0_2^+ state indicates shape coexistence, which is widely spread in the $A \approx 100$ region. The $Z \approx 40$ and $N \approx 60$ region is known for the coexistence and mixing of almost spherical and strongly deformed shapes [1,34]. The $\rho(E0)$ values describe the mixing of two states and are indicators for the exhibition of shape coexistence. In the case of small or nonexistent $\rho(E0)$ strengths, the mixing between the states is minimal and sharp mean square radii variations $\Delta\langle r^2 \rangle$ are seen. Large $\rho(E0)$ strengths correspond to strong mixing and more gradual mean square radii variations $\Delta\langle r^2 \rangle$ (see Figs. 5 and 6 in Ref. [34]). Using the measured lifetime, the obtained $10^3 \times \rho(E0) = 145(30)$ given in Table III is one of the largest values known along the nuclear chart where the ground state is weakly deformed [34,52]. Similar large values were observed in the corresponding isotones ^{100}Zr and ^{98}Sr with $10^3 \times \rho(E0) = 51(5)$ [52,53] and $10^3 \times \rho(E0) = 108(19)$ [52,54,55], respectively. For the higher- Z isotones,

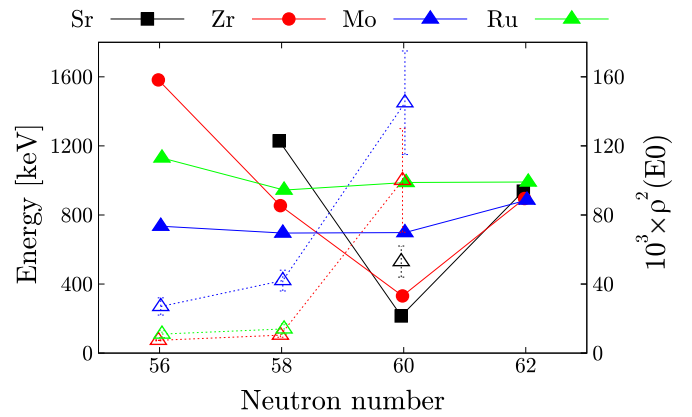


FIG. 8. The energies of the 0_2^+ state (filled symbols) for ($Z = 38$), Zr ($Z = 40$), Mo ($Z = 42$), and Ru ($Z = 44$) isotopes with $N = 56$ –62. The data are taken from the Nuclear Data Sheets [11–17]. If available, the $10^3 \times \rho^2(E0)$ are shown for the same isotopes (open symbols), where the data are taken from Refs. [34,52] and for ^{102}Mo from this work. Note that the values are slightly shifted along the x axis to have a better separation of the values.

namely ^{104}Ru and ^{106}Pd , this large $\rho(E0)$ seems to diminish [1]. However, static and dynamic quadrupole moments in ^{104}Ru show that the shape coexistence still persists [1,56,57]. Going along the isotopic chain of molybdenum isotopes it stands out that the energies of the 0_2^+ states are almost constant for the $N = 56$ –62 isotopes, as can be seen in Fig. 8. The same behavior holds for the ruthenium but not for strontium and zirconium isotopes. The strontium and zirconium isotopes show a “V-like” shape with its minimum at $N = 60$ where the well-known shape coexistence is expected. However, the investigation of $E0$ transition probabilities for the $N = 60$ isotones show a clear jump in $\rho^2(E0)$ values for ^{98}Sr , ^{100}Zr and ^{102}Mo (see Fig. 8). The sudden increase of $\rho^2(E0)$ values in the molybdenum isotopes underlines the shape coexisting structure [34]. With values around $10^3 \times \rho^2(E0) \approx 30$, the $N = 56, 58$ molybdenum isotopes possess already relatively large $\rho^2(E0)$ transition probabilities compared with their isotonic partners in the Zr and Ru isotopes, which concentrate in values around 10. The flat behavior of the 0_2^+ energies in molybdenum in combination with the sudden increase of $\rho^2(E0)$ values might be a hint that the shape coexistence is less pronounced. Or in other words that the change in shape evolves more moderate and smooth compared with the strontium and zirconium isotopes. Note that strong mixing is also required to explain the strong $B(E2; 0_2^+ \rightarrow 2_1^+)$ transition strength. Also different two-neutron reaction studies reveal that ^{102}Mo exhibits a coexisting character [1,58–61], which leads to the assumptions of transfer strength to different structures. This underlines the shape coexisting structures in ^{102}Mo and general trend of the $Z \approx 40$ and $N = 60$ isotones.

The IBM calculations could not reproduce the low-lying 0_2^+ state and the strong $0_2^+ \rightarrow 2_1^+$ transition strength. The experimental results of this work revealed that the inclusion of shape coexistence should be taken into account to get a more accurate description. A possible approach that has been used for the Zr isotopes might solve this issue [39,62].

D. γ softness

As seen in Fig. 7, the 2_γ^+ level energy lies close to the 4_1^+ state. In the Wilets-Jean γ soft rotor model [30], these states are degenerate, while the Davydov-Filippov rigid triaxial rotor model [27–29] predicts the 2_γ^+ state below the 4_1^+ state. To distinguish between those two extreme cases, the staggering parameter is a good indicator and defined as [31]:

$$S(J) = \frac{[E(J) - 2E(J-1) + E(J-2)]}{E(2_1^+)}, \quad (4)$$

where $E(J)$ represents the energy of the level with spin J in the γ band. The staggering parameter $S(J)$ is negative for even-spin levels and positive for odd-spin levels for a γ -soft nucleus and vice versa for a γ -rigid nucleus. Due to a lack of levels in the γ band, only the $S(4) = -0.83$ is calculated, which is clearly in favor of a γ -soft nucleus. The neighboring ^{100}Mo isotope has $S(4) = -0.91$ and $S(5) = 0.66$ and the ^{104}Mo isotope shows the typical even-odd staggering for a γ -soft nucleus. The IBM calculations further support the γ softness of ^{102}Mo where the energies show the same clustering behavior (see Fig. 7). The resulting potential-energy surface (PES) shows a broad minimum around 40° which has a tendency towards oblate deformation (see Fig. 6).

The deduced transition rates, where the $B(E2; 2_\gamma^+ \rightarrow 2_1^+)$ is relatively large and the $B(E2; 2_\gamma^+ \rightarrow 0_1^+)$ small, are similar to the γ -soft model and IBM calculations. The transition rates of the 3_γ^+ state are in agreement as well with a large $B(E2; 3_\gamma^+ \rightarrow 2_\gamma^+)$ and small $B(E2; 3_\gamma^+ \rightarrow 2_1^+)$. However, the $B(E2; 3_\gamma^+ \rightarrow 2_\gamma^+)$ is calculated within the limits of a pure $E2$ transition. Once the multipole mixing ratio is known the value could be lower.

VI. CONCLUSIONS

The lifetimes of the 2_1^+ , 4_1^+ , 6_1^+ , 0_2^+ , 2_γ^+ , 3_γ^+ , and 4_γ^+ states in ^{102}Mo were measured using the RDDS technique. The

results were compared with previous measurements and to an IBM calculation which is based on a microscopic energy density functional. All energy levels and transition strengths of the ground state and γ band are described with reasonable accuracy by the model calculation. The shape coexistence in ^{102}Mo has been re-investigated by measuring the lifetime of the 0_2^+ state. The experimental results suggest two coexisting structures which are mixed. Apparently, the microscopic PES fails in ^{102}Mo to predict this property, although it does for $^{104,106}\text{Mo}$. Furthermore, the deduced transition strengths of the γ band in combination with the energy level reveal signatures a γ -soft behavior. This is supported by the IBM calculation which shows a broad minimum at $\gamma \approx 40^\circ$ that spreads in the γ degree of freedom. The staggering parameter underlines the γ -soft behavior, although only the $S(4)$ has been used. The assignment of the 5_γ^+ and level energy of the 7_γ^+ would further increase the information about the even-odd staggering. The results show that the description of ^{102}Mo is challenging due to appearance of shape-coexistence and γ softness.

ACKNOWLEDGMENTS

We thank the operator team of the IKP FN Tandem accelerator for the professional support during the experiment. A.E., V.K., and M.B. acknowledge support by the BMBF under Grant No. 05P15PKFNA. G.H. acknowledges support from the ADI-IDEX programm. R.-B.G. acknowledges support by the DFG under Grant No. BL-1513/1-1. The work of K.N. is supported by the Tenure Track Pilot Programme of the Croatian Science Foundation and the École Polytechnique Fédérale de Lausanne, and the Project TTP-2018-07-3554 Exotic Nuclear Structure and Dynamics, with funds of the Croatian-Swiss Research Programme. The Work of L. M. R. is supported by the Spanish Ministry of Economy and Competitiveness (MINECO) Grant No. PGC2018-094583-B-I00.





-
- [1] K. Heyde and J. L. Wood, *Rev. Mod. Phys.* **83**, 1467 (2011).
 [2] P. Cejnar, J. Jolie, and R. F. Casten, *Rev. Mod. Phys.* **82**, 2155 (2010).
 [3] Y. Luo, S. Zhu, J. Hamilton, J. Rasmussen, A. Ramayya, C. Goodin, K. Li, J. Hwang, D. Almeded, S. Frauendorf, V. Dimitrov, J. ye Zhang, X. Che, Z. Jang, I. Stefanescu, A. Gelberg, G. Ter-Akopian, A. Daniel, M. Stoyer, R. Donangelo, J. Cole, and N. Stone, *Phys. Lett. B* **670**, 307 (2009).
 [4] D. Doherty, J. Allmond, R. Janssens, W. Korten, S. Zhu, M. Zielińska, D. Radford, A. Ayangeakaa, B. Bucher, J. Batchelder, C. Beausang, C. Campbell, M. Carpenter, D. Cline, H. Crawford, H. David, J. Delaroche, C. Dickerson, P. Fallon, A. Galindo-Uribarri *et al.*, *Phys. Lett. B* **766**, 334 (2017).
 [5] P. Möller, R. Bengtsson, B. G. Carlsson, P. Olivius, and T. Ichikawa, *Phys. Rev. Lett.* **97**, 162502 (2006).
 [6] I. Stefanescu, A. Gelberg, J. Jolie, P. Van Isacker, P. von Brentano, Y. Luo, S. Zhu, J. Rasmussen, J. Hamilton, A. Ramayya, and X. Che, *Nucl. Phys. A* **789**, 125 (2007).
 [7] P. Singh, R. G. Pillay, J. A. Sheikh, and H. G. Devare, *Phys. Rev. C* **45**, 2161 (1992).
 [8] K. Wrzosek-Lipska, L. Próchniak, M. Zielińska, J. Srebrny, K. Hadyńska-Klęk, J. Iwanicki, M. Kisieliński, M. Kowalczyk, P. J. Napiorkowski, D. Piętak, and T. Czosnyka, *Phys. Rev. C* **86**, 064305 (2012).
 [9] S. Basu and E. Mccutchan, *Nucl. Data Sheets* **165**, 1 (2020).
 [10] C. M. Baglin, *Nucl. Data Sheets* **113**, 2187 (2012).
 [11] D. Abriola and A. Sonzogni, *Nucl. Data Sheets* **107**, 2423 (2006).
 [12] D. Abriola and A. Sonzogni, *Nucl. Data Sheets* **109**, 2501 (2008).
 [13] J. Chen and B. Singh, *Nucl. Data Sheets* **164**, 1 (2020).
 [14] B. Singh and J. Chen, *Nucl. Data Sheets* **172**, 1 (2021).
 [15] D. De Frenne, *Nucl. Data Sheets* **110**, 1745 (2009).
 [16] J. Blachot, *Nucl. Data Sheets* **108**, 2035 (2007).
 [17] D. De Frenne and A. Negret, *Nucl. Data Sheets* **109**, 943 (2008).
 [18] J. Blachot, *Nucl. Data Sheets* **62**, 803 (1991).

- [19] S. Raman, C. Nestor, and P. Tikkanen, *At. Data Nucl. Data Tables* **78**, 1 (2001).
- [20] P. F. Mantica, A. E. Stuchbery, D. E. Groh, J. I. Prisciandaro, and M. P. Robinson, *Phys. Rev. C* **63**, 034312 (2001).
- [21] M. Liang, H. Ohm, B. De Sutter, K. Sistemich, B. Fazekas, and G. Molnar, *Z. Phys., A Hadrons Nucl.* **340**, 223 (1991).
- [22] J. Ha, T. Sumikama, F. Browne, N. Hinojara, A. M. Bruce, S. Choi, I. Nishizuka, S. Nishimura, P. Doornenbal, G. Lorusso, P.-A. Söderström, H. Watanabe, R. Daido, Z. Patel, S. Rice, L. Sinclair, J. Wu, Z. Y. Xu, A. Yagi, H. Baba, N. Chiga *et al.*, *Phys. Rev. C* **101**, 044311 (2020).
- [23] R. Rodríguez-Guzmán, P. Sarriguren, L. Robledo, and S. Perez-Martin, *Phys. Lett. B* **691**, 202 (2010).
- [24] A. G. Smith, J. L. Durell, W. R. Phillips, W. Urban, P. Sarriguren, and I. Ahmad, *Phys. Rev. C* **86**, 014321 (2012).
- [25] H. Hua, C. Y. Wu, D. Cline, A. B. Hayes, R. Teng, R. M. Clark, P. Fallon, A. Goergen, A. O. Macchiavelli, and K. Vetter, *Phys. Rev. C* **69**, 014317 (2004).
- [26] R. F. Casten, *Nuclear Structure from a Simple Perspective*, Oxford Studies in Nuclear Physics (Oxford University Press, Oxford, 2000).
- [27] A. Davydov and G. Filippov, *Nucl. Phys.* **8**, 237 (1958).
- [28] A. Davydov and V. Rostovsky, *Nucl. Phys.* **12**, 58 (1959).
- [29] A. Davydov and V. Rostovskii, *J. Expt. Theor. Phys. (USSR)* **36**, 1788 (1959) [*Sov. Phys. JETP* **36**, 1275 (1959)].
- [30] L. Willets and M. Jean, *Phys. Rev.* **102**, 788 (1956).
- [31] N. Zamfir and R. Casten, *Phys. Lett. B* **260**, 265 (1991).
- [32] E. A. McCutchan, D. Bonatsos, N. V. Zamfir, and R. F. Casten, *Phys. Rev. C* **76**, 024306 (2007).
- [33] P. E. Garrett, *J. Phys. G* **27**, R1 (2000).
- [34] J. Wood, E. Zganjar, C. De Coster, and K. Heyde, *Nucl. Phys. A* **651**, 323 (1999).
- [35] T. Thomas, K. Nomura, V. Werner, T. Ahn, N. Cooper, H. Duckwitz, M. Hinton, G. Ilie, J. Jolie, P. Petkov, and D. Radeck, *Phys. Rev. C* **88**, 044305 (2013).
- [36] M. Zielnińska, T. Czosnyka, J. Choiński, J. Iwanicki, P. Napiorkowski, J. Srebrny, Y. Toh, M. Oshima, A. Osa, Y. Utsuno, Y. Hatsukawa, J. Katakura, M. Koizumi, M. Matsuda, T. Shizuma, M. Sugawara, T. Morikawa, H. Kusakari, A. Efimov, and V. Mikhajlov, *Nucl. Phys. A* **712**, 3 (2002).
- [37] K. Nomura, R. Rodríguez-Guzmán, and L. M. Robledo, *Phys. Rev. C* **94**, 044314 (2016).
- [38] A. Dewald, O. Möller, and P. Petkov, *Prog. Part. Nucl. Phys.* **67**, 786 (2012).
- [39] V. Karayonchev, J. Jolie, A. Blazhev, A. Dewald, A. Esmaylzadeh, C. Fransen, G. Häfner, L. Knafla, J. Litzinger, C. Müller-Gatermann, J.-M. Régis, K. Schomacker, A. Vogt, N. Warr, A. Leviatan, and N. Gavrielov, *Phys. Rev. C* **102**, 064314 (2020).
- [40] A. Esmaylzadeh, V. Karayonchev, G. Häfner, J. Jolie, M. Beckers, A. Blazhev, A. Dewald, C. Fransen, A. Goldkuhle, L. Knafla, and C. Müller-Gatermann, *Phys. Rev. C* **103**, 054324 (2021).
- [41] M. Beckers, C. Müller-Gatermann, A. Blazhev, T. Braunroth, A. Dewald, C. Fransen, A. Goldkuhle, L. Kornweibel, J. Litzinger, F. von Spee, and K.-O. Zell, *Phys. Rev. C* **102**, 014324 (2020).
- [42] T. Alexander and A. Bell, *Nucl. Instrum. Methods* **81**, 22 (1970).
- [43] B. Saha, Ph.D. thesis, Universität zu Kön, 2004 (unpublished).
- [44] H. Bateman, *Proc. Cambridge Philos. Soc.* **15**, 423 (1910).
- [45] A. Dewald, S. Harissopulos, and P. von Brentano, *Z. Phys. At. Nucl.* **334**, 163 (1989).
- [46] J. Litzinger, A. Blazhev, A. Dewald, F. Didierjean, G. Duchêne, C. Fransen, R. Lozeva, K. Sieja, D. Verney, G. de Angelis, D. Bazzacco, B. Birkenbach, S. Bottoni, A. Bracco, T. Braunroth, B. Cederwall, L. Corradi, F. C. L. Crespi *et al.*, *Phys. Rev. C* **92**, 064322 (2015).
- [47] H. Bohn, P. Kienle, D. Proetel, and R. L. Hershberger, *Z. Phys. At. Nucl.* **274**, 327 (1975).
- [48] D. Ralet, S. Pietri, T. Rodríguez, M. Alaqaee, T. Alexander, N. Alkhomashi, F. Ameil, T. Arici, A. Ataç, R. Avigo, T. Bäck, D. Bazzacco, B. Birkenbach, P. Boutachkov, B. Bruyneel, A. M. Bruce, F. Camera, B. Cederwall, S. Ceruti, E. Clément, M. L. Cortés, D. Curien *et al.* (PreSPEC and AGATA Collaborations), *Phys. Rev. C* **95**, 034320 (2017).
- [49] F. Iachello and A. Arima, in *The Interacting Boson Model*, Cambridge Monographs on Mathematical Physics (Cambridge University Press, Cambridge, 1987).
- [50] J. Ginocchio and M. Kirson, *Nucl. Phys. A* **350**, 31 (1980).
- [51] J. M. Eldridge, B. Fenker, J. H. Hamilton, C. Goodin, C. J. Zachary, E. Wang, A. V. Ramayya, A. V. Daniel, G. M. Ter-Akopian, Y. T. Oganessian, Y. X. Luo, J. O. Rasmussen, and S. J. Zhu, *Eur. Phys. J. A* **54**, 15 (2018).
- [52] T. Kibédi and R. Spear, *At. Data Nucl. Data Tables* **89**, 77 (2005).
- [53] F. Schussler, J. Pinston, E. Monnard, A. Moussa, G. Jung, E. Koglin, B. Pfeiffer, R. Janssens, and J. van Klinken, *Nucl. Phys. A* **339**, 415 (1980).
- [54] T. A. Khan, W. D. Lauppe, K. Sistemich, H. Lawin, G. Sadler, and H. A. Selic, *Z. Phys. A* **283**, 105 (1977).
- [55] F. K. Wahn, J. C. Hill, C. B. Howard, K. Sistemich, R. F. Petry, R. L. Gill, H. Mach, and A. Piotrowski, *Phys. Rev. C* **33**, 677 (1986).
- [56] L. Svensson, C. Fahlander, L. Hasselgren, A. Bäcklin, L. Westerberg, D. Cline, T. Czosnyka, C. Wu, R. Diamond, and H. Kluge, *Nucl. Phys. A* **584**, 547 (1995).
- [57] J. Srebrny, T. Czosnyka, C. Droste, S. Rohoziński, L. Próchniak, K. Zajac, K. Pomorski, D. Cline, C. Wu, A. Bäcklin, L. Hasselgren, R. Diamond, D. Habs, H. Körner, F. Stephens, C. Baktash, and R. Kostecki, *Nucl. Phys. A* **766**, 25 (2006).
- [58] R. Casten, E. Flynn, O. Hansen, and T. Mulligan, *Nucl. Phys. A* **184**, 357 (1972).
- [59] E. R. Flynn, F. Ajzenberg-Selove, R. E. Brown, J. A. Cizewski, and J. W. Sunier, *Phys. Rev. C* **24**, 2475 (1981).
- [60] E. R. Flynn, R. E. Brown, J. A. Cizewski, J. W. Sunier, W. P. Alford, E. Sugarbaker, and D. Ardouin, *Phys. Rev. C* **22**, 43 (1980).
- [61] M. A. Rahman and M. S. Chowdhury, *Phys. Rev. C* **73**, 054311 (2006).
- [62] N. Gavrielov, A. Leviatan, and F. Iachello, *Phys. Rev. C* **99**, 064324 (2019).

4 | Publication III:

Triaxiality in the mid-shell nucleus ^{112}Pd

Triaxiality in the mid-shell nucleus ^{112}Pd

A. Esmaylzadeh ^{1,*}, V. Karayonchev,¹ G. Häfner,^{1,2} J. Jolie,¹ M. Beckers,¹ A. Blazhev,¹ A. Dewald ¹, C. Fransen ¹,
A. Goldkuhle,¹ L. Knafla,¹ and C. Müller-Gatermann ^{1,3}

¹*Institut für Kernphysik, Universität zu Köln, D-50937 Köln, Germany*

²*Univeristé Paris-Saclay, IJCLab, CNRS/IN2P3, F-91405 Orsay, France*

³*Argonne National Laboratory, 9700 South Cass Avenue, Argonne, Illinois 60439, USA*



(Received 11 January 2021; revised 24 March 2021; accepted 6 May 2021; published 25 May 2021)

Lifetimes of low-spin excited states in ^{112}Pd were measured using the recoil-distance Doppler-shift technique. The nucleus of interest was populated in a $^{110}\text{Pd}(^{18}\text{O}, ^{16}\text{O})^{112}\text{Pd}$ reaction using the Cologne FN Tandem accelerator. Three lifetimes of ground-state band members and one lifetime of the γ band were measured. From these lifetimes reduced transition probabilities were extracted and compared to interacting boson model, γ -soft calculations, and Davydov calculations. The lifetime of the 2_{γ}^{+} gives some insights on the nuclear shape and structure of the γ band. The deduced transition rates show an indicator for a rigid triaxial nucleus as well as more indicators for a γ -soft nucleus.

DOI: [10.1103/PhysRevC.103.054324](https://doi.org/10.1103/PhysRevC.103.054324)

I. INTRODUCTION

The isotopic chains of molybdenum, ruthenium, and palladium show evidence of γ -soft and rigid triaxial rotor behavior [1–5]. In even-even nuclei, the γ band is usually based on a 2^{+} state that is strongly related to triaxial motions, whereas the 2_{1}^{+} state is primarily sensitive to the quadrupole deformation [6]. The γ bandhead energy is related to the softness of vibrational motion in the γ direction, and the $E_{2_{\gamma}^{+}}/E_{4_{1}^{+}}$ ratio and the $E_{2_{\gamma}^{+}}/E_{2_{1}^{+}}$ ratio are important signatures of triaxiality. A triaxial shape rotates around all three axes of the intrinsic body and has its potential energy surface minimum between $\gamma = 0^{\circ}$ (prolate) and $\gamma = 60^{\circ}$ (oblate). Two models which discuss the γ -unstable case and the triaxial shape are the Wilets-Jean γ -unstable rotor model [7] and the Davydov-Filippov rigid triaxial rotor model [8–10], respectively. The former has a γ -independent minimum in the potential energy surface for a given deformation parameter β where the 2_{γ}^{+} and 4_{1}^{+} states are degenerated, while the latter predicts that the 2_{γ}^{+} state lies below the 4_{1}^{+} at the maximum of triaxiality at $\gamma = 30^{\circ}$. To distinguish between the γ softness and rigidity of a nucleus, the energy spacing within the γ band is a good indicator [11]. The staggering parameter $S(J)$ is able to characterize the rigidity or softness of a nucleus and is defined as [11]

$$S(J) = \frac{[E(J) - 2E(J-1) + E(J-2)]}{E(2_{1}^{+})}. \quad (1)$$

In this case, $E(J)$ represents the energy of the level with spin J in the γ band. If the staggering parameter $S(J)$ is positive for odd-spin levels and negative for even-spin levels, a γ -unstable nucleus is assumed, whereas the γ -rigid case is described by the opposite case [12].

The lower-mass Pd isotopes $^{108,110}\text{Pd}$ show indicators of vibrational behavior and the staggering parameter indicates evidence of a γ -soft rotor [13,14]. Figure 1 shows the staggering parameter for the $^{108-116}\text{Pd}$ isotopes ($Z = 46$). Below $N = 66$ (^{112}Pd), the nuclei exhibit a γ -soft pattern, where the staggering parameter $S(J)$ for even spins J is lower compared to the odd- J cases. As the chain is approaching $N = 68$ (^{114}Pd), the staggering parameter for the higher spin states ($J > 5$) follows the behavior expected for a triaxial rotor [22]. The investigations of higher mass $^{116-120}\text{Pd}$ ($N = 70-74$) isotopes suggest an anharmonic vibrator with less collectivity [18,23,24].

^{112}Pd ($N = 66$) lies at the neutron mid-shell between $N = 50$ and $N = 82$. A rotational collectivity is expected that has its maximum at $N = 68$ (^{114}Pd) for the isotopic chain [25]. The $R_{4/2} = E(4_{1}^{+})/E(2_{1}^{+})$ ratio increases from 2.4 (^{104}Pd) up to a maximum of 2.6 (^{114}Pd) and afterwards starts to decrease down to 2.4 in ^{120}Pd . The $B_{4/2} = B(E2; 4_{1}^{+} \rightarrow 2_{1}^{+})/B(E2; 2_{1}^{+} \rightarrow 0_{1}^{+})$ ratio is an additional signature which is usually used to characterize the shape and behavior of a nucleus. The ratio has already been studied in different works, starting with $^{108,110}\text{Pd}$ where the ratio is ≈ 1.5 [13,26–33], going to the recent lifetime measurements of ^{114}Pd where a ratio of 0.8 has been determined [15]. Furthermore, the nucleus ^{114}Pd was proposed to be an even-even wobblers [18], a phenomenon that has been observed in its isotone ^{112}Ru [34]. The neighboring ruthenium ($Z = 44$) isotopes show γ -soft and -rigid triaxial behavior, especially well pronounced for $^{110,112}\text{Ru}$ where the maximum of triaxiality is reached [1,2,35,36]. The former is the corresponding isotone of ^{112}Pd , where a similar behavior could be expected. The ground-state band of the cadmium isotopes $^{108-114}\text{Cd}$ were described as quadrupole vibrational states, but a recent study showed evidence of multishape coexistence in $^{110,112}\text{Cd}$, where the ground state shows a distinct minimum at an axial prolate deformation $\beta \approx 0.15$ [37,38]. To increase the insights of this diverse region of the

*Corresponding author: aesmaylzadeh@ikp.uni-koeln.de

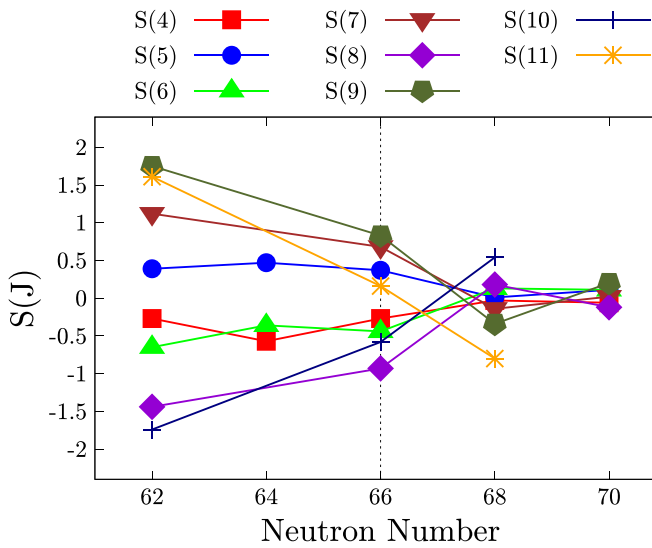


FIG. 1. The staggering parameter $S(J)$ for the $^{108-116}\text{Pd}$ isotopes calculated using Eq. (1), where ^{112}Pd is indicated with the dashed line at $N = 66$ (adapted from Ref. [15]). The energy values are taken from ^{108}Pd ($N = 62$) [16], ^{110}Pd ($N = 64$) [17], ^{112}Pd ($N = 66$) [18,19], ^{114}Pd ($N = 68$) [18,20], and ^{116}Pd ($N = 70$) [18,21]. Note that some energy levels are in parentheses, which means that the spins are not finally assigned. This holds especially for the states with spin higher than $J = 7$.

nuclear chart, the nucleus ^{112}Pd is investigated in this work. Lifetimes of four low-spin states were measured and the deduced transition probabilities are discussed in the context of the interacting boson model (IBM), a modified Willets-Jean model, and the Davydov-Filippov model to investigate the nuclear shapes and behavior in this region.

II. EXPERIMENT

The nucleus of interest was populated using a two-neutron transfer reaction, i.e., $^{110}\text{Pd}(^{18}\text{O}, ^{16}\text{O})^{112}\text{Pd}$. An average beam current of ≈ 1 pA with an energy of 56 MeV was provided by the Cologne 10 MV FN-Tandem accelerator. The highly enriched (99.98%) ^{110}Pd self-supporting target with a thickness of 0.7 mg/cm² was stretched inside the Cologne Plunger device [39]. A 6.5 mg/cm² Ta stopper foil was stretched in parallel to the target and acts as a stopper for the ejectiles. To detect the γ rays produced in the reaction, 11 high-purity germanium (HPGe) detectors were mounted in two rings (backward and forward) around the target chamber. The six forward detectors were positioned at an angle of 45° , whereas the five backward detectors were placed at an angle of 142° with respect to the beam direction. Similar to a previous experiment using the same configuration [40], six solar cells were installed at backward angles to detect the light backscattered recoiling fragments. To apply the recoil-distance Doppler-shift (RDDS) technique, 11 target-to-stopper distances (40, 59, 89, 109, 139, 239, 339, 489, 639, 789, and 1039 μm) were measured in 90 h of beam time. These distances were obtained by using the capacitance method which is described in Refs. [39,41]. The velocity of the recoiling ^{112}Pd was determined using the shifted and unshifted components of the

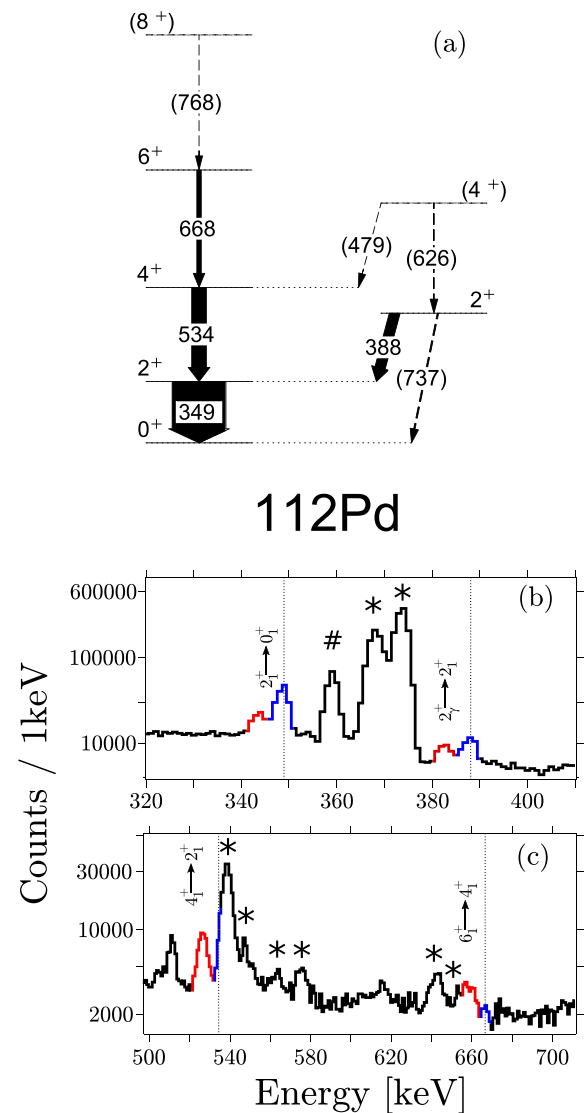


FIG. 2. (a) The level scheme of the observed states in ^{112}Pd , where the width of the transition arrows indicates the intensity (see Table I). Dashed lines are used to indicate possible feeding transitions, which have not been observed in this experiment. (b, c) The γ -ray spectrum with the sum over all distances using a particle gate on the backscattered $^{16,18}\text{O}$ fragments for the backward detectors. All transitions which were observed in the current work are colored blue for the unshifted and red for the shifted components. Additionally, a dashed line is indicating the unshifted peak. The transitions marked with a # belong to ^{181}Ta which was the stopper and transitions marked with a * belong to the Coulomb excitation channel, i.e., ^{110}Pd . Note the logarithmic y scale due to statistical reasons.

most intensive transitions and results in $v/c = 1.81(1)\%$. The sum of all particle-gated γ -ray spectra of each distance is shown in Fig. 2. A partial level scheme of ^{112}Pd is shown, where the dashed lines describe possible feeding transitions. Additionally, the 737 keV transition is shown that was not detected due to the low population of the 2_2^+ and its low intensity. The strongest γ rays belong to ^{110}Pd , ^{112}Pd , and ^{181}Ta . The exclusion of the Coulomb excitations of ^{110}Pd was not possible because due to the low energy resolution

TABLE I. Relative transition intensities observed in the two-neutron transfer $^{110}\text{Pd}(^{18}\text{O}, ^{16}\text{O})^{112}\text{Pd}$ reaction. The intensities were normalized to the $2_1^+ \rightarrow 0_1^+$ transition and the energies are taken from Ref. [19].

Transition	Transition energy (keV)	Intensity
$2_1^+ \rightarrow 0_1^+$	348.6	1000(19)
$2_\gamma^+ \rightarrow 2_1^+$	388.0	196(21)
$4_1^+ \rightarrow 2_1^+$	534.3	277(20)
$6_1^+ \rightarrow 4_1^+$	667.5	83(26)

the solar cells were not able to separate the recoiling ^{16}O and ^{18}O particles in the spectrum. Hence, the major peaks in the spectrum belong to the Coulomb excitation of the target (^{110}Pd). Furthermore, γ rays from the stopper (^{181}Ta) are visible where the beam particles can scatter and enter the solar cells. The peaks of the backscattered ^{18}O or ^{16}O particles from the target or stopper overlap in the solar cell spectrum and a complete separation of the γ rays from ^{181}Ta was not possible. Some transitions of ^{111}Pd and ^{124}Xe were detected, which were populated in the single-neutron transfer and in the fusion evaporation reaction, respectively. The transitions belonging to ^{112}Pd with their energies and intensities, normalized to the $2_1^+ \rightarrow 0_1^+$ transition, are summarized in Table I. During the analysis process, the intensities are used to determine the feeding population for the different states of interest.

III. ANALYSIS

To determine the lifetimes of the 2_γ^+ , 6_1^+ , 4_1^+ , and 2_1^+ states, the Bateman equations were used to analyze the recoil-distance Doppler-shift data. In addition, the well established differential decay curve method (DDCM) [42] was used, which is able to detect certain systematic errors. Due to the low statistics of the experiment, only particle-gated γ spectra were used to analyze the data. For a detailed review of both methods, the reader is referred to Ref. [39].

Due to the low statistics for the 6_1^+ state, the method explained in Ref. [43] is used to obtain the lifetimes from the summed spectra of all distances. Here the solution of the Bateman equations of the single distances j is given by

$$R_{\text{sum}} = \frac{\sum_j I_j^u}{\sum_j I_j^u + \sum_j I_j^s} = \sum_j n_j R(t_j) \quad (2)$$

where I_j^u and I_j^s are the intensities of the unshifted and shifted component, respectively. In Eq. (2), n_j describes the normalization factor for each distance, whereas t_j describes the flight time for each distance. The lifetime of the 6_1^+ state is important to adjust the feeding pattern for the lower-lying states, i.e., the 2_γ^+ and the 4_1^+ state. Hence, a top-to-bottom approach was used to determine the lifetimes.

A. The analysis of the 6_1^+ state

For the 6_1^+ state as the highest observed state, the spectra for each distance were summed up to obtain enough statistics. The particle-gated γ -ray spectrum of the backward ring for this state is shown in Fig. 3. The value R_{sum} is obtained using Eq. (2). To extract the lifetime, it is very important to de-

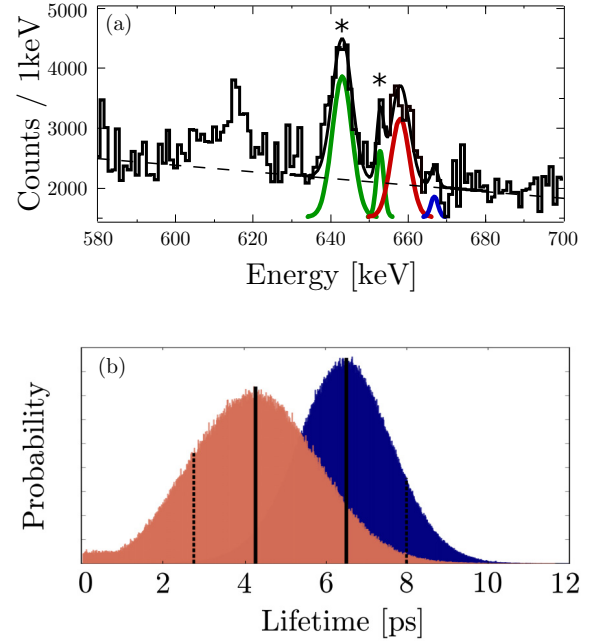


FIG. 3. (a) Fit of the decaying γ ray of the 6_1^+ state with the unshifted peak at 667.5 keV and the corresponding shifted peak at 658 keV, where the summed particle-gated γ -ray spectra of each distance were used due to the low statistics. The ratio R_{sum} was obtained with a fit and was used to determine the lifetime according to Eq. (2). The peaks marked with an asterisk are the shifted and unshifted components of the $6_1^+ \rightarrow 4_1^+$ transition in ^{110}Pd . A fit to those components (green) is included to eliminate the contributions on the investigated case where the shifted component is colored in red and the unshifted in blue. (b) The simulated lifetimes of the 6_1^+ state with (red) and without (blue) feeding. See text for details of the simulation. The upper and lower limits of the results are indicated with dashed lines.

termine the normalization factors carefully. Therefore, a gate on both components of the $2_1^+ \rightarrow 0_1^+$ transition was applied. The resulting particle spectra were integrated to obtain the normalization factors. The final lifetime is calculated by a Monte Carlo simulation (with 10^6 iterations), where different parameters are varied. The parameters R_{sum} , normalization factors n_j , and the velocity are varied within their uncertainties. Furthermore, the target-to-stopper distance was varied by $\pm 5 \mu\text{m}$ and the uncertainties are again obtained using a Monte Carlo simulation. In Fig. 3(b), the final result is shown where a lifetime of $\tau_{6_1^+} = 6.4(11)$ ps is obtained for the 6_1^+ state without considering feeding. In a two-neutron transfer experiment using the (t, p) reaction, the 8_1^+ state was observed, which is not observed in this experiment [44]. To investigate the possible feeding of the 8_1^+ and other unobserved feeding γ rays, the simulation is extended with an extra parameter which considers this feeding. An assumption for maximal feeding from the 8_1^+ state and the unobserved one can be extrapolated from the feeding of the lower-lying states and by the fact that the population of states in the transfer reaction is decreasing with increasing spin and excitation energies. According to the relative intensities given in Table I, a realistic amount of the 6_1^+ state feeding contribution is 10%. In other words, 90% of

the observed 6_1^+ state is directly populated through the reaction. The effective lifetime of the feeding states was chosen to be 100 ps, which is sufficiently long so that the feeding effect is reaching saturation. For the sake of simplicity, the feeding is modeled by a single hypothetical state. By including feeding in the simulation, the calculated lifetime becomes lower and results in $\tau_{6_1^+} = 4.2(15)$ ps [see Fig. 3(b)], where the lower limit (of the simulation with the inclusion of feeding) is used as a lower limit for the lifetime. The final result of the lifetime is $\tau_{6_1^+} = 6.4_{-3.7}^{+1.1}$ ps. The lifetime of the 6_1^+ state in combination with the determined relative intensities can be used to correct feeding contributions to lower states.

B. The lifetime of the 4_1^+ , 2_1^+ , and 2_2^+ states

After obtaining the lifetime of the highest observed state the lifetime of the lower-lying states can be determined starting with the 4_1^+ state. The lifetime and feeding population of the 6_1^+ state and the direct population of the 4_1^+ state are used as fixed parameters whereas the lifetime of the 4_1^+ state is the only free parameter to fit the data using the Bateman equations. The evolution of the shifted and unshifted peaks is shown in the third and fourth columns of Fig. 4 and the decay curve using the Bateman equations is shown in Fig. 5. Furthermore, in Fig. 6 the results of the backward ring using the DDCM are shown, where the program NAPATAU [45] was used to determine the lifetime. The results for the DDCM and Bateman equations for the backward and forward ring are summarized in Table II in which the final result of $\tau_{4_1^+} = 10(1)$ ps was obtained.

For the lifetime determination of the 2_2^+ state, the 388 keV $2_2^+ \rightarrow 2_1^+$ transition was used. The 737 keV transition cannot be used because the intensity was too small to extract the lifetime information from the data. The corresponding fit of the data is shown in the first and second columns of Fig. 4. The high statistical error is based on the low population of the 2_2^+ state and the disturbing 373 keV transition from ^{110}Pd . After applying the Bateman equations and the DDCM, the final result is $\tau_{2_2^+} = 51.2(25)$ ps, which is the weighted average of four determined lifetimes (see Table II).

After obtaining the lifetimes of all states above the 2_1^+ state, the lifetime of this state is now accessible and the feeding pattern can be included in its calculation. The 2_1^+ state is fed by the 2_2^+ state (388 keV) and the 4_1^+ state (534 keV). The fits of the shifted and unshifted peaks are shown in Fig. 4. For the forward angles, the 359 keV transition from ^{181}Ta was included in the fit to take care of the background influence on the shifted $2_1^+ \rightarrow 0_1^+$ (349 keV) transition with the energy 353 keV. After using the Bateman equations and the DDCM, shown in Figs. 5 and 6, a final lifetime for the 2_1^+ state of $\tau_{2_1^+} = 110(3)$ ps is obtained. The determined lifetime is consistent with a former RDDS lifetime measurement with a result of 121(20) ps [46] within the errors. Another upper limit of $\tau < 1$ ns can be confirmed as well [47].

IV. THEORETICAL CALCULATIONS

Three phenomenological models were used to describe the excited states and transition rates of ^{112}Pd , namely, the

Davydov-Filippov [8,9] and a modified version of the Wilets-Jean model described in Refs. [7,48,49] and the *sd*-interacting boson model (IBM-1). The Davydov-Filippov model represents a general phenomenological approach for quadrupole deformations where the nuclear deformation β and asymmetry parameter γ are fixed parameters for a given $\gamma \neq 0$. In this work, two calculations using $\gamma = 27.5^\circ$ and $\gamma = 30^\circ$ were used to compare with the experimental signatures. For further details of the model the reader is referred to Refs. [8,9]. The second phenomenological approach is a generalization of the Wilets-Jean model [7], where the Hamiltonian has a γ -independent potential and a constant mass parameter. In addition, the model describes a smooth transition from the standard quadrupole vibrational model through to large β deformation. Here, the reader is referred to Refs. [48,49] to get further details of the calculations and to Ref. [50] where the code used to calculate the excitation energies and transition probabilities is presented. Additional calculations were performed in the framework of the IBM-1, where no distinction between protons and neutrons is made. This model cannot yield triaxial deformation [51], but only either γ -soft deformation (γ independent), prolate ($\gamma = 0^\circ$), or oblate ($\gamma = 60^\circ$) deformation. In the following, the IBM-1 Hamiltonian and the transition-rate operators are described.

A. Framework of the IBM-1

For the *sd* IBM-1 calculations, the extended consistent *Q* formalism (ECQF) [52] with a Hamiltonian similar to the one in Ref. [53] is

$$\hat{H} = \epsilon_d \hat{n}_d + \kappa \hat{Q}^\chi \cdot \hat{Q}^\chi + \lambda \hat{L} \cdot \hat{L} + c_3 \hat{T}_3 \cdot \hat{T}_3, \quad (3)$$

where

$$\hat{Q}^\chi = (s^\dagger \tilde{d} + d^\dagger \tilde{s})^{(2)} + \chi (d^\dagger \tilde{d})^{(2)},$$

$$\hat{L} \hat{L} = \sqrt{10} (d^\dagger \tilde{d})^{(1)},$$

$$\hat{T}_3 = (d^\dagger \tilde{d})^{(3)},$$

and $\hat{n}_d = d^\dagger \cdot \tilde{d}$ is used. The *E2* operator is defined as

$$\hat{T}(E2) = e_B \hat{Q}, \quad (4)$$

where e_B is the effective boson charge. The Hamiltonian of Eq. (3) uses five parameters, namely, ϵ , κ , λ , c_3 , and χ , and the code ARBMODEL [54] was used to perform the calculations. Having four proton holes to the closed proton shell at $Z = 50$ and 16 neutron holes (particles) to the closed neutron shell at $N = 50$ (or $N = 82$), the boson number for ^{112}Pd is $N_B = 10$. In general, some key observables are taken into account to obtain the parameters [55]. The parameters are deduced by a fit to the following ratios:

$$(i) R_{4/2} = E(4_1^+)/E(2_1^+) = 2.53,$$

$$(ii) R_{6/2} = E(6_1^+)/E(2_1^+) = 4.45,$$

$$(iii) R_{2_2/2} = E(2_2^+)/E(2_1^+) = 2.11,$$

$$(iv) B_{4/2} = B(E2; 4_1^+ \rightarrow 2_1^+)/B(E2; 2_1^+ \rightarrow 0_1^+) = 1.29.$$

A full parameter scan of the five parameters (ϵ , λ , κ , c_3 , χ) in combination with a least χ^2 fit to the experimental ratios was used to determine the optimal parameters. The parameters

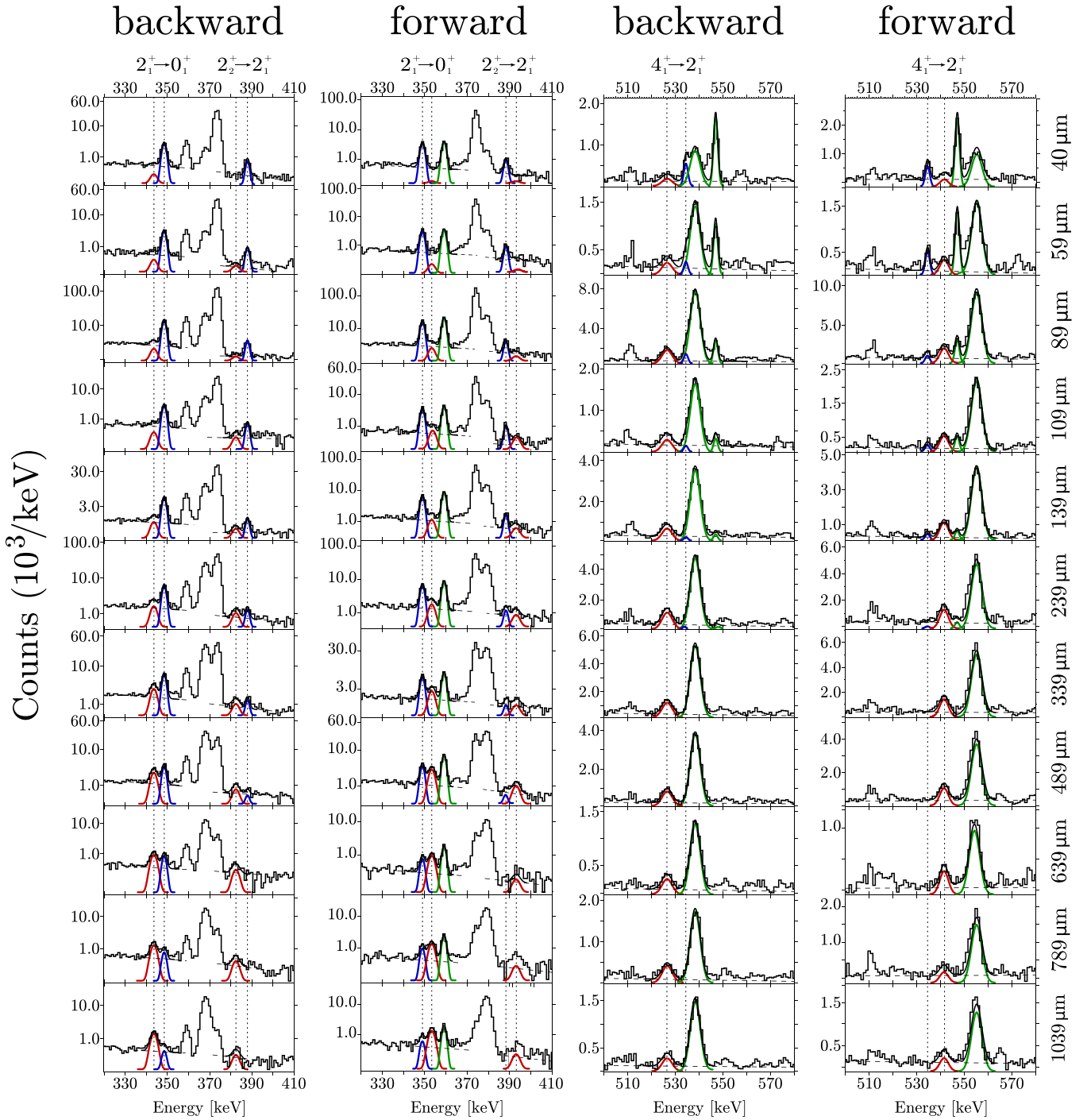


FIG. 4. Particle-gated spectrum of the backward and forward ring for all distances and the evolution of the $2_1^+ \rightarrow 0_1^+$ (348.6 keV), $2_2^+ \rightarrow 2_1^+$ (388.0 keV), and $4_1^+ \rightarrow 2_1^+$ (534.3 keV) transitions. The ring and the transition are indicated on the upper part of the figure. Furthermore, the distance is placed on the right hand side of the figure. The spectra indicate the background level, the shifted peak (red), the unshifted peak (blue), and also different disturbing transitions which were also fit (green). The disturbing transitions belong either to ^{110}Pd or to ^{181}Ta . Note that a logarithmic scale is used for the backward and forward spectra for the region 320 keV up to 410 keV.

$\epsilon = 1124$ keV, $\lambda = 0$ keV, $\kappa = -42$ keV, $c_3 = -179$ keV, and $\chi = -0.183$ yield the best agreement to the experimental data. The c_3 term is needed to adjust the γ -band energy levels to the observed excitation energies. The effective boson charge in the units of e_b was chosen to be $e_b = 0.0847$ in

order to match the experimental $B(E2; 2_1^+ \rightarrow 0_1^+)$ value. For ^{112}Pd the level energies of the yrast band up to the 10_1^+ state and for the γ band up to the 6_γ^+ state were determined. In addition, reduced transition probabilities were calculated for the transitions determined in this work.

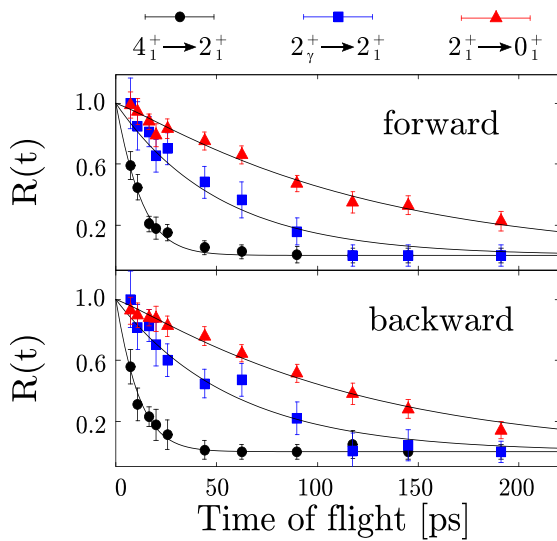


FIG. 5. The decay curves for the lifetime of the 4_1^+ , 2_2^+ , and 2_1^+ states using the Bateman equations to fit the data. The upper panel shows the data points of the forward ring at 45° and the lower panel of the backward ring at 142° . The resulting lifetimes are summarized in Table II.

V. RESULTS AND DISCUSSION

A. Comparison to calculations

1. Energy levels

The energy levels of the experimental data and the calculations, namely, IBM-1, γ soft, and the Davydov-Filippov (hereafter D-F) calculations, are shown in Fig. 7, starting with the ground-state band and the 2_1^+ state, where all models are able to describe the excitation energies. The ground-state band members 4_1^+ and 6_1^+ are well described by the IBM-1 while both D-F calculations overestimate the energy by around 50 keV and around 200 keV. Due to the properties of the γ -soft model, the energies of the 4_1^+ and 2_2^+ states are described as a doublet and that of the 3_2^+ , 4_2^+ , and 6_1^+ states as a triplet state. The energy of the 4_1^+ state is underestimated as well as the energy of the 6_1^+ state. The only model that is able to describe the 8_1^+ and 10_1^+ states with relatively good accuracy is the IBM-1. The D-F calculation overestimates the excitation energy of those states while the γ -soft model underestimates the excitation energy, both by about 500 keV. The γ bandhead, the 2_2^+ state, is well described by the IBM-1 calculation and the D-F calculations with 27.5° , whereas the doublet state in the γ -soft model overestimates the excitation energy. The IBM-1 is the only model that is able to describe the other γ -band members while slightly underestimating the excitation energy. The energy level of the γ band using the γ -independent potential (γ -soft model) shows a cluster as (2_2^+) , $(3_2^+, 4_2^+)$, and $(5_2^+, 6_2^+)$ whereas the rigid triaxial rotor (Davydov-Filippov model) shows a $(2_2^+, 3_2^+)$, $(4_2^+, 5_2^+)$ clustering pattern [56]. The experimental level energies do not favor either of the γ -soft or D-F models and, hence, neither of the models describes the energy pattern. An argument which could support that the γ -soft-type cluster pattern is slightly favored is due to the energies of the 3_2^+ and the 5_2^+ states which

are closer to the 4_2^+ and 6_2^+ states, respectively. A further signature is the staggering parameter that can be calculated using Eq. (1) and is shown in Fig. 8 for the experimental data and compared to the calculations. Note that the staggering values of the $S(8)$ are also shown whereas the level energies of the corresponding 8_2^+ states are not shown in Fig. 7 for the D-F calculations. The experimental $S(J)$ values of ^{112}Pd occur to have small oscillations around zero where the even $S(J)$ values are negative and the odd $S(J)$ values are positive. This behavior suggests a γ -soft pattern, where the γ -soft calculations are reproducing the pattern but are noticeably higher. Due to the rigid properties of the D-F calculations, an opposite behavior is observed and, hence, both are not able to describe the experimental oscillation of the $S(J)$ values. As for the energy levels, the only model calculations that describe the staggering parameter with good accuracy are the calculations performed using the IBM-1. Comparing the four calculations from the energetic point of view, the IBM-1 is the closest to the experimentally observed one. Therefore, a potential energy surface (PES) using the parameters of the IBM-1 was used to get a better overview of the β and γ deformation of this nucleus. The potential which is dependent on β and γ is deduced by calculating the expectation value of the Hamiltonian in the coherent state [57–59] and it is shown in Fig. 9. The PES shows a minimum around $\beta \approx 0.3$ and $\gamma = 0^\circ$, which corresponds to prolate deformation. The energy minimum in the PES is broad and spreading in the γ direction, which could be interpreted as an evidence for γ softness.

2. Reduced transition probabilities

The reduced transition probabilities are summarized in Table III. The calculated $B(E2; 2_1^+ \rightarrow 0_1^+)$ values for the D-F and IBM calculations were normalized to the experimental $B(E2; 2_1^+ \rightarrow 0_1^+)$ value. The γ -soft model was not normalized and therefore the calculations slightly underestimate the value. All calculations obtain an accurate description of the $B(E2; 4_1^+ \rightarrow 2_1^+)$ value, where it is notable that all theoretical values predict larger values that are above the experimentally deduced transition probability. Due to the high uncertainty of the lifetime of the 6_1^+ state, the transition probability ranges from 24 to 58 W.u. and does not allow for a clear interpretation of the result. All calculations predict $B(E2; 6_1^+ \rightarrow 4_1^+)$ values which are larger. A possible explanation could be a low-lying interband mixing which is not included in the calculations. A further investigation of this state is necessary to get a more accurate $B(E2; 6_1^+ \rightarrow 4_1^+)$ value so that a better description is possible. The $B(E2; 2_2^+ \rightarrow 0_1^+)$ value can only be described by the D-F calculation with $\gamma = 27.5^\circ$. The IBM-1 predicts a larger value and the γ -soft as well as the D-F calculation for $\gamma = 30^\circ$ computed a nonexisting probability for this transition. The other transition depopulating this state going to the 2_1^+ state is a mixed $M1/E2$ transition where the multipole mixing ratio of $\delta = 4.7_{-3.5}^{+1.7}$ is taken from Ref. [61]. The relatively large $B(E2; 2_2^+ \rightarrow 2_1^+)$ strength which can be an indicator for a rigid triaxial rotor is reproduced by the IBM-1, whereas the other calculations overestimate the value. Finally,

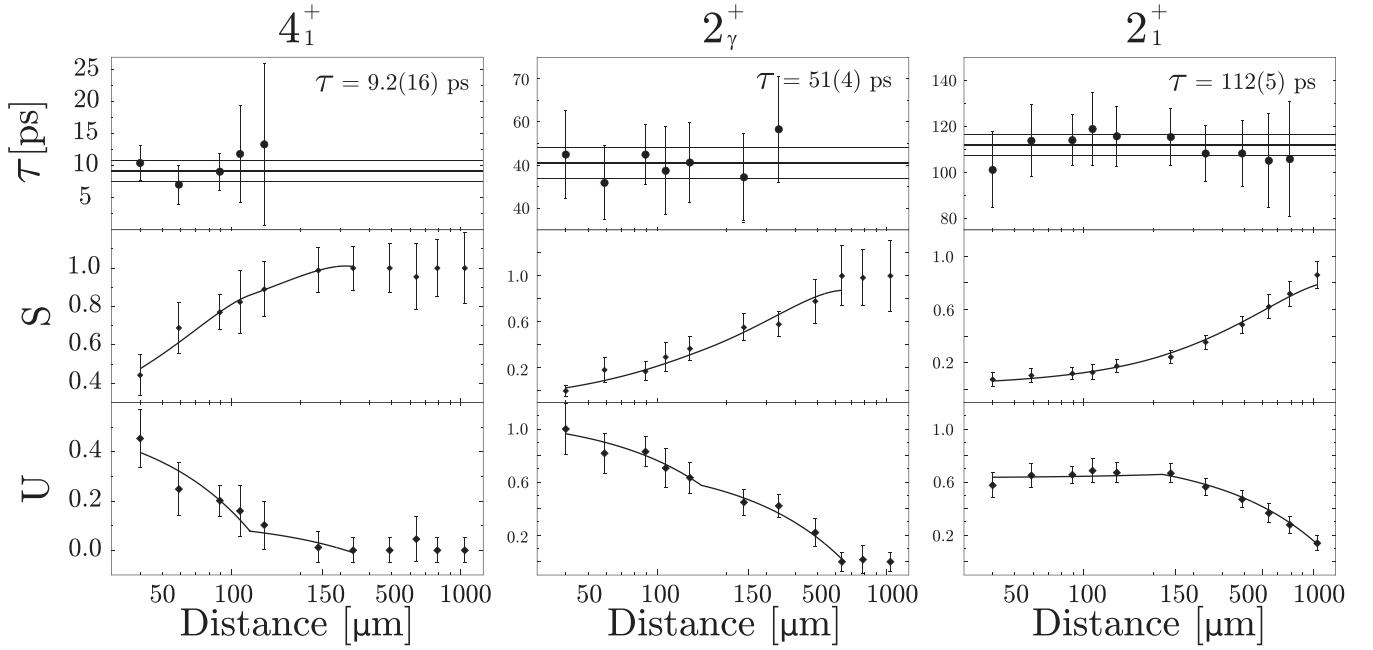


FIG. 6. The DDCM method for the 4_1^+ , 2_γ^+ , and 2_1^+ using the program NAPATAU [45] for the backward angle. The upper panel shows the individually obtained lifetime. The middle panel shows the evolution of the shifted component and the fit which is used to obtain the derivative $\frac{d}{dx}R_i(x)$, whereas the unshifted component and the corresponding fit are shown in the lower panel.

the $B(M1; 2_\gamma^+ \rightarrow 2_1^+)$ is not described by either calculation because the models are not able to calculation such transitions.

By examining the three ratios $B_{4/2}$, $B_{2_\gamma/2}$, and $B'_{2_\gamma/2}$ defined in Table III, all models reproduce the $B_{4/2}$ ratio within the 3σ error margin. The $B_{2_\gamma/2}$ ratio compares intraband transition rates where the IBM-1 obtained a similar ratio and the other models cannot provide an accurate description of this ratio. The maximal triaxial D-F model with $\gamma = 30^\circ$ and the γ -soft model overestimate the value by a factor of 2, with the same ratio of $B_{2_\gamma/2} = 1.64$. Furthermore, the same overestimation occurs for the $B'_{2_\gamma/2}$ ratio, where both approaches calculated give an infinite value. The D-F calculation at $\gamma = 27.5^\circ$ predicts this ratio with good accuracy whereas the IBM-1 underestimates the ratio.

TABLE II. Lifetimes measured in the experiment using the Bateman equation (BE) and the DDCM method together with the adopted values. The results from Ref. [46] are given for comparison.

State	Lifetime (ps)					Literature
	Backward ring		Forward ring		Adopted	
	BE	DDCM	BE	DDCM		
2_1^+	105(9)	112(5)	108(10)	110(5)	110(3)	121(20) ^a
2_γ^+	57(7)	51(4)	56(7)	48(4)	51.2(25)	
4_1^+	8.9(18)	9.2(16)	10.3(15)	11.2(14)	10(1)	
6_1^+	$6.4_{-3.7}^{+1.1}$				$6.4_{-3.7}^{+1.1}$	

^aFrom Ref. [46].

The formula

$$\chi^2 = \sum_i \frac{(x_{\text{theor},i} - x_{\text{expt},i})^2}{\Delta x_{\text{expt},i}} \quad (5)$$

was used to statistically describe the model with the most accuracy. The smaller the value the more accurate the calculation. The corresponding values are summarized in Table III and the IBM-1 and D-F calculation at $\gamma = 27.5^\circ$ provide the best values.

B. Indicators of triaxiality and γ softness in ^{112}Pd

With the assumed γ bandhead in combination with the newly reduced transition probabilities $B(E2; 2_2^+ \rightarrow 2_1^+)$ and $B(E2; 2_2^+ \rightarrow 0_1^+)$ can give insights of the triaxial or γ -soft behavior of this nucleus. Both possible structures are discussed within the newly obtained results in addition to comparisons to isotones and isotopes.

1. Making the case for rigid triaxiality

An indicator of a rigid triaxial rotor nucleus is that the excitation energy of the 2_γ^+ state is below the 4_1^+ state. This is the case for the $^{106-118}\text{Pd}$ ($N = 60-72$) isotopes. For the isotopic chain of palladium isotopes, the excitation energy of the 2_γ^+ has its minimum at ^{114}Pd ($N = 68$) with $E_{2_\gamma^+} = 695$ keV [60]. A similar behavior has been observed for the ruthenium isotopes with a maximum of triaxiality is reached for $^{110,112}\text{Ru}$ [1,35,36], where the former is the isotone of ^{112}Pd . This is supported by a recent study of ^{110}Ru where a relative rigid triaxial deformation near the ground state was suggested [2]. Another experimental relation that supports the rigid triaxiality in this nucleus is that the sum of the

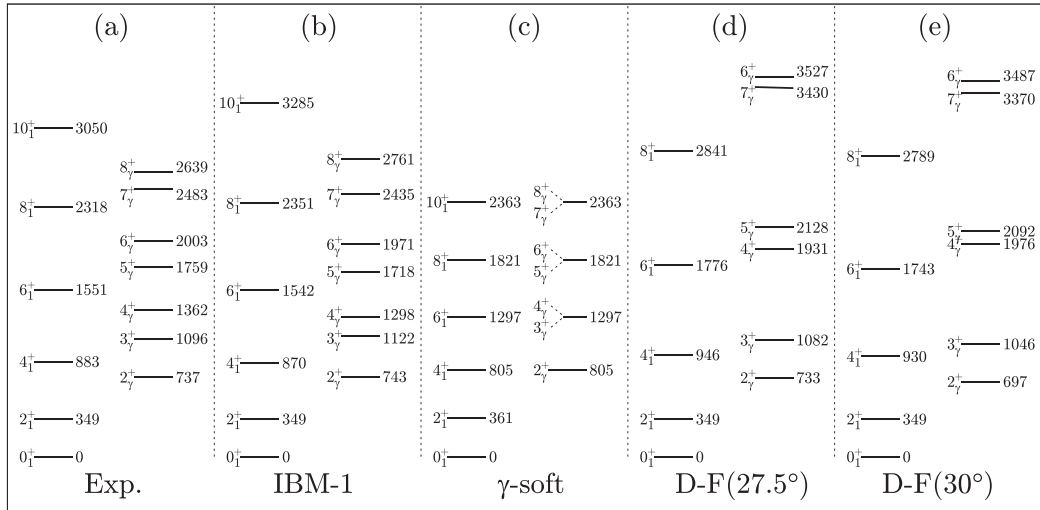


FIG. 7. The level energies of the ground state up to the 10_1^+ and the γ band up to the 8_2^+ state for the (a) experimental and (b) IBM-1 calculations. (c) The γ -soft calculations using the model explained in Refs. [48,49] and using the code from Ref. [50], where the parameters $B = 146$, $a = 0.12$, $C_2 = 47$, $G = 3.42$, and $C_8 = f = 0$ are used. Last, the Davydov-Filippov calculations with (d) $\gamma = 27.5^\circ$ and (e) $\gamma = 30^\circ$, where the 8_2^+ state is not shown which is positioned at about 5 MeV. All excitation energies are given in keV and a further description of the models and calculations are given in Sec. IV.

energies of the first and second 2^+ states is almost equal to the energy of the 3_1^+ state, i.e., $E(3_1^+) = E(2_1^+) + E(2_2^+)$ [2]. For ^{112}Pd this signature matches with less than 15 keV deviation which indicates a possible breaking of axial symmetry [2]. In addition, the $B(E2)$ reduced transition probabilities between levels of a $K = 2$ band, here in this case the γ band, and a $K = 0$ band which is the ground-state band are sensitive indicators of triaxial behavior [62]. Due to the relatively large $B(E2; 2_2^+ \rightarrow 2_1^+)$ and small $B(E2; 2_2^+ \rightarrow 0_1^+)$ values, a strong indicator of triaxial deformation is given. This indicator is also supported by the D-F calculations that reproduce the experimental signatures, namely, the $B(E2; 2_2^+ \rightarrow 0_1^+)$ and $B(E2; 2_2^+ \rightarrow 2_1^+)$, with reasonable accuracy at $\gamma = 27.5^\circ$.

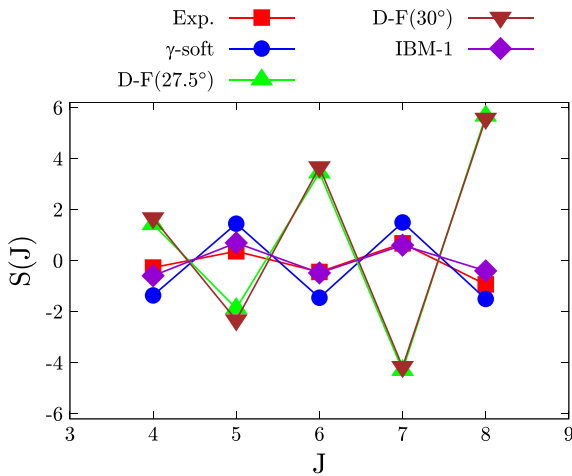


FIG. 8. The experimentally deduced staggering parameter compared to the staggering parameter of the IBM-1 calculations, γ -soft calculations, and the Davydov-Filippov calculations with 27.5° and 30° . For further explanations see text.

2. Making the case for a γ -soft nucleus

Not all signatures support the fact of a rigid rotor nucleus; some observables favor a γ -soft nucleus. The relatively large $B(E2; 2_2^+ \rightarrow 2_1^+)$ and small $B(E2; 2_2^+ \rightarrow 0_1^+)$ could also be an indicator for γ softness. Another important characteristic of a γ -soft nucleus is the small increasing $S(J)$ value for increasing spin J (for absolute values), i.e., the $S(4) = -1.36$, $S(5) = 1.45$, $S(6) = -1.45$, $S(7) = 1.50$, \dots , in contrast to the largely increasing $S(J)$ value for increasing spin J (see Fig. 8) in the rigid triaxial case. The experimental staggering parameter increases smoothly with increasing spin J , which is similar to the assumption of a γ -soft nucleus. Another supporting factor is the PES of the IBM-1 which is shown in Fig. 9. Note that these calculations obtained the most accurate description of ^{112}Pd . In Fig. 9, a tendency of γ softness can be observed as the minimum spreads in the direction of γ .

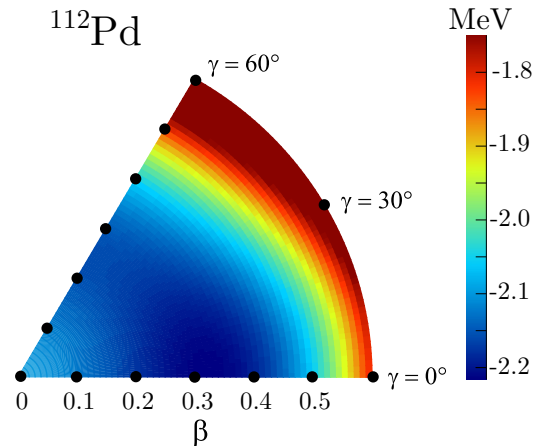


FIG. 9. The potential energy surface (PES) of the IBM-1 calculation using the parameters described in Sec. IV A.

TABLE III. The experimentally deduced transition probabilities for ^{112}Pd compared to the transition rates of the IBM-1, γ -soft, and two Davydov-Filippov calculations where 1 W.u. equals $32.07 e^2 \text{ fm}^4$. A parameter χ^2 defined in Eq. (5) is calculated to give a statistical overview of the model with the best description. Three $B(E2)$ ratios are calculated to get a more detailed picture of the comparison.

Transition	Experiment	IBM-1	γ soft	D-F (27.5°)	D-F (30°)
$B(E2; 2_1^+ \rightarrow 0_1^+)$ (W.u.)	44(1)	44	39	44	44
$B(E2; 4_1^+ \rightarrow 2_1^+)$ (W.u.)	58_{-5}^{+6}	67	64	61	62
$B(E2; 6_1^+ \rightarrow 4_1^+)$ (W.u.)	29_{-5}^{+29}	77	87	77	77
$B(E2; 2_\gamma^+ \rightarrow 0_1^+)$ (W.u.) ^a	0.50(3)	2.1	0	0.7	0
$B(E2; 2_\gamma^+ \rightarrow 2_1^+)$ (W.u.) ^{a,b}	40(1)	40	64	55	64
$B(M1; 2_\gamma^+ \rightarrow 2_1^+)$ ($10^{-4} \mu_N^2$) ^{a,b}	6.2_{-30}^{+80}				
χ^2		178	731	307	666
$B_{4/2} = \frac{B(E2; 4_1^+ \rightarrow 2_1^+)}{B(E2; 2_1^+ \rightarrow 0_1^+)}$	1.31(14)	1.52	1.64	1.39	1.41
$B_{2_\gamma/2} = \frac{B(E2; 2_\gamma^+ \rightarrow 2_1^+)}{B(E2; 2_1^+ \rightarrow 0_1^+)}$	0.91(3)	0.91	1.64	1.25	1.64
$B'_{2_\gamma/2} = \frac{B(E2; 2_\gamma^+ \rightarrow 2_1^+)}{B(E2; 2_\gamma^+ \rightarrow 0_1^+)}$	80(5)	19	∞	79	∞

^aA branching ratio of 76% for the $2_\gamma^+ \rightarrow 2_1^+$ and 24% for the $2_\gamma^+ \rightarrow 0_1^+$ was used [60,61].

^bA multipole mixing ratio $\delta = -4.7_{-3.5}^{+1.7}$ was used from Ref. [61].

The minimum energy in the PES is not flat in the γ degree of freedom as it is supposed for the γ -soft case and a minimum is visible for a prolate deformation. Observing the neighboring isotopes, ^{110}Pd shows evidences of a γ -soft behavior [14] so that it is reasonable to assume similar behavior for ^{112}Pd with increasing excitation energy. The even-odd nuclei $^{109,111}\text{Pd}$ were studied in Ref. [63] where an enhanced γ softness was observed, which would underline the γ softness of the Pd isotopes in this region. Another supporting factor is the overall staggering trend in Mo-Ru-Pd region, which shows a well pronounced staggering effect for $^{108-112}\text{Pd}$ [64]. Note that the staggering amplitudes are strongly suppressed for the isotope ^{110}Ru .

3. Summary

The γ -soft model describes the energetic properties of ^{112}Pd with more accuracy than the rigid triaxial rotor model. However, the reduced transition probabilities are better described by the D-F calculations, especially for $\gamma = 27.5^\circ$. Both the γ -soft and rigid triaxial structures have signatures and characteristics that match the experimental data and, hence, a clear conclusion cannot be made. A possible hypothesis which could support both models is that the low spin states, i.e., 2_γ^+ and 3_γ^+ , of the γ band possess a more rigid behavior while the higher spin states $J > 4$ show a γ -soft behavior. This would suggest a smooth transition from a relative rigid nuclear structure in the low spin states to a nearly γ -soft structure in the higher spin states within the γ band. This hypothesis is supported by the fact that the D-F calculations are capable to describe the lower states of the γ band with better accuracy than the γ -soft calculations and vice versa for the higher spin states. Such a phenomenon lies outside the model space of these models but has been studied for the Ru isotopes via cranked Hartree-Fock-Bogoliubov calculations [65].

The best description is given by the IBM-1. The PES obtained from the IBM calculations show a prolate minimum at $\beta \approx 0.3$ with a broad minimum γ in the degree of freedom which is not but close to γ soft. To clarify and give a better insight on the shape and structure of ^{112}Pd , lifetime measurements of the 3_γ^+ and 4_γ^+ states would be desirable. With the knowledge of these lifetimes a better description of the nucleus could be reached, especially the reduced transition probabilities using the lifetime of the 4_γ^+ state. An experimental ratio of $B_{4_\gamma/2_\gamma} = B(E2; 4_\gamma^+ \rightarrow 4_1^+)/B(E2; 4_\gamma^+ \rightarrow 2_\gamma^+) \approx 0.95$ can be obtained using the branching ratios given in Refs. [19,60]. Comparing this experimental signature to the D-F and γ -soft calculations, ratios of $B_{4_\gamma/2_\gamma} \approx 0.57$ and $B_{4_\gamma/2_\gamma} \approx 0.91$ can be obtained, respectively. This would be another argument of the mentioned hypothesis and, hence, a further investigation could verify this. An investigation of the γ -band transition probabilities in ^{114}Pd would give further experimental signatures to complement the conclusion. Up to now, no experimental transition probabilities within the γ band in ^{114}Pd are available.

VI. CONCLUSIONS

The lifetimes of the 2_1^+ , 4_1^+ , 6_1^+ , and 2_γ^+ states in ^{112}Pd were measured using the RDDS technique. The results were compared to IBM-1 calculations, to a modified γ -soft calculation, and to D-F calculations using two different γ parameters. All four descriptions of the energy levels lead to an overall good description for the lower spin states, whereas the higher spin states are strongly overestimated by all the D-F calculations. The deduced transition probabilities were compared to the models, and the IBM-1 calculation reproduces the values with the highest accuracy. The potential energy surface using the IBM-1 parameters does not show a clear minimum at $\gamma = 30^\circ$, which would be the case for a triaxial rotor nucleus, nor a γ -soft behavior. A shallow minimum at $\gamma = 0^\circ$ is shown,

which is not completely free in the γ degree of freedom which would support a γ -soft nucleus. Further investigations of lifetimes in the γ band would be of interest to complete the observations of this work.

ACKNOWLEDGMENTS

We thank the operator team of the IKP FN Tandem accelerator for the professional support during the experiment.

A.E. and V.K. acknowledge the support by the Bundesministerium für Bildung und Forschung (BMBF) under Grant No. 05P15PKFNA. The authors also thank Jacek Dobaczewski for providing the code to calculate the energies of the γ -soft and Davydov-Filippov model. G.H. acknowledges support from the Bonn-Cologne Graduate School for Physics and Astronomy (BCGS) and the IDEX API grant. C.M.-G. is supported by the US Department of Energy, Office of Nuclear Physics, under Contract No. DE-AC02-06CH11357.

-
- [1] Y. Luo, S. Zhu, J. Hamilton, J. Rasmussen, A. Ramayya, C. Goodin, K. Li, J. Hwang, D. Almeded, S. Frauendorf, V. Dimitrov, J. ye Zhang, X. Che, Z. Jang, I. Stefanescu, A. Gelberg, G. Ter-Akopian, A. Daniel, M. Stoyer, R. Donangelo, J. D. Cole, and N. J. Stone, *Phys. Lett. B* **670**, 307 (2009).
- [2] D. Doherty *et al.*, *Phys. Lett. B* **766**, 334 (2017).
- [3] H. Watanabe *et al.*, *Phys. Lett. B* **704**, 270 (2011).
- [4] J. Snyder, W. Reviol, D. Sarantites, A. Afanasjev, R. Janssens, H. Abusara, M. Carpenter, X. Chen, C. Chiara, J. Greene, T. Lauritsen, E. McCutchan, D. Seweryniak, and S. Zhu, *Phys. Lett. B* **723**, 61 (2013).
- [5] P.-A. Söderström, G. Lorusso, H. Watanabe, S. Nishimura, P. Doornenbal, G. Thiamova, F. Browne, G. Gey, H. S. Jung, T. Sumikama, J. Taprogge, Z. Vajta, J. Wu, Z. Y. Xu, H. Baba, G. Benzoni, K. Y. Chae, F. C. L. Crespi, N. Fukuda, R. Gernhäuser *et al.*, *Phys. Rev. C* **88**, 024301 (2013).
- [6] R. F. Casten, *Nuclear Structure from a Simple Perspective* (Oxford University Press, Oxford, NY, 2000).
- [7] L. Wilets and M. Jean, *Phys. Rev.* **102**, 788 (1956).
- [8] A. Davydov and G. Filippov, *Nucl. Phys.* **8**, 237 (1958).
- [9] A. Davydov and V. Rostovsky, *Nucl. Phys.* **12**, 58 (1959).
- [10] A. Davydov and V. Rostovskii, *J. Expt. Theor. Phys. (U.S.S.R.)* **36**, 1788 (1959) [*Sov. Phys. JETP* **36**, 1275 (1959)].
- [11] N. Zamfir and R. Casten, *Phys. Lett. B* **260**, 265 (1991).
- [12] H. Sobhani, H. Hassanabadi, and W. S. Chung, *Nucl. Phys. A* **973**, 33 (2018).
- [13] L. Svensson, C. Fahlander, L. Hasselgren, A. Bäcklin, L. Westerberg, D. Cline, T. Czosnyka, C. Wu, R. Diamond, and H. Kluge, *Nucl. Phys. A* **584**, 547 (1995).
- [14] S. Lalkovski, A. Minkova, M.-G. Porquet, A. Bauchet, I. Deloncle, A. Astier, N. Buforn, L. Donadille, O. Dorvaux, B. Gall, R. Lucas, M. Meyer, A. Prevost, N. Redon, N. Schulz, and O. Stezowski, *Eur. Phys. J. A* **18**, 589 (2003).
- [15] E. R. Gamba, A. M. Bruce, S. Lalkovski, M. Rudigier, S. Bottoni, M. P. Carpenter, S. Zhu, J. T. Anderson, A. D. Ayangeakaa, T. A. Berry, I. Burrows, M. C. Gallardo, R. J. Carroll, P. Copp, D. M. Cullen, T. Daniel, G. F. Martínez, J. P. Greene, L. A. Gurgi, D. J. Hartley *et al.*, *Phys. Rev. C* **100**, 044309 (2019).
- [16] J. Blachot, *Nucl. Data Sheets* **91**, 135 (2000).
- [17] G. Gürdal and F. Kondev, *Nucl. Data Sheets* **113**, 1315 (2012).
- [18] Y. Luo, J. Rasmussen, J. Hamilton, A. Ramayya, S. Frauendorf, J. Hwang, N. Stone, S. Zhu, N. Brewer, E. Wang, I. Lee, S. Liu, G. Ter-Akopian, A. Daniel, Y. Oganessian, M. Stoyer, R. Donangelo, W. Ma, J. Cole, Y. Shi *et al.*, *Nucl. Phys. A* **919**, 67 (2013).
- [19] S. Lalkovski and F. Kondev, *Nucl. Data Sheets* **124**, 157 (2015).
- [20] J. Blachot, *Nucl. Data Sheets* **113**, 515 (2012).
- [21] J. Blachot, *Nucl. Data Sheets* **111**, 717 (2010).
- [22] S. Frauendorf, *Int. J. Mod. Phys. E* **24**, 1541001 (2015).
- [23] M. Stoyer, W. Walters, C. Wu, D. Cline, H. Hua, A. Hayes, R. Teng, R. Clark, P. Fallon, A. Goergen, A. Macchiavelli, K. Vetter, P. Mantica, and B. Tomlin, *Nucl. Phys. A* **787**, 455 (2007).
- [24] X. Q. Zhang, J. H. Hamilton, A. V. Ramayya, S. J. Zhu, J. K. Hwang, C. J. Beyer, J. Kormicki, E. F. Jones, P. M. Gore, B. R. S. Babu, T. N. Ginter, R. Aryaeinejad, K. Butler-Moore, J. D. Cole, M. W. Drigert, J. K. Jewell, E. L. Reber, J. Gilat, I. Y. Lee, J. O. Rasmussen *et al.*, *Phys. Rev. C* **63**, 027302 (2001).
- [25] A. Dewald, K. Starosta, P. Petkov, M. Hackstein, W. Rother, P. Adrich, A. M. Amthor, T. Baumann, D. Bazin, M. Bowen, A. Chester, A. Dunomes, A. Gade, D. Galaviz, T. Glasmacher, T. Ginter, M. Hausmann, J. Jolie, B. Melon, D. Miller *et al.*, *Phys. Rev. C* **78**, 051302(R) (2008).
- [26] R. Robinson, F. McGowan, P. Stelson, W. Milner, and R. Sayer, *Nucl. Phys. A* **124**, 553 (1969).
- [27] H. H. Bolotin and D. A. McClure, *Phys. Rev. C* **3**, 797 (1971).
- [28] R. Harper, A. Christy, I. Hall, I. Naqib, and B. Wakefield, *Nucl. Phys. A* **162**, 161 (1971).
- [29] D. Eccleshall, B. Hinds, and M. Yates, *Nucl. Phys.* **32**, 190 (1962).
- [30] P. H. Stelson and F. K. McGowan, *Phys. Rev.* **110**, 489 (1958).
- [31] J. Wesseling, C. de Jager, J. Van Der Laan, H. De Vries, and M. Harakeh, *Nucl. Phys. A* **535**, 285 (1991).
- [32] J. W. Lightbody, S. Penner, S. P. Fivozinsky, P. L. Hallowell, and H. Crannell, *Phys. Rev. C* **14**, 952 (1976).
- [33] B. Kotlinski, D. Cline, A. Bäcklin, and D. Clark, *Nucl. Phys. A* **503**, 575 (1989).
- [34] J. Hamilton, S. Zhu, Y. Luo, A. Ramayya, S. Frauendorf, J. Rasmussen, J. Hwang, S. Liu, G. Ter-Akopian, A. Daniel, and Y. Oganessian, *Nucl. Phys. A* **834**, 28c (2010).
- [35] P. Möller, R. Bengtsson, B. G. Carlsson, P. Olivius, and T. Ichikawa, *Phys. Rev. Lett.* **97**, 162502 (2006).
- [36] I. Stefanescu, A. Gelberg, J. Jolie, P. Van Isacker, P. von Brentano, Y. Luo, S. Zhu, J. Rasmussen, J. Hamilton, A. Ramayya, and X. Che, *Nucl. Phys. A* **789**, 125 (2007).
- [37] P. E. Garrett, T. R. Rodríguez, A. D. Varela, K. L. Green, J. Bangay, A. Finlay, R. A. E. Austin, G. C. Ball, D. S. Bandyopadhyay, V. Bildstein, S. Colosimo, D. S. Cross, G. A. Demand, P. Finlay, A. B. Garnsworthy, G. F. Grinyer, G. Hackman, B. Jigmeddorj, J. Jolie, W. D. Kulp *et al.*, *Phys. Rev. Lett.* **123**, 142502 (2019).
- [38] P. E. Garrett, T. R. Rodríguez, A. Diaz Varela, K. L. Green, J. Bangay, A. Finlay, R. A. E. Austin, G. C. Ball, D. S.

- Bandyopadhyay, V. Bildstein, S. Colosimo, D. S. Cross, G. A. Demand, P. Finlay, A. B. Garnsworthy, G. F. Grinyer, G. Hackman, B. Jigmeddorj, J. Jolie, W. D. Kulp *et al.*, *Phys. Rev. C* **101**, 044302 (2020).
- [39] A. Dewald, O. Möller, and P. Petkov, *Prog. Part. Nucl. Phys.* **67**, 786 (2012).
- [40] V. Karayonchev, J. Jolie, A. Blazhev, A. Dewald, A. Esmaylzadeh, C. Fransen, G. Häfner, L. Knafla, J. Litzinger, C. Müller-Gatermann, J.-M. Régis, K. Schomacker, A. Vogt, N. Warr, A. Leviatan, and N. Gavrielov, *Phys. Rev. C* **102**, 064314 (2020).
- [41] T. Alexander and A. Bell, *Nucl. Instrum. Methods* **81**, 22 (1970).
- [42] A. Dewald, S. Harissopulos, and P. von Brentano, *Z. Phys. A: At. Nucl.* **334**, 163 (1989).
- [43] J. Litzinger, A. Blazhev, A. Dewald, F. Didierjean, G. Duchêne, C. Fransen, R. Lozeva, K. Sieja, D. Verney, G. de Angelis, D. Bazzacco, B. Birkenbach, S. Bottoni, A. Bracco, T. Braunroth, B. Cedervall, L. Corradi, F. C. L. Crespi, P. Désesquelles, J. Eberth *et al.*, *Phys. Rev. C* **92**, 064322 (2015).
- [44] R. J. Estep, R. K. Sheline, D. J. Decman, E. A. Henry, L. G. Mann, R. A. Meyer, W. Stoeffl, L. E. Ussery, and J. Kantele, *Phys. Rev. C* **35**, 1485 (1987).
- [45] B. Saha, Ph.D. thesis, Universität zu Köln, 2004.
- [46] G. Mamane, E. Cheifetz, E. Dafni, A. Zemel, and J. B. Wilhelmy, *Nucl. Phys. A* **454**, 213 (1986).
- [47] E. Cheifetz, R. C. Jared, S. G. Thompson, and J. B. Wilhelmy, *Phys. Rev. Lett.* **25**, 38 (1970).
- [48] S. G. Rohoziński, J. Srebrny, and K. Horbaczewska, *Z. Phys. A: At. Nucl.* **268**, 401 (1974).
- [49] J. Dobaczewski, S. G. Rohoziński, and J. Srebrny, *Z. Phys. A: At. Nucl.* **282**, 203 (1977).
- [50] γ -soft code, 2020, <http://kody.slcj.uw.edu.pl/index.php>.
- [51] R. Casten, P. Von Brentano, K. Heyde, P. Van Isacker, and J. Jolie, *Nucl. Phys. A* **439**, 289 (1985).
- [52] P. Lipas, P. Toivonen, and D. D. Warner, *Phys. Lett. B* **155**, 295 (1985).
- [53] S. Lalkovski and P. Van Isacker, *Phys. Rev. C* **79**, 044307 (2009).
- [54] S. Heinze, Ph.D. thesis, Universität zu Köln, 2008.
- [55] R. F. Casten, *J. Phys. G: Nucl. Part. Phys.* **42**, 034029 (2015).
- [56] E. A. McCutchan, D. Bonatsos, N. V. Zamfir, and R. F. Casten, *Phys. Rev. C* **76**, 024306 (2007).
- [57] A. E. L. Dieperink, O. Scholten, and F. Iachello, *Phys. Rev. Lett.* **44**, 1747 (1980).
- [58] J. N. Ginocchio and M. W. Kirson, *Phys. Rev. Lett.* **44**, 1744 (1980).
- [59] M. Böyükata, E. Ellinger, C. Fransen, and J. Jolie, *EPJ Web Conf.* **66**, 02013 (2014).
- [60] National Nuclear Data Center, 2020, <https://www.nndc.bnl.gov/ensdf/>.
- [61] G. Lhersonneau, J. C. Wang, S. Hankonen, P. Dendooven, P. Jones, R. Julin, and J. Äystö, *Phys. Rev. C* **60**, 014315 (1999).
- [62] H. Toki and A. Faessler, *Z. Phys. A: At. Nucl.* **276**, 35 (1976).
- [63] E. A. Stefanova, S. Lalkovski, A. Korichi, T. Kutsarova, A. Lopez-Martens, F. R. Xu, H. L. Liu, S. Kisyov, A. Minkova, D. Bazzacco, M. Bergström, A. Görgen, F. Hannachi, B. Herskind, H. Hübel, A. Jansen, T. L. Khoo, Z. Podolyák, and G. Schönwasser, *Phys. Rev. C* **86**, 044302 (2012).
- [64] S. Lalkovski and N. Minkov, *J. Phys. G: Nucl. Part. Phys.* **31**, 427 (2005).
- [65] I. Deloncle, A. Bauchet, M. G. AU Porquet, M. Girod, S. Péru, J. P. Delaroche, A. Wilson, B. J. P. Gall, F. Hoellinger, N. Schulz, E. Gueorguieva, A. Minkova, T. Kutsarova, T. Venkova, J. Duprat, H. Sergolle, C. Gautherin, R. Lucas, A. Astier, N. Bufoin *et al.*, *Eur. Phys. J. A* **8**, 177 (2000).

5 | Publication IV:

Investigation of γ -softness: Lifetime measurements in $^{104,106}\text{Ru}$


Investigation of γ softness: Lifetime measurements in $^{104,106}\text{Ru}$

A. Esmaylzadeh^{1,*}, A. Blazhev¹, K. Nomura², J. Jolie¹, M. Beckers¹, C. Fransen¹, R.-B. Gerst¹, A. Harter¹,
V. Karayonchev^{1,3}, L. Knafla¹, M. Ley¹, and F. von Spee¹

¹Universität zu Köln, Institut für Kernphysik, D-50937 Köln, Germany

²Department of Physics, Faculty of Science, University of Zagreb, 10000 Zagreb, Croatia

³TRIUMF, 4004 Wesbrook Mall, Vancouver, BC V6t 2A3, Canada

 (Received 7 July 2022; revised 26 October 2022; accepted 8 December 2022; published 21 December 2022)

Lifetimes of the 2_1^+ , 4_1^+ , 6_1^+ , 2_γ^+ , and 3_γ^+ states in $^{104,106}\text{Ru}$ were measured by using the recoil-distance Doppler-shift technique and the Cologne Plunger device. Low-lying excited states in both nuclei were populated in a $^{104}\text{Ru}(^{18}\text{O}, ^{18}\text{O})^{104}\text{Ru}^*$ inelastic scattering and in a $^{104}\text{Ru}(^{18}\text{O}, ^{16}\text{O})^{106}\text{Ru}$ two-neutron transfer reaction using the Cologne FN Tandem accelerator. The experimental energy levels and deduced electromagnetic transition probabilities are compared in the context of γ softness and the mapped interacting boson model with input from the microscopic self-consistent mean-field calculation using a Gogny interaction. The newly obtained results for the γ band give a more detailed insight about the triaxial behavior of $^{104,106}\text{Ru}$. The results will be discussed in the context of γ soft and rigid triaxial behavior which is present in the neutron-rich Ru isotopes.

DOI: [10.1103/PhysRevC.106.064323](https://doi.org/10.1103/PhysRevC.106.064323)

I. INTRODUCTION

The ruthenium ($Z = 44$) and palladium ($Z = 46$) isotopes are located between the strontium ($Z = 38$), zirconium ($Z = 40$), and molybdenum ($Z = 42$) isotopes, which undergo a transition from spherical to a strongly deformed type of structure [1–6], and the less deformed cadmium (Cd , $Z = 48$) and tin (Sn , $Z = 50$) isotopes [7,8]. In the neutron-rich region around $Z \approx 40$ and $N \approx 60$, the transition from a spherical to a deformed type of structure of the ground-state band accompanied by shape coexistence is expected to happen by going from 58 to 60 neutrons. Compared with the related Sr and Zr isotopes, no shape coexistence is observed for $^{102,104}\text{Ru}_{60}$ and the transition is more gradual. However, some studies of static and dynamic quadrupole moments indicate that the shape coexistence might still persist in this nucleus [2,9,10].

Different experiments show that the isotopic chains of molybdenum, ruthenium, and palladium possess signatures indicating γ -soft behavior [11–16,18]. In even-even nuclei the 2_1^+ state is related to the quadrupole deformation and the γ band is sensitive to the triaxial motion of the nucleus. A triaxial nucleus rotates around all three axes of the intrinsic body and has its potential-energy surface minimum at $\gamma = 30^\circ$. Two models discussing the triaxial shape are the Willets-Jean γ -soft rotor model [17] and the Davydov-Filippov rigid triaxial rotor model [18–20]. In the γ -soft model the potential-energy surface is independent of γ and shows a broad minimum in the γ degree of freedom, while the rigid-rotor model has a distinct minimum at $\gamma = 30^\circ$. A useful tool to distinguish between these two limits of a triaxial

nucleus is the staggering parameter, which is defined as [21]

$$S(J) = \frac{[E(J) - 2E(J-1) + E(J-2)]}{E(2_1^+)}, \quad (1)$$

where $E(J)$ represents the energy levels of the γ band with the corresponding spin J . The staggering parameter describes the clustering and spacing of states in the γ band where a positive value for odd-spin levels and negative value for even-spin levels corresponds to a γ -soft case and the opposite values for a γ -rigid nucleus. In Fig. 1 the staggering parameters for the Ru isotopes with neutron numbers from 56 to 68 ($^{100-112}\text{Ru}$) are shown, calculated for spin $J = 4, 5, 6, 7$ states of the γ band. According to the available data for ^{100}Ru , a γ -soft structure is expected. For the Ru isotopes with 58 to 64 neutrons ($^{102-108}\text{Ru}$) a less pronounced even-odd spin staggering is observed, which might be an indicator of a less pronounced softness in these nuclei. ^{110}Ru seems to be a transitional nucleus from a γ -soft behavior occurring in the lighter Ru isotopes to a rather more γ -rigid behavior in ^{112}Ru . The molybdenum and palladium isotones of $^{104,106}\text{Ru}$, i.e., $^{102,104}\text{Mo}$, and $^{106,108}\text{Pd}$ also show signs of γ softness in terms of staggering parameter and $R_{4/2}$ ratio [23–26,29]. However, the signs are only weakly pronounced for ^{104}Mo and the neutron-rich molybdenum isotopes [29,30].

Further signatures to characterize the shape and behavior of a nucleus are the $R_{4/2} = E(4_1^+)/E(2_1^+)$ and $B_{4/2} = B(E2; 4_1^+ \rightarrow 2_1^+)/B(E2; 2_1^+ \rightarrow 0_1^+)$ ratios. The $R_{4/2}$ ratio for the ruthenium isotopes increases from around 2.1 for ^{98}Ru up to a maximum of 2.8 for ^{110}Ru , which is also the midshell nucleus with $N = 66$. Afterwards the ratio decreases slowly down to 2.6 for ^{116}Ru . The $R_{4/2}$ ratios of $^{104,106}\text{Ru}$, discussed in this work, are 2.48(1) and 2.65(1), respectively. These values are close to the γ -soft limit which is at 2.5. The $B_{4/2}$

*aesmaylzadeh@ikp.uni-koeln.de

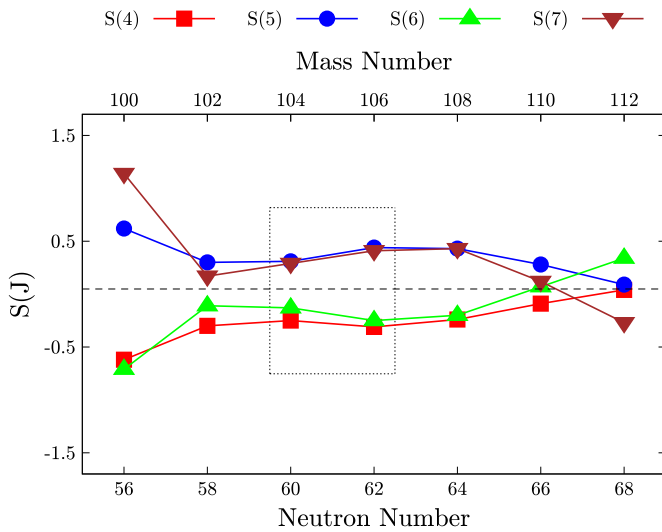


FIG. 1. (a) The staggering parameter $S(J)$ for the $^{100-112}\text{Ru}$ isotopes calculated using Eq. (1). The energy levels are taken from the Nuclear Data Sheets [22–28].

ratio for ^{98}Ru is 1.9(5) and thus nearly the spherical limit [31]. The $^{100,102,104}\text{Ru}$ isotopes show a $B_{4/2}$ ratio of ≈ 1.5 which is closer to the rotational limit [22–24]. The lifetime of the 4_1^+ state in ^{106}Ru was not available in the past, but will be determined in the course of this work. For the neutron-rich isotopes $^{108,110}\text{Ru}$, the ratios are 1.7(5) and 1.3(5), respectively [26,27]. The lifetime information about the 4_1^+ state in ^{106}Ru is important to close the gap between the stable and neutron-rich Ru isotopes, i.e., between $^{100-104}\text{Ru}$ and $^{108-112}\text{Ru}$.

II. EXPERIMENT

To populate low-lying states in ^{104}Ru and ^{106}Ru , the inelastic-scattering reaction $^{104}\text{Ru}(^{18}\text{O}, ^{18}\text{O}')^{104}\text{Ru}^*$ and the two-neutron transfer reaction $^{104}\text{Ru}(^{18}\text{O}, ^{16}\text{O})^{106}\text{Ru}$ were used. The enriched ^{104}Ru target had a thickness of 0.15 mg/cm² that was evaporated onto a natural vanadium 0.78 mg/cm² backing. The target was stretched in parallel to a natural vanadium stopper foil with a thickness of 3.1 mg/cm² inside the Cologne Plunger device [32]. Still traces of ^{102}Ru were observed in the reaction. The ^{18}O beam impinged on the target with a beam current of ≈ 1 pA using an energy of 57 MeV provided by the Cologne 10 MV FN-Tandem accelerator. The stopper foil acts as a stopper for the ejectiles produced in the reaction, i.e., recoiling $^{104,106}\text{Ru}$ nuclei. The Cologne Plunger device was used in conjunction with eleven high-purity germanium (HPGe) detectors forming two rings (backward and forward) around the target chamber to detect γ rays [32]. The six backward and five forward detectors were placed at angles of 45° and 142° with respect to the beam direction. As in previous experiments [15,16,33,34], six solar cells (PIN diodes) were installed at backward angles to detect the backscattered beam-like light recoiling fragments and to limit the kinematics of the recoiling reaction products. Ten target-to-stopper distances (44, 53, 63, 93, 143, 343, 843, 1543, 2843, and 3743 μm) with respect to the electrical contact of the foils were measured in seven days

of beam time to achieve sufficient coverage and statistics to apply the recoil distance Doppler-shift (RDDS) technique and the differential decay curve method (DDCM) [32,35]. To determine the absolute distance, the capacitance method described in Refs. [32,36] was used. In addition, an optical distance measurement device was used to obtain the absolute distances [37]. Both methods yield consistent results for the so-called zero distances of 43(5) μm where the uncertainty is used as an error for each absolute distance. The zero distance is defined as the minimal distance between target and stopper foil, where no electrical contact occurs. To determine the velocity of the recoiling nuclei, the Doppler shift of the most intense transitions are used. The resulting recoil velocity amounts to $v/c = 2.10(6)\%$ and $v/c = 2.01(10)\%$ for ^{104}Ru and ^{106}Ru , respectively. The red rectangle in Fig. 2(a) indicates the asymmetric gate that has been applied to select the backscattered $^{16,18}\text{O}$ particle to observe the coincident γ rays of the corresponding reaction partner (either ^{104}Ru or ^{106}Ru). An asymmetric gate has been applied to avoid a possible contamination of the α -transfer channel which results in ^{108}Pd , which is marked with a blue rectangle in Fig. 2(a). A distinction of the inelastic-scattering channels (^{102}Ru and ^{104}Ru) and the two neutron transfer channel (^{106}Ru) with the applied particle gate was not possible due to the energy and angular straggling of the recoiling ^{16}O and ^{18}O particles as well as the angular coverage of the solar cells. In Figs. 2(b) and 2(c), the γ -ray spectrum summing up all distances is shown for the energy range from 170 keV up to 1750 keV. In Figs. 3(b) and 3(c) the partial level scheme is shown which was built using the information of corresponding γ -ray spectrum, where the spins and parities are taken from the literature [24,25]. The states populated in this experiment are consistent with previous inelastic-scattering and two-neutron transfer experiments [10,25,38–41]. The arrow width in the partial level scheme describes the intensity of the observed transition that are summarized in Table I. The observation limit is about 0.2% and 2% relative to the $2_1^+ \rightarrow 0_1^+$ transitions of ^{104}Ru and ^{106}Ru , respectively. The large difference in the observation limit results from the approximately ten-times higher cross section for the inelastic scattering compared with the two-neutron transfer reaction. This leads to more statistics and hence a more sensitive observation limit. The strongest γ rays in coincidence to the particle gate onto $^{16,18}\text{O}$ belong to ^{102}Ru marked with *, ^{104}Ru and ^{106}Ru , where the γ rays are labeled with the corresponding transition between the two involved state, as can be seen in Figs. 2(b) and 2(c).

III. ANALYSIS

The lifetimes of the 2_1^+ , 4_1^+ , 6_1^+ , 2_2^+ , and 3_2^+ states in both nuclei were analyzed using the Bateman equations [42] and the well-established differential decay curve method (DDCM) [32,35]. The DDCM has specific advantages such as the minimization of systematic errors, the usage of directly derived experimental values and relative distances and the fact that no assumptions about the shape of the decay curve $R(t)$ are required. To determine lifetimes using the DDCM, the

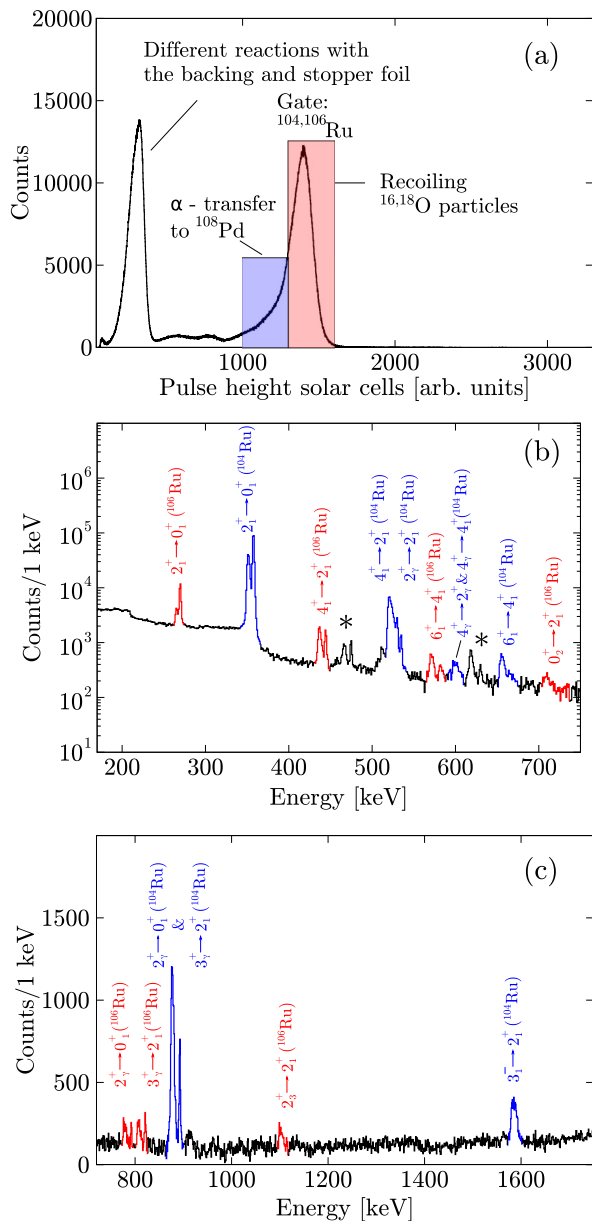


FIG. 2. (a) The summed solar cell spectrum of all distances. The red rectangle shows the applied gate to select the recoiling $^{16,18}\text{O}$ particles to obtain a γ spectrum of $^{104,106}\text{Ru}$. The gate on $^{16,18}\text{O}$ has been applied asymmetric to avoid a possible contamination of the α -transfer channel. (b), (c) The summed γ -ray spectrum for all distances after applying a particle gate which is indicated by the red rectangle in panel (a) for the energy range is from 170 up to 750 keV and 720 up to 1750 keV, respectively. The observed transitions of ^{104}Ru are marked in blue and for ^{106}Ru in red. The transitions marked with “*” belong to the inelastic scattering of ^{102}Ru , which are the $2_1^+ \rightarrow 0_1^+$ and $4_1^+ \rightarrow 2_1^+$ transitions. Note that the y scale is logarithmic in panel (b) and a linear scale is used in panel (c).

program NAPATAU [43] was used. A detailed description of both methods is given in Ref. [32]. Due to a lack of statistics in γ - γ coincidences, only particle-gated single γ -ray spectra were used to determine the lifetimes. For some low populated

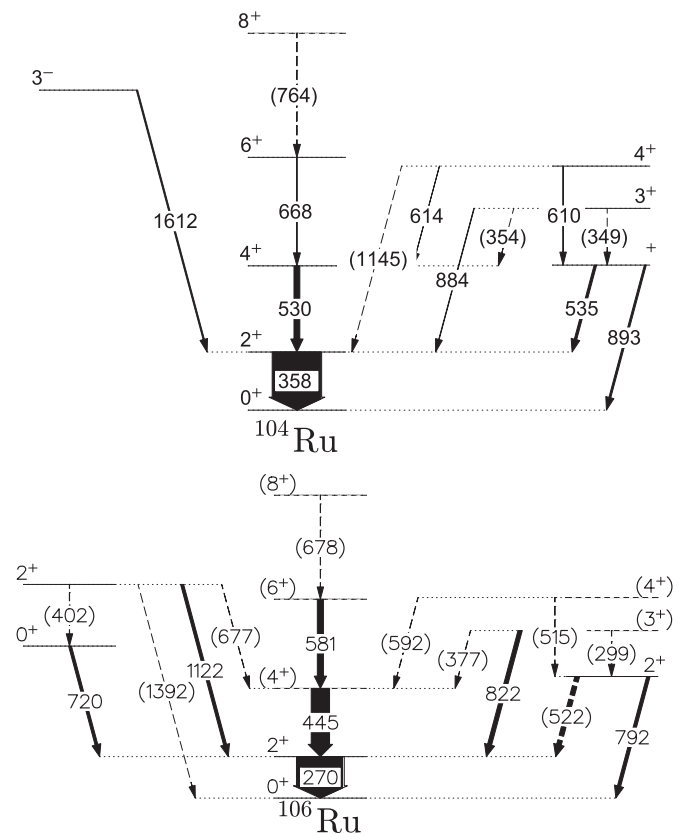


FIG. 3. Partial level scheme of the observed states in ^{104}Ru and ^{106}Ru populated in the inelastic scattering or in the two-neutron transfer reaction. The width of the transition arrows corresponds to the observed intensities (see Table I) and the dashed lines indicate known transitions not observed in this experiment.

states the method explained and applied in Refs. [15,16,44] was used to determine the lifetimes. Therefore, the summed spectra of all distances j was solved with the following equation:

$$R_{\text{sum}} = \frac{\sum_j I_j^u}{\sum_j I_j^u + \sum_j I_j^s} = \sum_j n_j R(t_j), \quad (2)$$

with I_j^u and I_j^s being the intensities of the unshifted and shifted components, respectively. The normalization factor n_j has been obtained by applying a gate for each distance on the $2_1^+ \rightarrow 0_1^+$ transition of ^{104}Ru and ^{106}Ru corresponding to 270.1 and 358.0 keV, respectively, and integrating the resulting particle spectrum. The time of flight for each distance is described by t_j and $R(t_j)$ is the decay curve described by the Bateman equations [42]. The lifetime τ is the only free parameter in solving this equation [15,16,44,45].

Here, a top-to-bottom approach was used to adjust the feeding pattern influencing the lifetimes of lower-lying states. For the cases of higher-lying states and of low statistics, Eq. (2) has been used to derive lifetimes. This is realized by applying a Monte Carlo approach with 10^7 iterations and which varies n_j , R_{sum} , v/c and the distance within the uncertainties. From the resulting distribution, the lifetimes and

TABLE I. Relative transition intensities observed in the inelastic scattering $^{104}\text{Ru}(^{18}\text{O}, ^{18}\text{O}')^{104}\text{Ru}^*$ and the two-neutron transfer $^{104}\text{Ru}(^{18}\text{O}, ^{16}\text{O})^{106}\text{Ru}$ reaction. The intensities were normalized to the $2_1^+ \rightarrow 0_1^+$ transition of the respective nucleus and the energies are taken from Refs. [24,25].

Transition	^{104}Ru		^{106}Ru	
	Transition energy [keV]	Intensity	Transition energy [keV]	Intensity
$2_1^+ \rightarrow 0_1^+$	358.0(1)	100.0(22)	270.1(1)	100.0(35)
$4_1^+ \rightarrow 2_1^+$	530.5(1)	11.4(32)	444.6(2)	41.1(17)
$6_1^+ \rightarrow 4_1^+$	667.9(3)	1.1(1)	581.1(2)	11.8(8)
$2_\gamma^+ \rightarrow 2_1^+$	535.1(1)	5.5(2)	522.2(1)	
$2_\gamma^+ \rightarrow 0_1^+$	893.1(1)	4.3(2)	792.3(1)	7.4(8)
$3_\gamma^+ \rightarrow 2_1^+$	884.4(1)	0.7(2)	821.5(1)	11.8(9)
$4_\gamma^+ \rightarrow 2_\gamma^+$	609.5(1)	0.4(1)	515	
$4_\gamma^+ \rightarrow 4_1^+$	614.2(1)	0.2(1)	592	
$2_3^+ \rightarrow 2_1^+$	1157.4(1)		1122.2(1)	8.1(9)
$3_1^- \rightarrow 2_1^+$	1612.4(1)	2.7(2)		
$0_2^+ \rightarrow 2_1^+$	630.3(3)		720.5(1)	5.2(8)

the corresponding uncertainty is derived as mean and standard deviation.

For the determination of the lifetimes of states with higher statistics of the decay transition, the Bateman equations were solved. Here, a Monte Carlo approach was also used which varies all parameters like absolute distance, $R(t)$, v/c , and possible feeding contributions like feeding intensity and feeding lifetime within their respective uncertainties. The adopted values and their corresponding errors are calculated by using a Monte Carlo simulation. To account for nonstatistical sources of uncertainty, a 5% systematic error is added to the adopted value. Potential systematic uncertainties are caused by various sources of contribution like opening angle of the detectors, slowing down effects within the stopper foil and deorientation effects which is especially pronounced for $\tau > 100$ ps [32].

Calculating the particle flight time using the recoil velocity and the zero distance of $43 \mu\text{m}$ results in a minimum flight time of ≈ 7 ps. Hence, we set the lower sensitivity limit of this experimental configuration at ≈ 5 ps. In the following section, the analysis procedure for the determination of the lifetimes in $^{104,106}\text{Ru}$ is explained. The analysis of the ^{104}Ru serves as consistency check of the experimental setup as well as the analysis procedure. Only the lifetime of the 3_γ^+ state was determined for the first time. All other determined lifetimes in this work confirm the literature values within the uncertainties. The spectra and fits for the data are only visualized for ^{106}Ru due to its novelty. The final lifetimes of $^{104,106}\text{Ru}$ are summarized in Table II.

A. Lifetimes in ^{104}Ru

1. Analysis of 4_γ^+ , 6_1^+ , and 3_1^- states

The observed transitions depopulating the 4_γ^+ state (609.5 and 614.2 keV), the 6_1^+ state (667.9 keV), and the 3_1^- (1612.3 keV) state, see Fig. 2, only show a shifted and no unshifted component. This indicates a lifetime too short to be measured with the properties of the experimental configuration. Therefore, an upper limit of ≈ 5 ps is set for these states i.e.,

$\tau_{4_\gamma^+} < 5$ ps, $\tau_{6_1^+} < 5$ ps, and $\tau_{3_1^-} < 5$ ps. Although it is not an absolute result, this is an important information to account for the feeding properties of lower-lying states. The derived upper limits of less than 5 ps for the 4_γ^+ , 6_1^+ are in good agreement with previously determined lifetimes of $\tau_{4_\gamma^+} = 3.9(4)$ ps and $\tau_{6_1^+} = 1.92_{-6}^{+17}$ ps [10,24,39,40,46–48], derived as the mean of several Coulomb excitation experiments. No information about the lifetime of the 3_1^- is given in the literature.

2. Analysis of 2_γ^+ and 3_γ^+ states

The 2_γ^+ and 3_γ^+ states are only weakly populated and therefore Eq. (2) was used to obtain the lifetimes. For the lifetimes of the 2_γ^+ state, the $2_\gamma^+ \rightarrow 2_1^+$ (535.1 keV) and the $2_\gamma^+ \rightarrow 0_1^+$ (893.1 keV) have been used to determine the lifetime. In the forward ring an overlap between the $2_\gamma^+ \rightarrow 2_1^+$ (535.1 keV) and $4_1^+ \rightarrow 2_1^+$ (530.5 keV) transition is observed and the analysis using the $2_\gamma^+ \rightarrow 2_1^+$ transition was only performed for the backward ring. For the 3_γ^+ state only the $3_\gamma^+ \rightarrow 2_1^+$ transition (884.4 keV) was observed and used to obtain the lifetime. The weighted mean of the results leads to the lifetimes of $\tau_{2_\gamma^+} = 8.9(18)$ ps and $\tau_{3_\gamma^+} = 7.3(23)$ ps. To investigate possible feeding contributions for the 3_γ^+ state from higher-lying unobserved states (e.g., 5_γ^+ state as a feeder of the 3_γ^+ state) and other unobserved, unknown feeding γ rays, the simulation has been expanded to take these unobserved feeders into account. By considering the observation limit ($\approx 0.2\%$) and the observed intensities of the decay transitions of the 3_γ^+ states (see Table I), a maximum of unobserved feeding contributions is 30%. A feeding lifetime of 100 ps is assumed, which is sufficiently long to be considered as a pure long-lived feeding [15,34] with the result of $\tau_{3_\gamma^+} = 2.8(12)$ ps. The lower limit derived from the maximum feeding approach is used as the lower limit of the final lifetime. The final result is $\tau_{3_\gamma^+} = 7.3_{-57}^{+23}$ ps, where no lifetime information is available in the literature. The lifetime of the 2_γ^+ with $\tau_{2_\gamma^+} = 8.9(18)$ ps is in agreement with the mean lifetime measured by

TABLE II. Lifetimes of $^{104,106}\text{Ru}$ measured in the experiment using the Bateman equation (BE), the DDCM method, the Simulations (SIM) using Eq. (2) together with the adopted values. The literature values from Refs. [49,50] are summarized in the last column.

		Lifetime [ps]								
State	Decay transition [keV] [24,25]	Backward ring			Forward ring			<i>Adopted</i>	Lit.	
		BE	DDCM	SIM	BE	DDCM	SIM			
^{104}Ru	2_1^+	358.0(1)	79.5(86)	82.8(28)	79.1(66)	78.3(86)	82.4(28)	79.1(67)	80.2(66)	81.5(14) ^a
	4_1^+	530.5(1)	8.0(10)	9.0(8)	8.1(22)				8.4(13)	8.1(9) ^a
	6_1^+	667.9(3)							<5	1.92 ⁺¹⁷ ₋₆ ^a
	2_γ^+	535.1(1)			8.3(23)				} 8.9(18)	7.2(7) ^a
	2_γ^+	893.1(1)			9.2(24)			9.3(24)		
	3_γ^+	884.1(1)			9.3(50)			7.0(20)	7.3 ⁺²³ ₋₅₇	
	4_γ^+	609.5(1)							<5	3.9(4) ^a
3_1^-	1612.4(1)							<5		
^{106}Ru	2_1^+	270.1(1)	267(29)	261(12)	273(25)	282(30)	283(12)	279(26)	274(23)	264(4) ^b 375(101) ^c
	4_1^+	444.6(2)	14.6(29)	12.5(13)	13.3(15)	14.7(27)	12.4(12)	13.6(13)	13.5(15)	< 20 ^b
	6_1^+	581.1(2)			10.0 ⁺²⁵ ₋₅₅				10.0 ⁺²⁵ ₋₅₅	—
	2_γ^+	792.3(1)			13.9 ⁺⁵² ₋₄₈				13.9 ⁺⁵² ₋₄₈	10.8(43) ^b
	3_γ^+	821.5(1)			17.3 ⁺⁵² ₋₉₉				17.3 ⁺⁵² ₋₉₉	< 38 ^b
	0_2^+	720.5(1)							<5	< 8.7 ^b
	2_3^+	1122.2(1)							<5	< 19 ^b

^aFrom Refs. [10,24,39,40,46–48].

^bFrom Ref. [49].

^cFrom Ref. [50].

different Coulomb excitation experiments with a mean value of $\tau_{2_3^+} = 7.2(7)$ ps [10,24,39,40,46–48].

3. Analysis of 4_1^+ and 2_1^+ states

After the determination of the lifetime of higher-lying states, this information can be used to obtain the lifetimes of the two lowest states, namely the 4_1^+ and 2_1^+ states. The $4_1^+ \rightarrow 2_1^+$ transition (530.5 keV) has an overlap with the $2_\gamma^+ \rightarrow 2_1^+$ transition (535.1 keV), hence, only the backward angles could be used to determine the lifetime. Here, the Bateman equation, the DDCM using the program NAPATAU [43] as well as Eq. (2) were used to determine the lifetime. The weighted mean of all results was used to adopt as lifetime and results in $\tau_{4_1^+} = 8.4(13)$ ps. The result is in good agreement with the adopted value of $\tau_{4_1^+} = 8.1(9)$ ps, given in the literature [24]. The $2_1^+ \rightarrow 0_1^+$ (358.0 keV) transition in combination with the Bateman equations, DDCM, and Eq. (2) were used to determine the lifetime of the 2_1^+ state. The final lifetime of $\tau_{2_1^+} = 80.2(66)$ ps agrees within its uncertainties to the adopted literature value of 81.5(14) ps [10,24,39,40,46–48].

B. Lifetimes in ^{106}Ru

1. Analysis of 2_3^+ and 0_2^+ states

The observed decay branches of the $2_3^+ \rightarrow 2_1^+$ state (1122.2 keV) and $0_2^+ \rightarrow 2_1^+$ state (720.5 keV) only show a shifted component, suggesting a lifetime too short to be measured

with the experimental configuration. Just as for some states in ^{104}Ru , an upper limit of 5 ps can be determined, representing the level of sensitivity in this case. No lifetime information for these two states are given in the literature.

2. Analysis of 2_γ^+ , 3_γ^+ , and 6_1^+ states

The 2_γ^+ , 3_γ^+ , and 6_1^+ states have a low population and hence Eq. (2) has been employed to obtain the lifetimes. The fits to the data are shown in Figs. 4(a) and 4(b). The resulting lifetimes are $\tau_{6_1^+} = 10.0(25)$ ps and $\tau_{3_\gamma^+} = 17.3(52)$ ps assuming no feeding. However, to investigate possible feeding contributions from unobserved higher-lying states (e.g., 8_1^+ state as a feeder of the 6_1^+ state) and other unobserved feeding γ rays, the simulation has been expanded to take these feeders into account. By considering the observation limit ($\approx 2\%$) and the observed intensities of the decay transitions of the 6_1^+ and 3_γ^+ states (see Table I), maximal contribution of unobserved feeding are in the order of 15% and 20%, respectively. Assuming a feeding lifetime of 100 ps which is sufficiently long to be considered as a pure long-lived feeding [15,34] the resulting lifetimes amount to $\tau_{6_1^+} = 6.6(21)$ ps and $\tau_{3_\gamma^+} = 11.3(39)$ ps. The lower limit of the simulation is used as the lower limit of the lifetime and the final results are $\tau_{6_1^+} = 10.0⁺²⁵₋₅₅$ ps and $\tau_{3_\gamma^+} = 17.3⁺⁵²₋₉₉$ ps. The results of the simulation with and without feeding are shown in Figs. 4(c) and 4(d). The determined value for the 3_γ^+ state is consistent with the upper limit of $\tau_{3_\gamma^+} < 38$ ps given in Ref. [49].

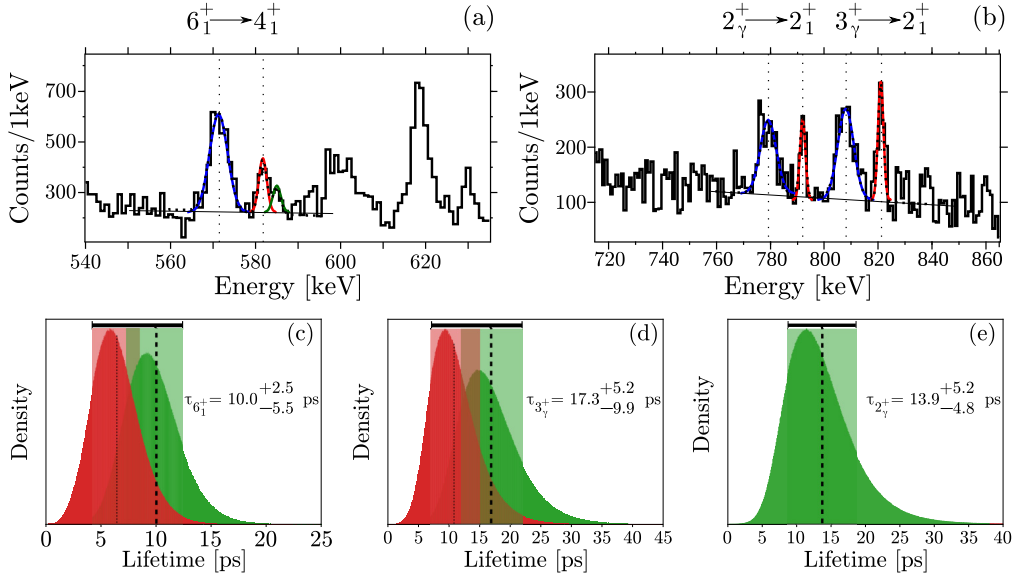


FIG. 4. (a), (b) Particle-gated γ -ray spectrum detected by the backward detectors of the $6_1^+ \rightarrow 4_1^+$ (581.1 keV), $2_\gamma^+ \rightarrow 0_1^+$ (792.3 keV), and $3_\gamma^+ \rightarrow 2_1^+$ (821.5 keV) decay transitions in ^{106}Ru with the corresponding shifted peaks. A peak at 585 keV has included in the fit procedure to account for its contribution [see panel (a)], marked in green. However, the origin of the γ ray is unclear. The γ -ray spectra of all distances are summed up due to low statistics and the fits of the shifted (blue) and unshifted (red) peaks are shown. (c)–(e) The result of the Monte Carlo simulation using Eq. (2), where no feeding is assumed (green) and the case where feeding is taken into account (red). Also the final lifetimes with the error bars are shown. See text in Sec. III B 2 for more details.

For the 2_γ^+ state only the feeding of the 3_γ^+ state has been considered which results in a final lifetime of $\tau_{2_\gamma^+} = 13.9^{+5.2}_{-4.8}$ ps. The simulation for the 2_γ^+ state with its error bar is shown in Fig. 4(e). The final result is in agreement with a previous measurement with a result of $\tau_{2_\gamma^+} = 10.8(43)$ ps [49]. The determined lifetimes and literature values are summarized in Table II.

3. Analysis of 4_1^+ and 2_1^+ states

As the lifetimes of the higher-lying states have been determined, they can be used to obtain the lifetimes of the 4_1^+ and 2_1^+ states. The evolution of the shifted and unshifted components for these states is shown in Fig. 5 for four selected distances (53, 143, 843, and 2843 μm) for the backward detectors. The solution of the Bateman equations and the DDCM using the program NAPATAU [43] are shown in the lower part of Fig. 5. For the 4_1^+ state the 444.6 keV transition ($4_1^+ \rightarrow 2_1^+$) has been used to determine the lifetime. The feeding contribution of the 6_1^+ and 3_γ^+ states have been taken into account. The final lifetime is calculated using the weighted average of the six measurements [backward and forward each Bateman equations, DDCM and simulations using Eq. (2)]. The final result for the lifetime of the 4_1^+ state is $\tau_{4_1^+} = 13.5(15)$ ps and in agreement with the upper limit of $\tau_{4_1^+} < 20$ ps given in Ref. [49].

The decay transition of the 2_1^+ state (270.1 keV) has been used to determine the lifetime. Here, the contributions of the 4_1^+ , 3_γ^+ , and 2_γ^+ states were considered. The intensity of the contribution of the $2_\gamma^+ \rightarrow 2_1^+$ (522.2 keV) transition has been calculated using the intensities given in Ref. [25]. The intensity of the 522.2 keV transition could not be determined

due to an overlap of the shifted components of the 530.5 keV ($4_1^+ \rightarrow 2_1^+$) and 535.1 keV ($2_2^+ \rightarrow 2_1^+$) transitions which are populated in the inelastic-scattering reaction of ^{104}Ru . The final lifetime is calculated the same way as discussed before and the adopted value is $\tau_{2_1^+} = 274(23)$ ps. This result is in agreement with the results of two previous lifetimes measurements, resulting in lifetimes of 264(4) ps [49] and 375(101) ps [50].

IV. CALCULATIONS

To describe the nuclei of interest calculations using the proton-neutron interacting boson model (IBM-2) [51] were performed, which are based on the microscopic energy density functional (EDF) [52–54]. The parameters of the mapped-IBM-2 Hamiltonian are determined by mapping the deformation-energy surface, which is provided by the constrained Gogny-D1M SCMF calculations [55], onto the expectation value of the mapped-IBM Hamiltonian computed with the boson condensate intrinsic wave function [56–59]. With the resulting mapped-IBM Hamiltonian energy levels and transition probabilities can be determined. In the left part of Fig. 6 the potential-energy surface (PES) of the mean-field Gogny-D1M energy density functional exhibits only a single minimum. Therefore, the single configuration of the Hamiltonian described in Ref. [56] is used. In this section, only a short description of the calculations is given. A more detailed description of the calculations is given in Ref. [56]. The Hamiltonian \hat{H}_B is defined as

$$\hat{H}_B = \epsilon \hat{n}_d + \kappa \hat{Q}_\pi \cdot \hat{Q}_v + \kappa' \sum_{\rho' \neq \rho} \hat{T}_{\rho\rho\rho'}, \quad (3)$$

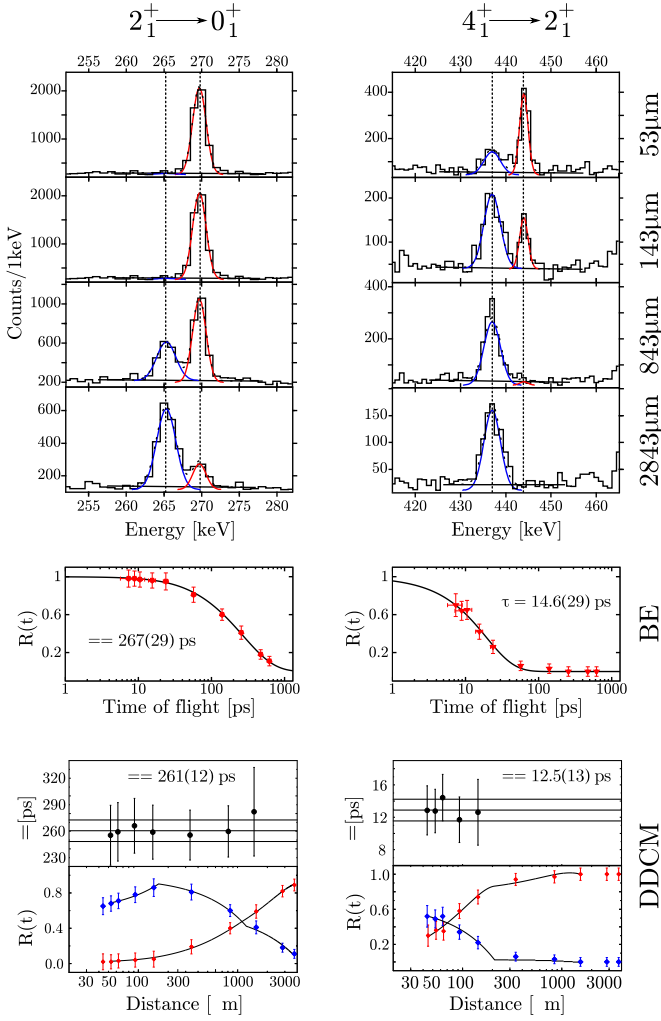


FIG. 5. The evolution of the shifted (blue) and unshifted (red) components in the backward ring for the $2_1^+ \rightarrow 0_1^+$ (left panel) and $4_1^+ \rightarrow 2_1^+$ (right panel) transitions for four selected distances, namely 53, 143, 843, and 2843 μm . Furthermore, the decay curves for the lifetimes of the 2_1^+ and 4_1^+ states using the Bateman equations to fit the data are shown. The DDC method for the 2_1^+ and 4_1^+ states using the program NAPATAU [43] for the backward angle. The individual obtained lifetimes are shown in the upper panel, and the lower panel shows the evolution of the shifted (red) and unshifted (blue) component. In addition the fit of the data is shown, which is used to obtain the derivative $\frac{d}{dx}R_i(x)$. Note that the x scale is logarithmic for the decay curves.

where $\hat{n}_d = \hat{n}_{dv} + \hat{n}_{d\pi}$ and $\hat{n}_{d\rho} = d_\rho^\dagger \cdot \tilde{d}_\rho$ ($\rho = v, \pi$) describes the d -boson number operator. The quadrupole operator is defined as $\hat{Q}_\rho = s_\rho^\dagger \tilde{d}_\rho + d_\rho^\dagger \tilde{s}_\rho + \chi_\rho [d_\rho^\dagger \times \tilde{d}_\rho]^{(2)}$ ($\rho = v, \pi$) and the third term is a specific three-boson interaction term with $\hat{T}_{\rho\rho\rho'} = \sum_L [d_\rho^\dagger \times d_\rho^\dagger \times d_{\rho'}^\dagger]^{(L)} \cdot [\tilde{d}_{\rho'} \times \tilde{d}_\rho \times \tilde{d}_\rho]^{(L)}$ with L being the total angular momentum in the boson system [60–62]. To calculate the electromagnetic $E2$ transition rates the following relation is used:

$$\hat{T}^{(E2)} = e_{B,\pi} \hat{Q}_\pi + e_{B,v} \hat{Q}_v, \quad (4)$$

with $e_{B,\pi}$ and $e_{B,v}$ being the effective charges and \hat{Q}_π and \hat{Q}_v the quadrupole operators described before. The boson

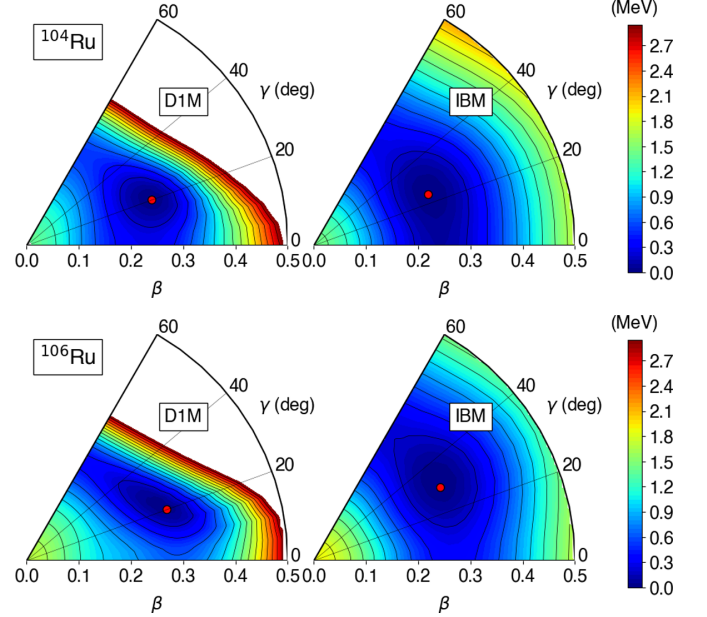


FIG. 6. Contour plot of the deformation-energy surface in the (β, γ) plane for ^{104}Ru (top) and ^{106}Ru (bottom) computed with the constrained SCMF method by using the Gogny functional D1M (left) and with the mapped IBM (right). The red dot indicates the minima of the energy surface plots and the difference between two neighboring contours is 100 keV

numbers were obtained by using the shell closures at $Z = N = 50$ and half the number of valence protons and neutrons. The $^{104,106}\text{Ru}$ nuclei have six protons and are ten (twelve) neutrons away from the closed shell. The proton boson number is $N_\pi = 3$ and the neutron boson number is $N_v = 5$ and $N_v = 6$, respectively. The minimized Hamiltonian parameters for ^{104}Ru are $\epsilon = 0.40$ MeV, $\kappa = -0.078$ MeV, $\chi_v = -0.10$, $\chi_\pi = -0.10$, $\kappa' = 0.25$ MeV. For ^{106}Ru the parameters $\epsilon = 0.37$ MeV, $\kappa = -0.067$ MeV, $\chi_v = 0.08$, $\chi_\pi = -0.05$, $\kappa' = 0.25$ MeV were used. An effective charge of $e_{B,\pi} = e_{B,v} = 0.108 e$ (^{104}Ru) and $e_{B,\pi} = e_{B,v} = 0.104 e$ (^{106}Ru) has been used. The effective g factors for both nuclei are $g_v = 0$ for neutrons and $g_\pi = 1$ for protons which are given in units of μ_N . An $E0$ operator of -0.068 fm² for proton and neutron bosons has been used to obtain the $\rho(E0)$ value for ^{106}Ru . In Fig. 6 the mean-field Gogny-D1M (left) and the mapped-IBM potential-energy surfaces (PESs) (right) are shown for ^{104}Ru and ^{106}Ru . For ^{104}Ru , the mean-field PES shows a distinct minimum around $\beta \approx 0.25$ and $\gamma \approx 20^\circ$ which was used to obtain the mapped-IBM parameters. The minimum in the mapped-IBM PES shows a minimum around $\beta \approx 0.25$ and $\gamma \approx 25^\circ$. In the case of ^{106}Ru , similar values are visible with a minimum around $\beta \approx 0.25$ and $\gamma \approx 20^\circ$ in the Gogny-D1M PES and $\beta \approx 0.25$ and $\gamma \approx 30^\circ$ for the mapped-IBM PES.

V. DISCUSSION

The experimental results of $^{104,106}\text{Ru}$ will be discussed and compared with the previously explained mapped-IBM calculations and to the values of the Willets-Jean γ -soft model [63] (hereafter called the γ -soft model) taken from Ref. [17]. The

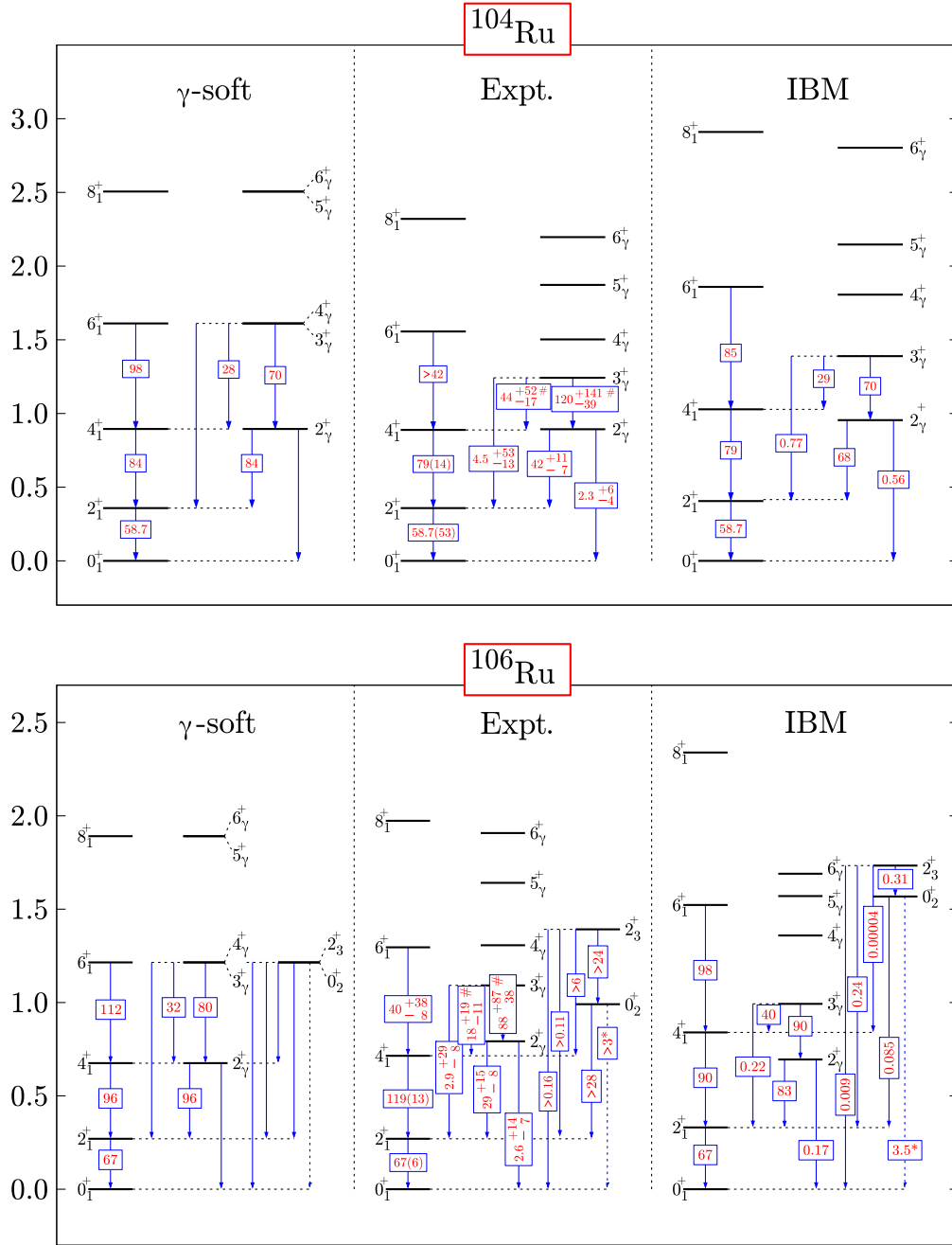


FIG. 7. The experimental (Expt.) and calculated (γ soft and mapped IBM) low energy level scheme for ^{104}Ru (top) and ^{106}Ru (bottom). The deduced $B(E2)$ transition probabilities values are placed on the corresponding arrow and are given in Weisskopf units. Due to a lack of multipole mixing ratios, some $B(E2)$ values are calculated in the limits of a pure $E2$ transitions, which are marked with #. The transition probability of the $0_2^+ \rightarrow 0_1^+$ is given in $10^3 \times \rho(E0)$.

Willets-Jean model is similar to the $O(6)$ limit for $N \rightarrow \infty$ in the IBM [64]. The results from the calculations as well as the experimental $B(E2)$ values are visualized in Fig. 7. Additionally, all transition strengths and ratios including energies as well as transitions strength are summarized in Tables III and IV, which will be discussed in the context of triaxiality. The ratios that have been calculated are defined as follows:

$$R_{4/2} = E_{4_1^+}/E_{2_1^+}, \quad (5)$$

$$R_{6/2} = E_{6_1^+}/E_{2_1^+}, \quad (6)$$

$$R_{8/2} = E_{8_1^+}/E_{2_1^+}, \quad (7)$$

$$R_{2_\gamma/2} = E_{2_\gamma^+}/E_{2_1^+}, \quad (8)$$

$$B_{4/2} = \frac{B(E2; 4_1^+ \rightarrow 2_1^+)}{B(E2; 2_1^+ \rightarrow 0_1^+)}, \quad (9)$$

$$B_{2\gamma/2} = \frac{B(E2; 2_\gamma^+ \rightarrow 2_1^+)}{B(E2; 2_1^+ \rightarrow 0_1^+)}, \quad (10)$$

$$B'_{2\gamma/2} = \frac{B(E2; 2_\gamma^+ \rightarrow 2_1^+)}{B(E2; 2_\gamma^+ \rightarrow 0_1^+)}. \quad (11)$$

Due to asymmetric uncertainties, the lower and upper limits of the last two ratios ($B_{2\gamma/2}$ and $B'_{2\gamma/2}$) were calculated using

TABLE III. The experimental, the mapped-IBM calculated and γ -soft model (taken from Ref. [17]) reduced transition probabilities of ^{104}Ru . The branching ratios are taken from the Nuclear Data Sheets [24]. For transitions with unknown multipole mixing ratios, the corresponding transition strength are calculated in the limit of pure $E2$ and $M1$ transitions and are marked with an asterisk. The $B(E2)$, $B(E1)$, and $B(M2)$ values are given in W.u. and the $B(M1)$ values are given in $10^{-4}\mu_N^2$. Furthermore, the ratios defined in Eqs. (5)–(11), were calculated for a comparison with the mapped-IBM and the γ -soft limit to discuss triaxiality.

Reduced transition strength	Experiment	IBM	γ soft [17]
$B(E2; 2_1^+ \rightarrow 0_1^+)$	58.7(53)	58.7	58.7
$B(E2; 4_1^+ \rightarrow 2_1^+)$	79(14)	79	84
$B(E2; 6_1^+ \rightarrow 4_1^+)$	>42	85	98
$B(E2; 2_\gamma^+ \rightarrow 0_1^+)$	2.3_{-4}^{+6}	0.56	
$B(E2; 2_\gamma^+ \rightarrow 2_1^+)^a$	42_{-7}^{+11}	68	84
$B(M1; 2_\gamma^+ \rightarrow 2_1^+)^a$	1.9_{-10}^{+34}	0.66	
$B(E2; 3_\gamma^+ \rightarrow 2_1^+)^b$	4.5_{-13}^{+53}	0.77	
$B(M1; 3_\gamma^+ \rightarrow 2_1^+)^b$	7.3_{-29}^{+88}	9.7	
$B(E2; 3_\gamma^+ \rightarrow 4_1^+)^*$	44_{-17}^{+52}	29	28
$B(M1; 3_\gamma^+ \rightarrow 4_1^+)^*$	110_{-40}^{+130}	4.4	
$B(E2; 3_\gamma^+ \rightarrow 2_\gamma^+)^*$	120_{-39}^{+141}	70	70
$B(M1; 3_\gamma^+ \rightarrow 2_\gamma^+)^*$	300_{-100}^{+350}	1.7	
$B(E2; 4_\gamma^+ \rightarrow 2_1^+)$	>0.3	0.068	
$B(E2; 4_\gamma^+ \rightarrow 4_1^+)^*$	>21	27	46
$B(M1; 4_\gamma^+ \rightarrow 4_1^+)^*$	>160	30	
$B(E2; 4_\gamma^+ \rightarrow 2_\gamma^+)$	>37	34	51
$B(E1; 3_1^- \rightarrow 2_1^+)^c$	$>2 \times 10^{-5} / >8 \cdot 10^{-7}$		
$B(M2; 3_1^- \rightarrow 2_1^+)^c$	$>4 \times 10^{-2} / >36$		
$R_{4/2} = E_{4_1^+}/E_{2_1^+}$	2.48(1)	2.53	2.5
$R_{6/2} = E_{6_1^+}/E_{2_1^+}$	4.35(1)	4.58	4.5
$R_{8/2} = E_{8_1^+}/E_{2_1^+}$	6.48(1)	7.17	7
$R_{2\gamma/2} = E_{2_\gamma^+}/E_{2_1^+}$	2.49(1)	2.35	2.5
$B_{4/2} = \frac{B(E2; 4_1^+ \rightarrow 2_1^+)}{B(E2; 2_1^+ \rightarrow 0_1^+)}$	1.35(27)	1.35	1.43
$B_{2\gamma/2} = \frac{B(E2; 2_\gamma^+ \rightarrow 2_1^+)}{B(E2; 2_1^+ \rightarrow 0_1^+)}$	0.73_{-20}^{+7} ^d	1.18	1.43
$B'_{2\gamma/2} = \frac{B(E2; 2_\gamma^+ \rightarrow 2_1^+)}{B(E2; 2_\gamma^+ \rightarrow 0_1^+)}$	22_{-21}^{+22} ^d	121	∞

^aA $M1/E2$ mixing ratio of $\delta = -36_{-54}^{+14}$ was used [65].

^bA $M1/E2$ mixing ratio of $\delta = -3.2(4)$ was used [65].

^cA $E1/M2$ mixing ratio of $\delta = 0.01$ or 5.2_{-11}^{+18} was used [65]. However, the results with the large mixing ratio of $\delta = 5.2_{-11}^{+18}$ seem unreasonable.

^dDue to asymmetric uncertainties, the error is calculated using a maximum value estimation. See text for more details.

the maximum value of the numerator and the minimum of the denominator as the upper limit and vice versa for the lower limit. Note that this does not result in an 1σ error.

A. ^{104}Ru

1. Energy levels

Level energies and $B(E2)$ transition probabilities derived for the experiment and from the calculations of the mapped-IBM and γ -soft model for ^{104}Ru are shown in Fig. 7. The level energies of the 2_1^+ and 4_1^+ are well described by both calculations. The energy levels of the 6_1^+ and 8_1^+ state are overestimated by both calculations, where the γ -soft calculations has a smaller deviation. The energy levels of the γ band are slightly overestimated by the γ -soft calculations. However, the clustering of the $(3_\gamma^+, 4_\gamma^+)$ and $(5_\gamma^+, 6_\gamma^+)$ states

TABLE IV. Same as Table III but for ^{106}Ru . The branching ratios are taken from the Nuclear Data Sheets [25].

Transition strength	Experiment	IBM	γ soft [17]
$B(E2; 2_1^+ \rightarrow 0_1^+)$	67(6)	67	67
$B(E2; 4_1^+ \rightarrow 2_1^+)$	116(14)	90	96
$B(E2; 6_1^+ \rightarrow 4_1^+)$	40_{-8}^{+38}	98	112
$B(E2; 2_\gamma^+ \rightarrow 0_1^+)$	2.6_{-7}^{+14}	0.17	
$B(E2; 2_\gamma^+ \rightarrow 2_1^+)^a$	29_{-8}^{+15}	83	96
$B(M1; 2_\gamma^+ \rightarrow 2_1^+)^a$	3.5_{-15}^{+36}	12	
$B(E2; 3_\gamma^+ \rightarrow 2_1^+)^b$	2.9_{-8}^{+29}	0.22	
$B(M1; 3_\gamma^+ \rightarrow 2_1^+)^b$	3.3_{-18}^{+61}	7.5	
$B(E2; 3_\gamma^+ \rightarrow 4_1^+)^*$	18_{-11}^{+19}	40	32
$B(M1; 3_\gamma^+ \rightarrow 4_1^+)^*$	5.3_{-33}^{+57}	2.1	
$B(E2; 3_\gamma^+ \rightarrow 2_\gamma^+)^*$	88_{-38}^{+87}	90	80
$B(M1; 3_\gamma^+ \rightarrow 2_\gamma^+)^*$	160_{-70}^{+160}	26	
$B(E2; 2_3^+ \rightarrow 0_1^+)$	>0.16	0.009	
$B(E2; 2_3^+ \rightarrow 2_1^+)^c$	>0.11	0.24	
$B(M1; 2_3^+ \rightarrow 2_1^+)^c$	>49	2.6	
$B(E2; 2_3^+ \rightarrow 4_1^+)$	>6	0.000039	0
$B(E2; 2_3^+ \rightarrow 0_2^+)$	>24	0.31	45
$\rho(E0; 0_2^+ \rightarrow 0_1^+)^d$	>3	3.5	
$B(E2; 0_2^+ \rightarrow 2_1^+)$	>28	0.085	
$R_{4/2} = E_{4_1^+}/E_{2_1^+}$	2.65(1)	2.54	2.5
$R_{6/2} = E_{6_1^+}/E_{2_1^+}$	4.80(1)	4.60	4.5
$R_{8/2} = E_{8_1^+}/E_{2_1^+}$	7.31(1)	7.07	7
$R_{2\gamma/2} = E_{2_\gamma^+}/E_{2_1^+}$	2.93(1)	2.10	2.5
$B_{4/2} = \frac{B(E2; 4_1^+ \rightarrow 2_1^+)}{B(E2; 2_1^+ \rightarrow 0_1^+)}$	1.82(29)	1.33	1.43
$B_{2\gamma/2} = \frac{B(E2; 2_\gamma^+ \rightarrow 2_1^+)}{B(E2; 2_1^+ \rightarrow 0_1^+)}$	0.45_{-13}^{+24} ^e	1.24	1.43
$B'_{2\gamma/2} = \frac{B(E2; 2_\gamma^+ \rightarrow 2_1^+)}{B(E2; 2_\gamma^+ \rightarrow 0_1^+)}$	11.5_{-60}^{+127} ^e	512.5	∞

^aA $M1/E2$ mixing ratio of $\delta = 7.1_{-11}^{+16}$ was used [41].

^bA $M1/E2$ mixing ratio of $\delta = -3.8_{-16}^{+9}$ was used [41].

^cA $M1/E2$ mixing ratio of $\delta = -0.24_{-12}^{+13}$ was used [41].

^dThe electric monopole transition strength between 0^+ states is given in $10^3 \times \rho^2(E0)$ and were calculated using the method explained in Refs. [66,67].

^eDue to asymmetric uncertainties, the error is calculated using a maximum value estimation. See text for more details.

resembles the expectations from the γ -soft model. Although the mapped-IBM predicts the states of the γ band higher than the experimental observations, it gives a reasonable description of these states and breaks down starting with 6_γ^+ state.

The experimental ratios of the ground-state band (see Table III), namely, the $R_{4/2} = 2.48(1)$, $R_{6/2} = 4.35(1)$, and $R_{8/2} = 6.48(1)$ are overestimated by the mapped-IBM by a small margin and lie closer to the ratios of the γ -soft rotational limits which are 2.5, 4.5, and 7.

The experimental $R_{2_\gamma/2} = E_{2_\gamma^+}/E_{2_1^+}$ ratio cannot be reproduced by the mapped-IBM but is in good agreement with the γ -soft limit which has a value of 2.5. The experimentally observed spacing in the sequence 2_γ^+ , 3_γ^+ , 4_γ^+ , 5_γ^+ , and 6_γ^+ states of the γ band is rather constant. This is supported by the staggering parameters $S(4) = -0.25(1)$, $S(5) = 0.31(1)$, and $S(6) = -0.13(1)$ that lie around zero (see Fig. 1), which translates to a constant spacing between the states. However, these values show weak signs of a γ -soft type of nucleus where the staggering parameter is negative for even spins and positive for odd spins [21]. Although the mapped-IBM calculations overestimate all of the level energies, the spacing in the γ band is also constant with the exception of the 6_γ^+ state. From an energy-level point of view, the ^{104}Ru nucleus show signs of γ softness which is supported by the prediction of the γ -soft model and indicated by the mapped-IBM calculations.

2. Reduced transition probabilities

To further discuss γ softness in this nucleus, a closer look to the reduced transition rates is necessary. The mapped-IBM and γ -soft calculations are adjusted to the experimental $B(E2; 2_1^+ \rightarrow 0_1^+)$ value. The $B(E2; 4_1^+ \rightarrow 2_1^+)$ value is in good agreement with both calculations within the given uncertainties. The mapped-IBM $B(E2; 6_1^+ \rightarrow 4_1^+)$ value of 85 W.u. is able to describe the experimental lower limit of 42 W.u. of this work. In comparison, the adopted literature value of the $B(E2; 6_1^+ \rightarrow 4_1^+) = 110_{-9}^{+4}$ W.u. [10] is lower than the prediction by the IBM. However, the literature value has a very good agreement with the expected at the γ -soft limit. The $B(E2; 2_\gamma^+ \rightarrow 0_1^+)$ value is underestimated and the $B(E2; 2_\gamma^+ \rightarrow 2_1^+)$ value is overestimated by both theoretical approaches. For the $E2$ transitions decaying from the 3_γ^+ state, all the values are predict to low by both calculations. Note that the $B(E2; 3_\gamma^+ \rightarrow 4_1^+)$ strength and $B(E2; 3_\gamma^+ \rightarrow 2_\gamma^+)$ strength are calculated assuming a pure $E2$ transition due to a lack of information of multipole mixing ratios. Hence, these experimental values might be significantly lower depending on the mixing ratio. The γ -soft model as well as the mapped-IBM are capable to describe the $B_{4/2}$ ratio within the uncertainties in contrast to the overestimation of the $B_{2_\gamma/2}$ and $B'_{2_\gamma/2}$ ratios.

B. ^{106}Ru

1. Energy levels

Level energies and $B(E2)$ transition probabilities derived for the experiment and from the calculations of the mapped-IBM and γ -soft model for ^{106}Ru are shown in Fig. 7. The level energies of the 2_1^+ and 4_1^+ are well described by both calculations. But for both calculations, the energy levels of

the 6_1^+ and 8_1^+ state are overestimated, where the γ -soft calculations have a smaller deviation. The γ -soft model is able to predict a reasonable energy level for the 2_γ^+ state and 4_γ^+ state. Note that the mapped-IBM calculations predict the 2_γ^+ state below the 4_1^+ state. This is an indicator that can be found in a rigid triaxial deformation. The 3_γ^+ , 5_γ^+ , and 6_γ^+ states in the γ -soft calculations are overestimated while the mapped-IBM calculation underestimates the experimental energy levels of these states. The $R_{4/2}$, $R_{6/2}$, $R_{8/2}$, and $R_{2_\gamma/2}$ ratios for the experiment, for the mapped-IBM calculations and for a γ -soft nucleus, according to the Ref. [17], are summarized in Table IV. The experimental ratios for the yrast band are predicted with reasonable accuracy by both approaches. The $R_{2_\gamma/2}$ ratios including the 2_γ^+ of the γ band cannot be predicted by either calculation.

2. Reduced transition probabilities

In Table IV the experimental $B(E2)$ and $B(M1)$ values are summarized and compared with the results from the mapped-IBM calculations and the γ -soft calculations. In Fig. 7 the $B(E2)$ strengths given in Weisskopf units are shown for the experiment, the mapped-IBM calculations, and the γ -soft calculations. The calculations have been adjusted to reproduce the $B(E2; 2_1^+ \rightarrow 0_1^+)$ transition strength. The mapped-IBM and γ -soft value for the $B(E2; 4_1^+ \rightarrow 2_1^+)$ strength lies within the 3σ range of the experimental observation. The $B(E2; 6_1^+ \rightarrow 4_1^+)$ on the other hand is overestimated by both calculations, where one has to note the large uncertainties of the experimental transitions strength. The $M1/E2$ mixed $2_\gamma^+ \rightarrow 2_1^+$ transition has been calculated using a multipole mixing ratio of $\delta = 7.1_{-1.1}^{+1.5}$ [41] and suggests a strong $E2$ component. Both calculations overestimate the $B(E2)$ value and the mapped-IBM calculation underestimates the corresponding $B(M1)$ value. The mapped-IBM $B(E2; 2_\gamma^+ \rightarrow 0_1^+)$ strength is an order of magnitude smaller than the experimental value, while the γ -soft limit predicts a vanishing transition strength. The experimental $B(E2; 3_\gamma^+ \rightarrow 4_1^+)$ and $B(E2; 3_\gamma^+ \rightarrow 2_\gamma^+)$ values are described by both theoretical approaches within the uncertainties. Note that both values were calculated assuming a pure $E2$ transition due to the lack of information about the mixing ratios. For the remaining $3_\gamma^+ \rightarrow 2_1^+$ transition, the mapped-IBM calculations is not capable of describing the value while the γ -soft approach is not capable of calculating a value. The $B_{4/2}$ ratio calculated using the mapped-IBM and the γ -soft limit lies within the 2σ interval of the experimental ratio. The experimental ratio lies closer to the vibrational limit ($B_{4/2} = 2$), whereas the calculated ratios suggest a more rotational or γ -soft behavior with both limits being $B_{4/2} = 1.43$. The calculated $B_{2_\gamma/2}$ value slightly overestimate the experimental ratio. The experimental $B'_{2_\gamma/2}$ value is order(s) of magnitudes smaller than the calculated values.

C. γ softness in $^{104,106}\text{Ru}$

Both nuclei are located in a region where triaxiality and γ softness have been suggested by different works [11–16,20,30,68,69]. First, the $R_{4/2}$ ratio for this two nuclei in

particular are around the typical γ -soft ratio of ≈ 2.5 [70]. The corresponding molybdenum and palladium isotones of ^{104}Ru , i.e., ^{102}Mo and ^{106}Pd , have similar ratios. The higher Z isotone of ^{106}Ru , namely, ^{108}Pd shows a similar ratio, whereas ^{104}Mo is closer to a ratio of $R_{4/2} \approx 3$ [24]. Furthermore, the energy levels of the 4_1^+ and 2_γ^+ states in $^{104,106}\text{Ru}$ are almost equal, which is a hint for triaxiality. Note that the mapped-IBM calculations predict the 2_γ^+ state below the 4_1^+ state for both nuclei, which can be found in a rigid triaxial deformation. Although the even-odd staggering is not well pronounced, it reveals signs of γ softness (see Fig. 1). This is also supported by the neighboring ^{102}Ru and ^{108}Ru isotopes which have similar staggering parameter $S(4) \approx -0.3$, $S(5) \approx 0.35$, $S(6) \approx -0.15$, and $S(7) \approx 0.3$ values. The same holds for the corresponding isotones $^{106,108}\text{Pd}$ and ^{102}Mo , but not for ^{104}Mo .

The mapped-IBM calculation delivers a capable description of the low-spin 2_γ^+ , 3_γ^+ , and 4_γ^+ states of the γ band in $^{104,106}\text{Ru}$. As shown in Fig. 6, the corresponding potential-energy surfaces show pronounced γ -soft and triaxial minima for both nuclei. The lifetimes of the 2_γ^+ state in both nuclei revealed a more collective $B(E2; 2_\gamma^+ \rightarrow 2_1^+)$ strength as well as an almost noncollective $B(E2; 2_\gamma^+ \rightarrow 0_1^+)$ transition probability. Both transition probabilities are comparable to the mapped-IBM calculation and the γ -soft calculations. The experimental transition rates of the 3_γ^+ state are in agreement with both calculations showing a large $B(E2; 3_\gamma^+ \rightarrow 2_\gamma^+)$ and a small $B(E2; 3_\gamma^+ \rightarrow 2_1^+)$ value.

For the investigation of γ softness, the inclusion of quadrupole moments can be insightful [71]. Therefore, the quadrupole moments up to the sixth order of the mapped-IBM approach have been calculated. They are defined as a relative dimensionless shape invariant parameter according to the following relation [71]:

$$K_n = \frac{q_n}{q_2^{n/2}} \text{ for } n \in \{3, 4, 5, 6\}, \quad (12)$$

where q_n are the quadrupole moment of the n th order. The shape invariant K_n can be used to determine the fluctuation of the effective deformation and are defined as [71]

$$\sigma_\beta = K_4 - 1, \quad (13)$$

$$\sigma_\gamma = K_6 - K_3^2. \quad (14)$$

A more detailed description of the calculation of these values is given in Ref. [71]. The resulting shape invariant of the mapped-IBM calculations are summarized in Table V and compared with the dynamical symmetry limits of the mapped IBM, namely, the U(5) (spherical vibrator) and γ -soft limit. The K_3 shape invariant is rather small for both nuclei. K_4 is an important invariant to distinguish between the U(5) and γ -soft symmetry, where the mapped-IBM calculations lie close to the γ -soft value for both nuclei. The same holds for the K_6 invariant which is significantly closer to the γ -soft limit compared with the U(5) limit. For both fluctuations of the effective deformation (σ_β and σ_γ) the values are better described by the γ -soft limit as well. The calculated effective β_{eff} and γ_{eff} given in Table V are consistent with the global

TABLE V. The quadrupole shape invariant K_n generated from the IBM calculations for $^{104,106}\text{Ru}$. For comparison the U(5) symmetry as well as the γ -soft limit is shown.

	$^{104}\text{Ru}_{\text{IBM}}$	$^{106}\text{Ru}_{\text{IBM}}$	γ soft	U(5)
$q_2 [e^2 \text{ b}^2]$	0.814	1.011		
K_3	0.157	0.074	0	0
K_4	1.009	1.010	1	1.4
K_5	0.192	0.068	0	0
K_6	0.278	0.264	$\frac{1}{3}$	0.84
β_{eff}	0.269	0.297		
γ_{eff}	27.0°	31.6°	30.0°	30.0°
σ_β	0.009	0.009	0	0.4
σ_γ	0.253	0.257	$\frac{1}{3}$	0.84

minima of the potential-energy surfaces. In general, most of the γ -soft invariant are capable of describing the properties of $^{104,106}\text{Ru}$. This fact in addition with the staggering parameter and the reduced transition strength that are well described by the γ -soft limit, suggest that both nuclei show signatures of softness in the γ degree of freedom.

VI. CONCLUSIONS

The lifetimes of the 2_1^+ , 4_1^+ , 2_γ^+ , 3_γ^+ states and upper limits for the lifetimes of the 6_1^+ , 4_γ^+ , and 3_1^- states in ^{104}Ru were measured using the RDDS technique. Furthermore, the lifetimes of the 2_1^+ , 4_1^+ , 6_1^+ , 2_γ^+ , 3_γ^+ states and upper limits for the lifetimes of the 0_2^+ and 2_3^+ states were determined in ^{106}Ru . The results were compared with previous measurements and to a mapped-IBM calculation which is based on a microscopic energy density functional and to the γ -soft limit. The mapped IBM describes the energy levels and transition strength of the ground-state band and the low-spin states of the γ band for both nuclei with reasonable accuracy. The deduced transition strength of the γ band in combination with the energy level and the energy spacing within the γ band reveal signatures of γ -soft behavior in $^{104,106}\text{Ru}$. This is supported by the mapped-IBM calculations which show a broad minimum at $\gamma \approx 30^\circ$ that spreads in the γ degree of freedom. The even odd staggering underlines the γ soft behavior and pointing towards slight γ softness. The transition strengths were compared with the γ -soft limit which further manifest the γ softness of these nuclei. Higher-order quadrupole moments were used to calculate shape invariants. These invariants are used as signatures of triaxiality and also indicated γ softness in $^{104,106}\text{Ru}$.

ACKNOWLEDGMENTS

We thank the operator team of the IKP FN Tandem accelerator for the professional support during the experiment. A.E., V.K., and M.B. acknowledge the support by the BMBF under Grant No. 05P15PKFNA. K.N. acknowledges the support by the Tenure Track Pilot Programme of the Croatian Science Foundation and the École Polytechnique Fédérale de Lausanne, and the Project TTP-2018-07-3554 Exotic Nuclear Structure and Dynamics, with funds of the Croatian-Swiss Research Programme.

- [1] P. Cejnar, J. Jolie, and R. F. Casten, *Rev. Mod. Phys.* **82**, 2155 (2010).
- [2] K. Heyde and J. L. Wood, *Rev. Mod. Phys.* **83**, 1467 (2011).
- [3] P. E. Garrett, M. Zielińska, and E. Clément, *Prog. Part. Nucl. Phys.* **124**, 103931 (2022).
- [4] A. Esmaylzadeh, J.-M. Régis, Y. H. Kim, U. Köster, J. Jolie, V. Karayonchev, L. Knafla, K. Nomura, L. M. Robledo, and R. Rodríguez-Guzmán, *Phys. Rev. C* **100**, 064309 (2019).
- [5] E. Clément, M. Zielińska, A. Görgen, W. Korten, S. Péru, J. Libert, H. Goutte, S. Hilaire, B. Bastin, C. Bauer, A. Blazhev, N. Bree, B. Bruyneel, P. A. Butler, J. Butterworth, P. Delahaye, A. Dijon, D. T. Doherty, A. Ekström, C. Fitzpatrick *et al.*, *Phys. Rev. Lett.* **116**, 022701 (2016).
- [6] J.-M. Régis, J. Jolie, N. Saed-Samii, N. Warr, M. Pfeiffer, A. Blanc, M. Jentschel, U. Köster, P. Mutti, T. Soldner, G. S. Simpson, F. Drouet, A. Vancraeynest, G. de France, E. Clément, O. Stezowski, C. A. Ur, W. Urban, P. H. Regan, Z. Podolyák *et al.*, *Phys. Rev. C* **95**, 054319 (2017).
- [7] P. E. Garrett, K. L. Green, and J. L. Wood, *Phys. Rev. C* **78**, 044307 (2008).
- [8] P. E. Garrett, T. R. Rodríguez, A. D. Varela, K. L. Green, J. Bangay, A. Finlay, R. A. E. Austin, G. C. Ball, D. S. Bandyopadhyay, V. Bildstein, S. Colosimo, D. S. Cross, G. A. Demand, P. Finlay, A. B. Garnsworthy, G. F. Grinyer, G. Hackman, B. Jigmeddorj, J. Jolie, W. D. Kulp *et al.*, *Phys. Rev. Lett.* **123**, 142502 (2019).
- [9] L. Svensson, C. Fahlander, L. Hasselgren, A. Bäcklin, L. Westerberg, D. Cline, T. Czosnyka, C. Wu, R. Diamond, and H. Kluge, *Nucl. Phys. A* **584**, 547 (1995).
- [10] J. Srebrny, T. Czosnyka, C. Droste, S. Rohoziński, L. Próchniak, K. Zajac, K. Pomorski, D. Cline, C. Wu, A. Bäcklin, L. Hasselgren, R. Diamond, D. Habs, H. Körner, F. Stephens, C. Baktash, and R. Kostecki, *Nucl. Phys. A* **766**, 25 (2006).
- [11] Y. Luo, S. Zhu, J. Hamilton, J. Rasmussen, A. Ramayya, C. Goodin, K. Li, J. Hwang, D. Almeded, S. Frauendorf, V. Dimitrov, J. ye Zhang, X. Che, Z. Jang, I. Stefanescu, A. Gelberg, G. Ter-Akopian, A. Daniel, M. Stoyer, R. Donangelo *et al.*, *Phys. Lett. B* **670**, 307 (2009).
- [12] D. Doherty, J. Allmond, R. Janssens, W. Korten, S. Zhu, M. Zielińska, D. Radford, A. Ayangeakaa, B. Bucher, J. Batchelder, C. Beausang, C. Campbell, M. Carpenter, D. Cline, H. Crawford, H. David, J. Delaroche, C. Dickerson, P. Fallon, A. Galindo-Uribarri *et al.*, *Phys. Lett. B* **766**, 334 (2017).
- [13] P.-A. Söderström, G. Lorusso, H. Watanabe, S. Nishimura, P. Doornenbal, G. Thiamova, F. Browne, G. Gey, H. S. Jung, T. Sumikama, J. Taprogge, Z. Vajta, J. Wu, Z. Y. Xu, H. Baba, G. Benzoni, K. Y. Chae, F. C. L. Crespi, N. Fukuda, R. Gernhäuser *et al.*, *Phys. Rev. C* **88**, 024301 (2013).
- [14] I. Stefanescu, A. Gelberg, J. Jolie, P. Van Isacker, P. von Brentano, Y. Luo, S. Zhu, J. Rasmussen, J. Hamilton, A. Ramayya, and X. Che, *Nucl. Phys. A* **789**, 125 (2007).
- [15] A. Esmaylzadeh, V. Karayonchev, G. Häfner, J. Jolie, M. Beckers, A. Blazhev, A. Dewald, C. Fransen, A. Goldkuhle, L. Knafla, and C. Müller-Gatermann, *Phys. Rev. C* **103**, 054324 (2021).
- [16] A. Esmaylzadeh, V. Karayonchev, K. Nomura, J. Jolie, M. Beckers, A. Blazhev, A. Dewald, C. Fransen, R.-B. Gerst, G. Häfner, A. Harter, L. Knafla, M. Ley, L. M. Robledo, R. Rodríguez-Guzmán, and M. Rudigier, *Phys. Rev. C* **104**, 064314 (2021).
- [17] L. Wilets and M. Jean, *Phys. Rev.* **102**, 788 (1956).
- [18] A. Davydov and G. Filippov, *Nucl. Phys.* **8**, 237 (1958).
- [19] A. Davydov and V. Rostovsky, *Nucl. Phys.* **12**, 58 (1959).
- [20] A. S. Davydov and V. S. Rostovskii, *J. Exptl. Theoret. Phys.* **36**, 1788 (1959) [*Sov. Phys. JETP* **36** (1959)].
- [21] N. Zamfir and R. Casten, *Phys. Lett. B* **260**, 265 (1991).
- [22] B. Singh and J. Chen, *Nucl. Data Sheets* **172**, 1 (2021).
- [23] D. De Frenne, *Nucl. Data Sheets* **110**, 1745 (2007).
- [24] J. Blachot, *Nucl. Data Sheets* **108**, 2035 (2007).
- [25] D. De Frenne and A. Negret, *Nucl. Data Sheets* **109**, 943 (2008).
- [26] J. Blachot, *Nucl. Data Sheets* **62**, 803 (1991).
- [27] G. Gürdal and F. Kondev, *Nucl. Data Sheets* **113**, 1315 (2012).
- [28] S. Lalkovski and F. Kondev, *Nucl. Data Sheets* **124**, 157 (2015).
- [29] D. Ralet, S. Pietri, T. Rodríguez, M. Alaqaee, T. Alexander, N. Alkhomashi, F. Ameil, T. Arici, A. Ataç, R. Avigo, T. Bäck, D. Bazzacco, B. Birkenbach, P. Boutachkov, B. Bruyneel, A. M. Bruce, F. Camera, B. Cederwall, S. Ceruti, E. Clément, and M. Zielińska (for the PreSPEC and AGATA Collaborations), *Phys. Rev. C* **95**, 034320 (2017).
- [30] J. Ha, T. Sumikama, F. Browne, N. Hinohara, A. M. Bruce, S. Choi, I. Nishizuka, S. Nishimura, P. Doornenbal, G. Lorusso, P.-A. Söderström, H. Watanabe, R. Daido, Z. Patel, S. Rice, L. Sinclair, J. Wu, Z. Y. Xu, A. Yagi, H. Baba *et al.*, *Phys. Rev. C* **101**, 044311 (2020).
- [31] J. Chen and B. Singh, *Nucl. Data Sheets* **164**, 1 (2020).
- [32] A. Dewald, O. Möller, and P. Petkov, *Prog. Part. Nucl. Phys.* **67**, 786 (2012).
- [33] V. Karayonchev, J. Jolie, A. Blazhev, A. Dewald, A. Esmaylzadeh, C. Fransen, G. Häfner, L. Knafla, J. Litzinger, C. Müller-Gatermann, J.-M. Régis, K. Schomacker, A. Vogt, N. Warr, A. Leviatan, and N. Gavrielov, *Phys. Rev. C* **102**, 064314 (2020).
- [34] M. Beckers, C. Müller-Gatermann, A. Blazhev, T. Braunroth, A. Dewald, C. Fransen, A. Goldkuhle, L. Kornwebel, J. Litzinger, F. von Spee, and K.-O. Zell, *Phys. Rev. C* **102**, 014324 (2020).
- [35] A. Dewald, S. Harissopoulos, and P. von Brentano, *Z. Phys. A: At. Nucl.* **334**, 163 (1989).
- [36] T. Alexander and A. Bell, *Nucl. Instrum. Methods* **81**, 22 (1970).
- [37] M. Beckers, A. Dewald, C. Fransen, L. Kornwebel, C.-D. Lakenbrink, and F. von Spee, *Nucl. Inst. Meth. Phys. Res. Sec. A* **1042**, 167416 (2022).
- [38] J. Koenig, H. Bohn, T. Faestermann, P. Kienle, H. J. Körner, W. A. Mayer, D. Pereira, K. E. Rehm, and H. J. Scheerer, *Phys. Rev. C* **24**, 2076 (1981).
- [39] S. Landsberger, R. Lecomte, P. Paradis, and S. Monaro, *Phys. Rev. C* **21**, 588 (1980).
- [40] F. McGowan, R. Robinson, P. Stelson, and W. Milner, *Nucl. Phys. A* **113**, 529 (1968).
- [41] J. Stachel, N. Kaffrell, N. Trautmann, K. Brodén, G. Skarnemark, and D. Eriksen, *Z. Phys. A: Hadrons Nuclei* **316**, 105 (1984).
- [42] H. Bateman, *Proc. Camb. Philos. Soc. Math. Phys. Sci.* **15**, 423 (1910).
- [43] B. Saha, Ph.D. thesis, Universität zu Kön, 2004, <https://kups.ub.uni-koeln.de/1246/>.
- [44] J. Litzinger, A. Blazhev, A. Dewald, F. Didierjean, G. Duchêne, C. Fransen, R. Lozeva, K. Sieja, D. Verney, G. de Angelis, D.

- Bazzacco, B. Birkenbach, S. Bottoni, A. Bracco, T. Braunroth, B. Cederwall, L. Corradi, F. C. L. Crespi, P. Désesquelles, J. Eberth *et al.*, *Phys. Rev. C* **92**, 064322 (2015).
- [45] J. Litzinger, Ph.D. thesis, Universität zu Köln, 2018, <https://kups.uni-koeln.de/8987/>.
- [46] J. Stachel, P. Hill, N. Kaffrell, H. Emling, H. Grein, E. Grosse, C. Michel, H.-J. Wollersheim, D. Schwalm, S. Brüssermann, and F. May, *Nucl. Phys. A* **419**, 589 (1984).
- [47] P. H. Stelson and F. K. McGowan, *Phys. Rev.* **110**, 489 (1958).
- [48] G. M. Temmer and N. P. Heydenburg, *Phys. Rev.* **104**, 967 (1956).
- [49] M. Sanchez-Vega, H. Mach, R. B. E. Taylor, B. Fogelberg, A. Lindroth, A. J. Aas, P. Dendooven, A. Honkanen, M. Huhta, G. Lhersonneau, M. Oinonen, J. M. Parmonen, H. Penttilä, J. Åystö, J. R. Persson, and J. Kurpeta, *Eur. Phys. J. A* **35**, 159 (2008).
- [50] S. Schoedder, G. Lhersonneau, A. Wöhr, G. Skarnemark, J. Alstad, A. Nähler, K. Eberhardt, J. Åystö, N. Trautmann, and K. L. Kratz, *Z. Phys. A: Hadrons Nucl.* **352**, 237 (1995).
- [51] F. Iachello and A. Arima, in *The Interacting Boson Model*, Cambridge Monographs on Mathematical Physics (Cambridge University Press, Cambridge, 1987).
- [52] M. Bender, P.-H. Heenen, and P.-G. Reinhard, *Rev. Mod. Phys.* **75**, 121 (2003).
- [53] T. Nikšić, D. Vretenar, and P. Ring, *Prog. Part. Nucl. Phys.* **66**, 519 (2011).
- [54] L. M. Robledo, T. R. Rodríguez, and R. R. Rodríguez-Guzmán, *J. Phys. G* **46**, 013001 (2019).
- [55] S. Goriely, S. Hilaire, M. Girod, and S. Péru, *Phys. Rev. Lett.* **102**, 242501 (2009).
- [56] K. Nomura, R. Rodríguez-Guzmán, and L. M. Robledo, *Phys. Rev. C* **94**, 044314 (2016).
- [57] J. Ginocchio and M. Kirson, *Nucl. Phys. A* **350**, 31 (1980).
- [58] K. Nomura, N. Shimizu, and T. Otsuka, *Phys. Rev. Lett.* **101**, 142501 (2008).
- [59] K. Nomura, N. Shimizu, and T. Otsuka, *Phys. Rev. C* **81**, 044307 (2010).
- [60] K. Nomura, N. Shimizu, D. Vretenar, T. Nikšić, and T. Otsuka, *Phys. Rev. Lett.* **108**, 132501 (2012).
- [61] P. Van Isacker and J.-Q. Chen, *Phys. Rev. C* **24**, 684 (1981).
- [62] K. Heyde, P. Van Isacker, M. Waroquier, and J. Moreau, *Phys. Rev. C* **29**, 1420 (1984).
- [63] D. J. Rowe and J. L. Wood, *Fundamentals of Nuclear Models* (World Scientific, 2010).
- [64] J. Meyer-Ter-Vehn, *Phys. Lett. B* **84**, 10 (1979).
- [65] K. Stümmerer, N. Kaffrell, and N. Trautmann, *Nucl. Phys. A* **308**, 1 (1978).
- [66] T. Kibédi and R. Spear, *At. Data Nucl. Data Tables* **89**, 77 (2005).
- [67] T. Kibédi, A. Garnsworthy, and J. Wood, *Prog. Part. Nucl. Phys.* **123**, 103930 (2022).
- [68] H. Watanabe, K. Yamaguchi, A. Odahara, T. Sumikama, S. Nishimura, K. Yoshinaga, Z. Li, Y. Miyashita, K. Sato, L. Próchniak, H. Baba, J. Berryman, N. Blasi, A. Bracco, F. Camera, J. Chiba, P. Doornenbal, S. Go, T. Hashimoto, S. Hayakawa *et al.*, *Phys. Lett. B* **704**, 270 (2011).
- [69] J. Snyder, W. Reviol, D. Sarantites, A. Afanasjev, R. Janssens, H. Abusara, M. Carpenter, X. Chen, C. Chiara, J. Greene, T. Lauritsen, E. McCutchan, D. Seweryniak, and S. Zhu, *Phys. Lett. B* **723**, 61 (2013).
- [70] R. F. Casten, *Nuclear Structure from a Simple Perspective* (Oxford University Press, Oxford, 2000).
- [71] V. Werner, N. Pietralla, P. von Brentano, R. F. Casten, and R. V. Jolos, *Phys. Rev. C* **61**, 021301(R) (2000).

6 | Summary and Conclusion

Lifetimes of excited states in different nuclei in the $A \approx 100$ region were measured to investigate the underlying structure of these nuclei. The lifetimes ranging from a few picoseconds up to a few hundred nanoseconds were measured using the RDDS and the fast-timing technique. A summary of the particular cases is given in the following sections.

Lifetime measurements and shape coexistence in ^{97}Sr

In this doctoral thesis, the rapid shape change in the strontium isotopes which occurs by going from $N = 58$ to $N = 60$ corresponding to the ^{96}Sr and ^{98}Sr nuclei, was studied. The nucleus ^{97}Sr possess $N = 59$ neutrons and hence lies at the spherical-deformed border, and investigating the low-lying excited states is of key importance to understand the shape change. Therefore, an experiment using the Lohengrin spectrometer [111, 112] in combination with LaBr(Ce) detectors and the fast-timing method was performed [94]. Due to an isomeric state in ^{97}Sr with a half-life of around 750 ns [113–115] which is sufficiently long to pass the Lohengrin spectrometer and an ionization chamber gate on $A = 97$, the remaining γ -ray spectrum mostly contains transitions in ^{97}Sr fed by its $9/2^+$ isomeric state. The lifetimes of all states that are fed by the isomeric state as well as the lifetime of the isomeric states are measured by using the γ - γ and the particle- γ fast timing method [45]. The lifetimes of the $7/2^+$ and $9/2^+$ states are confirmed within the uncertainties of earlier works [113–118]. For the lifetime of the $3/2^+$ state, the previously measured lifetimes can not be confirmed, where the result benefit from the high statistics. The spin of the state at 522 keV was unclear and assumed to be either $3/2^+$ or $5/2^+$. With the newly obtained lifetime information and the reduced transition strength the state is suggested to be a $5/2^+$ state which could be interpreted as a high seniority shell-model state. Here, it is indicated that the spherical configuration of this nucleus is still preferred for this state. The interpretation is based on the partial half-life of the state [115] and the calculations which have a better agreement by assuming a $5/2^+$ state. Furthermore, by assuming a $5/2^+$ state an $E2$ multipolarity transition would connect this state with the $9/2^+$ states while by assuming a $3/2^+$ would suggest a $M3/E4$ transition which seems unlikely.

Lifetime measurements to investigate γ -softness and shape coexistence in ^{102}Mo

The ^{102}Mo nucleus is located within the shape coexistence region as well as the γ -soft region. The lifetimes of the 2_1^+ , 4_1^+ , 6_1^+ , 0_2^+ , 2_γ^+ , 3_γ^+ and 4_γ^+ were measured using the RDDS technique to investigate both phenomena. The lifetime of the 0_2^+ state has been used to determine the $E0$

transition probability, namely the $\rho(E0)$ value. This transition probability can be used as an indicator of the exhibition of shape coexistence as explained in chapter 1.1.1 and in Ref. [14]. The obtained value in ^{102}Mo is one of the largest value along the nuclear chart for nuclei with a weakly deformed ground state [14, 16, 17]. Similar large values were observed in the ^{100}Zr and ^{98}Sr [16, 17, 119] which are the isotonic partners of ^{102}Mo . These values suggest that the phenomenon of shape coexistence might be still present in ^{102}Mo . However, the evolution of the energy of the 0_2^+ state along the molybdenum isotopes is rather flat in contrast to the strontium and zirconium isotopes which show a "V-like" shape with a minimum at $N = 60$ [10–13, 23, 24]. The combination of a flat behavior of the 0_2^+ states in the molybdenum isotopes and the increase of the $\rho(E0)$ value at $N = 60$ (^{102}Mo) might be a hint that the shape coexistence is less pronounced compared to the same phenomenon in the strontium and zirconium isotopes [18]. To investigate the triaxiality in ^{102}Mo , the relative position of the levels play a major role. In this work, the addition of lifetime measurements of states in the γ band were added to discuss this phenomenon. The staggering parameters of the states in the γ band shows tendencies towards a γ -soft nucleus. The surrounding ^{100}Mo and ^{104}Mo isotopes show similar values with the typical even-odd staggering for a γ -soft nucleus [12, 24]. Additionally, the reduced transition strength of the states within the γ band further supports this assumption. The IBM calculations with its broad PES minimum located around $\gamma \approx 40^\circ$ which spreads in the γ degree of freedom, also emphasize the softness of this nucleus [120]. The deduced transition strength of the states in the γ band in combination with the energy level reveals signs of a γ -soft behavior. In summary, the ^{102}Mo nucleus seems to exhibit a less pronounced shape coexistence compared with its lower- Z isotonic partners (^{98}Sr and ^{100}Zr) and possess signatures of a γ -soft type of triaxial deformation within the γ -band.

Triaxiality in the mid-shell nucleus ^{112}Pd

To investigate the triaxial behavior in ^{112}Pd , lifetimes of the 2_1^+ , 4_1^+ , 6_1^+ and 2_γ^+ states were measured using the RDDS technique. The determined lifetime of the 2_1^+ state is in agreement with former measurements and the lifetimes of the 4_1^+ and 6_1^+ states were determined for the first time and were used to discuss the quadrupole deformation within this nucleus. The lifetime of the 2_γ^+ state was used to extract transition strengths which were discussed in the context of triaxiality. Calculations within the frameworks of the IBM-1, Wilets-Jean and the Davydov-Filippov model were performed. Different indicators for a rigid triaxial case were observed like the excitation energy of the 2_γ^+ which is located below the 4_1^+ state. Recently, the isotonic partner of ^{112}Pd which is ^{110}Ru has been studied where a relatively rigid triaxial deformation near the ground state was suggested [41]. Another notable evidence is the sum of the energies of the first and second 2^+ states which almost equals the energy of the 3^+ state, which matches with less than 15 keV deviation for ^{112}Pd [41]. On the other hand, some observables suggest a γ -soft type of nucleus like the staggering parameter which shows the typical even-odd staggering. The IBM calculations provide the best description of this nucleus and the PES indicates a broad minimum

which spreads in the γ degree of freedom. Based on the neighboring $^{109,110,111}\text{Pd}$ isotopes which show evidence of γ -soft behavior [121, 122], a similar behavior is expected in ^{112}Pd . A clear interpretation is not possible due to a lack of lifetime information for the higher spin states in the γ band. The Davydov-Filippov model describes the lower-spin states i.e. 2_{γ}^{+} and the 3_{γ}^{+} state, with better accuracy than the γ -soft model while most of the signatures tend to indicate a γ -soft nucleus. A possible hypothesis which would include most of the observed evidence is that the lower-spin states possess a rigid behavior while the higher spin states show γ -soft behavior. In this case a smooth transition from a relatively rigid nuclear structure in the low spin states to a γ -soft nuclear structure for the high spin states occurs.

Investigation of γ -softness: Lifetime measurements in $^{104,106}\text{Ru}$

The γ -softness in the $^{104,106}\text{Ru}$ isotopes was also investigated in the scope of this work, where different observables indicate a γ -soft behavior. For this purpose lifetimes of states in the yrast- and γ -band were measured using the RDDS method. For the states in ^{104}Ru , i.e. the 2_1^{+} , 4_1^{+} , 6_1^{+} , 2_{γ}^{+} and 4_{γ}^{+} states, all lifetimes adopted from the literature were confirmed within their respective uncertainties. In the scope of this work, the lifetime of the 3_{γ}^{+} state and an upper limit for the lifetime of the 3_1^{-} state have been determined for the first time. The lifetimes of the 2_1^{+} and 2_{γ}^{+} states in ^{106}Ru agree with the literature values within the errors. For the previously known upper limits of the lifetimes of the 4_1^{+} and 3_{γ}^{+} states a lifetime has been determined, which are both important for the nuclear structure discussion. To describe both nuclei, an IBM calculation has been performed, where the parameters of the Hamiltonian are determined by mapping the deformation energy surface from mean field calculations onto the expectation value of the IBM Hamiltonian [70, 71, 120, 123]. All energy levels and transition strength of the ground state and the γ band are described with reasonable accuracy by the model calculations. The resulting IBM potential energy surfaces show pronounced γ -soft and triaxial minima for both nuclei by predicting a shallow minimum around $\gamma \approx 30^{\circ}$. To further quantify, the quadrupole moments up to the sixth order were used to calculate different shape invariants. These invariants emphasize the γ -soft behavior for both nuclei, which further manifests the γ softness of these nuclei.

7 | Outlook

Ongoing analyses and future experiments using the Lohengrin spectrometer

Further studies of the $N \sim 60$ and $Z \sim 40$ nuclei are ongoing and planned. The Lohengrin spectrometer [111, 112] is a powerful tool to investigate these nuclei produced in neutron induced fission experiments. Recently, different experiments have been conducted to study nuclei in this region. A β -decay experiment to study $A = 99$ nuclei and especially ^{99}Zr using the Lohengrin spectrometer was carried out. The $A = 99$ nuclei were implanted and the β -decay products were investigated in which the main observed nuclei are ^{99}Y , ^{99}Zr , ^{99}Nb and ^{99}Mo . The states in ^{99}Zr which are populated in the decay of ^{99}Y , are of key interest due to its similarities to ^{97}Sr which would further improve the phase transition in the zirconium isotopes. Furthermore, preliminary lifetime results of states in ^{99}Nb and ^{99}Y were determined [124]. The lifetimes allow to investigate the shape coexistence phenomenon within the odd- Z isotopic chains of yttrium and niobium. The analysis of the decay chain of mass $A = 99$ is ongoing and preliminary results suggest promising insights on this topic [124]. Another experiment using the same setup and principle was conducted to investigate the decay chain of the nuclei with $A = 98$ of which the ^{98}Y , ^{98}Zr , ^{98}Nb and ^{98}Mo nuclei were observed. Especially, the lifetimes of the 2_1^+ , 4_1^+ , 2_2^+ and 2_3^+ states in ^{98}Zr will be analyzed and discussed in the context of shape coexistence, but also lifetimes of states in ^{98}Y might be used to discuss the $N = 59$ isotones. However, the analysis of ^{98}Y turns out to be difficult because it is an odd-proton and odd-neutron nucleus which tend to have a high level density in the low-energy region. To investigate the low-energy structure in ^{95}Kr , a similar experiment as for ^{97}Sr (see Sec. 2 or Ref. [45]) was conducted [125]. Here, the $(7/2^+)$ isomeric state with a half-life of $T_{1/2} = 1.4 \mu\text{s}$ is sufficiently long to reach the implantation zone of the Lohengrin spectrometer. The $(3/2^+)$ state is the only state fed below the isomeric state, which simplifies the analysis. The analysis seems promising and a lifetime of around 350 ps is expected based from preliminary analysis. Similar results were obtained for the $3/2^+$ state in ^{97}Sr [45]. Although, the low-lying structure of ^{95}Kr is scarcely known [126], this might be an important result to investigate similarities of these two isotonic partners.

Although many studies have been performed in this region some aspects of this interesting shape phase transition are still not clearly understood. Therefore, more similar experiments to investigate this region would be of highest interest. Therefore, the investigation of the yttrium isotopic chain, which is located between the already well investigated strontium and zirconium isotopes, would be of major interest. In recent years, different experiments were performed to investigate the yttrium isotopes from an γ spectroscopic point of view [127–130]. However, lifetime information which could provide important ingredients for the nuclear structure discussion is scarcely known for the low-lying states. Another odd- Z isotopic chain to study would be the

niobium isotopes around $N = 60$, i.e. $^{98-101}\text{Nb}$. Some lifetimes of states in $^{98,99}\text{Y}$ and $^{98,99}\text{Nb}$ will be analyzed from data of experiments explained above. Similar experiments to study $A = 100$ and $A = 101$ nuclei are beneficial for the understanding in this region, especially lifetime measurements of states in ^{100}Nb , although the odd-odd configuration suggest a complex analysis. Another nucleus to study along the $N = 59$ isotones is ^{101}Mo which can be investigated either by fission products in combination with the Lohengrin spectrometer or by thermal neutron capture using a ^{100}Mo target in combination with the Fission Product Prompt γ -ray spectrometer (FIPPS) [131] which is also located at the Institut Laue Langevin in Grenoble, France. To investigate lifetimes of low-lying states in ^{101}Mo the implantation of ^{101}Nb nuclei using the Lohengrin spectrometer could be used. The half-life of ^{101}Nb is $T_{1/2} = 7.1$ s and sufficiently long to reach the implantation zone. Further, the fission yield of ^{101}Nb using a standard ^{235}U target amounts to 1.7% which enables a high population of low-lying states and high statistics of transitions in ^{101}Mo . The advantage of using the Lohengrin spectrometer is the almost contamination-free γ -ray spectrum containing only few transitions of the nucleus of interest. Another advantage is the population of only low-energy states, which are favorable to study the low-energy nuclear structure. However, by taking a close look to the β -decay ^{101}Nb only a few strong γ - γ cascades in ^{101}Mo have been observed [132]. A possible solution resolving this problem might be the usage of a β scintillator and perform β - γ fast-timing lifetime measurements. Such an experimental configuration has been used in previous experiments [133] and at the Lohengrin spectrometer [134]. Another approach to study the nuclear structure is the $^{100}\text{Mo}(n_{\text{th}},\gamma)^{101}\text{Mo}$ thermal neutron capture reaction. The cross section for thermal neutron capture is 190 mb for ^{100}Mo [135] and in combination with the FIPPS spectrometer the data can be analyzed using the HPGe triggered fast-timing method with γ - γ - γ coincidences.

Ongoing analyses and future experiments using the two neutron transfer reaction

The two-neutron transfer reaction experimental routine at the Institut für Kernphysik at the Universität zu Köln is powerful to populate neutron-rich nuclei along the whole nuclear chart [3, 18, 58, 136, 137]. The lifetime analysis of states in ^{57}Mn , ^{90}Sr , ^{118}Cd , $^{130,132}\text{Te}$, ^{206}Pb and ^{210}Pb which all were populated in two-neutron reactions are distributed along the nuclear chart is ongoing. With ^{57}Mn an odd-even nucleus was populated in such a reaction to analyze the lifetime of different states using the Doppler-Shift Attenuation Method (DSAM) [138, 139]. The $N = 32$ neutron sub-shell closure seems to affect states in ^{56}Cr but not in ^{58}Fe . The nucleus of ^{57}Mn is exactly located between these two nuclei and experiments were carried out to study if these effect already vanish in Mn.

A quantification of the proton-neutron symmetry of an IBM-2 wave function is given by the F -spin quantum number [140–142]. The F -spin describes the isospin for the elementary proton and neutron bosons ($F_z = +1/2$ for protons and $F_z = -1/2$ for neutrons) and IBM-2 wave

functions with F -spin quantum numbers $F < F_{max}$ contain at least one pair of proton and neutron bosons. This leads to an anti-symmetry of the wave function by exchanging the proton and neutron labels. Such states are called mixed-symmetry (MS) states. The MS states were investigated in different works along the $N = 52$ isotones around $Z \approx 40$, i.e. ^{88}Kr [143, 144], ^{90}Sr [145], ^{92}Zr [146, 147], ^{94}Mo [148–150], ^{96}Ru [151–153], ^{98}Pd [154]. What stands out are the anomalous $B(E2)$ and $B(M1)$ strengths of the $2_{ms}^+ \rightarrow 2_1^+$ state in ^{90}Sr which are both significantly smaller than the surrounding $N = 52$ isotones (see Fig. 5 in Ref. [143]). This stems mainly from the inaccurate lifetime of $\tau = 3(2)$ ps which was obtained using the fast-timing method. To determine a more accurate value the two-neutron transfer reaction has been used to populate this 2_{ms}^+ state and other low-lying states and measure the lifetimes using DSAM. The analysis is still ongoing and the results suggest a lifetime below 1 ps which would increase the $B(M1)$ value to around $0.6\mu_N$ fitting the general trend of the $N = 52$ isotones and confirming the mixed-symmetry nature of this state [155].

Mixed-symmetry states in the near spherical Te nuclei were investigated by different experiments [156–160] and by different theoretical calculations [161–165]. The 2_2^+ states in $^{130,132}\text{Te}$ might be mixed symmetry states but the lifetimes and the corresponding $B(E2)$ and especially $B(M1)$ strength are not available. Two neutron-transfer reactions using a ^{128}Te and ^{130}Te target were performed to populate these states and clarify a possible mixed-symmetry configuration. The analysis of these nuclei is ongoing and first results are expected in the near future.

To further extend the research on γ softness in the region around ruthenium, a two-neutron transfer experiment to populate and measure lifetimes of low-lying states in ^{118}Cd was performed. The lifetimes, especially of the 4_1^+ and 2_2^+ states, will help to extend the understanding of the complex nuclear structure along the cadmium isotopes that features different phenomena like shape coexistence and γ -softness [166, 167].

The nuclear shell model is well suited to describe the region around the doubly magic nucleus ^{208}Pb as shown by different works [168–171]. Recently, lifetime measurements of states in this region have been measured extensively [103, 105, 106, 172, 173]. The low-lying structure of the polonium isotopes cannot be predicted by shell model calculations. Calculations carried out using the Kuo-Herling residual interaction [169] overestimate the $B(E2; 2_1^+ \rightarrow 0_1^+)$ transition which is interpreted as an admixture of particle-hole excitations across the $Z = 82$ shell closure. To improve the interactions of the shell model in this region, lifetimes in ^{206}Pb and ^{210}Pb are crucial ingredients. Two neutron transfer experiments were carried out using a ^{204}Pb and ^{208}Pb targets to measure lifetimes in this region.

Future two-neutron transfer experiments to study the low-lying structure of neutron-rich nuclei are planned in the rare-earth region, i.e. ^{152}Nd , ^{156}Sm , $^{160,162}\text{Gd}$, ^{166}Dy , ^{172}Er , ^{178}Yb , ^{182}Hf , ^{188}W , ^{194}Os and ^{200}Pt . The region around neodymium and samarium, especially around $N = 90$ (^{152}Sm and ^{150}Nd) are good examples of shape coexistence and shape transition [1, 9, 14, 174, 175]. Furthermore, these nuclei are located around a so called "octupole magic" number, i.e. $N = 88$ [176]. Lifetime measurements in the neutron-rich ^{152}Nd and ^{156}Sm nuclei will show if the

mentioned effects still persist.

The midshell-midshell nuclei from gadolinium to hafnium are considered as rigid rotors, where also low-lying 0_2^+ states occur. These states are related to the β vibration of a nucleus and the confined β -soft model yields an analytical solution of the Bohr-Hamiltonian which could be used to describe some of these nuclei [177]. Lifetime measurements of these nuclei will extend the evolution of $B_{4/2}$ ratios in this region and will help to further manifest the β -soft hypothesis.

The tungsten, but more so the osmium and platinum isotopes, are considered transitional nuclei between a pronounced rigid rotor and a spherical vibrator. Clear signatures from the shape transition are visible by the drop of the $R_{4/2}$ ratio for the tungsten and osmium isotopes. Another shape related phenomenon which is observed in this region is the γ -softness. This is pronounced in the Pt isotopes, but also show effects in the Os and W isotopes [178–180]. As shown in this work lifetime measurements and deduced transition strengths are helpful in the discussion of such effects. Therefore, two-neutron transfer experiments to populate these states in ^{188}W , ^{194}Os and ^{200}Pt might be helpful to extend the knowledge in this region.

Further transfer reactions to populate low-lying states in nuclei

During the research of improving the two-neutron transfer reaction and the experimental setup, different other transfer reactions were investigated at the 10 MV Tandem accelerator. For example the α -transfer reactions has been proven to be a suitable reaction to study low-lying states [172, 173]. Different reactions were tested, i.e. the $(^{18}\text{O}, ^{14}\text{C})$, $(^{16}\text{O}, ^{12}\text{C})$ and $(^{12}\text{C}, ^8\text{Be})$ reactions, to optimize the reaction yield. The $(^{12}\text{C}, ^8\text{Be})$ reactions show the best results, if the solar cells were covered with a thin aluminum foil, which prevents heavier nuclei to be detected. The thickness of the aluminum foil has to be calculated depending on the energy and target. Another transfer channel which has been tested, is the $(^{16}\text{O}, ^{14}\text{C})$ reaction corresponding to a two-proton transfer. The transfer channel is clearly observed in two former works [172, 173] and has been applied to study the low-lying structure of ^{211}At [181].

In general, transfer reactions performed around the Coulomb barrier of the reaction offer a variety of possibilities to study the low-energy structure of nuclei. These reactions populate only a few states which makes the analysis and the feeding pattern relatively manageable. However, the data cannot be analyzed in γ - γ coincidences due to the low cross sections of such reactions. A further improvement of the experimental setup would be favorable, i.e. the addition of more HPGe detectors and the addition of ΔE -E detectors instead of solar cells which will allow a better discrimination between the different reaction channels, especially the $(^{18}, ^{18}\text{O})$ and $(^{18}, ^{16}\text{O})$ channels.

Bibliography

- [1] P. Cejnar, J. Jolie and R. F. Casten. “Quantum phase transitions in the shapes of atomic nuclei.” *Rev. Mod. Phys.* 82 (2010), 2155–2212.
- [2] K. Heyde and J. L. Wood. “Shape coexistence in atomic nuclei.” *Rev. Mod. Phys.* 83 (2011), 1467–1521.
- [3] V. Karayonchev, J. Jolie, A. Blazhev, A. Dewald, A. Esmaylzadeh, C. Fransen, G. Häfner, L. Knafla, J. Litzinger, C. Müller-Gatermann, J.-M. Régis, K. Schomacker, A. Vogt, N. Warr, A. Leviatan and N. Gavrielov. “Tests of collectivity in ^{98}Zr by absolute transition rates.” *Phys. Rev. C* 102 (2020), 064314.
- [4] P. Singh, W. Korten, T. W. Hagen, A. Görgen, L. Grente, M.-D. Salsac, F. Farget, E. Clément, G. de France, T. Braunroth, B. Bruyneel, I. Celikovic, O. Delaune, A. Dewald, A. Dijon, J.-P. Delaroche, M. Girod, M. Hackstein, B. Jacquot, J. Libert, J. Litzinger, J.Ljungvall, C. Louchart, A. Gottardo, C. Michelagnoli, C. Müller-Gatermann, D. R. Napoli, T. Otsuka, N. Pillet, F. Recchia, W. Rother, E. Sahin, S. Siem, B. Sulignano, T. Togashi, Y. Tsunoda, C. Theisen and J. J. Valiente-Dobon. “Evidence for Coexisting Shapes through Lifetime Measurements in ^{98}Zr .” *Phys. Rev. Lett.* 121 (2018), 192501.
- [5] S. Ansari, J.-M. Régis, J. Jolie, N. Saed-Samii, N. Warr, W. Korten, M. Zielińska, M.-D. Salsac, A. Blanc, M. Jentschel, U. Köster, P. Mutti, T. Soldner, G. S. Simpson, F. Drouet, A. Vancraeynest, G. de France, E. Clément, O. Stezowski, C. A. Ur, W. Urban, P. H. Regan, Z. Podolyák, C. Larijani, C. Townsley, R. Carroll, E. Wilson, H. Mach, L. M. Fraile, V. Pazyi, B. Olaizola, V. Vedia, A. M. Bruce, O. J. Roberts, J. F. Smith, M. Scheck, T. Kröll, A.-L. Hartig, A. Ignatov, S. Ilieva, S. Lalkovski, N. Mărginean, T. Otsuka, N. Shimizu, T. Togashi and Y. Tsunoda. “Experimental study of the lifetime and phase transition in neutron-rich $^{98,100,102}\text{Zr}$.” *Phys. Rev. C* 96 (2017), 054323.
- [6] E. Cheifetz, R. C. Jared, S. G. Thompson and J. B. Wilhelmy. “Experimental Information Concerning Deformation of Neutron Rich Nuclei in the $A \sim 100$ Region.” *Phys. Rev. Lett.* 25 (1970), 38–43.
- [7] P. Federman and S. Pittel. “Towards a unified microscopic description of nuclear deformation.” *Phys. Lett. B* 69.4 (1977), 385–388.
- [8] P. Federman and S. Pittel. “Unified shell-model description of nuclear deformation.” *Phys. Rev. C* 20 (1979), 820–829.
- [9] P. E. Garrett, M. Zielińska and E. Clément. “An experimental view on shape coexistence in nuclei.” *Prog. Part. Nucl. Phys.* 124 (2022), 103931.
- [10] D. Abriola and A. Sonzogni. “Nucl. Data Sheets for $A = 96$.” *Nucl. Data Sheets* 109.11 (2008), 2501–2655.
- [11] J. Chen and B. Singh. “Nucl. Data Sheets for $A = 98$.” *Nucl. Data Sheets* 164 (2020), 1–477.
- [12] B. Singh and J. Chen. “Nucl. Data Sheets for $A = 100$.” *Nucl. Data Sheets* 172 (2021), 1–542.
- [13] D. De Frenne. “Nucl. Data Sheets for $A = 102$.” *Nucl. Data Sheets* 110.8 (2009), 1745–1915.

- [14] J. Wood, E. Zganjar, C. De Coster and K. Heyde. “Electric monopole transitions from low energy excitations in nuclei.” *Nucl. Phys. A* 651.4 (1999), 323–368.
- [15] Colorful Nuclide chart. Accessed: 23.06.2022. URL: <https://people.physics.anu.edu.au/~ecs103/chart/>.
- [16] T. Kibédi, A. Garnsworthy and J. Wood. “Electric monopole transitions in nuclei.” *Prog. Part. Nucl. Phys.* 123 (2022), 103930.
- [17] T. Kibédi and R. Spear. “Electric monopole transitions between 0^+ states for nuclei throughout the periodic table.” *At. Data. Nucl. Data Tables* 89.1 (2005), 77–100.
- [18] A. Esmaylzadeh, V. Karayonchev, K. Nomura, J. Jolie, M. Beckers, A. Blazhev, A. Dewald, C. Fransen, R.-B. Gerst, G. Häfner, A. Harter, L. Knafla, M. Ley, L. M. Robledo, R. Rodríguez-Guzmán and M. Rudigier. “Lifetime measurements to investigate γ softness and shape coexistence in ^{102}Mo .” *Phys. Rev. C* 104 (2021), 064314.
- [19] J. Srebrny, T. Czosnyka, C. Droste, S. Rohoziński, L. Próchniak, K. Zajač, K. Pomorski, D. Cline, C. Wu, A. Bäcklin, L. Hasselgren, R. Diamond, D. Habs, H. Körner, F. Stephens, C. Baktash and R. Kostecki. “Experimental and theoretical investigations of quadrupole collective degrees of freedom in ^{104}Ru .” *Nucl. Phys. A* 766 (2006), 25–51.
- [20] E. McCutchan and A. Sonzogni. “Nucl. Data Sheets for $A = 88$.” *Nucl. Data Sheets* 115 (2014), 135–304.
- [21] S. Basu and E. McCutchan. “Nucl. Data Sheets for $A = 90$.” *Nucl. Data Sheets* 165 (2020), 1–329.
- [22] C. M. Baglin. “Nucl. Data Sheets for $A = 92$.” *Nucl. Data Sheets* 113.10 (2012), 2187–2389.
- [23] D. Abriola and A. Sonzogni. “Nucl. Data Sheets for $A = 94$.” *Nucl. Data Sheets* 107.9 (2006), 2423–2578.
- [24] J. Blachot. “Nucl. Data Sheets for $A = 104$.” *Nucl. Data Sheets* 108.10 (2007), 2035–2172.
- [25] D. De Frenne and A. Negret. “Nucl. Data Sheets for $A = 106$.” *Nucl. Data Sheets* 109.4 (2008), 943–1102.
- [26] J. Blachot. “Nucl. Data Sheets for $A = 108$.” *Nucl. Data Sheets* 91.2 (2000), 135–296.
- [27] G. Gürdal and F. Kondev. “Nucl. Data Sheets for $A = 110$.” *Nucl. Data Sheets* 113.5 (2012), 1315–1561.
- [28] S. Lalkovski and F. Kondev. “Nucl. Data Sheets for $A = 112$.” *Nucl. Data Sheets* 124 (2015), 157–412.
- [29] J. Blachot. “Nucl. Data Sheets for $A = 114$.” *Nucl. Data Sheets* 113.2 (2012), 515–714.
- [30] J. Blachot. “Nucl. Data Sheets for $A = 116$.” *Nucl. Data Sheets* 111.3 (2010), 717–895.
- [31] M. Albers, K. Nomura, N. Warr, A. Blazhev, J. Jolie, D. Mücher, B. Bastin, C. Bauer, C. Bernards, L. Bettermann, V. Bildstein, J. Butterworth, M. Cappellazzo, J. Cederkäll, D. Cline, I. Darby, S. Das Gupta, J. Daugas, T. Davinson, H. De Witte, J. Diriken, D. Filipescu, E. Fiori, C. Fransen, L. Gaffney, G. Georgiev, R. Gernhäuser, M. Hackstein, S. Heinze, H. Hess, M. Huyse, D. Jenkins, J. Konki, M. Kowalczyk, T. Kröll, R. Krücken, J. Litzinger, R. Lutter, N. Mărginean, C. Mihai, K. Moschner, P. Napiorkowski, B. Nara Singh, K. Nowak, J. Pakarinen, M. Pfeiffer, D. Radeck, P. Reiter, S. Rigby, L. Robledo, R. Rodríguez-Guzmán, M. Rudigier, M. Scheck, M. Seidlitz, B. Siebeck, G. Simpson, P. Thöle,

- T. Thomas, J. Van de Walle, P. Van Duppen, M. Vermeulen, D. Voulot, R. Wadsworth, F. Wenander, K. Wimmer, K. Zell and M. Zielinska. “Shape dynamics in neutron-rich Kr isotopes: Coulomb excitation of ^{92}Kr , ^{94}Kr and ^{96}Kr .” *Nucl. Phys. A* 899 (2013), 1–28.
- [32] M. Albers, N. Warr, K. Nomura, A. Blazhev, J. Jolie, D. Mucher, B. Bastin, C. Bauer, C. Bernardis, L. Bettermann, V. Bildstein, J. Butterworth, M. Cappellazzo, J. Cederkll, D. Cline, I. Darby, S. Das Gupta, J. M. Daugas, T. Davinson, H. De Witte, J. Diriken, D. Filipescu, E. Fiori, C. Fransen, L. P. Gaffney, G. Georgiev, R. Gernhuser, M. Hackstein, S. Heinze, H. Hess, M. Huyse, D. Jenkins, J. Konki, M. Kowalczyk, T. Krll, R. Krcken, J. Litzinger, R. Lutter, N. Mrginean, C. Mihai, K. Moschner, P. Napiorkowski, B. S. Nara Singh, K. Nowak, T. Otsuka, J. Pakarinen, M. Pfeiffer, D. Radeck, P. Reiter, S. Rigby, L. M. Robledo, R. Rodrguez-Guzmn, M. Rudigier, P. Sarriguren, M. Scheck, M. Seidlitz, B. Siebeck, G. Simpson, P. Thle, T. Thomas, J. Van de Walle, P. Van Duppen, M. Vermeulen, D. Voulot, R. Wadsworth, F. Wenander, K. Wimmer, K. O. Zell and M. Zielinska. “Evidence for a Smooth Onset of Deformation in the Neutron-Rich Kr Isotopes.” *Phys. Rev. Lett.* 108 (2012), 062701.
- [33] J.-M. Rgis, J. Jolie, N. Saed-Samii, N. Warr, M. Pfeiffer, A. Blanc, M. Jentschel, U. Kster, P. Mutti, T. Soldner, G. S. Simpson, F. Drouet, A. Vancraeynest, G. de France, E. Clment, O. Stezowski, C. A. Ur, W. Urban, P. H. Regan, Z. Podolyk, C. Larijani, C. Townsley, R. Carroll, E. Wilson, L. M. Fraile, H. Mach, V. Pazyi, B. Olaizola, V. Vedia, A. M. Bruce, O. J. Roberts, J. F. Smith, M. Scheck, T. Krll, A.-L. Hartig, A. Ignatov, S. Ilieva, S. Lalkovski, W. Korten, N. Mrginean, T. Otsuka, N. Shimizu, T. Togashi and Y. Tsunoda. “Abrupt shape transition at neutron number $N = 60$: $B(E2)$ values in $^{94,96,98}\text{Sr}$ from fast $\gamma - \gamma$ timing.” *Phys. Rev. C* 95 (2017), 054319.
- [34] E. Clment, M. Zieliska, A. Grgen, W. Korten, S. Pru, J. Libert, H. Goutte, S. Hilaire, B. Bastin, C. Bauer, A. Blazhev, N. Bree, B. Bruyneel, P. A. Butler, J. Butterworth, P. Delahaye, A. Dijon, D. T. Doherty, A. Ekstrm, C. Fitzpatrick, C. Fransen, G. Georgiev, R. Gernhuser, H. Hess, J. Iwanicki, D. G. Jenkins, A. C. Larsen, J. Ljungvall, R. Lutter, P. Marley, K. Moschner, P. J. Napiorkowski, J. Pakarinen, A. Petts, P. Reiter, T. Renstrm, M. Seidlitz, B. Siebeck, S. Siem, C. Sotty, J. Srebrny, I. Stefanescu, G. M. Tveten, J. Van de Walle, M. Vermeulen, D. Voulot, N. Warr, F. Wenander, A. Wiens, H. De Witte and K. Wrzosek-Lipska. “Spectroscopic Quadrupole Moments in $^{96,98}\text{Sr}$: Evidence for Shape Coexistence in Neutron-Rich Strontium Isotopes at $N = 60$.” *Phys. Rev. Lett.* 116 (2016), 022701.
- [35] E. Clment, M. Zieliska, S. Pru, H. Goutte, S. Hilaire, A. Grgen, W. Korten, D. T. Doherty, B. Bastin, C. Bauer, A. Blazhev, N. Bree, B. Bruyneel, P. A. Butler, J. Butterworth, J. Cederkll, P. Delahaye, A. Dijon, A. Ekstrm, C. Fitzpatrick, C. Fransen, G. Georgiev, R. Gernhuser, H. Hess, J. Iwanicki, D. G. Jenkins, A. C. Larsen, J. Ljungvall, R. Lutter, P. Marley, K. Moschner, P. J. Napiorkowski, J. Pakarinen, A. Petts, P. Reiter, T. Renstrm, M. Seidlitz, B. Siebeck, S. Siem, C. Sotty, J. Srebrny, I. Stefanescu, G. M. Tveten, J. Van de Walle, M. Vermeulen, D. Voulot, N. Warr, F. Wenander, A. Wiens, H. De Witte and K. Wrzosek-Lipska. “Low-energy Coulomb excitation of $^{96,98}\text{Sr}$ beams.” *Phys. Rev. C* 94 (2016), 054326.
- [36] G. Lhersonneau, B. Pfeiffer, M. Huhta, A. Whr, I. Klckl, K.-L. Kratz, J. yst and The ISOLDE Collaboration. “First evidence for the 2^+ level in the very neutron-rich nucleus ^{102}Sr .” *Z. Phys. A* 351 (1995), 357.

- [37] F. Browne, A. Bruce, T. Sumikama, I. Nishizuka, S. Nishimura, P. Doornenbal, G. Lorusso, P.-A. Söderström, H. Watanabe, R. Daido, Z. Patel, S. Rice, L. Sinclair, J. Wu, Z. Xu, A. Yagi, H. Baba, N. Chiga, R. Carroll, F. Didierjean, Y. Fang, N. Fukuda, G. Gey, E. Ideguchi, N. Inabe, T. Isobe, D. Kameda, I. Kojouharov, N. Kurz, T. Kubo, S. Lalkovski, Z. Li, R. Lozeva, H. Nishibata, A. Odahara, Z. Podolyák, P. Regan, O. Roberts, H. Sakurai, H. Schaffner, G. Simpson, H. Suzuki, H. Takeda, M. Tanaka, J. Taprogge, V. Werner and O. Wieland. “Lifetime measurements of the first 2^+ states in $^{104,106}\text{Zr}$: Evolution of ground-state deformations.” *Phys. Lett. B* 750 (2015), 448–452.
- [38] J. Ha, T. Sumikama, F. Browne, N. Hinohara, A. M. Bruce, S. Choi, I. Nishizuka, S. Nishimura, P. Doornenbal, G. Lorusso, P.-A. Söderström, H. Watanabe, R. Daido, Z. Patel, S. Rice, L. Sinclair, J. Wu, Z. Y. Xu, A. Yagi, H. Baba, N. Chiga, R. Carroll, F. Didierjean, Y. Fang, N. Fukuda, G. Gey, E. Ideguchi, N. Inabe, T. Isobe, D. Kameda, I. Kojouharov, N. Kurz, T. Kubo, S. Lalkovski, Z. Li, R. Lozeva, H. Nishibata, A. Odahara, Z. Podolyák, P. H. Regan, O. J. Roberts, H. Sakurai, H. Schaffner, G. S. Simpson, H. Suzuki, H. Takeda, M. Tanaka, J. Taprogge, V. Werner and O. Wieland. “Shape evolution of neutron-rich $^{106,108,110}\text{Mo}$ isotopes in the triaxial degree of freedom.” *Phys. Rev. C* 101 (2020), 044311.
- [39] M. Sanchez-Vega, H. Mach, R. B. E. Taylor, B. Fogelberg, A. Lindroth, A. J. Aas, P. Dendooven, A. Honkanen, M. Huhta, G. Lhersonneau, M. Oinonen, J. M. Parmonen, H. Penttilä, J. Äystö, J. R. Persson and J. Kurpeta. “Studies of quadrupole collectivity in the γ -soft ^{106}Ru .” *Eur. Phys. J. A* 35 (2008), 159–165.
- [40] E. Gamba, A. Bruce and M. Rudigier. “Treatment of background in γ - γ fast-timing measurements.” *Nucl. Instrum. Methods Phys. Res. A* 928 (2019), 93–103.
- [41] D. Doherty, J. Allmond, R. Janssens, W. Korten, S. Zhu, M. Zielińska, D. Radford, A. Ayangeakaa, B. Bucher, J. Batchelder, C. Beausang, C. Campbell, M. Carpenter, D. Cline, H. Crawford, H. David, J. Delaroche, C. Dickerson, P. Fallon, A. Galindo-Uribarri, F. Kondev, J. Harker, A. Hayes, M. Hendricks, P. Humby, M. Girod, C. Gross, M. Klintefjord, K. Kolos, G. Lane, T. Lauritsen, J. Libert, A. Macchiavelli, P. Napiorkowski, E. Padilla-Rodal, R. Pardo, W. Reviol, D. Sarantites, G. Savard, D. Seweryniak, J. Srebrny, R. Varner, R. Vondrasek, A. Wiens, E. Wilson, J. Wood and C. Wu. “Triaxiality near the ^{110}Ru ground state from Coulomb excitation.” *Phys. Lett. B* 766 (2017), 334–338.
- [42] A. Dewald, K. Starosta, P. Petkov, M. Hackstein, W. Rother, P. Adrich, A. M. Amthor, T. Baumann, D. Bazin, M. Bowen, A. Chester, A. Dunomes, A. Gade, D. Galaviz, T. Glasmacher, T. Ginter, M. Hausmann, J. Jolie, B. Melon, D. Miller, V. Moeller, R. P. Norris, T. Pissulla, M. Portillo, Y. Shimbara, A. Stolz, C. Vaman, P. Voss and D. Weisshaar. “Collectivity of neutron-rich palladium isotopes and the valence proton symmetry.” *Phys. Rev. C* 78 (2008), 051302.
- [43] N. Boelaert, A. Dewald, C. Fransen, J. Jolie, A. Linnemann, B. Melon, O. Möller, N. Smirnova and K. Heyde. “Low-spin electromagnetic transition probabilities in $^{102,104}\text{Cd}$.” *Phys. Rev. C* 75 (2007), 054311.
- [44] P. Federman and S. Pittel. “Hartree-Fock-Bogolyubov study of deformation in the Zr-Mo region.” *Phys. Lett. B* 77.1 (1978), 29–32.
- [45] A. Esmaylzadeh, J.-M. Régis, Y. H. Kim, U. Köster, J. Jolie, V. Karayonchev, L. Knafla, K. Nomura, L. M. Robledo and R. Rodríguez-Guzmán. “Lifetime measurements and shape coexistence in ^{97}Sr .” *Phys. Rev. C* 100 (2019), 064309.

- [46] P. Spagnoletti, G. Simpson, S. Kisiov, D. Bucurescu, J.-M. Régis, N. Saed-Samii, A. Blanc, M. Jentschel, U. Köster, P. Mutti, T. Soldner, G. de France, C. A. Ur, W. Urban, A. M. Bruce, C. Bernards, F. Drouet, L. M. Fraile, L. P. Gaffney, D. G. Ghită, S. Ilieva, J. Jolie, W. Korten, T. Kröll, S. Lalkovski, C. Larijarni, R. Lică, H. Mach, N. Mărginean, V. Pazyi, Z. Podolyák, P. H. Regan, M. Scheck, J. F. Smith, G. Thiamova, C. Townsley, A. Vancraeynest, V. Vedia, N. Warr, V. Werner and M. Zielińska. “Lifetimes and shape-coexisting states of ^{99}Zr .” *Phys. Rev. C* 100 (2019), 014311.
- [47] R. Rodríguez-Guzmán, P. Sarriguren, L. Robledo and S. Perez-Martin. “Charge radii and structural evolution in Sr, Zr, and Mo isotopes.” *Phys. Lett. B* 691.4 (2010), 202–207.
- [48] J. Dudouet, A. Lemasson, G. Duchêne, M. Rejmund, E. Clément, C. Michelagnoli, F. Didierjean, A. Korichi, G. Maquart, O. Stezowski, C. Lizarazo, R. M. Pérez-Vidal, C. Andreoiu, G. de Angelis, A. Astier, C. Delafosse, I. Deloncle, Z. Dombradi, G. de France, A. Gadea, A. Gottardo, B. Jacquot, P. Jones, T. Konstantinopoulos, I. Kuti, F. Le Blanc, S. M. Lenzi, G. Li, R. Lozeva, B. Million, D. R. Napoli, A. Navin, C. M. Petrache, N. Pietralla, D. Ralet, M. Ramdhane, N. Redon, C. Schmitt, D. Sohler, D. Verney, D. Barrientos, B. Birkenbach, I. Burrows, L. Charles, J. Collado, D. M. Cullen, P. Désesquelles, C. Domingo Pardo, V. González, L. Harkness-Brennan, H. Hess, D. S. Judson, M. Karolak, W. Korten, M. Labiche, J. Ljungvall, R. Menegazzo, D. Mengoni, A. Pullia, F. Recchia, P. Reiter, M. D. Salsac, E. Sanchis, C. Theisen, J. J. Valiente-Dobón and M. Zielińska. “ $^{96}_{36}\text{Kr}_{60}$ –Low- Z Boundary of the Island of Deformation at $N = 60$.” *Phys. Rev. Lett.* 118 (2017), 162501.
- [49] T. Thomas, K. Nomura, V. Werner, T. Ahn, N. Cooper, H. Duckwitz, M. Hinton, G. Ilie, J. Jolie, P. Petkov and D. Radeck. “Evidence for shape coexistence in ^{98}Mo .” *Phys. Rev. C* 88 (2013), 044305.
- [50] M. Zielińska, T. Czosnyka, J. Choiński, J. Iwanicki, P. Napiorkowski, J. Srebrny, Y. Toh, M. Oshima, A. Osa, Y. Utsuno, Y. Hatsukawa, J. Katakura, M. Koizumi, M. Matsuda, T. Shizuma, M. Sugawara, T. Morikawa, H. Kusakari, A. Efimov and V. Mikhajlov. “Electromagnetic structure of ^{98}Mo .” *Nucl. Phys. A* 712.1 (2002), 3–13.
- [51] R. Casten. Nuclear Structure from a Simple Perspective. Oxford Science Publications. Oxford University Press, 2000.
- [52] K. Wrzosek-Lipska, L. Próchniak, M. Zielińska, J. Srebrny, K. Hadyńska-Klęk, J. Iwanicki, M. Kisieliński, M. Kowalczyk, P. J. Napiorkowski, D. Piętak and T. Czosnyka. “Electromagnetic properties of ^{100}Mo : Experimental results and theoretical description of quadrupole degrees of freedom.” *Phys. Rev. C* 86 (2012), 064305.
- [53] A. G. Smith, J. L. Durell, W. R. Phillips, W. Urban, P. Sarriguren and I. Ahmad. “Lifetime measurements and nuclear deformation in the $A \approx 100$ region.” *Phys. Rev. C* 86 (2012), 014321.
- [54] H. Hua, C. Y. Wu, D. Cline, A. B. Hayes, R. Teng, R. M. Clark, P. Fallon, A. Goergen, A. O. Macchiavelli and K. Vetter. “Triaxiality and the aligned $h_{11/2}$ neutron orbitals in neutron-rich Zr and Mo isotopes.” *Phys. Rev. C* 69 (2004), 014317.
- [55] Y. Luo, S. Zhu, J. Hamilton, J. Rasmussen, A. Ramayya, C. Goodin, K. Li, J. Hwang, D. Almehed, S. Frauendorf, V. Dimitrov, J.-y. Zhang, X. Che, Z. Jang, I. Stefanescu, A. Gelberg, G. Ter-Akopian, A. Daniel, M. Stoyer, R. Donangelo, J. Cole and N. Stone. “Evolution of chirality from γ -soft ^{108}Ru to triaxial $^{110,112}\text{Ru}$.” *Phys. Lett. B* 670.4 (2009), 307–312.

- [56] P.-A. Söderström, G. Lorusso, H. Watanabe, S. Nishimura, P. Doornenbal, G. Thiamova, F. Browne, G. Gey, H. S. Jung, T. Sumikama, J. Taprogge, Z. Vajta, J. Wu, Z. Y. Xu, H. Baba, G. Benzoni, K. Y. Chae, F. C. L. Crespi, N. Fukuda, R. Gernhäuser, N. Inabe, T. Isobe, A. Jungclaus, D. Kameda, G. D. Kim, Y.-K. Kim, I. Kojouharov, F. G. Kondev, T. Kubo, N. Kurz, Y. K. Kwon, G. J. Lane, Z. Li, A. Montaner-Pizá, K. Moschner, F. Naqvi, M. Niikura, H. Nishibata, A. Odahara, R. Orlandi, Z. Patel, Z. Podolyák, H. Sakurai, H. Schaffner, G. S. Simpson, K. Steiger, H. Suzuki, H. Takeda, A. Wendt, A. Yagi and K. Yoshinaga. “Shape evolution in $^{116,118}\text{Ru}$: Triaxiality and transition between the $O(6)$ and $U(5)$ dynamical symmetries.” *Phys. Rev. C* 88 (2013), 024301.
- [57] I. Stefanescu, A. Gelberg, J. Jolie, P. Van Isacker, P. von Brentano, Y. Luo, S. Zhu, J. Rasmussen, J. Hamilton, A. Ramayya and X. Che. “IBM-1 description of the fission products $^{108,110,112}\text{Ru}$.” *Nucl. Phys. A* 789.1 (2007), 125–141.
- [58] A. Esmaylzadeh, V. Karayonchev, G. Häfner, J. Jolie, M. Beckers, A. Blazhev, A. Dewald, C. Fransen, A. Goldkuhle, L. Knafla and C. Müller-Gatermann. “Triaxiality in the mid-shell nucleus ^{112}Pd .” *Phys. Rev. C* 103 (2021), 054324.
- [59] N. Zamfir and R. Casten. “Signatures of γ softness or triaxiality in low energy nuclear spectra.” *Phys. Lett. B* 260.3 (1991), 265–270.
- [60] A. Davydov and G. Filippov. “Rotational states in even atomic nuclei.” *Nucl. Phys.* 8 (1958), 237–249.
- [61] A. Davydov and V. Rostovsky. “Relative transition probabilities between rotational levels of non-axial nuclei.” *Nucl. Phys.* 12.1 (1959), 58–68.
- [62] A. Davydov and V. Rostovskii. “Transition probabilities between the levels of rotational band of non-axial nuclei.” *Soviet Physics JETP* 36 (1959), 1788–1796.
- [63] L. Wilets and M. Jean. “Surface Oscillations in Even-Even Nuclei.” *Phys. Rev.* 102 (1956), 788–796.
- [64] F. Iachello and A. Arima. *The Interacting Boson Model*. Cambridge Monographs on Mathematical Physics. Cambridge University Press, 1987.
- [65] R. Casten and E. McCutchan. “Quantum phase transitions and structural evolution in nuclei.” *Journal of Physics G: Nuclear and Particle Physics* 34.7 (2007), R285.
- [66] F. Iachello and A. Arima. “Boson symmetries in vibrational nuclei.” *Phys. Lett. B* 53.4 (1974), 309–312.
- [67] A. Arima and F. Iachello. “Collective Nuclear States as Representations of a $SU(6)$ Group.” *Phys. Rev. Lett.* 35 (1975), 1069–1072.
- [68] S. Heinze. “Eine Methode zur Lösung beliebiger bosonischer und fermionischer Vielteilchensysteme.” PhD thesis. Universität zu Köln, 2008.
- [69] R. Casten. *Nuclear Structure from a Simple Perspective*. Oxford Science Publications. Oxford University Press, 2000.
- [70] K. Nomura, N. Shimizu and T. Otsuka. “Mean-Field Derivation of the Interacting Boson Model Hamiltonian and Exotic Nuclei.” *Phys. Rev. Lett.* 101 (2008), 142501.
- [71] K. Nomura, N. Shimizu and T. Otsuka. “Formulating the interacting boson model by mean-field methods.” *Phys. Rev. C* 81 (2010), 044307.
- [72] T. H. R. Skyrme. “CVII. The nuclear surface.” *Philos. Mag.* 1.11 (1956), 1043–1054.

- [73] T. Skyrme. “The spin-orbit interaction in nuclei.” *Nucl. Phys.* 9.4 (1958), 635–640.
- [74] D. Vautherin, M. Veneroni and D. Brink. “A Hartree-Fock calculation for the stability of super-heavy nuclei.” *Phys. Lett. B* 33.6 (1970), 381–384.
- [75] D. Vautherin and D. M. Brink. “Hartree-Fock Calculations with Skyrme’s Interaction. I. Spherical Nuclei.” *Phys. Rev. C* 5 (1972), 626–647.
- [76] Y. Engel, D. Brink, K. Goeke, S. Krieger and D. Vautherin. “Time-dependent hartree-fock theory with Skyrme’s interaction.” *Nucl. Phys. A* 249.2 (1975), 215–238.
- [77] D. Gogny. “Simple separable expansions for calculating matrix elements of two-body local interactions with harmonic oscillator functions.” *Nucl. Phys. A* 237.3 (1975), 399–418.
- [78] D. Gogny. Hartree-Fock Bogolyubov method with density-dependent interaction. North-Holland Publishing Company, 1973.
- [79] P. Ring and P. Schuck. The nuclear many-body problem. New York: Springer-Verlag, 1980.
- [80] J. Decharge, M. Girod and D. Gogny. “Self consistent calculations and quadrupole moments of even Sm isotopes.” *Phys. Lett. B* 55.4 (1975), 361–364.
- [81] S. Goriely, S. Hilaire, M. Girod and S. Péru. “First Gogny-Hartree-Fock-Bogoliubov Nuclear Mass Model.” *Phys. Rev. Lett.* 102 (2009), 242501.
- [82] K. Nomura, R. Rodríguez-Guzmán and L. M. Robledo. “ β decay of even- A nuclei within the interacting boson model with input based on nuclear density functional theory.” *Phys. Rev. C* 101 (2020), 044318.
- [83] K. Nomura, D. Vretenar, Z. P. Li and J. Xiang. “Coupling of pairing and triaxial shape vibrations in collective states of γ -soft nuclei.” *Phys. Rev. C* 103 (2021), 054322.
- [84] K. Nomura, R. Rodríguez-Guzmán, L. M. Robledo and J. E. García-Ramos. “Quadrupole-octupole coupling and the onset of octupole deformation in actinides.” *Phys. Rev. C* 103 (2021), 044311.
- [85] K. Nomura, T. Nikšić and D. Vretenar. “Shape phase transitions in odd- A Zr isotopes.” *Phys. Rev. C* 102 (2020), 034315.
- [86] K. Nomura, R. Rodríguez-Guzmán and L. M. Robledo. “Structure of odd-odd Cs isotopes within the interacting boson-fermion-fermion model based on the Gogny-D1M energy density functional.” *Phys. Rev. C* 101 (2020), 014306.
- [87] K. Nomura and Y. Zhang. “Two-neutron transfer reactions and shape phase transitions in the microscopically formulated interacting boson model.” *Phys. Rev. C* 99 (2019), 024324.
- [88] H. Bateman. “Solution of a system of differential equations occurring in the theory of radioactive transformation.” *Proceedings of the Cambridge Philosophical Society, Mathematical and Physical Sciences* 15 (1910), 423–427.
- [89] A. Dewald, S. Harissopulos and P. von Brentano. “The differential plunger and the differential decay curve method for the analysis of recoil distance Doppler-shift data.” *Z. Phys. A* (1989), 163–175.
- [90] J.-M. Régis, H. Mach, G. Simpson, J. Jolie, G. Pascovici, N. Saed-Samii, N. Warr, A. Bruce, J. Degenkolb, L. Fraile, C. Fransen, D. Ghita, S. Kisyov, U. Koester, A. Korgul, S. Lalkovski, N. Mărginean, P. Mutti, B. Olaizola, Z. Podolyak, P. Regan, O. Roberts,

- M. Rudigier, L. Stroe, W. Urban and D. Wilmsen. “The generalized centroid difference method for picosecond sensitive determination of lifetimes of nuclear excited states using large fast-timing arrays.” *Nucl. Instrum. Methods Phys. Res. A* 726 (2013), 191–202.
- [91] J.-M. Régis, M. Dannhoff, J. Jolie, C. Müller-Gatermann and N. Saed-Samii. “On the time response of background obtained in γ -ray spectroscopy experiments using $\text{LaBr}_3(\text{Ce})$ detectors with different shielding.” *Nucl. Instrum. Methods Phys. Res. A* 811 (2016), 42–48.
- [92] J.-M. Régis, N. Saed-Samii, M. Rudigier, S. Ansari, M. Dannhoff, A. Esmaylzadeh, C. Fransen, R.-B. Gerst, J. Jolie, V. Karayonchev, C. Müller-Gatermann and S. Stegemann. “Reduced $\gamma - \gamma$ time walk to below 50 ps using the multiplexed-start and multiplexed-stop fast-timing technique with $\text{LaBr}_3(\text{Ce})$ detectors.” *Nucl. Instrum. Methods Phys. Res. A* 823 (2016), 72–82.
- [93] J.-M. Régis, M. Dannhoff and J. Jolie. “A simple procedure for $\gamma - \gamma$ lifetime measurements using multi-element fast-timing arrays.” *Nucl. Instrum. Methods Phys. Res. A* 897 (2018), 38–46.
- [94] J.-M. Régis, A. Esmaylzadeh, J. Jolie, V. Karayonchev, L. Knafla, U. Köster, Y. Kim and E. Strub. “ $\gamma - \gamma$ fast timing at X-ray energies and investigation on various timing deviations.” *Nucl. Instrum. Methods Phys. Res. A* 955 (2020), 163258.
- [95] A. Dewald, O. Möller and P. Petkov. “Developing the Recoil Distance Doppler-Shift technique towards a versatile tool for lifetime measurements of excited nuclear states.” *Prog. Part. Nucl. Phys.* 67.3 (2012), 786–839.
- [96] T. Alexander and A. Bell. “A target chamber for recoil-distance lifetime measurements.” *Nucl. Instrum. Methods* 81.1 (1970), 22–26.
- [97] G. Böhm, A. Dewald, P. Petkov and P. von Brentano. “The differential decay curve method for the analysis of Doppler shift timing experiments.” *Nucl. Instrum. Methods Phys. Res. A* 329.1 (1993), 248–261.
- [98] J. Litzinger, A. Blazhev, A. Dewald, F. Didierjean, G. Duchêne, C. Fransen, R. Lozeva, K. Sieja, D. Verney, G. de Angelis, D. Bazzacco, B. Birkenbach, S. Bottoni, A. Bracco, T. Braunroth, B. Cederwall, L. Corradi, F. C. L. Crespi, P. Désesquelles, J. Eberth, E. Ellinger, E. Farnea, E. Fioretto, R. Gernhäuser, A. Goasduff, A. Görgen, A. Gottardo, J. Grebosz, M. Hackstein, H. Hess, F. Ibrahim, J. Jolie, A. Jungclaus, K. Kolos, W. Korten, S. Leoni, S. Lunardi, A. Maj, R. Menegazzo, D. Mengoni, C. Michelagnoli, T. Mijatovic, B. Million, O. Möller, V. Modamio, G. Montagnoli, D. Montanari, A. I. Morales, D. R. Napoli, M. Niikura, G. Pollarolo, A. Pullia, B. Quintana, F. Recchia, P. Reiter, D. Rosso, E. Sahin, M. D. Salsac, F. Scarlassara, P.-A. Söderström, A. M. Stefanini, O. Stezowski, S. Szilner, C. Theisen, J. J. Valiente Dobón, V. Vandone and A. Vogt. “Transition probabilities in neutron-rich $^{84,86}\text{Se}$.” *Phys. Rev. C* 92 (2015), 064322.
- [99] A. Esmaylzadeh. “Nuclear Structure Analysis in $^{192,194,196}\text{Hg}$ via γ - γ Fast-Timing Spectroscopy.” MA thesis. 2017.
- [100] Z. Bay. “Calculation of Decay Times from Coincidence Experiments.” *Phys. Rev.* 77 (1950), 419–419.
- [101] P. Koseoglou, V. Werner, N. Pietralla, S. Ilieva, T. Nikšić, D. Vretenar, P. Alexa, M. Thürauf, C. Bernardis, A. Blanc, A. M. Bruce, R. B. Cakirli, N. Cooper, L. M. Fraile, G. de France, M. Jentschel, J. Jolie, U. Köster, W. Korten, T. Kröll, S. Lalkovski, H. Mach,

- N. Mărginean, P. Mutti, Z. Patel, V. Pazyi, Z. Podolyák, P. H. Regan, J.-M. Régis, O. J. Roberts, N. Saed-Samii, G. S. Simpson, T. Soldner, C. A. Ur, W. Urban, D. Wilmsen and E. Wilson. “Low- Z boundary of the $N = 88$ – 90 shape phase transition: ^{148}Ce near the critical point.” *Phys. Rev. C* 101 (2020), 014303.
- [102] A. Esmaylzadeh, L. M. Gerhard, V. Karayonchev, J.-M. Régis, J. Jolie, M. Bast, A. Blazhev, T. Braunroth, M. Dannhoff, F. Dunkel, C. Fransen, G. Häfner, L. Knafla, M. Ley, C. Müller-Gatermann, K. Schomacker, N. Warr and K.-O. Zell. “Lifetime determination in $^{190,192,194,196}\text{Hg}$ via $\gamma - \gamma$ fast-timing spectroscopy.” *Phys. Rev. C* 98 (2018), 014313.
- [103] V. Karayonchev, A. Blazhev, A. Esmaylzadeh, J. Jolie, M. Dannhoff, F. Diel, F. Dunkel, C. Fransen, L. M. Gerhard, R.-B. Gerst, L. Knafla, L. Kornwebel, C. Müller-Gatermann, J.-M. Régis, N. Warr, K. O. Zell, M. Stoyanova and P. Van Isacker. “Lifetimes in ^{211}At and their implications for the nuclear structure above ^{208}Pb .” *Phys. Rev. C* 99 (2019), 024326.
- [104] C. M. Petrache, J.-M. Régis, C. Andreoiu, M. Spieker, C. Michelagnoli, P. E. Garrett, A. Astier, E. Dupont, F. Garcia, S. Guo, G. Häfner, J. Jolie, F. Kandzia, V. Karayonchev, Y.-H. Kim, L. Knafla, U. Köster, B. F. Lv, N. Mărginean, C. Mihai, P. Mutti, K. Ortner, C. Porzio, S. Prill, N. Saed-Samii, W. Urban, J. R. Vanhoy, K. Whitmore, J. Wisniewski and S. W. Yates. “Collectivity of the 2p-2h proton intruder band of ^{116}Sn .” *Phys. Rev. C* 99 (2019), 024303.
- [105] M. Stoyanova, G. Rainovski, J. Jolie, N. Pietralla, A. Blazhev, M. Beckers, A. Dewald, M. Djongolov, A. Esmaylzadeh, C. Fransen, L. M. Gerhard, K. A. Gladnishki, S. Herb, P. R. John, V. Karayonchev, J. M. Keatings, R. Kern, L. Knafla, D. Kocheva, L. Kornwebel, T. Kröll, M. Ley, K. M. Mashtakov, C. Müller-Gatermann, J.-M. Régis, M. Scheck, K. Schomacker, J. Sinclair, P. Spagnoletti, C. Sürder, N. Warr, V. Werner and J. Wiederhold. “Lifetimes of the 4_1^+ states of ^{206}Po and ^{204}Po : A study of the transition from noncollective seniority-like mode to collectivity.” *Phys. Rev. C* 100 (2019), 064304.
- [106] V. Karayonchev, M. Stoyanova, G. Rainovski, J. Jolie, A. Blazhev, M. Djongolov, A. Esmaylzadeh, C. Fransen, K. Gladnishki, L. Knafla, D. Kocheva, L. Kornwebel, J.-M. Régis, G. De Gregorio and A. Gargano. “Lifetimes and structures of low-lying negative-parity states of ^{209}Po .” *Phys. Rev. C* 103 (2021), 044309.
- [107] L. Knafla, G. Häfner, J. Jolie, J.-M. Régis, V. Karayonchev, A. Blazhev, A. Esmaylzadeh, C. Fransen, A. Goldkuhle, S. Herb, C. Müller-Gatermann, N. Warr and K. O. Zell. “Lifetime measurements of ^{162}Er : Evolution of collectivity in the rare-earth region.” *Phys. Rev. C* 102 (2020), 044310.
- [108] L. Knafla, P. Alexa, U. Köster, G. Thiamova, J.-M. Régis, J. Jolie, A. Blanc, A. M. Bruce, A. Esmaylzadeh, L. M. Fraile, G. de France, G. Häfner, S. Ilieva, M. Jentschel, V. Karayonchev, W. Korten, T. Kröll, S. Lalkovski, S. Leoni, H. Mach, N. Mărginean, P. Mutti, G. Pascovici, V. Pazyi, Z. Podolyák, P. H. Regan, O. J. Roberts, N. Saed-Samii, G. S. Simpson, J. F. Smith, T. Soldner, C. Townsley, C. A. Ur, W. Urban, A. Vancraeynest and N. Warr. “Lifetime measurements in the odd- A nucleus ^{177}Hf .” *Phys. Rev. C* 102 (2020), 054322.
- [109] Characteristics of the Lohengrin spectrometer. Accessed: 02.06.2022. URL: <https://www.iill.eu/users/instruments/instruments-list/pn1/characteristics>.
- [110] M. Rudigier. “Nuclear structure studies of odd-odd and odd- A nuclei in the shape transition region around $N = 60$.” PhD thesis. Universität zu Köln, 2013.

- [111] P. Armbruster, M. Asghar, J. Bocquet, R. Decker, H. Ewald, J. Greif, E. Moll, B. Pfeiffer, H. Schrader, F. Schussler, G. Siegert and H. Wollnik. “The recoil separator Lohengrin: Performance and special features for experiments.” *Nucl. Instrum. Methods* 139 (1976), 213–222.
- [112] G. Fioni, H. Faust, M. Gross, M. Hesse, P. Armbruster, F. Gönnerwein and G. Münzenberg. “Reduction of energy dispersion on a parabola mass spectrometer.” *Nucl. Instrum. Methods Phys. Res. A* 332.1 (1993), 175–180.
- [113] A. Złomaniec, H. Faust, J. Genevey, J. A. Pinston, T. Rzaca-Urban, G. S. Simpson, I. Tsekhanovich and W. Urban. “Half-life of the 830.2 keV isomer in ^{97}Sr .” *Phys. Rev. C* 72 (2005), 067302.
- [114] D. Kameda, T. Kubo, T. Ohnishi, K. Kusaka, A. Yoshida, K. Yoshida, M. Ohtake, N. Fukuda, H. Takeda, K. Tanaka, N. Inabe, Y. Yanagisawa, Y. Gono, H. Watanabe, H. Otsu, H. Baba, T. Ichihara, Y. Yamaguchi, M. Takechi, S. Nishimura, H. Ueno, A. Yoshimi, H. Sakurai, T. Motobayashi, T. Nakao, Y. Mizoi, M. Matsushita, K. Ieki, N. Kobayashi, K. Tanaka, Y. Kawada, N. Tanaka, S. Deguchi, Y. Satou, Y. Kondo, T. Nakamura, K. Yoshinaga, C. Ishii, H. Yoshii, Y. Miyashita, N. Uematsu, Y. Shiraki, T. Sumikama, J. Chiba, E. Ideguchi, A. Saito, T. Yamaguchi, I. Hachiuma, T. Suzuki, T. Moriguchi, A. Ozawa, T. Ohtsubo, M. A. Famiano, H. Geissel, A. S. Nettleton, O. B. Tarasov, D. Bazin, B. M. Sherrill, S. L. Manikonda and J. A. Nolen. “Observation of new microsecond isomers among fission products from in-flight fission of 345 MeV/nucleon ^{238}U .” *Phys. Rev. C* 86 (2012), 054319.
- [115] M. Rudigier, G. S. Simpson, J. M. Daugas, A. Blazhev, C. Fransen, G. Gey, M. Hackstein, J. Jolie, U. Köster, T. Malkiewicz, T. Materna, M. Pfeiffer, M. Ramdhane, J.-M. Régis, W. Rother, T. Thomas, N. Warr, D. Wilmsen, J. Le Bloas and N. Pillet. “Delayed γ -ray and conversion-electron spectroscopy of $A = 97$ fission fragments.” *Phys. Rev. C* 87 (2013), 064317.
- [116] K.-L. Kratz, H. Ohm, A. Schröder, H. Gabelmann, W. Ziegert, B. Pfeiffer, G. Jung, E. Monnard, J. A. Pinston, F. Schussler, G. I. Crawford, S. G. Prussin and Z. M. de Oliveira. “The β -decay of ^{95}Rb and ^{97}Rb .” *Z. Phys. A* 312.1 (1983), 43–57.
- [117] M. Czerwiński, T. Rząca-Urban, W. Urban, P. Bączyk, K. Sieja, B. M. Nyakó, J. Timár, I. Kuti, T. G. Tornyi, L. Atanasova, A. Blanc, M. Jentschel, P. Mutti, U. Köster, T. Soldner, G. de France, G. S. Simpson and C. A. Ur. “Neutron-proton multiplets in the nucleus ^{88}Br .” *Phys. Rev. C* 92 (2015), 014328.
- [118] J. K. Hwang, A. V. Ramayya, J. H. Hamilton, Y. X. Luo, A. V. Daniel, G. M. Ter-Akopian, J. D. Cole and S. J. Zhu. “Half-life measurements of several states in $^{95,97}\text{Sr}$, $^{97,100,104}\text{Zr}$, ^{106}Mo , and ^{148}Ce .” *Phys. Rev. C* 73 (2006), 044316.
- [119] F. Schussler, J. Pinston, E. Monnard, A. Moussa, G. Jung, E. Koglin, B. Pfeiffer, R. Janssens and J. van Klinken. “Discovery of a very low-lying 0^+ state in ^{98}Sr and shape coexistence implication in ^{98}Sr .” *Nucl. Phys. A* 339.3 (1980), 415–428.
- [120] K. Nomura, R. Rodríguez-Guzmán and L. M. Robledo. “Structural evolution in $A \approx 100$ nuclei within the mapped interacting boson model based on the Gogny energy density functional.” *Phys. Rev. C* 94 (2016), 044314.
- [121] S. Lalkovski, A. Minkova, M.-G. Porquet, A. Bauchet, I. Deloncle, A. Astier, N. Buforn, L. Donadille, O. Dorvaux, B. Gall, R. Lucas, M. Meyer, A. Prevost, N. Redon, N. Schulz

- and O. Stézowski. “Two-quasiparticle and collective excitations in transitional $^{108,110}\text{Pd}$ nuclei.” *Eur. Phys. J. A* 18 (2003), 589–596.
- [122] E. A. Stefanova, S. Lalkovski, A. Korichi, T. Kutsarova, A. Lopez-Martens, F. R. Xu, H. L. Liu, S. Kisiov, A. Minkova, D. Bazzacco, M. Bergström, A. Görgen, F. Hannachi, B. Herskind, H. Hübel, A. Jansen, T. L. Khoo, Z. Podolyák and G. Schönwasser. “Observation of positive-parity bands in ^{109}Pd and ^{111}Pd : Enhanced γ softness.” *Phys. Rev. C* 86 (2012), 044302.
- [123] J. Ginocchio and M. Kirson. “An intrinsic state for the interacting boson model and its relationship to the Bohr-Mottelson model.” *Nucl. Phys. A* 350.1 (1980), 31–60.
- [124] A. Pfeil. “Lifetime measurements in the region $A = 99$ via γ - γ fast-timing spectroscopy.” MA thesis. 2022.
- [125] C. Michelagnoli. private communication. 2018.
- [126] S. Basu, G. Mukherjee and A. Sonzogni. “Nucl. Data Sheets for $A = 95$.” *Nucl. Data Sheets* 111.10 (2010), 2555–2737.
- [127] W. Urban, M. Czerwiński, J. Kurpeta, T. Rząca-Urban, J. Wiśniewski, T. Materna, Ł. W. Iskra, A. G. Smith, I. Ahmad, A. Blanc, H. Faust, U. Köster, M. Jentschel, P. Mutti, T. Soldner, G. S. Simpson, J. A. Pinston, G. de France, C. A. Ur, V.-V. Elomaa, T. Eronen, J. Hakala, A. Jokinen, A. Kankainen, I. D. Moore, J. Rissanen, A. Saastamoinen, J. Szerypo, C. Weber and J. Äystö. “Shape coexistence in the odd-odd nucleus ^{98}Y : The role of the $g_{9/2}$ neutron extruder.” *Phys. Rev. C* 96 (2017), 044333.
- [128] Ł. W. Iskra, S. Leoni, B. Fornal, C. Michelagnoli, F. Kandzia, N. Mărginean, M. Barani, S. Bottoni, N. Cieplicka-Oryńczak, G. Colombi, C. Costache, F. C. L. Crespi, J. Dudouet, M. Jentschel, Y. H. Kim, U. Köster, R. Lica, R. Mărginean, C. Mihai, R. E. Mihai, C. R. Nita, S. Pascu, C. Porzio, D. Reygadas, E. Ruiz-Martinez and A. Turturica. “ γ spectroscopy of the ^{96}Y isotope: Searching for the onset of shape coexistence before $N = 60$.” *Phys. Rev. C* 102 (2020), 054324.
- [129] A. Petrovici and A. S. Mare. “Triple shape coexistence and β decay of ^{96}Y to ^{96}Zr .” *Phys. Rev. C* 101 (2020), 024307.
- [130] T. W. Hagen, A. Görgen, W. Korten, L. Greife, M.-D. Salsac, F. Farget, I. Ragnarsson, T. Braunroth, B. Bruyneel, I. Celikovic, E. Clément, G. de France, O. Delaune, A. Dewald, A. Dijon, M. Hackstein, B. Jacquot, J. Litzinger, J. Ljungvall, C. Louchart, C. Michelagnoli, D. R. Napoli, F. Recchia, W. Rother, E. Sahin, S. Siem, B. Sulignano, C. Theisen and J. J. Valiente-Dobon. “Evolution of nuclear shapes in odd-mass yttrium and niobium isotopes from lifetime measurements following fission reactions.” *Phys. Rev. C* 95 (2017), 034302.
- [131] C. Michelagnoli, A. Blanc, E. Ruiz-Martinez, A. Chebboubi, H. Faust, E. Froidefond, G. Kessedjian, M. Jentschel, U. Köster, P. Mutti and G. Simpson. “FIPPS (Fission Product Prompt Spectrometer) and its first experimental campaign.” *EPJ Web Conf.* 193 (2018), 04009.
- [132] J. Blachot. “Nuclear Data Sheets for $A = 101$.” *Nucl. Data Sheets* 83.1 (1998), 1–144.
- [133] H. Mach, R. Gill and M. Moszyński. “A method for picosecond lifetime measurements for neutron-rich nuclei: (1) Outline of the method.” *Nucl. Instrum. Methods Phys. Res. A* 280.1 (1989), 49–72.

- [134] L. Bettermann, J.-M. Régis, T. Materna, J. Jolie, U. Köster, K. Moschner and D. Radeck. “Lifetime measurement of excited states in the shape-phase-transitional nucleus ^{98}Zr .” *Phys. Rev. C* 82 (2010), 044310.
- [135] S. Mughabghab, ed. Recommended Thermal Cross Sections, Resonance Properties, and Resonance Parameters for $Z = 1-60$. Sixth Edition. Amsterdam: Elsevier, 2018, pp. 89–822.
- [136] M. Beckers, C. Müller-Gatermann, A. Blazhev, T. Braunroth, A. Dewald, C. Fransen, A. Goldkuhle, L. Kornwebel, J. Litzinger, F. von Spee and K.-O. Zell. “Lifetime measurement of excited states in ^{144}Ce : Enhanced $E1$ strengths in a candidate for octupole deformation.” *Phys. Rev. C* 102 (2020), 014324.
- [137] A. Esmaylzadeh, A. Blazhev, K. Nomura, J. Jolie, M. Beckers, C. Fransen, R.-B. Gerst, A. Harter, V. Karayonchev, L. Knafla, M. Ley and F. von Spee. “Investigation of γ -softness: Lifetime measurements in $^{104,106}\text{Ru}$.” *submitted to Phys. Rev. C* (2022).
- [138] D. Fossan and E. Warburton. “VII.H - Lifetime Measurements.” *Nuclear Spectroscopy and Reactions, Part C*. Ed. by J. CERNEY. Vol. 40. Pure and Applied Physics. Elsevier, 1974, pp. 307–374.
- [139] P. J. Nolan and J. F. Sharpey-Schafer. “The measurement of the lifetimes of excited nuclear states.” *Rep. Prog. Phys.* 42.1 (1979), 1–86.
- [140] A. Arima, T. Ohtsuka, F. Iachello and I. Talmi. “Collective nuclear states as symmetric couplings of proton and neutron excitations.” *Phys. Lett. B* 66.3 (1977), 205–208.
- [141] F. Iachello. “Electron scattering in the interacting boson model.” *Nucl. Phys. A* 358 (1981), 89–112.
- [142] T. Otsuka, A. Arima and F. Iachello. “Nuclear shell model and interacting bosons.” *Nucl. Phys. A* 309.1 (1978), 1–33.
- [143] K. Moschner, A. Blazhev, J. Jolie, N. Warr, P. Boutachkov, P. Bednarczyk, K. Sieja, A. Algora, F. Ameil, M. A. Bentley, S. Brambilla, N. Braun, F. Camera, J. Cederkäll, A. Corsi, M. Danchev, D. DiJulio, C. Fahlander, J. Gerl, A. Giaz, P. Golubev, M. Górska, J. Grebosz, T. Habermann, M. Hackstein, R. Hoischen, I. Kojouharov, N. Kurz, N. Mărginean, E. Merchán, T. Möller, F. Naqvi, B. S. Nara Singh, C. Nociforo, N. Pietralla, S. Pietri, Z. Podolyák, A. Prochazka, M. Reese, P. Reiter, M. Rudigier, D. Rudolph, T. Sava, H. Schaffner, L. Scruton, J. Taprogge, T. Thomas, H. Weick, A. Wendt, O. Wieland and H.-J. Wollersheim. “Relativistic Coulomb excitation of ^{88}Kr .” *Phys. Rev. C* 94 (2016), 054323.
- [144] D. Mücher, J. Iwanicki, J. Jolie, I. Stefanescu, J. Van de Walle, F. Becker, U. Bergmann, A. Blazhev, E. Bouchez, P. Butler, J. Cederkäll, T. Czosnyka, T. Davinson, J. Eberth, T. Faestermann, S. Franchoo, C. Fransen, J. Gerl, R. Gernhäuser, D. Habs, R.-D. Herzberg, M. Huyse, D. Jenkins, G. Jones, O. Kester, W. Korten, J. Kownacki, T. Kröll, R. Krücken, Z. Liu, S. Mandal, P. Napiorkowski, T. Nilsson, N. Pietralla, G. Rainovski, H. Scheit, A. Scherillo, D. Schwalm, T. Sieber, C. Theisen, P. Van Duppen, N. Warr, D. Weisshaar, F. Wenander, B. Wolf, P. Woods and M. Zielinska. “Shell Structure and Shape Changes in Neutron Rich Krypton Isotopes.” *AIP Conf. Proc.* 1090.1 (2009), 587–588.
- [145] H. Mach, F. Wohn, G. Molnár, K. Sistemich, J. C. Hill, M. Moszyński, R. Gill, W. Krips and D. Brenner. “Retardation of $B(E2; 0_1^+ \rightarrow 2_1^+)$ rates in $^{90-96}\text{Sr}$ and strong subshell closure effects in the $A \sim 100$ region.” *Nucl. Phys. A* 523.2 (1991), 197–227.

- [146] E. Elhami, J. N. Orce, S. Mukhopadhyay, S. N. Choudry, M. Scheck, M. T. McEllistrem and S. W. Yates. “Anomalous behavior of the 2^+ mixed-symmetry state in ^{94}Zr .” *Phys. Rev. C* 75 (2007), 011301.
- [147] V. Werner, D. Belic, P. von Brentano, C. Fransen, A. Gade, H. von Garrel, J. Jolie, U. Kneissl, C. Kohstall, A. Linnemann, A. Lisetskiy, N. Pietralla, H. Pitz, M. Scheck, K.-H. Speidel, F. Stedile and S. Yates. “Proton–neutron structure of the $N = 52$ nucleus ^{92}Zr .” *Phys. Lett. B* 550.3 (2002), 140–146.
- [148] N. Pietralla, C. Fransen, P. von Brentano, A. Dewald, A. Fitzler, C. Friessner and J. Gableske. “Proton-Neutron Mixed-Symmetry 3_{ms}^+ State in ^{94}Mo .” *Phys. Rev. Lett.* 84 (2000), 3775–3778.
- [149] C. Fransen, N. Pietralla, P. von Brentano, A. Dewald, J. Gableske, A. Gade, A. Lisetskiy and V. Werner. “First observation of a mixed-symmetry two-Q-phonon $2_{2,\text{ms}}^+$ state in ^{94}Mo .” *Phys. Lett. B* 508.3 (2001), 219–224.
- [150] C. Fransen, N. Pietralla, Z. Ammar, D. Bandyopadhyay, N. Boukharouba, P. von Brentano, A. Dewald, J. Gableske, A. Gade, J. Jolie, U. Kneissl, S. R. Leshner, A. F. Lisetskiy, M. T. McEllistrem, M. Merrick, H. H. Pitz, N. Warr, V. Werner and S. W. Yates. “Comprehensive studies of low-spin collective excitations in ^{94}Mo .” *Phys. Rev. C* 67 (2003), 024307.
- [151] H. Klein, A. F. Lisetskiy, N. Pietralla, C. Fransen, A. Gade and P. von Brentano. “Proton-neutron mixed-symmetry 2_{ms}^+ and 3_{ms}^+ states in ^{96}Ru .” *Phys. Rev. C* 65 (2002), 044315.
- [152] N. Pietralla, C. J. Barton, R. Krücken, C. W. Beausang, M. A. Caprio, R. F. Casten, J. R. Cooper, A. A. Hecht, H. Newman, J. R. Novak and N. V. Zamfir. “Coulomb excitation of the 2_{ms}^+ state of ^{96}Ru in inverse kinematics.” *Phys. Rev. C* 64 (2001), 031301.
- [153] A. Hennig, T. Ahn, V. Anagnostatou, A. Blazhev, N. Cooper, V. Derya, M. Elvers, J. Endres, P. Goddard, A. Heinz, R. O. Hughes, G. Ilie, M. N. Mineva, P. Petkov, S. G. Pickstone, N. Pietralla, D. Radeck, T. J. Ross, D. Savran, M. Spieker, V. Werner and A. Zilges. “Collective excitations of ^{96}Ru by means of $(p, p'\gamma)$ experiments.” *Phys. Rev. C* 92 (2015), 064317.
- [154] C. Fransen, A. Blazhev, A. Dewald, J. Jolie, D. Muecher, O. Möller and T. Pissulla. “Collectivity of ^{98}Pd .” *AIP Conf. Proc.* 1090.1 (2009), 529–533.
- [155] V. Karayonchev. private communication. 2022.
- [156] J. Ott, C. Doll, T. von Egidy, R. Georgii, M. Grinberg, W. Schauer, R. Schwengner and H.-F. Wirth. “The nuclear structure of ^{126}Te studied with (d,p) , $(d,^3\text{He})$ and (d,d) reactions.” *Nucl. Phys. A* 625.3 (1997), 598–620.
- [157] W. Schauer, C. Doll, T. von Egidy, R. Georgii, J. Ott, H.-F. Wirth, A. Gollwitzer, G. Graw, R. Hertenberger, B. Valnion, M. Grinberg and C. Stoyanov. “Study of ^{122}Te with charged particle reactions.” *Nucl. Phys. A* 652.4 (1999), 339–369.
- [158] J. R. Vanhoy, J. A. Tanyi, K. A. Crandell, T. H. Churchill, S. F. Hicks, M. C. Burns, P. A. Roddy, N. V. Warr, T. B. Brown and S. R. Leshner. “Lifetimes in ^{126}Te from in-beam $(n, n'\gamma)$ measurements.” *Phys. Rev. C* 69 (2004), 064323.
- [159] S. F. Hicks, G. K. Alexander, C. A. Aubin, M. C. Burns, C. J. Collard, M. M. Walbran, J. R. Vanhoy, E. Jensen, P. E. Garrett, M. Kadi, A. Martin, N. Warr and S. W. Yates.

- “Intruder structures observed in ^{122}Te through inelastic neutron scattering.” *Phys. Rev. C* 71 (2005), 034307.
- [160] S. F. Hicks, J. R. Vanhoy and S. W. Yates. “Fragmentation of mixed-symmetry excitations in stable even-even tellurium nuclei.” *Phys. Rev. C* 78 (2008), 054320.
- [161] R. Nojarov and A. Faessler. “A collective model for isovector quadrupole vibrations.” *J. Phys. G* 13.3 (1987), 337–355.
- [162] R. Schwengner, G. Winter, W. Schauer, M. Grinberg, F. Becker, P. von Brentano, J. Eberth, J. Enders, T. von Egidy, R.-D. Herzberg, N. Huxel, L. Käubler, P. von Neumann-Cosel, N. Nicolay, J. Ott, N. Pietralla, H. Prade, S. Raman, J. Reif, A. Richter, C. Schlegel, H. Schnare, T. Servene, S. Skoda, T. Steinhardt, C. Stoyanov, H. Thomas, I. Wiedenhöver and A. Zilges. “Two-phonon $J = 1$ states in even-mass Te isotopes with $A = 122\text{--}130$.” *Nucl. Phys. A* 620.3 (1997), 277–295.
- [163] A. Subber, W. D. Hamilton, P. Park and K. Kumar. “An application of the dynamic deformation model to the tellurium isotopes.” *J. Phys. G* 13.2 (1987), 161–175.
- [164] J. Rikovska, N. Stone, P. Walker and W. Walters. “Intruder states in even-even Te nuclei.” *Nucl. Phys. A* 505.2 (1989), 145–172.
- [165] S. F. Hicks, A. E. Stuchbery, T. H. Churchill, D. Bandyopadhyay, B. R. Champine, B. J. Coombes, C. M. Davoren, J. C. Ellis, W. M. Faulkner, S. R. Leshner, J. M. Mueller, S. Mukhopadhyay, J. N. Orce, M. D. Skubis, J. R. Vanhoy and S. W. Yates. “Nuclear structure of ^{130}Te from inelastic neutron scattering and shell model analysis.” *Phys. Rev. C* 105 (2022), 024329.
- [166] P. E. Garrett, T. R. Rodríguez, A. D. Varela, K. L. Green, J. Bangay, A. Finlay, R. A. E. Austin, G. C. Ball, D. S. Bandyopadhyay, V. Bildstein, S. Colosimo, D. S. Cross, G. A. Demand, P. Finlay, A. B. Garnsworthy, G. F. Grinyer, G. Hackman, B. Jigmeddorj, J. Jolie, W. D. Kulp, K. G. Leach, A. C. Morton, J. N. Orce, C. J. Pearson, A. A. Phillips, A. J. Radich, E. T. Rand, M. A. Schumaker, C. E. Svensson, C. Sumithrarachchi, S. Triambak, N. Warr, J. Wong, J. L. Wood and S. W. Yates. “Multiple Shape Coexistence in $^{110,112}\text{Cd}$.” *Phys. Rev. Lett.* 123 (2019), 142502.
- [167] P. E. Garrett, T. R. Rodríguez, A. Diaz Varela, K. L. Green, J. Bangay, A. Finlay, R. A. E. Austin, G. C. Ball, D. S. Bandyopadhyay, V. Bildstein, S. Colosimo, D. S. Cross, G. A. Demand, P. Finlay, A. B. Garnsworthy, G. F. Grinyer, G. Hackman, B. Jigmeddorj, J. Jolie, W. D. Kulp, K. G. Leach, A. C. Morton, J. N. Orce, C. J. Pearson, A. A. Phillips, A. J. Radich, E. T. Rand, M. A. Schumaker, C. E. Svensson, C. Sumithrarachchi, S. Triambak, N. Warr, J. Wong, J. L. Wood and S. W. Yates. “Shape coexistence and multiparticle-multihole structures in $^{110,112}\text{Cd}$.” *Phys. Rev. C* 101 (2020), 044302.
- [168] J. McGrory and T. Kuo. “Shell model calculations of two to four identical-“particle” systems near ^{208}Pb .” *Nucl. Phys. A* 247.2 (1975), 283–316.
- [169] E. K. Warburton and B. A. Brown. “Appraisal of the Kuo-Herling shell-model interaction and application to $A=210\text{--}212$ nuclei.” *Phys. Rev. C* 43 (1991), 602–617.
- [170] L. Coraggio, A. Covello, A. Gargano, N. Itaco and T. T. S. Kuo. “Bonn potential and shell-model calculations for $^{206,205,204}\text{Pb}$.” *Phys. Rev. C* 58 (1998), 3346–3350.
- [171] E. Caurier, M. Rejmund and H. Grawe. “Large-scale shell model calculations for the $N = 126$ isotones Po–Pu.” *Phys. Rev. C* 67 (2003), 054310.

- [172] D. Kocheva, G. Rainovski, J. Jolie, N. Pietralla, A. Blazhev, A. Astier, R. Altenkirch, S. Ansari, T. Braunroth, M. L. Cortés, A. Dewald, F. Diel, M. Djongolov, C. Fransen, K. Gladnishki, A. Hennig, V. Karayonchev, J. M. Keatings, E. Kluge, J. Litzinger, C. Müller-Gatermann, P. Petkov, M. Rudigier, M. Scheck, P. Scholz, P. Spagnoletti, M. Spieker, C. Stahl, R. Stegmann, M. Stoyanova, P. Thöle, N. Warr, V. Werner, W. Witt, D. Wölk, K. O. Zell, P. Van Isacker and V. Y. Ponomarev. “A revised $B(E2; 2_1^+ \rightarrow 0_1^+)$ value in the semi-magic nucleus ^{210}Po .” *Eur. Phys. J. A* 53.9 (2017), 175.
- [173] D. Kocheva, G. Rainovski, J. Jolie, N. Pietralla, A. Blazhev, R. Altenkirch, S. Ansari, A. Astier, M. Bast, M. Beckers, T. Braunroth, M. Cappellazzo, A. Dewald, F. Diel, M. Djongolov, C. Fransen, K. Gladnishki, A. Goldkuhle, A. Hennig, V. Karayonchev, J. M. Keatings, E. Kluge, T. Kröll, J. Litzinger, K. Moschner, C. Müller-Gatermann, P. Petkov, M. Scheck, P. Scholz, T. Schmidt, P. Spagnoletti, C. Stahl, R. Stegmann, A. Stolz, A. Vogt, N. Warr, V. Werner, D. Wölk, J. C. Zamora, K. O. Zell, V. Y. Ponomarev and P. Van Isacker. “Low collectivity of the 2_1^+ state of ^{212}Po .” *Phys. Rev. C* 96 (2017), 044305.
- [174] P. E. Garrett, W. D. Kulp, J. L. Wood, D. Bandyopadhyay, S. Choudry, D. Dashdorj, S. R. Leshner, M. T. McEllistrem, M. Mynk, J. N. Orce and S. W. Yates. “New Features of Shape Coexistence in ^{152}Sm .” *Phys. Rev. Lett.* 103 (2009), 062501.
- [175] W. D. Kulp, J. L. Wood, P. E. Garrett, C. Y. Wu, D. Cline, J. M. Allmond, D. Bandyopadhyay, D. Dashdorj, S. N. Choudry, A. B. Hayes, H. Hua, M. G. Mynk, M. T. McEllistrem, C. J. McKay, J. N. Orce, R. Teng and S. W. Yates. “Search for intrinsic collective excitations in ^{152}Sm .” *Phys. Rev. C* 77 (2008), 061301.
- [176] P. A. Butler and W. Nazarewicz. “Intrinsic reflection asymmetry in atomic nuclei.” *Rev. Mod. Phys.* 68 (1996), 349–421.
- [177] N. Pietralla and O. M. Gorbachenko. “Evolution of the “ β excitation” in axially symmetric transitional nuclei.” *Phys. Rev. C* 70 (2004), 011304.
- [178] P. J. R. Mason, Z. Podolyák, N. Mărginean, P. H. Regan, P. D. Stevenson, V. Werner, T. Alexander, A. Algora, T. Alharbi, M. Bowry, R. Britton, A. M. Bruce, D. Bucurescu, M. Bunce, G. C ăta-Danil, I. C ăta-Danil, N. Cooper, D. Deleanu, D. Delion, D. Filipescu, W. Gelletly, D. Ghi ț ă, I. Gheorghe, T. Glodariu, G. Ilie, D. Ivanova, S. Kisiov, S. Lalkovski, R. Lica, S. N. Liddick, R. Mărginean, C. Mihai, K. Mulholland, C. R. Nita, A. Negret, S. Pascu, S. Rice, O. J. Roberts, T. Sava, J. F. Smith, P.-A. Söderström, L. Stroe, G. Suliman, R. Suvaila, S. Toma, C. Townsley, E. Wilson, R. T. Wood, M. Zhekova and C. Zhou. “Half-life of the yrast 2^+ state in ^{188}W : Evolution of deformation and collectivity in neutron-rich tungsten isotopes.” *Phys. Rev. C* 88 (2013), 044301.
- [179] V. S. Prasher, A. J. Mitchell, C. J. Lister, P. Chowdhury, L. Afanasieva, M. Albers, C. J. Chiara, M. P. Carpenter, D. Cline, N. D’Olympia, C. J. Guess, A. B. Hayes, C. R. Hoffman, R. V. F. Janssens, B. P. Kay, T. L. Khoo, A. Korichi, T. Lauritsen, E. Merchan, Y. Qiu, D. Seweryniak, R. Shearman, S. K. Tandel, A. Verras, C. Y. Wu and S. Zhu. “Shapes, softness, and nonyrast collectivity in ^{186}W .” *Phys. Rev. C* 104 (2021), 044318.
- [180] L. M. Robledo, R. Rodríguez-Guzmán and P. Sarriguren. “Role of triaxiality in the ground-state shape of neutron-rich Yb, Hf, W, Os and Pt isotopes.” *Journal of Physics G: Nuclear and Particle Physics* 36.11 (2009), 115104.
- [181] V. Karayonchev et al. “New aspects of the low-energy structure of ^{211}At .” *submitted to Phys. Rev. C* (2022).

List of Figures

1	Partial chart of nuclei for the region of interest	4
2	The energies of the first excited 2_1^+ states for the even-even nuclei with $Z = 38 - 46$ and $N = 52 - 68$	5
3	Schematic representation of two possible coexisting configurations in ^{98}Zr	6
4	Comparison of the staggering parameter $S(J)$ for the Davydov-Filippov model (D-F) with $\gamma = 30^\circ$ and the Wilets-Jean model (γ -soft).	10
5	The Casten triangle	12
6	Contour plot of the deformation-energy surface in the (β, γ) plane for ^{102}Mo computed with the constrained HFB method by using the Gogny functional D1M (left) and with the mapped IBM (right).	14
7	Schematic picture of a RDDS setup using particle detectors at the Cologne facility.	16
8	Schematic drawing of a fast-timing setup with two $\text{LaBr}_3(\text{Ce})$ detectors.	19
9	Schematic drawing of the delayed and anti-delayed time distributions generated by the fast-timing setup shown in Fig. 8.	19
10	The prompt response difference (PRD) curve obtained using ^{152}Eu , ^{133}Ba and ^{207}Bi sources.	20
11	Plunger setup components	22
12	Schematic top view (top) and side view (bottom) of the Lohengrin mass spectrometer.	24

List of publications

Publications in refereed journals

- [1] J.-M. Régis, N. Saed-Samii, M. Rudigier, S. Ansari, M. Dannhoff, A. Esmaylzadeh, C. Fransen, R.-B. Gerst, J. Jolie, V. Karayonchev, C. Müller-Gatermann and S. Stegemann.
Reduced γ - γ time walk to below 50 ps using the multiplexed-start and multiplexed-stop fast-timing technique with LaBr₃(Ce) detectors.
Nucl. Instrum. Methods Phys. Res. A 823 (2016), 72–82.
- [2] V. Karayonchev, J.-M. Régis, J. Jolie, A. Blazhev, R. Altenkirch, S. Ansari, M. Dannhoff, F. Diel, A. Esmaylzadeh, C. Fransen, R.-B. Gerst, K. Moschner, C. Müller-Gatermann, N. Saed-Samii, S. Stegemann, N. Warr and K. O. Zell.
Evolution of collectivity in the $N = 100$ isotones near ^{170}Yb .
Phys. Rev. C 95 (2017), 034316.
- [3] A. Esmaylzadeh, L. M. Gerhard, V. Karayonchev, J.-M. Régis, J. Jolie, M. Bast, A. Blazhev, T. Braunroth, M. Dannhoff, F. Dunkel, C. Fransen, G. Häfner, L. Knafla, M. Ley, C. Müller-Gatermann, K. Schomacker, N. Warr and K.-O. Zell.
Lifetime determination in $^{190,192,194,196}\text{Hg}$ via $\gamma - \gamma$ fast-timing spectroscopy.
Phys. Rev. C 98 (2018), 014313.
- [4] V. Karayonchev, A. Blazhev, A. Esmaylzadeh, J. Jolie, M. Dannhoff, F. Diel, F. Dunkel, C. Fransen, L. M. Gerhard, R.-B. Gerst, L. Knafla, L. Kornwebel, C. Müller-Gatermann, J.-M. Régis, N. Warr, K. O. Zell, M. Stoyanova and P. Van Isacker.
Lifetimes in ^{211}At and their implications for the nuclear structure above ^{208}Pb .
Phys. Rev. C 99 (2019), 024326.
- [5] L. Kaya, A. Vogt, P. Reiter, M. Siciliano, N. Shimizu, Y. Utsuno, H.-K. Wang, A. Gargano, L. Coraggio, N. Itaco, K. Arnsward, D. Bazzacco, B. Birkenbach, A. Blazhev, A. Bracco, B. Bruyneel, L. Corradi, F. C. L. Crespi, G. de Angelis, M. Droste, J. Eberth, A. Esmaylzadeh, E. Farnea, E. Fioretto, C. Fransen, A. Gadea, A. Giaz, A. Görgen, A. Gottardo, K. Hadyńska-Klęk, H. Hess, R. Hirsch, P. R. John, J. Jolie, A. Jungclaus, V. Karayonchev, L. Kornwebel, W. Korten, S. Leoni, L. Lewandowski, S. Lunardi, R. Menegazzo, D. Mengoni, C. Michelagnoli, T. Mijatović, G. Montagnoli, D. Montanari, C. Müller-Gatermann, D. Napoli, Z. Podolyák, G. Pollarolo, F. Recchia, J.-M. Régis, N. Saed-Samii, E. Şahin, F. Scarlassara, K. Schomacker, M. Seidlitz, B. Siebeck, P.-A. Söderström, A. M. Stefanini, O. Stezowski, S. Szilner, B. Szpak, E. Teruya, C. Ur, J. J. Valiente-Dobón, K. Wolf, K. Yanase, N. Yoshinaga and K. O. Zell.
Isomer spectroscopy in ^{133}Ba and high-spin structure of ^{134}Ba .
Phys. Rev. C 100 (2019), 024323.
- [6] M. Stoyanova, G. Rainovski, J. Jolie, N. Pietralla, A. Blazhev, M. Beckers, A. Dewald, M. Djongolov, A. Esmaylzadeh, C. Fransen, L. M. Gerhard, K. A. Gladnishki, S. Herb, P. R. John, V. Karayonchev, J. M. Keatings, R. Kern, L. Knafla, D. Kocheva, L. Kornwebel, T. Kröll, M. Ley, K. M. Mashtakov, C. Müller-Gatermann, J.-M. Régis, M. Scheck, K. Schomacker, J. Sinclair, P. Spagnoletti, C. Sürder, N. Warr, V. Werner and J. Wiederhold.
Lifetimes of the 4_1^+ states of ^{206}Po and ^{204}Po : A study of the transition from

- noncollective seniority-like mode to collectivity.**
Phys. Rev. C 100 (2019), 064304.
- [7] A. Esmaylzadeh, J.-M. Régis, Y. H. Kim, U. Köster, J. Jolie, V. Karayonchev, L. Knafla, K. Nomura, L. M. Robledo and R. Rodríguez-Guzmán.
Lifetime measurements and shape coexistence in ^{97}Sr .
Phys. Rev. C 100 (2019), 064309.
- [8] J.-M. Régis, A. Esmaylzadeh, J. Jolie, V. Karayonchev, L. Knafla, U. Köster, Y. Kim and E. Strub.
 γ - γ fast timing at X-ray energies and investigation on various timing deviations.
Nucl. Instrum. Methods Phys. Res. A 955 (2020), 163258.
- [9] L. Knafla, G. Häfner, J. Jolie, J.-M. Régis, V. Karayonchev, A. Blazhev, A. Esmaylzadeh, C. Fransen, A. Goldkuhle, S. Herb, C. Müller-Gatermann, N. Warr and K. O. Zell.
Lifetime measurements of ^{162}Er : Evolution of collectivity in the rare-earth region.
Phys. Rev. C 102 (2020), 044310.
- [10] L. Knafla, P. Alexa, U. Köster, G. Thiamova, J.-M. Régis, J. Jolie, A. Blanc, A. M. Bruce, A. Esmaylzadeh, L. M. Fraile, G. de France, G. Häfner, S. Ilieva, M. Jentschel, V. Karayonchev, W. Korten, T. Kröll, S. Lalkovski, S. Leoni, H. Mach, N. Märginean, P. Mutti, G. Pascovici, V. Pazi, Z. Podolyák, P. H. Regan, O. J. Roberts, N. Saed-Samii, G. S. Simpson, J. F. Smith, T. Soldner, C. Townsley, C. A. Ur, W. Urban, A. Vancraeynest and N. Warr.
Lifetime measurements in the odd- A nucleus ^{177}Hf .
Phys. Rev. C 102 (2020), 054322.
- [11] V. Karayonchev, J. Jolie, A. Blazhev, A. Dewald, A. Esmaylzadeh, C. Fransen, G. Häfner, L. Knafla, J. Litzinger, C. Müller-Gatermann, J.-M. Régis, K. Schomacker, A. Vogt, N. Warr, A. Leviatan and N. Gavrielov.
Tests of collectivity in ^{98}Zr by absolute transition rates.
Phys. Rev. C 102 (2020), 064314.
- [12] V. Karayonchev, M. Stoyanova, G. Rainovski, J. Jolie, A. Blazhev, M. Djongolov, A. Esmaylzadeh, C. Fransen, K. Gladnishki, L. Knafla, D. Kocheva, L. Kornwebel, J.-M. Régis, G. De Gregorio and A. Gargano.
Lifetimes and structures of low-lying negative-parity states of ^{209}Po .
Phys. Rev. C 103 (2021), 044309.
- [13] G. Häfner, A. Esmaylzadeh, J. Jolie, J.-M. Régis, C. Müller-Gatermann, A. Blazhev, C. Fransen, R.-B. Gerst, V. Karayonchev, L. Knafla, N. Saed-Samii and Z. K.-O.
Lifetime measurements in ^{182}Pt using γ - γ fast-timing.
Eur. Phys. J. A 57 (2021), 174.
- [14] A. Esmaylzadeh, V. Karayonchev, G. Häfner, J. Jolie, M. Beckers, A. Blazhev, A. Dewald, C. Fransen, A. Goldkuhle, L. Knafla and C. Müller-Gatermann.
Triaxiality in the mid-shell nucleus ^{112}Pd .
Phys. Rev. C 103 (2021), 054324.
- [15] D. Kalaydjieva, D. Kocheva, G. Rainovski, V. Karayonchev, J. Jolie, N. Pietralla, M. Beckers, A. Blazhev, A. Dewald, M. Djongolov, A. Esmaylzadeh, C. Fransen, K. A. Gladnishki, A. Goldkuhle, C. Henrich, I. Homm, K. E. Ide, P. R. John, R. Kern, J.

- Kleemann, T. Kröll, C. Müller-Gatermann, M. Scheck, P. Spagnoletti, M. Stoyanova, K. Stoychev, V. Werner, A. Yaneva, S. S. Dimitrova, G. De Gregorio, H. Naïdja and A. Gargano.
- Microscopic structure of the one-phonon 2^+ states of ^{208}Po .**
Phys. Rev. C 104 (2021), 024311.
- [16] A. Esmaylzadeh, V. Karayonchev, K. Nomura, J. Jolie, M. Beckers, A. Blazhev, A. Dewald, C. Fransen, R.-B. Gerst, G. Häfner, A. Harter, L. Knafla, M. Ley, L. M. Robledo, R. Rodríguez-Guzmán and M. Rudigier.
Lifetime measurements to investigate γ softness and shape coexistence in ^{102}Mo .
Phys. Rev. C 104 (2021), 064314.
- [17] B. Das, B. Cederwall, C. Qi, M. Górska, P. H. Regan, Ö. Aktas, H. M. Albers, A. Banerjee, M. M. R. Chishti, J. Gerl, N. Hubbard, S. Jazrawi, J. Jolie, A. K. Mistry, M. Polettini, A. Yaneva, S. Alhomaidhi, J. Zhao, T. Arici, S. Bagchi, G. Benzoni, P. Boutachkov, T. Davinson, T. Dickel, E. Haettner, O. Hall, C. Hornung, J. P. Hucka, P. R. John, I. Kojouharov, R. Knöbel, D. Kostyleva, N. Kuzminchuk, I. Mukha, W. R. Plass, B. S. Nara Singh, J. Vasiljević, S. Pietri, Z. Podolyák, M. Rudigier, H. Rösch, E. Sahin, H. Schaffner, C. Scheidenberger, F. Schirru, A. Sharma, R. Shearman, Y. Tanaka, J. Vesić, H. Weick, H. J. Wollersheim, U. Ahmed, A. Algora, C. Appleton, J. Benito, A. Blazhev, A. Bracco, A. M. Bruce, M. Brunet, R. Canavan, A. Esmaylzadeh, L. M. Fraile, G. Häfner, H. Heggen, D. Kahl, V. Karayonchev, R. Kern, A. Korgul, G. Kosir, N. Kurz, R. Lozeva, M. Mikolajczuk, P. Napiralla, R. Page, C. M. Petrache, N. Pietralla, J.-M. Régis, P. Ruotsalainen, L. Sexton, V. Sanchez-Temble, M. Si, J. Vilhena, V. Werner, J. Wiederhold, W. Witt, P. J. Woods and G. Zimba.
Nature of seniority symmetry breaking in the semimagic nucleus ^{94}Ru .
Phys. Rev. C 105 (2022), L031304.
- [18] A. Mistry, H. Albers, T. Arıcı, A. Banerjee, G. Benzoni, B. Cederwall, J. Gerl, M. Górska, O. Hall, N. Hubbard, I. Kojouharov, J. Jolie, T. Martinez, Z. Podolyák, P. Regan, J. Tain, A. Tarifeno-Saldivia, H. Schaffner, V. Werner, G. Ağgez, J. Agramunt, U. Ahmed, O. Aktas, V. Alcayne, A. Algora, S. Alhomaidhi, F. Amjad, C. Appleton, M. Armstrong, M. Balogh, K. Banerjee, P. Bednarczyk, J. Benito, C. Bhattacharya, P. Black, A. Blazhev, S. Bottoni, P. Boutachkov, A. Bracco, A. Bruce, M. Brunet, C. Bruno, I. Burrows, F. Calvino, R. Canavan, D. Cano-Ott, M. Chishti, P. Coleman-Smith, M. Cortés, G. Cortes, F. Crespi, B. Das, T. Davinson, A. De Blas, T. Dickel, M. Doncel, A. Ertoprak, A. Esmaylzadeh, B. Fornal, L. Fraile, F. Galtarossa, A. Gottardo, V. Guadilla, J. Ha, E. Haettner, G. Häfner, H. Heggen, P. Herrmann, C. Hornung, S. Jazrawi, P. John, A. Jokinen, C. Jones, D. Kahl, V. Karayonchev, E. Kazantseva, R. Kern, L. Knafla, R. Knöbel, P. Koseoglou, G. Kosir, D. Kostyleva, N. Kurz, N. Kuzminchuk, M. Labiche, J. Lawson, I. Lazarus, S. Lenzi, S. Leoni, M. Llanos-Expósito, R. Lozeva, A. Maj, J. Meena, E. Mendoza, R. Menegazzo, D. Mengoni, T. Mertzimekis, M. Mikolajczuk, B. Million, N. Mont-Geli, A. Morales, P. Morral, I. Mukha, J. Murias, E. Nacher, P. Napiralla, D. Napoli, B. Nara-Singh, D. O'Donnell, S. Orrigo, R. Page, R. Palit, M. Pallas, J. Pellumaj, S. Pelonis, H. Pentilla, A. Pérez de Rada, R. Pérez-Vidal, C. Petrache, N. Pietralla, S. Pietri, S. Pigliapoco, J. Plaza, M. Polettini, C. Porzio, V. Pucknell, F. Recchia, P. Reiter, K. Rezykina, S. Rinta-Antila, E. Rocco, H. Rösch, P. Roy, B. Rubio, M. Rudigier, P. Ruotsalainen, S. Saha, E. Şahin, C. Scheidenberger, D. Seddon, L. Sexton, A. Sharma, M. Si, J. Simpson, A. Smith, R. Smith, P. Söderström, A. Sood, A. Soylu, Y. Tanaka, J. Valiente-Dobón, P. Vasileiou,

- J. Vasiljevic, J. Vesic, D. Villamarin, H. Weick, M. Wiebusch, J. Wiederhold, O. Wieland, H. Wollersheim, P. Woods, A. Yaneva, I. Zanon, G. Zhang, J. Zhao, R. Zidarova, G. Zimba and A. Zyriliou.
The DESPEC setup for GSI and FAIR.
Nucl. Instrum. Methods Phys. Res. A 1033 (2022), 166662.
- [19] S. Jazrawi, A. Yaneva, M. Polettini, B. Das, P. Regan, M. Górska, B. Cederwall, J. Jolie, H. Albers, M. Chishti, A. Banerjee, N. Hubbard, A. Mistry, M. Rudigier, G. Benzoni, J. Gerl, A. Bruce, Z. Podolyák, B. Nara Singh, G. Zhang, S. Alhomaidhi, C. Appleton, T. Arici, A. Blazhev, T. Davinson, A. Esmaylzadeh, L. Fraile, G. Häfner, O. Hall, P. John, V. Karayonchev, I. Koujoharov, N. Kurz, M. Mikolajczuk, N. Pietralla, S. Pietri, J. Regis, E. Sahin, L. Sexton, H. Schaffner, C. Scheidenberger, A. Sharma, J. Vesic, H. Weick and V. Werner.
Commissioning the FASt TIMing array (FATIMA) at FAIR Phase-0: Half-lives of excited states in the N=50 isotones ^{96}Pd and ^{94}Ru .
Radiat. Phys. Chem. (2022), 110234.
- [20] A. Harter, L. Knafla, G. Frießner, G. Häfner, J. Jolie, A. Blazhev, A. Dewald, F. Dunkel, A. Esmaylzadeh, C. Fransen, V. Karayonchev, K. Lawless, M. Ley, J.-M. Régis and K. O. Zell.
Lifetime measurements in the tungsten isotopes $^{176,178,180}\text{W}$.
Phys. Rev. C 106 (2022), 024326.
- [21] D. Kumar, T. Bhattacharjee, S. S. Alam, S. Basak, L. Gerhard, L. Knafla, A. Esmaylzadeh, M. Ley, F. Dunkel, K. Schomaker, J.-M. Régis, J. Jolie, Y. H. Kim, U. Köster, G. S. Simpson and L. M. Fraile.
Lifetimes and transition probabilities for low-lying yrast levels in $^{130,132}\text{Te}$.
Phys. Rev. C 106 (2022), 034306.
- [22] L. Knafla, A. Esmaylzadeh, A. Harter, J. Jolie, U. Köster, M. Ley, C. Michelagnoli and J.-M. Régis.
Development of a new γ - γ angular correlation analysis method using a symmetric ring of clover detectors.
Nucl. Instrum. Methods Phys. Res. A (2022), 167463.
- [23] V. Karayonchev, A. Blazhev, J. Jolie, A. Dewald, A. Esmaylzadeh, C. Fransen, G. Häfner, L. Knafla, C. Müller-Gatermann, G. Rainovski, J.-M. Régis, K. Schomacker and P. Van Isacker.
New aspects of the low-energy structure of ^{211}At .
Phys. Rev. C 106 (2022), 044321.
- [24] V. Karayonchev, G. Rainovski, J. Jolie, A. Blazhev, A. Dewald, A. Esmaylzadeh, C. Fransen, P. John, L. Knafla, D. Kocheva, K. Schomacker, V. Werner and H. Naïdja.
Lifetime measurements in the yrast band of ^{212}Po with a shell-model investigation.
Phys. Rev. C 106 (2022), 064305.
- [25] A. Esmaylzadeh, A. Blazhev, K. Nomura, J. Jolie, M. Beckers, C. Fransen, R.-B. Gerst, A. Harter, V. Karayonchev, L. Knafla, M. Ley and F. von Spee.
Investigation of γ softness: Lifetime measurements in $^{104,106}\text{Ru}$.
Phys. Rev. C 106 (2022), 064323.

Publications in conference proceedings

- [26] M. Stoyanova, G. Rainovski, J. Jolie, N. Pietralla, A. Blazhev, M. Djongolov, A. Esmaylzadeh, L. Gerhard, K. Gladnishki, V. Karayonchev, J. Keatings, R. Kern, D. Kocheva, T. Kröll, K. Mashtakov, O. Möller, J.-M. Régis, M. Scheck, K. Schomacker, J. Sinclair, C. Sürder, V. Werner and J. Wiederhold.
A study on the transition between seniority-type and collective excitations in ^{204}Po and ^{206}Po .
EPJ. Web Conf. 194, 03002 (2018), 03002.
- [27] D. Kocheva, A. Yaneva, D. Kalaydjieva, G. Rainovski, J. Jolie, N. Pietralla, M. Beckers, A. Blazhev, L. Bussmann, M. Cappellazzo, A. Dewald, F. Diel, M. Djongolov, F. Dunkel, A. Esmaylzadeh, B. Falk, C. Fransen, J. Garbe, L. Gerhard, R.-B. Gerst, K. A. Gladnishki, A. Goldkuhle, G. Hackenberg, C. Henrich, I. Homm, K. Ide, V. Karayonchev, R. Kern, J. Kleeman, L. Knafla, L. Kornwebel, T. Kröll, M. Ley, C. Müller-Gatermann, M. Scheck, T. Schmidt, P. Spagnoletti, M. Stoyanova and V. Werner.
Lifetime measurements of the low-lying excited states of ^{208}Po .
J. Phys. Conf. Ser. 1555 (2020), 012020.
- [28] M. Stoyanova, V. Karayonchev, G. Rainovski, J. Jolie, N. Pietralla, A. Blazhev, A. Dewald, M. Djongolov, A. Esmaylzadeh, C. Fransen, J. Garbe, L. Gerhard, K. A. Gladnishki, K. Ide, P. R. John, R. Kern, J. Kleemann, D. Kocheva, T. Kröll, C. Müller-Gatermann, J.-M. Régis, P. Spagnoletti, V. Werner and A. Yaneva.
Evolution of the structure of the 4_1^+ states in Po isotopes.
J. Phys. Conf. Ser. 1555 (2020), 012019.
- [29] M. Polettini, S. Jazrawi, M. M. R. Chishti, A. Y. and B. Das, A. Banerjee, N. Hubbard, A. K. Mistry, H. M. Albers, R. Shearman, M. Górska, J. Gerl, P. H. Regan, B. Cederwall, J. Jolie, S. Alhomaidhi, T. Arici, G. Benzoni, P. Boutachkov, T. Davinson, T. Dickel, E. Haettner, O. Hall, H. Heggen, P. R. John, I. Kojouharov, N. Kurz, B. S. N. Singh, S. Pietri, Z. Podolyak, M. Rudigier, E. Sahin, H. Schaffner, C. Scheidenberger, A. Sharma, J. Vesic, H. Weick, H. J. Wollersheim, U. Ahmed, Ö. Aktas, A. Algora, C. Appleton, J. Benito, A. Blazhev, A. Bracco, A. Bruce, M. Brunet, R. Canavan, A. Esmaylzadeh, L. M. Fraile, H. Grawe, G. Häfner, D. Kahl, V. Karayonchev, R. Kern, G. Kosir, R. Lozeva, P. Napiralla, R. Page, C. M. Petrache, J. Petrovic, N. Pietralla, J.-M. Régis, P. Ruotsalainen, L. Sexton, V. Sanchez-Temble, M. Si, J. Vilhena, V. Werner, J. Wiederhold, W. Witt, P. Woods and G. Zimba.
DESPEC Phase-0 campaign at GSI.
IL Nuovo Cimento C 044 (2021).
- [30] M. Polettini, J. Pellumaj, G. Benzoni, J. J. Valiente-Dobón, G. Zhang, D. Mengoni, R. M. P. Vidal, D. Genna, A. Bracco, G. Aggez, U. Ahmed, Ö. Aktas, M. A. Aqueel, B. Alayed, H. M. Albers, A. Algora, S. Alhomaidhi, C. Appleton, T. Arici, M. Armstrong, K. Arnsward, M. Balogh, A. Banerjee, J. B. Garcia, A. Blazhev, S. Bottoni, P. Boutachkov, A. Bruce, C. Bruno, F. Camera, B. Cederwall, M. M. R. Chishti, M. L. Cortés, D. M. Cox, F. C. L. Crespi, B. Das, T. Davinson, G. D. Angelis, T. Dickel, M. Doncel, R. Donthi, A. Ertoprak, R. Escudeiro, A. Esmaylzadeh, L. M. Fraile, L. Gaffney, E. R. Gamba, J. Gerl, M. Górska, A. Gottardo, J. Ha, E. Haettner, O. Hall, H. Heggen, Y. Hrabar, N. Hubbard, S. Jazrawi, P. R. John, J. Jolie, C. Jones, D. Joss, D. Judson, D. Kahl, V. Karayonchev, E. Kazantseva, R. Kern, L. Knafla, I. Kojouharov, A. Korgul, W. Korten, P. Koseoglou, G. Kosir, D. Kostyleva, T. Kurtukian-Nieto, N. Kurz, N. Kuzminchuk, M. Labiche, S.

Lenzi, S. Leoni, M. L. Expósito, R. Lozeva, T. J. Mertzimekis, M. Mikolajczuk, B. Million, A. K. Mistry, A. Morales, I. Mukha, J. R. Murias, D. Napoli, B. S. N. Singh, D. O'Donnell, S. E. A. Orrigo, R. Page, S. Pelonis, J. Petrovic, N. Pietralla, S. Pietri, S. Pigliapoco, Z. Podolyak, C. Porzio, B. Q. Arnes, F. Recchia, P. H. Regan, J.-M. Régis, P. Reiter, K. Rezyunkina, P. Roy, M. Rudigier, P. Ruotsalainen, E. Sahin, L. G. Sarmiento, M.-M. Satrazani, H. Schaffner, C. Scheidenberger, L. Sexton, A. Sharma, J. Smallcombe, P.-A. Söderström, A. Sood, P. Vasileiou, J. Vesic, J. Vilhena, L. Waring, H. Weick, V. Werner, J. Wiederhold, O. Wieland, K. Wimmer, H. J. Wollersheim, P. Woods, A. Yaneva, I. Zanon, J. Zhao, R. Zidarova, S. Ziliani, G. Zimba and A. Zyriliou.

Decay studies in the $A \sim 225$ Po-Fr region from the DESPEC campaign at GSI in 2021.

IL Nuovo Cimento C 045 (2022).

Acknowledgements – *Danksagung*

I would like to thank all the people who contributed and helped me over my years working on this thesis. My special thank goes to:

- Prof. Dr. Jan Jolie for giving me the opportunity to conduct many experiments at the FN-Tandem accelerator and supporting any idea that I tried to accomplish. For helping me with theoretical approaches, especially the IBM, and the interpretation of my results. But also for my scientific and personal development.
- Prof. Dr. Andreas Zilges for his time and willingness to be the second examiner and review my work. His nuclear physics lecture in my bachelors studies is the reason I started my research in nuclear physics.
- Prof. Dr. Andreas Schadschneider for his time being the chairman of the examination.
- Prof. Dr. Alfred Dewald for his time, help and interest in performing two-neutron transfer reaction experiments. Also for his help and the fruitful discussions about the RDDS technique.
- Dr. Christoph Fransen for keeping the many setups at the Tandem operator always in good shape which is of key importance for the whole institute. I am grateful to him for being always available to make sure every experiments is running optimally. For sharing his knowledge about the RDDS technique and many fruitful discussions.
- Dr. Andrey Blazhev for many useful discussion on different nuclear structure aspects. I thank him also for providing excellent plunger targets for many of the experiments in this work.
- Dr. Vasil Karayonchev for helping me during the analysis, showing me different approaches and ideas to resolve problems, fruitful discussions about new experiments and our friendship.
- Dr. Jean-Marc Régis for his expertise of the fast-timing method and helping during the analysis.
- Dr. Nigel Warr for all the discussion we had on a large variety of topics and for proofreading this thesis.
- Marcel Beckers, Franziskus von Spee and Claus Müller-Gatermann for their help during Plunger experiments, useful discussions about the analysis process and helping me with their experience about the RDDS technique.
- Ulli Köster and Yung-Hee Kim for helping me to perform the experiment at the Lohengrin spectrometer where I learned a lot about the spectrometer and nuclear structure in general. Also I thank them for the very good time we had at the ILL in Grenoble.

- the Tandem operators for keeping the Tandem operator in good shape and providing the needed beams to perform the experiments for this work.
- for all the shifters during my experiments and all members of the IKP Köln for a nice working atmosphere.
- Lukas Knafla for his patience proofreading of all my works (and even this sentence) and his interest in improving the analysis. For fruitful discussions about nuclear physics and our friendship where we also discussed many other problems.
- Mario Ley, Andreas Harter, Guillaume Häfner and Rosa-Belle Gerst for all the discussions we had on large variety of topics and fun during our time together in the institute.
- Ulrich Michel, Felix Heim and Susan Herb for the time from school to finishing our doctoral thesis.
- all my friends (outside of physics), especially Felix Heider and Oliver Mohs for the years of friendship, you were always there to motivate me.
- last but not least my family, especially my brother, for their general support in every way

Contribution to publications essential for this thesis

Publication I:

Lifetimes and shape coexistence in ^{97}Sr

- A. Esmaylzadeh, J.-M. Régis, Y. H. Kim and U. Köster commissioned the setup at the Lohengrin spectrometer
- A. Esmaylzadeh and J.-M. Régis planned and carried out the experiment
- A. Esmaylzadeh performed the data analysis of the experiment
- K. Nomura, L. M. Robledo and R. Rodríguez-Guzmán performed the interacting boson-fermion model calculation
- A. Esmaylzadeh wrote the paper

Publication II:

Triaxiality in the mid-shell nucleus ^{112}Pd

- A. Esmaylzadeh, V. Karayonchev, C. Müller-Gatermann and C. Fransen commissioned the Plunger setup
- A. Esmaylzadeh and V. Karayonchev, planned and carried out the experiment
- A. Esmaylzadeh performed the data analysis of the experiment
- A. Esmaylzadeh performed the interacting boson model calculation, the Davydov-Filippov calculation and the γ -soft calculation
- A. Esmaylzadeh wrote the paper

Publication III:

Lifetime measurements to investigate γ -softness and shape coexistence in ^{102}Mo

- A. Esmaylzadeh, V. Karayonchev, M. Beckers and C. Fransen commissioned the Plunger setup
- A. Esmaylzadeh and V. Karayonchev, planned and carried out the experiment
- A. Esmaylzadeh performed the data analysis of the experiment
- K. Nomura performed the interacting boson model calculation
- A. Esmaylzadeh wrote the paper

Manuscript I:

Lifetime measurements to investigate γ -softness in $^{104,106}\text{Ru}$

- A. Esmaylzadeh, M. Beckers, C. Fransen and F. von Spee commissioned the Plunger setup
- A. Esmaylzadeh, M. Beckers, C. Fransen and F. von Spee planned and carried out the experiment

- A. Blazhev produced the target
- A. Esmaylzadeh performed the data analysis of the experiment
- K. Nomura performed the interacting boson model calculation
- A. Esmaylzadeh wrote the paper

Curriculum vitae

Persönliche Daten

Name: Arwin Esmaylzadeh
Anschrift: Wevelinghovener Straße 19, 50670 Köln
Geburtsdatum: 23. März 1993
Geburtsort: Köln
Nationalität: deutsch
Familienstand: ledig

Hochschulstudium und Promotion

2018-2022 Promotion an der Universität zu Köln
im Fach Experimentalphysik
2015-2017 Studium der Physik an der Universität zu Köln
(M.Sc. Physik)
2012-2015 Studium der Physik an der Universität zu Köln
(B.Sc. Physik)

Arbeitsverhältnisse

seit 2018 Wissenschaftlicher Mitarbeiter am Institut für Kernphysik
der Universität zu Köln
2015-2017 Studentische Hilfskraft am Institut für Kernphysik
der Universität zu Köln

Schulbildung

2006-2012 Ernst-Mach Gymnasium, Hürth
2003-2006 Johann-Gottfried-Herder Gymnasium, Köln
1999-2003 Montessori Grundschule, Köln

Erklärung zur Dissertation

Hiermit versichere ich an Eides statt, dass ich die vorliegende Dissertation selbstständig und ohne die Benutzung anderer als der angegebenen Hilfsmittel und Literatur angefertigt habe. Alle Stellen, die wörtlich oder sinngemäß aus veröffentlichten und nicht veröffentlichten Werken dem Wortlaut oder dem Sinn nach entnommen wurden, sind als solche kenntlich gemacht. Ich versichere an Eides statt, dass diese Dissertation noch keiner anderen Fakultät oder Universität zur Prüfung vorgelegen hat; dass sie - abgesehen von unten angegebenen Teilpublikationen und eingebundenen Artikeln und Manuskripten - noch nicht veröffentlicht worden ist sowie, dass ich eine Veröffentlichung der Dissertation vor Abschluss der Promotion nicht ohne Genehmigung des Promotionsausschusses vornehmen werde. Die Bestimmungen dieser Ordnung sind mir bekannt. Darüber hinaus erkläre ich hiermit, dass ich die Ordnung zur Sicherung guter wissenschaftlicher Praxis und zum Umgang mit wissenschaftlichem Fehlverhalten der Universität zu Köln gelesen und sie bei der Durchführung der Dissertation zugrundeliegenden Arbeiten und der schriftlich verfassten Dissertation beachtet habe und verpflichte mich hiermit, die dort genannten Vorgaben bei allen wissenschaftlichen Tätigkeiten zu beachten und umzusetzen. Ich versichere, dass die eingereichte elektronische Fassung der eingereichten Druckfassung vollständig entspricht.

Teilpublikationen

- A. Esmaylzadeh *et al.* "Lifetimes and shape coexistence in ^{97}Sr ".
Phys. Rev. C 100, 064309 (2019)
- A. Esmaylzadeh *et al.* "Triaxiality in the mid-shell nucleus ^{112}Pd ".
Phys. Rev. C 103, 054324 (2021)
- A. Esmaylzadeh *et al.* "Lifetime measurements to investigate γ softness and shape coexistence in ^{102}Mo ".
Phys. Rev. C 104, 064314 (2021)
- A. Esmaylzadeh *et al.* "Investigation of γ softness: Lifetime measurements in $^{104,106}\text{Ru}$ ".
Phys. Rev. C 106, 064323 (2022)

Köln, den 16. Januar 2023

(Arwin Esmaylzadeh)